Wetting Mechanisms on Silicone Surfaces with Liquid, Frozen, and Vaporous Water

Dissertation
zur Erlangung des Grades
Doktor der Ingenieurwissenschaften (Dr.-Ing.)

Lukas Hauer
geboren in Bad Soden, Ts.

Fachbereich Maschinenbau
Technische Universität Darmstadt
Darmstadt 2023

Wetting Mechanisms on Silicone Surfaces with Liquid, Frozen, and Vaporous Water

Dissertation
von Lukas Hauer aus Bad Soden Ts.

Berichterstatter: Prof. Dr. Ing. Peter Stephan
Mitberichterstatterin: Prof. Dr. phil. Doris Vollmer
Tag der Einreichung: 24. Januar 2023
Tag der mündlichen Prüfung: 18. April 2023
Darmstadt 2023
D17 (Diss. Darmstadt)

Kurzfassung

Silikonbeschichtungen sind wasserabweisend und haben geringe Kontaktreibung, was sich in einer hohen Mobilität von benetzenden Tropfen ausdrückt. Oberflächen mit solchen Eigenschaften eignen sich für Selbstreinigung, Schmierung, Anti-Icing/Biofouling, Verringerung des Fließwiderstandes und verbesserte Wärme- und Stoffübertragung. Daher haben Silikonbeschichtungen Relevanz in zahlreichen Bereichen, z. B. in der Biomedizintechnik, Automobilindustrie, Luft- und Raumfahrt und im Elektronik-Sektor. Silikone bestehen aus Polymerketten; das am häufigsten vorkommende Silikon ist Polydimethylsiloxan (PDMS). PDMS ist untoxisch, umweltfreundlich, sicher und einfach verarbeitbar mit gut einstellbaren Materialeigenschaften. Im Folgenden werden drei PDMS-Beschichtungen besprochen, die sich in ihrer Kettenvernetzung unterscheiden: PDMS-Öl-Beschichtungen (freie Ketten), PDMS-Elastomer-Beschichtungen (vernetzte Ketten) und PDMS-Ketten-Beschichtungen (einzeln verankerte Ketten). Benetzende Tropfen (und auch Festkörper) induzieren Anpassungen der PDMS-Beschichtung in ihrer Form und/oder ihrer Zusammensetzung. Solche induzierten Anpassungen verändern die Kontaktreibung und können im Laufe der Zeit zu irreversiblen strukturellen Verschlechterungen der Beschichtung führen. Wenn Phasenwechsel (Kondensation/Sublimation/Frostbildung) auf der Beschichtung stattfinden, fallen die Beschichtungsanpassungen (Kontaktreibung und Funktionalitätsabnahme) anders aus. Ein Verständnis der Benetzungsszenarien (z. B. erzwungene Benetzung oder Phasenwechsel) und deren Konsequenzen ist maßgeblich zur Entwicklung optimierter und dauerhafter Beschichtungen. Untersuchungen dieser Prozesse sind mit Herausforderungen verbunden, da die Beschichtungsanpassungen auf Zeit- und Längenskalen um Größenordnungen streuen, eine Vielzahl physikalischer und chemischer Konzepte involviert ist und die Benetzungskomponenten (Tropfen/Beschichtung) stark gekoppelt sind. Dies bringt selbst moderne experimentelle/ numerische Methoden an ihre Grenzen.

In dieser kumulativen Dissertation untersuche ich die Mechanismen, die mit Benetzung einhergehen (Tropfengleiten, Kondensation, Frostbildung, Sorption) auf PDMS-Beschichtungen (Öl/Elastomer). Ich nutze direkte Visualisierung der Benetzung von PDMS-Beschichtungen mit mikro- und makroskopischen Techniken (z. B. konfokale Mikroskopie). Ich konzentriere mich auf Nicht-Gleichgewichts-Prozesse (z. B. Tropfengleiten oder Reif- und Frostbildung) um die dynamischen Anpassungen der PDMS-Beschichtung zu untersuchen. Ich verwende kontinuumsmechanische und thermodynamische Konzepte, um experimentelle Resultate analytisch und numerisch zu modellieren. Dieser komplementäre Ansatz liefert ein grundlegendes Verständnis der Benetzungsinteraktionen auf theoretischer Ebene, das durch experimentelle Erkenntnisse gestützt wird. Dadurch kann die Beschichtung optimal auf das Benetzungsszenario (und die Anwendung) abgestimmt werden. Erfolgt eine solche Abstimmung nicht, ist die Oberflächenfunktionalität suboptimal und verschlechtert sich im Laufe der Zeit. Ich veranschauliche dies anhand von Tropfengleiten auf PDMS-Elastomeren: Schnelles Gleiten führt zu hohen Oberflächenreibungen und damit zu schlechten Tropfenmobilitäten. Langsames Gleiten führt zur schnellen Abnutzung der Oberfläche, da Teile des Beschichtungsmaterials vom Tropfen mitgenommen werden. Der optimale Betriebspunkt wird bei mittlerer Gleitgeschwindigkeit erreicht, bei der Oberflächenreibung und -alterung gering sind. Ein ähnliches Optimum zeige ich bei der Frostbildung auf PDMS-Ölbeschichtungen: Schnelle und "stachelige" Frostbildung in Verbindung mit schlechter Ölrückhaltung bewirkt schnelle Ölverarmung. Der optimale Betriebspunkt liegt in wärmeren, sehr trockenen oder sehr feuchten Atmosphären. Ist die Oberfläche mit nanometrischen Strukturen ausgestattet, erhöht dies die Ölrückhaltung.

Abstract

Silicone coatings show low contact friction, water repellency, and high mobility of wetting drops - features that are necessary for self-cleaning, lubrication, anti-icing/-biofouling, drag-reduction, and enhanced heat and mass transfer. For this, silicone coatings are found in numerous fields, such as life science, aerospace, automotive, and electronic industry. Silicones comprise polymeric chains; the most abundant silicone is polydimethylsiloxane (PDMS). PDMS is benign, environmentally friendly, safe, and easy to process, while its material properties are highly tunable. In the following, three distinct PDMS coatings are considered, which are distinguished by chain reticulation: PDMS oil coatings (mobile chains), PDMS elastomer coatings (crosslinked chains), and PDMS chain coatings (single-grafted chains). Contacting drops (and solids, too) induce shape and/or composition adaptations on the PDMS coating. Such wetting-induced coating responses alter the contact friction temporally and may cause irreversible structural degradation, over time. When phase change (condensation/sublimation/frosting) is involved the coating response (contact friction and surface deterioration) can be different. Understanding the coating responses to imposed wetting scenarios (e.g. forced wetting or phase change) is pivotal for smart coating designs with optimized and lasting surface functionality. Gaining insight, however, is challenging as the surface responses scatter over orders of magnitude on time and length scales, a multitude of physical and chemical concepts are involved, and the wetting interplayers are highly coupled. This brings even modern experimental and numerical methods to their limits and the full spectrum of surface responses is still elusive.

In this cumulative dissertation, I explore wetting-associated mechanisms (*i.e.*, drop sliding, condensation, frosting, and sorption) on PDMS coatings (*i.e.*, oil, elastomer). I utilize micro- and macroscopic visualization (e.g. confocal microscopy) of different wetting scenarios. I focus on non-equilibrium wetting processes (e.g. drop sliding or frost formation) to explore the dynamic response of the PDMS coating. I use continuum mechanical and thermodynamical concepts to model experimental observations analytically and numerically. This complementary approach delivers a fundamental understanding of the wetting interactions on a theoretical level, supported by experimental evidence. This understanding allows coating and application to be matched, providing optimized surface functionality. In cases of mismatches, the surface may malfunction and degrade over time. In particular, I illustrate this with moving drops on PDMS elastomers: fast drop movement yields high surface dissipation, thus, poor drop mobility. However, slow movement yields strong surface deterioration as the coating material is (partially) entrained by the drop. The optimal operation point is met at intermediate sliding speeds, where surface dissipation and deterioration are low. In another demonstration, I show this optimal operation point for PDMS oil coatings under frost conditions: when frost forms fast and spiky, and the oil retention on the surface is poor, rapid oil depletion is unavoidable. The optimal operating point is found in warmer, very dry, or very humid atmospheres while the surface is equipped with nanometric scaffold structures to increase oil retention.

Acknowledgements

This now is the gist of my three-and-a-half-year journey as a Ph.D. student at the Max Planck Institute for Polymer Research. I feel very grateful for the experiences I could make and the brilliant people I got to know. A couple of these people shaped me and my thinking very much and, in that sense, had great contributions to this thesis. Here I want to thank them.

First of all, I want to thank my advisor **Dr. Doris Vollmer**. Her high scientific standards and complementary thinking constantly motivated me to critically consider my scientific work, leading to results that I am very much proud of. I also want to thank **Dr. Hans-Jürgen Butt** and **Dr. Peter Stephan** for co-advising me and providing me with helpful insight.

I wish to thank my collaboration partners **Dr. Lou Kondic** and **Dr. Burkhard Dünweg** with whom I had the honor to have excellent theoretical discussions, where I learned a lot about fluid dynamics and soft matter physics.

I am also thanking my collaborators **Zhuoyun Cai** and **Dr. Jonathan T. Pham** in Lexington, KY, who I could visit during my secondment and learn much about silicones and confocal microscopy.

I want to thank my (ex)colleagues, **Dr. Abhinav Naga** and **Dr. William S. Y. Wong** for endless discussions, hiking and biking sessions, and companionship in my scientific journey. I also want to thank **Dr. Philipp Baumli**, **Dr. Katharina I. Hegner**, and **Dr. Maria D'Acunzi**, who helped me with chemistry and material science, and **Rodrique G. M. Badr** with whom I had great discussions on polymers and wetting. I want to thank **Dr. Anke Kaltbeitzel** for helping me with optics and for great discussions and **Azadeh Sharifi-Aghili** who provided me with many many test surfaces for my experiments. I am thanking **Dr. Md Ehsanul Alam** who introduced me to the domain of research and soft wetting.

Finally, I would like to thank my partner **Ronja Becker** who supported me and was a great help to manage the pressure, particularly during my last year - but also my sister **Sina Hauer**, her small family **Philippe R.** and **Lias P. Kässler**, and all my friends. I want to thank my parents **Sylke Witt** and **Harald Hauer** who always supported me and sparked my dedication and curiosity.

This work was supported by the German Research Foundation (DFG) with the Priority Programme 2171 on Dynamic Wetting of Flexible, Adaptive, and Switchable Surfaces.

Contents

List of Publications

This cumulative dissertation includes five appended publications [1–5] (cf. appendices B.1-B.5), listed below.

- [1] (cf. App. B.1) Lukas Hauer†, Zhuoyun Cai†, Artem Skabeev, Doris Vollmer Jonathan T. Pham, Phase Separation in Wetting Ridges of Sliding Drops on Soft and Swollen Surfaces Aug. 2022. arXiv: 2208.11177 [cond-mat]. (accepted in *Physical Review Letters*)
- [2] (cf. App. B.2) William SY Wong, Lukas Hauer, Abhinav Naga, Anke Kaltbeitzel, Philipp Baumli, Rüdiger Berger, Maria D ‘Acunzi, Doris Vollmer, and Hans-Jürgen Butt, Adaptive Wetting of Polydimethylsiloxane. *Langmuir* 36, no. 26 (2020): 7236-7245.
- [3] (cf. App. B.3) Philipp Baumli†, Lukas Hauer†, Emanuela Lorusso†, Azadeh Sharifi Aghili, Katharina I. Hegner, Maria D’Acunzi, Jochen S. Gutmann, Burkhard Dünweg, and Doris Vollmer *Soft Matter* 18, no. 2 (2022): 365-371.
- [4] (cf. App. B.4) Lukas Hauer†, William SY Wong†, Valentina Donadei, Katharina I. Hegner, Lou Kondic, and Doris Vollmer *ACS Nano* 15, no. 3 (2021): 4658-4668.
- [5] (cf. App. B.5) Lukas Hauer, William SY Wong, Azadeh Sharifi-Aghili, Lou Kondic, and Doris Vollmer *Physical Review E* 104, no. 4 (2021): 044901.

† equal contribution

Author Contribution

In Sec. B.1, I conceptualized the project with Doris Vollmer and Jonathan T. Pham. Zhuoyun Cai and I planned and conducted the experiments. Artem Skabeev synthesized the fluorescence dye, and I conducted image processing with self-written code. Zhuoyun Cai, Doris Vollmer, and Jonathan T. Pham assisted with data analysis. I developed a theoretical model to explain the experimental findings, and discussed it with Zhuoyun Cai, Doris Vollmer, and Jonathan T. Pham. Doris Vollmer, Jonathan T. Pham, and I did the drafting and revision of the manuscript. All authors reviewed and approved the manuscript.

In Sec. B.2, I provided the data processing and assisted with expertise in diffusion processes. I, along with William S. Y. Wong, analyzed the system analytically to understand the phenomenon. Maria D‘Acunzi and William S. Y. Wong fabricated the surfaces. William S. Y. Wong carried out the experiments and characterization unless otherwise stated. Abhinav Naga and Anke Kaltbeitzel supported experiments on surface tension measurements and confocal microscopy. Philipp Baumli and Rüdiger Berger discussed and improved our understanding of ultra-thin PDMS controls (brushes) and supplementary atomic force microscopy measurements, respectively. William S. Y. Wong, I, Doris Vollmer, and Hans-Jürgen Butt contributed to experimental planning, data analysis, and manuscript preparation. All authors reviewed and approved the manuscript.

In Sec. B.3, I developed image processing code and contributed to the formal analysis of the experimental finding of the experiments. I created the numerical simulation of the microchannel flow, coupled to the mass transport of the shared interface between hydrogel and oil flow. Together with Burkhard Dünweg, I created a kinematic boundary condition at the shared interface, to account for the dehydration mass transport under non-equilibrium conditions. I validated the model using experimental data. I participated in the original drafting of the manuscript and the revision process, together with Philipp Baumli, Burkhard Dünweg, and Doris Vollmer. Philipp Baumli contributed to the conceptualization and conducted the experiments. Emanuela Lorusso contributed to the conceptualization and synthesis of the hydrogels. She participated in writing the original draft. Azadeh Sharifi Aghili, Katharina I. Hegner, and Maria D'Acunzi synthesized the SU-8 surfaces. Jochen S. Gutmann, Burkhard Dünweg, and Doris Vollmer provided supervision. All authors reviewed and approved the manuscript.

In Sec. B.4, I constructed the experimental setup together with William S. Y. Wong. Valentina Donadei and I carried out the experiments. I wrote the analysis software and conducted the data analysis. I developed the long wave approximation and wrote the numerical solver with the help of Lou Kondic. I, William S. Y. Wong, Lou Kondic, and Doris Vollmer did the original drafting of the manuscript and did the revision process. William S. Y. Wong and Katherina I. Hegner fabricated the surfaces. All authors reviewed and approved the manuscript.

In Sec. B.5, I conceptualized the project, together with William S. Y. Wong, Lou Kondic, and Doris Vollmer. I planned and conducted the experiments, wrote software for image analysis to recognize frost fractals, and analyzed the data in terms of geometry, fractality, and dynamics. I developed the mass transport model. I participated in the original drafting and revision of the manuscript, together with William S. Y. Wong, Lou Kondic, and Doris Vollmer. Azadeh Sharifi Aghili synthesized the SU-8 surfaces. All authors reviewed and approved the manuscript.

Declartation

I hereby declare that I have written this thesis independently, except for the help expressly mentioned in it.

Lukas Hauer, Mainz 24. January 2023

Nomenclature

Symbol	Meaning	Unit
A	Area	m^2
$A_{\mathrm{nuc,base}}$	Nucleus Base Area	m^2
$A_{\mathrm{nuc,cap}}$	Nucleus Cap Area	m^2
A_l	Area (Liquid)	m^2
A_s	Area (Solid)	m^2
A_{sl}	Area (Solid-Liquid)	m^2
α	Texture Area Fraction	–
$\boldsymbol{\epsilon}^{\boldsymbol{S}}$	Surface Strain Tensor	–
$\boldsymbol{\epsilon}$	Strain Tensor	–
$\boldsymbol{\sigma}$	Stress Tensor	$\mathrm{N/m}^2$
$\boldsymbol{\tau}$	Internal Stress Tensor	$\mathrm{N/m}^2$
$\boldsymbol{\Upsilon}$	Surface Tension Tensor	N/m
$\boldsymbol{I}$	Identity Matrix	–
δF	Free Energy Variation	J
δF_{max}	Nucleation Free Energy Barrier	J
Δh	Latent Heat	$\mathrm{J/m}^3$
Δp_o	Laplace Pressure (Oil-Ambient)	$\mathrm{N/m}^2$
Δp_{ow}	Laplace Pressure (Oil-Water)	$\mathrm{N/m}^2$
Δp_{wa}	Laplace Pressure (Water-Ambient)	$\mathrm{N/m}^2$
ΔU	Excess Free Energy	J
$\delta_{e,\mathrm{I}}$	Elastocapillary Length (Drop)	m
$\delta_{e,\mathrm{II}}$	Elastocapillary Length (Elastomer)	m
η_0	Shear Modulus	$\mathrm{N/m}^2$
γ	Surface Energy	$\mathrm{J/m}^2$
γ_c	Surface Energy (Cloak)	$\mathrm{J/m}^2$
γ_l	Surface Energy (Liquid)	$\mathrm{J/m}^2$
γ_o	Surface Energy (Oil)	$\mathrm{J/m}^2$
γ_o^Σ	Thin Film Surface Energy (Oil)	$\mathrm{J/m}^2$
γ_{ow}	Surface Energy (Oil-Water)	$\mathrm{J/m}^2$
γ_{ow}^Σ	Thin Film Surface Energy (Oil-Water)	$\mathrm{J/m}^2$
γ_w	Surface Energy (Water)	$\mathrm{J/m}^2$
κ	Mean Curvature	$1/\mathrm{m}^2$
Π	Disjoining Pressure	$\mathrm{N/m}^2$
ρ	Mass Density	$\mathrm{kg/m}^3$
$\sigma_\perp$	Normal Stress Component	$\mathrm{N/m}^2$
$\sigma_{\|\|}$	Lateral Stress Component	$\mathrm{N/m}^2$
θ	Contact Angle	°
θ_{app}	Apparent Contact Angle	°
θ_{app}^S	Apparent Pseudo Yang Contact Angle	°
θ_a	Advancing Contact Angle	°
θ_c	Critical Imbibition Angle	°
θ_r	Receding Contact Angle	°
θ_Y	Young's Angle	°
Υ	Surface Tension	N/m
Υ_e	Surface Tension (Elastomer)	N/m
Υ_{el}	Surface Tension (Elastomer-Liquid)	N/m
Υ_s	Surface Tension (Solid)	N/m
$\Upsilon_s^{\mathrm{eff}}$	Effective Surface Tension (Solid)	N/m

Symbol	**Meaning**	**Unit**
Υ_{sl}	Surface Tension (Solid-Liquid)	N/m
$\Upsilon_{sl}^{\text{eff}}$	Effective Surface Tension (Solid-Liquid)	N/m
ϑ	Neumann Angle	°
$\vec{f}$	Force Vector	N
$\vec{n}$	Normal Vector	–
$\vec{t}$	Tangential Vector	–
$\vec{t}_{ow}$	Tangential Vector (Oil-Water)	–
$\vec{t}_l$	Tangential Vector (Liquid)	–
$\vec{t}_o$	Tangential Vector (Oil)	–
$\vec{t}_s$	Tangential Vector (Solid)	–
$\vec{t}_w$	Tangential Vector (Water)	–
$\vec{u}$	Displacement Vector	m
$\vec{x}$	Coordinate Vector	m
D^*	Imbibition Mobility	m^2/s
f	Force	N
f_{cap}	Capillary Force	N
g	Acceleration due to Gravity	m/s^2
h_0	Initial Film Height	m
h_c	Cloak Film Height	m
h_f	Oil Film Height	m
k	Geometrical Coefficient	–
n	Number of Molecules	–
p	Pressure	N/m^2
P_{diss}	Dissipation Power	N m/s
p_a	Pressure (Ambient)	N/m^2
p_l	Pressure (Liquid)	N/m^2
r	Radius	m
r_{nuc}	Nucleus Radius	m
r_{oa}	Radius of Curvature (Oil-Ambient)	m
r_{ow}	Radius of Curvature (Oil-Water)	m
ρ	Density	kg/m^3
s	Surface Curve	m^2
S	Spreading Coefficient	N/m
t	Time	s
V_{nuc}	Volume (Nucleus)	m^3
V_e	Volume (Wetting Ridge)	m^3
V_a	Volume (Ambient)	m^3
V_l	Volume (Liquid)	m^3
w	Width	m
x_{cl}	Location of Three-Phase-Contact Line	m
x_1, x_2, x_3	Coordinate Component	m
z	Vertical Coordinate Component	m

Chapter 1

Introduction

When water comes in contact with the surface of another medium, we call their interactions 'wetting'. If the two interact very well, water tends to fully cover the other medium. In this 'complete wetting' case, water forms a closed film over the entire surface of the second medium. In nature, this feature is utilized by plants and insects to harvest water when groundwater is scarce. Water vapor in the atmosphere condenses on water-attracting surfaces, ready for consumption [6–9]. Inspired by nature, engineers and scientists develop similar techniques. Fog harvesting via engineered materials might help to resolve drinking water scarcity in desolated regions of the planet [10, 11]. On windshields or optical lenses, condensation might be unavoidable. On these surfaces, closed water films are advantageous since they do not scatter the transmitted light but maintain clear visuals [12].

The interactions between liquid and surface are not always sufficiently strong to form a closed film. When the interactions gradually weaken, the closed film can rupture at a critical crossover point [13–16]. In this 'dewetting' process isolated drops gradually form on the surface. This wetting mode corresponds to 'partial wetting'. The geometry of a sessile drop tells a lot about the affinity between the liquid and the surface [17]. Flat drops indicate attraction between the drop and the surface. Opposingly, round drops translate to repulsion[1]. A more quantitative metric that tells how well drop and surface interact is the contact angle [18, 19]. This angle measures the opening angle of the drop to the surface and lies between 0° and 180°. A surface that forms contact angles below 90° is considered to be a good water attractor - they are 'hydrophilic'. When the contact angle exceeds 90°, the surface is 'hydrophobic'. Surfaces that create contact angles between 150° and 180° form the special class of 'superhydrophobic' surfaces [20, 21]. Drops on such kinds of surfaces are very mobile because of the little contact area between drop and surface [22, 23]. The lotus leaf is probably the most prominent illustration of superhydrophobicity [24]. The evolutionary reason for the plant leaves to develop water repellency is their self-cleaning capability. Contacting drops roll over the leaves, pick up dust and dirt, and entrain the contaminants along [25]. Cleaner leaves improve

---

[1] This is true for water drops with radii smaller than ≈ 3 mm. Bigger drops flatten by gravity, independent of the underlying surface.

photosynthesis and hence, optimize carbohydrate production. Self-cleaning finds high interest and acute relevance in many technical applications such as solar cells, drag reduction, anti-fouling in biomedical equipment, outdoor textiles, etc [26–32].

The contact behavior of water varies with the chemical and structural properties of the surface. In the past, the properties of surfaces used to be considered inert to wetting liquids. But this is not necessarily the case. Polymeric surfaces, *i.e.*, surfaces that comprise long, polymer chains are excellent examples where the surface properties can change in course of wetting [33]. Such polymeric surfaces are abundant in engineering applications and a frequent material choice for biomaterials, membranes, semiconductors, coatings, etc. [34–42]. The rich wetting interactions enable smart surface designs in a plethora of applications ranging from sophisticated high-tech to day-to-day household products. The softness and the flexibility of the surface yields low contact friction and thus excellent lubrication properties [43–45] which can be utilized for joint lubrication [46] or drag reduction [47, 48]. The low surface adhesion is exploited for applications in anti-icing [41, 49–51], anti-marine fouling [52], and anti-microbial formation [53–57]. Heat and mass transfer can be optimized as polymeric surfaces provide high nucleation rates while maintaining also high drop mobility [58–60]. Polymeric surfaces are also used to interface biological systems, e.g. to control the growth and the size of cells [61, 62].

The wetting interactions on a polymeric surface govern the coating function. To provide optimal and lasting coating functionality it is elemental to understand the wetting interactions in a given application. Misinterpretation of the wetting interactions can lead to malfunction and deterioration of the coating. However, such understanding is challenging as the interactions are complex with strong coupling between the interplayers and requires consideration on many levels. During polymer wetting, various forms of mass, momentum, and energy exchange take place on length scales ranging from the molecular structure of the polymer (Å) to the macroscopic drop (cm). The associated timescales scatter accordingly from picoseconds up to days. The liquid drop can mix to some extent with the underlying polymer and vice versa [2, 63, 64]. The various materials can undergo chemical reactions or change their state of matter [65]. This alters the molecular structure of either or both, the surface and the liquid [33, 66]. If the polymer is a liquid, interesting wetting competitions emerge, where the polymer might engulf and cloak the drop [67–69]. The cloak changes the drop affinity to the surface and therefore affects the contact angle. Interactions between drop and surface are particularly high in the vicinity of the so-called ’three-phase-contact line’ [70, 71]. At this location, the drop meets with the surface and surrounding medium (a third fluid such as air). Here, the surface tension of the sessile drop exerts pulling stress on the surface. On many rigid surfaces such as metals or glass, the stress is minor compared to the internal material stresses. Polymers, however, are soft, even when they come as a rubber. The cohesive forces in the polymer might not be sufficient to oppose the pulling stress. Consequently the surface deforms [72–75]. These observations illustrate that polymeric materials undergo all kinds of wetting-induced responses; considering them as inert draws an incomplete picture of their wetting behavior. The multitude of the wetting interactions requires an interdisciplinary approach from engineering, physics, chemistry, material science, and even mathematics to grasp the entirety of polymeric wetting. All this makes experimental and theoretical investigations challenging, and the full spectrum of polymeric wetting interactions is still elusive.

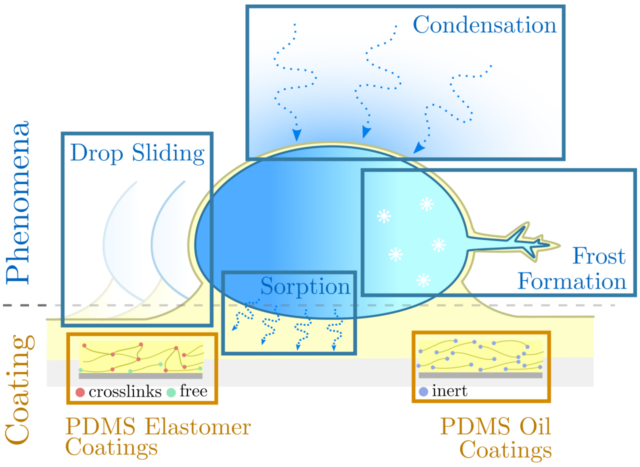

Figure 1.1: This cumulative thesis discusses (water) drop sliding on crosslinked PDMS elastomer coatings - and also condensation, frosting and sorption of water on/in liquid PDMS oil coatings.

In this thesis, I explore the wetting interactions between water and a special class of polymeric surfaces that are silicone coatings. The investigations aim to develop a detailed picture of the coating response. In particular, I will discuss wetting mechanisms that consider I) forced wetting on rubbery silicone, [1] and [2]; II) water transport in silicone oil, [3]; and III) wetting induced by phase-change, *i.e.*, condensation and frosting, on silicone oil lubricated surfaces, [4] and [5]. The investigations link coating design parameters and operation conditions to coating functionality (drop mobility, condensation/frosting rates, sorption control) and durability (when and why surface malfunctions occur). The core result in each of the investigation is to list the parameters, both on the coating side and the imposed condition, that need to be optimized to find the best operation point.

In Sec. 1.1, I will start to introduce general wetting concepts that are helpful and utilized throughout every chapter. I will focus on the wetting interactions of water. Water is abundant in many technical and biological systems and is therefore a particularly interesting working fluid [76–79]. Water does not always wet surfaces in a liquid state. In Sec. 1.2, I discuss how water condenses, freezes, or sublimates on surfaces. On the surface side, I focus on silicone coatings as silicones count as the most important and widely used polymers in engineering applications [80]. Silicone coatings can be either 'lubricant-infused', 'elastomeric', or 'liquid-like', depending on the reticulation of the silicone polymer. Each of these coatings exhibits different wetting properties. In Sec. 1.3 I give a general discussion on silicone, the different coating types, and their wetting behavior.

1.1 Wetting Concepts

When two, immiscible phases - where at least one is liquid - come in contact with each other we call this process wetting. A range of important physical features is associated with this process, which shall be discussed now, starting with the surface tension.

1.1.1 Surface Energy and Surface Tension

The contact area (or the contact line, in 2D) between the two media is the 'shared interface'. To form this interface, energy is required. To convince oneself about this fact, one can consider how much energy δF it requires to rip up a medium and increase the area δA, Fig 1.2 a. The energy δF balances to the energy of the newly created interface

$$\delta F = \delta \left(A\gamma \right). \tag{1.1}$$

Here, γ is the intrinsic energy of the surface ('surface energy'). The energy δF can be induced mechanically. In this picture, a 'surface tension' Υ acts against the imposed mechanical stress, such that they (energetically) balance per

$$\delta \left(A\gamma \right) = \Upsilon \delta A. \tag{1.2}$$

On a microscopic level, molecules interact by a range of forces (e.g. van der Waals, electrostatic, steric, hydrophobic, and many more [81]). Interactions in the bulk are usually symmetric and isotropic around each molecule and material specific. At the interface where two materials meet, this symmetry is broken, leading to excess energy ΔU [82], Fig 1.2 b. The excess energy is related to the surface energy by the number of molecules δn, sitting at the interface

$$\gamma = \frac{\delta n}{\delta A} \Delta U. \tag{1.3}$$

The surface tension can also be approached from molecular mechanics. For this, one can evaluate the isotropy of the internal stress tensor [83]. This is the Eulerian norm of the difference between the normal and the shear stress components, *i.e.*, $\left\| \sigma_\perp - \sigma_{||} \right\|$, Fig 1.2 c. Tracking the stress isotropy along an interface normal and integrating it along this rectangular variable yields the surface tension

$$\Upsilon = \int \left\| \sigma_\perp - \sigma_{||} \right\| dz. \tag{1.4}$$

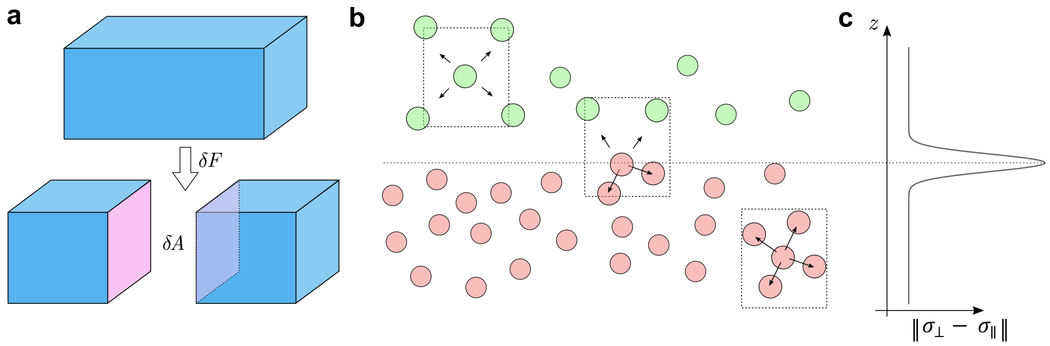

Figure 1.2: Concepts of surface tension and surface energy. **a)** The energy to bisect the large box is δF. Two smaller boxes have an increased area δA, compared to the large box. **b)** Molecular picture of two phases, represented by green (top) and red (bottom) beads. Molecular interactions are symmetric in the bulk. Symmetry is broken at the interface, leading to excess free energy and surface energy. **c)** Stress isotropy $\|\sigma_\perp - \sigma_\parallel\|$ along the interface normal z.

For interfaces shared by a liquid and a fluid, γ usually is not affected by surface deformations. This is due to the ability of molecules at the interface to rearrange. The average distance and the average excess energy ΔU [Eq. (1.3)] remain constant. The total free energy of a liquid is therefore

$$\delta F = \gamma \delta A, \tag{1.5}$$

According to the energy minimization principle, in equilibrium, the free energy is $\delta F = 0$. This condition is fulfilled with a 'minimal energy surface'. In practice, this leads to spherical droplets but also more complex shapes are possible (e.g. catenoid, unduloid, nodoid, etc.). However, these more complex shapes are found very rarely. Another feature of liquid-fluid interfaces is that surface energy and surface tension are equivalent, $\gamma = \Upsilon$. The surface energy of a fluid surface can therefore be mechanically measured by imposing an external force. One of the most common practical methods in research and industry is the pendant drop method [84], where a large drop[2] hangs from the outlet of a syringe and is suspended to gravity, Fig. 1.3a. The free energy functional becomes

$$\delta F = \gamma \delta A + g\rho\delta z, \tag{1.6}$$

where the second term on the right-hand side is the hydrostatic potential, with $g = 9.81$ m/s^2 being the gravitational acceleration, ρ the density, and z the vertical distance from the null level. The surface tension can be found at equilibrium, where $\delta F = 0$. The geometrical coefficient $\delta z/\delta A$ can be measured directly by profiling the shape of the deformed drop. Other methods such as the Wilhelmy plate method or the Du Noüy ring measure surface tensions by deforming the liquid-fluid interface, Fig. 1.3b,c. Usually, these methods are more sensitive. In practice, however, they find less application due to the more skillful measurement conduction.

---

[2] The drop size should exceed the capillary length, $\sqrt{\gamma/\rho g}$.

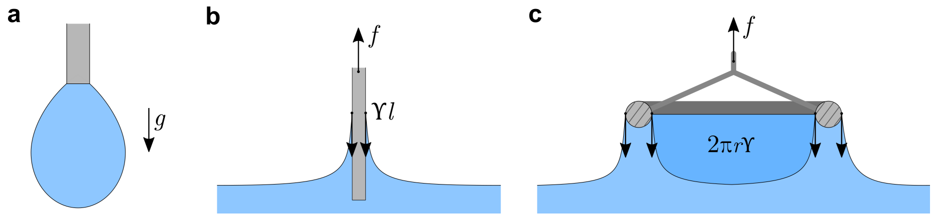

Figure 1.3: Different types of surface tension methods. **a)** Pendant drop. A large drop hangs from the tip of the syringe and deforms due to gravity. **b)** Wilhelmy plate method. A plate (typically platinum) is pulled out of a liquid reservoir. The required force f balances with the surface tension Υ. **c)** Du Noüy ring method. Similar to Wilhelmy's plate but with a ring.

On solids - and in particular, on soft gels - the surface energy is not the same as the surface tension [85]. Because molecules at a solid-fluid interface cannot freely rearrange, deformation can introduce internal stresses. The internal stresses add to the excess energy ΔU per molecule. Internal stresses do not need to be homogeneously distributed but can vary along the location on the surface. The surface tension becomes a second-order tensor $\boldsymbol{\Upsilon}$. On solid-fluid interfaces, the relation between the surface energy and the surface stress can be found by equating Eqs. (1.1) and (1.2),

$$\mathrm{tr}\left(\boldsymbol{\Upsilon}\right)\delta A = A\delta\gamma + \gamma\delta A, \tag{1.7}$$

Stretching or compressing the interface changes the interfacial area changes[3] with $A = A_0\left[1 + \mathrm{tr}(\boldsymbol{\epsilon}^S)\right]$. Here, A_0 is the area of reference configuration and $\boldsymbol{\epsilon}^{\boldsymbol{S}}$ the interfacial strain tensor. Hence, the surface tension can be expressed as

$$\boldsymbol{\Upsilon} = \gamma\boldsymbol{I} + \left[1 + \mathrm{tr}\left(\boldsymbol{\epsilon}^{\boldsymbol{S}}\right)\right]\frac{\partial\gamma}{\partial\boldsymbol{\epsilon}^S}. \tag{1.8}$$

Eq. (1.8) is known as the Shuttleworth equation [86, 87]. While originally introduced in 1950 it obtained recent momentum in the wetting community. The Shuttleworth effect was utilized to show anisotropic wetting behavior on unidirectional stretched PDMS surfaces [88–90].

1.1.2 Contact Angle and Laplace Pressure

Most broadly, wetting considers interactions between a liquid and a second medium which can be another liquid or a solid (or some exotic combination of both). Historically, however, the second medium is considered to be a flat, solid surface. In this picture, the shape of the liquid can deform freely while the solid surface is rigid and maintains an invariant shape. This system of liquid in contact with the solid surface is solely governed by surface energies. The surface tension between the liquid and the solid is denoted as Υ_{sl}. Liquid and solid are both exposed to a third, fluid phase (most of the time air). In theoretical considerations, the third phase is sometimes assumed to be a vacuum. Here, we denote the surface tension between each, the solid and the liquid to the third phase

---

[3] For small deformations.

as Υ_s and γ_l. To find the liquid configuration in equilibrium, we write down the total free energy function and apply the variational principle. We constrain this search by enforcing conservation of mass in the liquid and the ambient, *i.e.*, $dV_l = dV_a = 0$. The functional reads then

$$\delta F = \Upsilon_{sl}\delta A_{sl} + \gamma_l \delta A_l + \Upsilon_s \delta A_s - p_l dV_l - p_a dV_a, \tag{1.9}$$

where p_l and p_a are Lagrangian multipliers that are interpreted as the pressure in the respective phases. Eq. (1.9) shows that, indeed, to minimize δF the liquid needs to assume a shape with a minimal surface. Consequently, the liquid forms spherical drops, Fig. 1.4. However, due to the interaction with the solid surface, the liquid does not form a complete sphere but only the cap of a sphere. Thus, the changes in surface area between liquid and solid are given by

$$\delta A_{sl} = \left\{2\pi r \sin^2\theta\right\}\delta r + \left\{2\pi r^2 \sin\theta\cos\theta\right\}\delta\theta, \tag{1.10}$$

where r is the radius of the spherical cap and $r\sin\theta$ is the radius of the liquid footprint on the solid. θ is the 'contact angle' that the liquid forms with the solid surface. This contact angle is extremely important as it gives a direct and measurable metric on the affinity between liquid and solid. The radius r and the contact angle θ are the two independent variables that govern the shape of the drop. Changes in surface area between the liquid and the exterior (ambient) phase are

$$\delta A_l = \left\{4\pi r\left(1-\cos\theta\right)\right\}\delta r + \left\{2\pi r^2\sin\theta\right\}\delta\theta, \tag{1.11}$$

The volume of the liquid spherical cap changes by

$$\delta V_l = \left\{r^2\pi\left(2+\cos\theta\right)\left(1-\cos\theta\right)^2\right\}\delta r - \left\{r^3\pi\sin\theta\left(\cos\theta-\tfrac{1}{3}\right)\right\}\delta\theta. \tag{1.12}$$

Another perk of this approach is, that the sum of the surface area $A_s + A_{sl}$ and the total volume $V_l + V_a$ stay constant. Therefore, their changes sum up to zero, $\delta A_s + \delta A_{sl} = 0$ and $\delta V_l + \delta V_a = 0$. Introducing the expressions of the geometrical changes into the functional (1.9) yields

$$\begin{aligned}\delta F = \Big\{&2\pi r\sin^2\theta\left(\Upsilon_{sl}-\Upsilon_s\right) + \gamma_l 4\pi r\left(1-\cos\theta\right) + \\ &\left(p_l-p_a\right)\pi r^2\left(\cos\theta-1\right)^2\left(\cos\theta+2\right)\Big\}\delta r + \\ \Big\{&2\pi r^2\cos\theta\sin\theta\left(\Upsilon_{sl}-\Upsilon_s\right) + \gamma_l 2\pi r^2\sin\theta - \\ &\left(p_l-p_a\right)\pi r^3\sin\theta\left(\cos\theta-\tfrac{1}{3}\right)\Big\}\delta\theta.\end{aligned} \tag{1.13}$$

Minimizing this functional for r and θ[4] gives two independent equilibrium equations. The first one is the Young-Dupré equation,

---

[4] Both terms in the curly brackets on the right-hand side of Eq. (1.13) need to be zero for small variations on δr and $\delta\theta$.

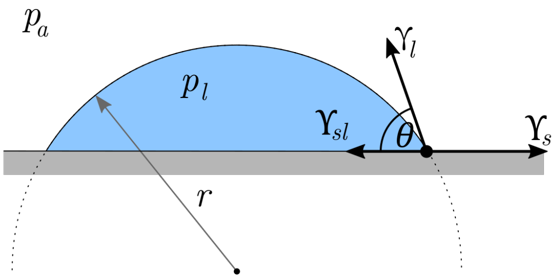

Figure 1.4: Shape of a wetting liquid. The liquid forms a spherical drop when the shape of the drop is only governed by surface energies. The drop is defined by the contact angle θ and the radius r. The difference between the pressure in the ambient p_a and in the drop interior p_l is due to the curved interface. The pressure differential is the Laplace pressure $\Delta p = 2\gamma_l/r$.

$$\gamma_l \cos\theta + \Upsilon_{sl} - \Upsilon_s = 0. \tag{1.14}$$

Solid wetting in this configuration (rigid solid) was rigorously investigated for centuries and observed even longer. In 1805 was the first time it was scientifically documented by Thomas Young [17]. Notably, in his original work Young characterizes wetting without a mathematical framework but purely phenomenological. Only later, in 1896 Athanase Dúrpe formulated Young's findings mathematically [91]. However, both approached their findings, not from an energetic point of view but rationalized with forces as physical energies were no common concept at the time.

The second equilibrium equation from Eq. (1.13) concerns the pressure difference between the ambient and the inside of the liquid. This pressure differential reads

$$p_a - p_l = \frac{2\gamma_l}{r}. \tag{1.15}$$

This equation is known as the 'Young-Laplace equation', and the pressure differential $\Delta p = p_a - p_l$ is the 'Laplace pressure'[5]. The Laplace pressure is not a unique feature of spherical drops but occurs whenever a liquid interface with a non-zero surface tension becomes curved. Generally, the Young-Laplace equation relates the pressure differential to the surface tension multiplied by the curvature. The curvature κ is a feature from differential geometry and is related to the second derivative of the interfacial profile[6]. The general formulation of the Laplace pressure is

$$\Delta p = \kappa\gamma_l. \tag{1.16}$$

Typically, it comprises two main curvatures from two principal directions. In the special case of a (symmetric) spheroid, the curvature becomes $\kappa = 2/r$.

---

[5] After Pierre-Simon Laplace who developed the mathematical framework of the pressure, shortly after Thomas Young's considerations [92].

[6] Let an interfacial profile be parameterized by the curve s. The curvature is then $\kappa = \nabla \cdot (\nabla s / \|\nabla s\|)$

1.1.3 Surface Wettability

The contact angle assumes values between 0° and 180°. According to Young's equation (1.14), the contact angle at $\theta = 90°$ is special: For $\theta < 90°$ the surface tension of the solid exceeds the one between solid and liquid, *i.e.*, $\Upsilon_{sl} < \Upsilon_s$. In this case, the drop tends to cover the surface as the smaller surface tension of the solid-liquid surface minimizes the total free energy. If the liquid is water, surfaces with $0° < \theta < 90°$ are considered to be 'hydrophilic', Fig. 1.5a. In the case of $\theta > 90°$, the argument goes in the other direction. Now, it is more favorable for the drop to cover less surface area as the $\Upsilon_{sl} > \Upsilon_s$. Surfaces are referred to as 'hydrophobic', Fig. 1.5b.

A special class of these surfaces is formed by the 'superhydrophobic' surfaces where $\theta > 150°$, Fig. 1.5c. These surfaces are characterized by strong water repellency and high drop mobility. While this kind of surface attained strong academic interest within the last two decades[7] they usually lack robustness or scalability which makes them seldom encounters in practical applications.

Young's equation limits cases where $\Upsilon_s - \Upsilon_{sl} - \gamma_l < 0$, as $\cos\theta \leq 1$. This regime describes cases where drops form on the surface. However, some liquids rather form closed films without drop formation, Fig. 1.5d. This case applies when the surface tension of the solid exceeds the one of the summed surface tension of liquid-ambient and liquid-solid surface, $\Upsilon_s - \Upsilon_{sl} - \gamma_l > 0$. A useful metric to distinguish between the two cases is the spreading coefficient

$$S = \Upsilon_s - \Upsilon_{sl} - \gamma_l, \tag{1.17}$$

which is negative ($S < 0$) in the case of 'partial wetting', and positive ($S \geq 0$) in cases of 'complete wetting'.

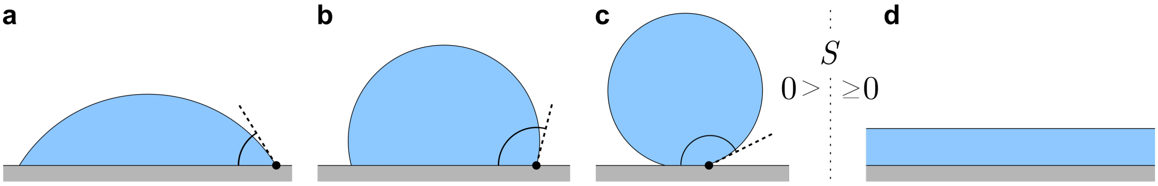

Figure 1.5: Different states of wetting. Partial wetting ($S < 0$) with **a)** hydrophilic surface ($0° < \theta < 90°$), **b)** hydrophobic surfaces ($90° < \theta < 180°$), and **c)** superhydrophobic surfaces ($150° < \theta < 180°$). **d)** Complete wetting for $S \geq 0$.

1.1.4 Contact Angle Hysteresis

The contact angle given in Eq. (1.14) is the concept of an 'ideal' surface. Such a surface is perfectly smooth, chemically homogeneous, and mostly a theoretical concept. The contact angle on an ideal surface is also known as the 'Young's angle' θ_Y. In reality, however, surfaces are always rough and

---

[7] Over 20,000 publications are listed under 'superhydrophobicity' or 'superhydrophobic' in Web of Science ™. 2022 is the first year of a declining record count.

heterogeneous. Therefore, the contact angle around the three-phase contact line of a drop has not one single value. The contact angle rather lies in a range between a maximum and a minimum. A straightforward method to gauge these two limiting angles is to bring the contact line into very slow motion. The subjective 'very slow motion' implies, that the contact line propagation takes place in quasi-equilibrium, *i.e.*, all transient relaxations are over-damped. When the contact line is brought into advancing (the contact line moves towards the ambient), the contact angle first increases while the contact line is pinned. At some point, the contact angle approaches the maximum angle and stays at this level while the contact line starts to move, Fig. 1.6a. This angle is the advancing contact angle θ_a. In the receding case when the contact line is brought into movements towards the liquid, the contact angle first decreases until it reaches the 'receding contact angle' θ_r, Fig. 1.6b. Note that the previously discussed quasi-equilibrium implies no dependency of the θ_a and θ_r on the contact line propagation speed. The difference between the two angles is the 'contact angle hysteresis'

$$\Delta\theta = \theta_a - \theta_r. \tag{1.18}$$

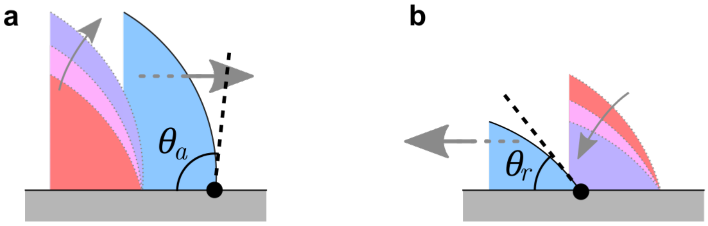

Figure 1.6: Contact angle hysteresis is limited by **a)** advancing contact angle θ_a and **b)** receding contact angle θ_r. Red, pink, and purple are pinned drops.

$\Delta\theta$ is a measure of the smoothness/homogeneity of the surface. Thus, a perfect (ideal) surface is characterized by $\Delta\theta \to 0$. The contact angle hysteresis can also be utilized as a proxy for the dissipation that builds up during drop motion on the surface. This is because the local contact angle is associated with the capillary force at the contact line that balances with dissipative forces. The capillary force around the three-phase contact line in the lateral direction follows from the ring integral around the contact line of the surface tension (vector) in the parallel plane of the horizontal:

$$f_{\text{cap}} = \oint \gamma_l \vec{t_l} \cdot \vec{t_s} dS. \tag{1.19}$$

Here, $\vec{t_l}$ and $\vec{t_s}$ are tangential vectors of the drop at the three-phase contact line and the horizontal plane, respectively. The dot product gives $\vec{t_l} \cdot \vec{t_s} = \cos\theta$, where θ is modulated around $[\theta_a, \theta_r]$ on the contact line. The definite integral computes to [93–95]

$$f_{\text{cap}} = wk\gamma_l \left(\cos\theta_a - \cos\theta_r\right), \tag{1.20}$$

where w is the width of the drop and k is a geometrical constant, related to the exact footprint shape of the moving drop. Values for k were reported in the range between $1/2$ to $\pi/2$, considering circular to highly distorted footprint profiles [96–99]. The dissipation force is of viscous origin; A molecular model explaining the dissipation considers that the contact line propagates by jumping from one (molecular) surface site to the next [100, 101]. The jump from one site to the next is considered a process whereby a characteristic activation barrier needs to be overcome. In that sense, contact line propagation can be regarded as a successive overcoming of (thermodynamic) meta-stable states. The activation energy here is related to the adhesive interactions between the molecular surface site and the liquid, their spatial distribution frequency, and the viscosity of the liquid.

Recently, wetting induced surface adaptations were considered to invoke contact angle hysteresis. Wetting induced surface adaptions may be molecular reorientation, diffusion/swelling (composition), surface charging, electric double layer formation, adsorption or the removal of contaminants, etc [2, 33, 64, 102, 103]. As a consequence, the surface tension between liquid and solid changes and the wetting configuration is altered [per Eq. (1.14)]. Each of these adaption process is associated with characteristic time scales. The time scales can range from picoseconds to days, depending on the process. Upon drop sliding, the contact time between drop and the underlying surface differs from the front and the rear end. Therefore, the surfaces are locally adapted differently, leading to different local surface tension, and hence, to a $\Delta\theta$. The adaptation induced $\Delta\theta$ will then depend on the adaptation time scale, the drop sliding speed, and the size of the moving drop.

1.2 Wetting and Phase Change

In the previously discussed examples, we see that not only the chemical and structural properties of the surface are relevant merits for water behavior on surfaces - but also ambient conditions such as temperature and humidity play a pivotal role. To understand this better, I will first discuss the concept of nucleation of water on surfaces.

At room temperature[8] and moderate humidity water usually comes over mechanical (gravitational) actions in contact with surfaces, such as impinging rain drops. When the temperature of the surface subceeds the temperature in the ambient water can condense on the surface through thermodynamic phase change [104]. Water is abundant in the atmosphere; the amount can vary but is limited by the 'saturation point'. The thermodynamic state variables (pressure, volume, temperature) set the level of the saturation point. The ambient atmosphere maintains mostly (*i.e.*, on average) constant volume and pressure. Hence, the ambient temperature is the dominator of the terrestrial saturation point. Increasing the temperature leads to a higher saturation point, and more

---

[8] $T \approx 19 - 25^\circ$ C.

water can reside in the air. Decreasing the temperature brings the saturation point down. When hot air with high water content is objected to a cold surface, the air cools down while its saturation point drops until the water content in the air surpasses the saturation point. Consequently, water precipitates from the air and starts to condense. Condensation starts with the formation of nanometric-sized spherical nuclei [105, 106]. The free energy of the nuclei rises with the surface area A_{nuc} as the formation of surface costs energy (cf. Sec. 1.1.1) and falls with the volume V_{nuc} as the bulk reduces its energy by undergoing phase change (*i.e.*, the latent heat Δh is released upon nucleation). A stable nucleus is formed when the surface energy balances with the bulk energy. Such a balance is found when the nucleus size is r_{nuc}, Fig. 1.7a. The surface energy costs of nucleation of spherical water drops in air are extremely high. For pure substances, the energetic price of a water-air interface counts as the most expensive one (72 mJ/m^2) and is only exceeded by mercury-air (485 mJ/m^2) [107], Fig. 1.7b. But there is a cheaper alternative: water can nucleate directly on the surface [108]. Since the surface is colder than the ambient, the saturation point is accordingly stronger suppressed. Here, the affinity to precipitate water is the highest. More importantly, water can nucleate directly on the surface leading to an (energetical) cheap interface with the surface. Energetic costs for interfaces between materials whereof none is gaseous are significantly reduced. This stems from the increased interactions between water molecules and the molecules from the non-gaseous surface [109]. Hence, it is much more favorable for water to build an interface on the surface and not toward the air, Fig. 1.7b inset. This mode of nucleation is known as heterogeneous nucleation. Hydrophilic and hydrophobic surfaces do not have the same tendency to initiate condensation. Here, the interfacial-cost argument holds again. Hydrophilicity is associated with water attraction. This reflects in low energy costs per interface on hydrophilic surfaces. For hydrophobic surfaces, this reasoning goes oppositely. The total energy cost of nucleation is [105, 110]

$$\delta F = \Delta h \delta V_{\text{nuc}} - \delta A_{\text{nuc,cap}} \gamma_l + \delta A_{\text{nuc,base}} \left(\Upsilon_{sl} - \Upsilon_s \right). \tag{1.21}$$

Here, $A_{\text{nuc,cap}}$ and $A_{\text{nuc,base}}$ are the area of the base and the cap of the nucleus, respectively. Fig. 1.7 plots the free energy change upon nucleation. The maximum peak is the energy barrier to form stable nuclei, found at r_{nuc}. The inset in plot Fig. 1.7b shows how the surface affinity, represented by the contact angle θ (cf. Sec. 1.1.2) decreases the energy costs of the interface.

Tuning a surface from hydrophilic to hydrophobic can engineer condensation initializers or dampers, depending on the requirements at hand. Cooling applications show interesting examples since they often demand both design features: hydrophilicity to increase nucleation rates and hydrophobicity to prevent surface flooding. Drop condensation is a very good method to transport heat (approx. 2.2 MJ for each condensed kg). When the condensation progresses the nucleated drops grow, coalesce, and might form closed water films. The heat is then conducted through the

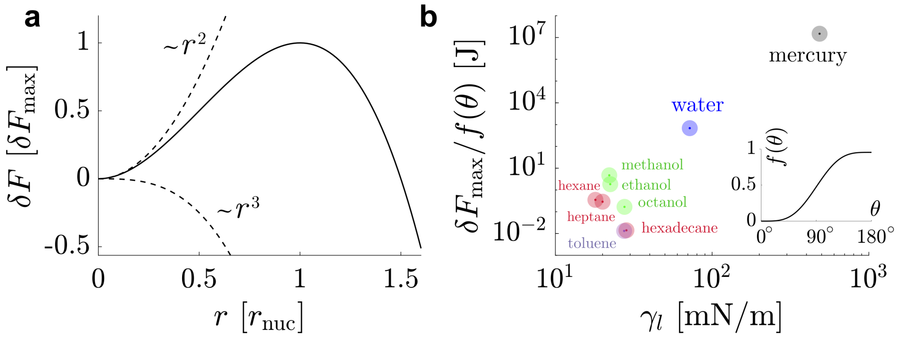

Figure 1.7: Energy costs for nucleation. **a)** Free energy landscape of nucleation. $\Delta F_{\max}$ is the maximum energy and the barrier of nucleation, found at r_{nuc}. **b)** Energy costs for condensation of some alkanes, some alcohols, water, and mercury. Inset; Contribution of the surface wettability to $\Delta F_{\max}$, $f(\theta) = (2 + \cos\theta)(1 - \cos\theta)^2$ [111].

film where only approx. 4.2 kJ/kg is transported. This switch of heat transport results in an efficiency loss of around 500 times. To keep the heat transfer efficiency high drop-wise condensation with the associated nucleation is required. This demands a trade-off between hydrophilic and hydrophobicity for the surface design choice [112–114]. When the surface temperature is sufficiently low, water starts to form not in a liquid but a solid state. Icing from vapor can happen directly as a desublimation process. This is a typical mode of ice formation in extremely cold and dry conditions. Under moderate but still sufficiently cold conditions a phase of liquid water condensation precedes ice formation, generally known as 'condensation-frosting' [115]. In technical systems, the formation of frost is nearly always undesired. When ice forms on wind turbines, they need to be shut off for security reasons. Iced power lines bend and break under the increased load. In cryogenic plants, frozen valves and displays can not be steadily operated. Thus, designing surfaces that retard or repel frost formation is highly desired. Silicone-based surfaces showed promising features for the retardation, repellency, and removal of ice [41, 50, 51, 116]. However, water forming on surfaces *via* phase-change tears differently on the surface, compared to liquid wetting. Solid ice adheres much stronger to the surface compared to liquid water [117]. Ice removal leads to surface damage and loss of function. Ice and frost[9] to an even stronger degree attracts liquids such as silicone oil due to the porous topology (a process driven by capillarity called 'wicking') [118]. This can lead to silicone depletion and surface damage [4, 49]. Understanding the complex interactions between silicone surface and phase-change induces water formation is key to overcoming these durability issues.

1.3 Silicones and Wetting

Silicones form one of the most relevant classes of polymers. In the year 2020 alone, the annual production of some silicones is estimated to be in the order of 45-227 thousand tons [119]. The most

---

[9] The formation of frost from water vapor.

abundant silicone is the linear polymer 'polydimethylsiloxane' (PDMS). PDMS is biocompatible, flexible, water repellent, provides low contact friction, is chemically stable, and easy and safe to process [80, 120–127]. These properties make PDMS a popular material choice in e.g., the medical sector, rapid prototyping, and coatings in industry and households.

Chemically, PDMS is a compound of sub-molecules, comprising silicon and organic radicals, bound by oxygen[10]. PDMS has a glass transition temperature[11] of approximately -150 °C and is therefore very flexible and liquid at room temperature [128]. With the addition of a chemical agent (a so-called 'crosslinker'), the material can cure and obtain solid-like features. The molecular group that sits at the ends of the chain (*i.e.*, end-group) determines if crosslinking is possible. If the chains are terminated by reactive hydroxyl[12] or vinyl[13] groups, the PDMS is susceptible to cross-linking and the formation of networks. These networks carry the name 'elastomers' due to the elastic component added by the crosslinks. Depending on the added amount of cross-linker, the material obtains stiffness between 1 kPa and 10 MPa [129–133]. The curing process is extremely safe and does neither involve any toxic chemicals, nor hazardous reaction-conditions such as extreme temperatures or pressures. Termination with nonreactive trimethylsilyl[14] keeps PDMS in a liquid oil state [122]. The viscosity of PDMS oil is highly tunable *via* the chain length of the polymer, ranging from 0.65 cSt to $20,000,000$ cSt [134]. When PDMS chains meet hydroxyl surface groups[15], they tend to form covalent bonds and form molecular thin layers. This happens on many metal oxide surfaces (such as glass) as they abundantly provide hydroxyl surface groups [135]. Silicones have both organic and inorganic compounds. The organic content in PDMS is relatively low compared to other silicones due to the small organic methyl radical[16]. Some literature suggests that this is the reason for the poor miscibility of alcohols in PDMS [136]. More recent studies, however, suggest that the immiscibility stems rather from the polar nature of alcohols[17], which is incompatible with apolar PDMS [137]. Water interacts very weakly with PDMS and dissolves to only ≈ 770 ppm in PDMS [138–140].

The surface of PDMS is water repellent (hydrophobic) because of the apolar methyl groups that interact only weakly with the polar H_2O water molecules. Especially for coating applications, the wetting interactions of PDMS surfaces are interesting. Different types of coatings can be created by changing how PDMS polymers are arranged on the surface. The three main types are PDMS oil coatings (cf. Sec. 1.3.1), PDMS elastomer coating (cf. Sec. 1.3.2), and PDMS chain coating (cf. Sec.

---

[10] Chem. struct. of monomers: $(CH_3)_2SiO$

[11] Temperature below the amorphous material transition to a hard, 'glassy' state.

[12] Chem. struct.: OH

[13] Chem. struct.: $R - CH = CH_2$; Note the double bond between the carbon atoms.

[14] Chem. struct.: $(CH_3)_3Si$

[15] Molecules attached to a surface.

[16] Chem. struct.: CH_3; Methyl is the smallest of all organic groups.

[17] Most alcohol molecules (R) are polar due to their ubiquitous hydroxyl end group

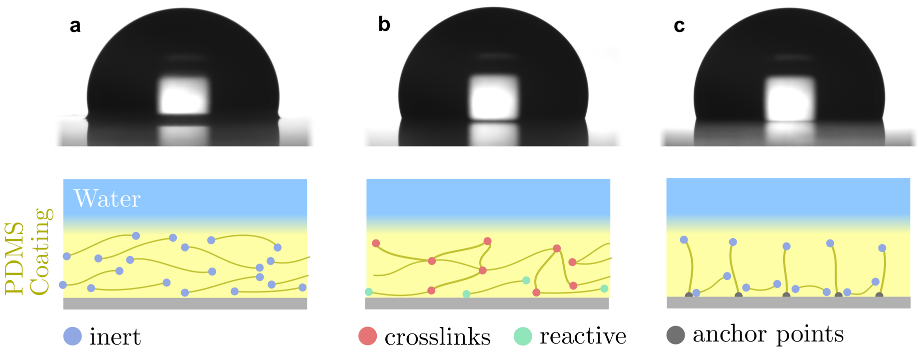

Figure 1.8: Shadowgraphs of sessile water drops (10 μl) on surfaces with different kinds of PDMS coatings. The molecular structure of each PDMS coating is illustrated below. The contact line aligns (roughly) with the horizontal reflection axis of the drops. **a)** PDMS oil-infused surface. The meniscus at the contact line is the characteristic, annular wetting ridge that wetting drops on liquid-infused surfaces develop. PDMS is liquid as the end groups of molecule chains are inter (blue; trimethylsilyl terminated). **b)** PDMS gel-coated surfaces. The thickness of the coating is approximately 100 μm. The coating consists mostly of cross-linked (red points) end groups. Depending on the synthesis, not all chains are cross-linked but some remain free, with reactive end groups (green; vynil or hydroxy). **c)** PDMS brush-coated, liquid-like surface. The brushes have a molecular weight of 6000 mol/g.

1.3.3). On a molecular level, they all comprise mostly of the same monomer $[(CH_3)_2SiO]_n$. However, the polymerization and chain reticulation greatly differ which yields different material characteristics and individual wetting behavior, Fig. 1.8. In the following three sections I will introduce each surface structure and the associated wetting characteristics, both statically and dynamically. Some wetting features are shared by all coating types, such as water repellency, low contact friction, or the formation of a 'wetting ridge' (cf. Sections 1.3.1.2, 1.3.2.1, and 1.3.3.1). Others differ such as the constitutive material laws that become important for accessing drop mobility and the associated surface dissipation.

1.3.1 PDMS Oil Coatings

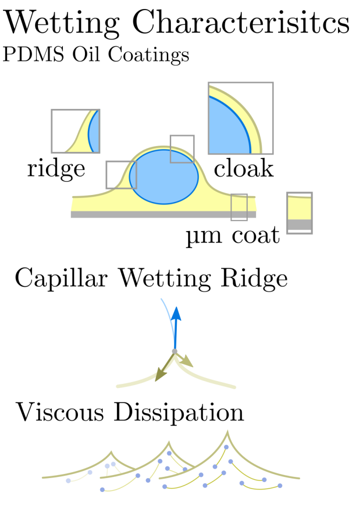

The most straightforward way to create a PDMS coating is to spread a thin film of PDMS oil on top of a surface [141, 142]. The liquid oil film creates lubrication friction which is orders of magnitudes lower compared to dry friction. This enables high drop mobility and the potential for self-cleaning. Nearly every surface is 'siliconephilic' ($S > 0$, Fig. 1.5d) that facilitates a rapid spreading of the oil on the surface [143, 144]. Often, rigid micro- or nanotextures are added to the surface to create stronger retention of the oil film [145], Fig. 1.9a. Such surface designs are known under the acronyms 'SLIPS' (slippery liquid infused porous surface) or 'LIS' (lubricant infused surface) [142, 146]. The design of the surface is to some extent nature inspired - carnivorous plants such as the *Nepenthes* pitcher plant utilizes leaf texture and lubrication[18] to prey on insects such as ants [147], Fig. 1.9b. The retention of the lubricant, however, is the greatest concern of the surface.

1.3.1.1 Textures and Oil Infusion

The rigid texture can be regular ('structured') or irregular ('unstructured') depending on the manufacturing procedure. The advantage of some of these procedures is that they are potentially scalable. Regular structures typically require more extensive procedures. However, regularity is often needed to understand surface fundamentals, such as, how geometrical structure metrics including porosity, affect surface performance. Examples of some manufacturing procedures that produce regular and irregular textures are listed in Tab. 1.1 (cf. [148–151] for comprehensive reviews).

Table 1.1: Examples of procedure to manufacture regular and irregular textures on to hold PDMS oil film.

regular	irregular
photolithography [152], Fig. 1.9c	teflon wrinkles [153], Fig. 1.9d
laser ablation [154]	electrochemical [50]
colloidal self-assembly [155], Fig. 1.9c	sol-gel transitions [156]
	layer-by-layer deposition [157]

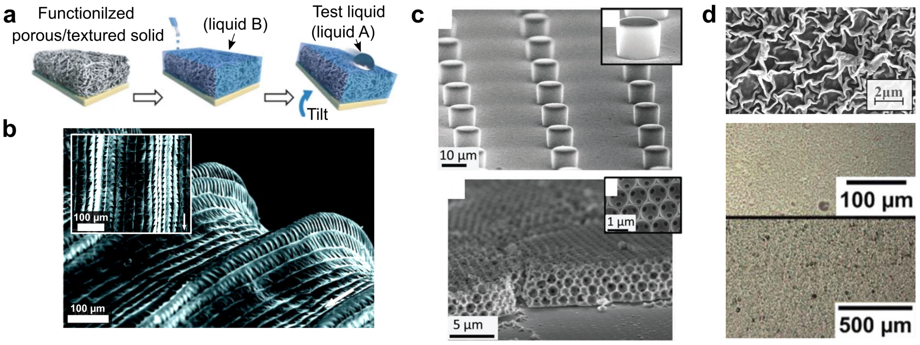

Figure 1.9: Surface texture for increased lubricant retention. **a)** Schematics of the impregnation process of lubricant into a porous, unstructured solid scaffold. **b** SEM image of texture of the *Nepenthes* pitcher plant peristome. **c)** The solid scaffold is often structured. Top, SEM image on micro-pillar posts. These textures were manufactured by photo-lithography. Bottom, SEM image of the honeycomp pattern. These complex geometries are facilitated with colloidal self-assembly manufacturing methods [155]). **d)** Unstructured Teflon wrinkles. Top, SEM image of Teflon wrinkles and bottom light-microscope image of PDMS oil-infused Teflon wrinkles. Reproduced from references and with the permission of **a)** Wong et al. [142] Nature Publishing Group, **b** Bohn et al. [147] National Academy of Sciences, **c)** Schellenberger et al. [158], Royal Society of Chemistry, **d)** Ware et al. [153] American Chemical Society.

Liquid PDMS oil infuses the porous texture by capillary action, Fig. 1.10. The PDMS oil spreads as a thin film on the porous texture. As the contact angle between texture and oil is effectively zero

---

[18] The plant uses water as a lubricant.

the free interface is consequently curved concave, yielding a negative curvature. At the curved interface, a Laplace pressure builds up [per Eq. (1.16)] that drives the PDMS oil into the interstices of the porous textures. The criterion for the oil to form negatively curved interfaces is the good affinity between texture material and PDMS oil. Gauging the affinity between PDMS oil and the texture material via the Young angle[19] θ_Y gives a the condition of $\theta_Y < \theta_c$, with the critical angle [159]

$$\cos\theta_c = \frac{1-\alpha}{r-\alpha}, \tag{1.22}$$

where α is the fraction of texture area exposed at the surface[20] and r measures the roughness of the surface. The roughness relates the total area of the porous texture to the surface area. For very porous textures the roughness goes $r \to \infty$, while for very smooth/flat textures, $r \to 1$. As many surfaces form a low θ_Y with PDMS, the choice of the texture design parameters α and r is relatively uncritical.

This form of PDMS oil suction is known as wicking, and the oil front propagation is diffusive-like [160]. The temporal evolution of the oil front location z follows the law of Lucas and Washburn [161, 162]

$$z = \sqrt{tD^*}, \tag{1.23}$$

where t is the time. The infusion timescale is set by the mobility D^*. The mobility coefficient scales with the (chemical) affinity to -, and the porosity of the texture, and inversely with the viscosity of the oil [163–165]. While the influence of chemical affinity and viscosity is straightforward, the porosity affects the mobility in a more complicated way; small texture features yield high curvatures and therefore high suction (Laplace) pressures but also impose more wall friction. The impregnation timescales can thus vary between minutes to days, depending on the composition of PDMS oil, texture material, and structure.

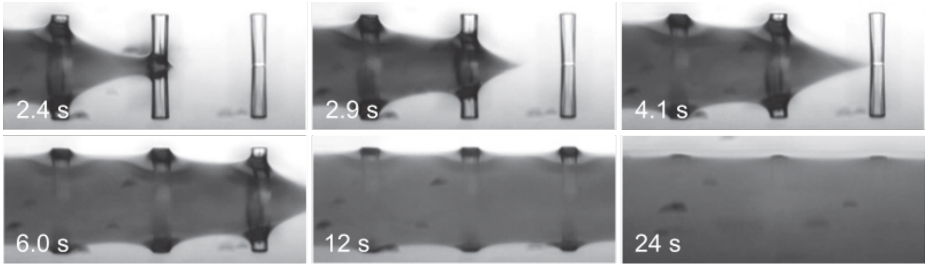

Figure 1.10: Silicone oil infuses micro-pillar array *via* diffusive-like wicking. The viscosity of the silicone oil was 4.6 mPa s. Reproduced from Lafuma et al. [146] with the permission of IOP on behalf of the EPL Association.

---

[19] The angle between a drop of PDMS oil and a flat surface of the texture material.

[20] Correspondingly, $1-\alpha$ is the fraction of PDMS oil exposed at the surface.

1.3.1.2 Liquid Wetting Ridge

In addition to the hydrophobic properties of the PDMS oil, the film acts as a lubricant. This kind of lubrication reduces the friction of contacting objects on the surface immensely. High mobility implies the capability of self-cleaning[21] [146]. As previously discussed, the more prominent superhydrophobic surface struggles with robustness issues that might be overcome by lubricant-infused surfaces: mechanical stretches that may permanently destroy superhydrophobic surfaces can 'self-heal' on lubricant infused surfaces, due to the ability of liquids to reorganize. However, surface operability is directly linked to the presence of the lubricant. Once the PDMS oil is drained from the surface, contacting drops are no longer lubricated and lose their mobility. Maintaining the PDMS oil on the surface is, hence, the most important priority when such kinds of surfaces are designed [51, 145]. Oil depletion is already triggered by contacting water drops, that induce the formation of annular 'wetting ridges', Fig. 1.11a. Wetting ridges, formed on lubricant-infused surfaces can be already detected by the bare eye, Fig. 1.8a. Still, the characteristic sizes are usually in the micron domain and microscopic images help to reveal more detail, Fig. 1.11b.

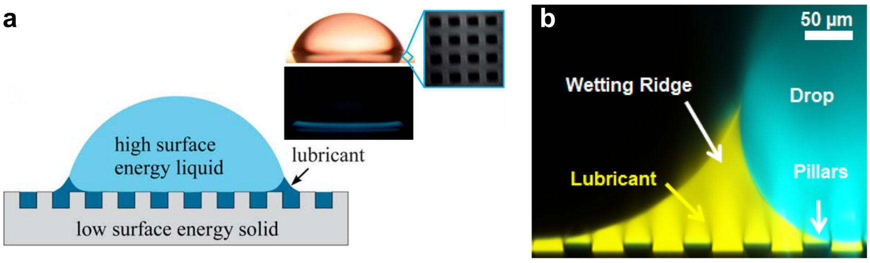

Figure 1.11: Annular wetting ridge around aqueous drop on the oil-infused surface. **a)** Water drop of 8 μl sits on a lubricant-infused surface. Fluorescence dye was mixed in the silicone oil to visualize the wetting ridge in yellow. **b)** Laser scanning confocal images show the microscopic image of the wetting ridge that forms on silicone (yellow) impregnated surfaces around water (turquoise) drops. Reproduced from references and with the permission of **a)** Smith et al. [144] Royal Society of Chemistry and **b)** Baumli et al. [149] Elsevier.

The formation and the shape of the wetting ridge are solely governed by capillarity and the surface energy of the lubricant and the water drop. The three-phase contact line lies between the two liquids and the ambient. To describe this wetting configuration, a single angle, such as the Young angle, does not suffice any longer. The underlying material (the lubricant) adapts to the wetting drop resulting in a deformed surface, *i.e.*, the wetting ridge. In equilibrium, the (liquid) wetting ridge is in a so-called 'Neumann configuration', which implies a balance between the three liquid interfaces at the contact line, Fig. 1.12a. The vector force balance reads

$$\gamma_o \vec{t_o} + \gamma_w \vec{t_w} + \gamma_{ow} \vec{t_{ow}} = 0. \tag{1.24}$$

---

[21] Inspired by the more prominent superhydrophobic surface, cf. Chapter 1.

The vectors $\vec{t}_o$, $\vec{t}_w$, and $\vec{t}_{ow}$ correspond to the tangential vectors of the respective interfaces at the three-phase contact line. The resulting vector triangle [enforced by the balance Eq. (1.24)] is characterized by the associated three Neumann triangles ϑ_1, ϑ_2, and ϑ_3. Each of these angles results from the interfacial tensions as

$$\cos\vartheta_1 = \frac{\gamma_o^2 - \gamma_w^2 - \gamma_{ow}^2}{2\gamma_w\gamma_{ow}}, \tag{1.25a}$$

$$\cos\vartheta_2 = \frac{\gamma_w^2 - \gamma_{ow}^2 - \gamma_o^2}{2\gamma_{ow}\gamma_o}, \tag{1.25b}$$

$$\cos\vartheta_3 = \frac{\gamma_{ow}^2 - \gamma_o^2 - \gamma_w^2}{2\gamma_o\gamma_w}. \tag{1.25c}$$

The height of the wetting ridge (or the location of the three-phase contact line) is found where the balance condition Eq. (1.24) is met (*i.e.*, 'Neumann point'). In equilibrium, each of the fluid interfaces (water-oil, water-air, lubricant-air) assumes a 'minimal energy surface'[22] where the mean curvature is constant ('constant mean curvature, CMC') [167–169]. As a consequence, the (Laplace) pressure jump at the interfaces is constant. In two dimensions, this yields the set of equations that govern the wetting ridge shape

$$\Delta p_{wa} = \frac{\gamma_w}{r}, \tag{1.26a}$$

$$\Delta p_{ow} = \frac{\gamma_{ow}}{r_{ow}}, \tag{1.26b}$$

$$\Delta p_{oa} = \frac{\gamma_o}{r_{oa}}. \tag{1.26c}$$

Here, r, r_{ow}, and r_{oa} are the radii of curvature of the respective interfaces, Fig. 1.12a. The ternary fluid system of oil, water, and air, together with solid texture create a wetting situation that is different from the one, illustrated in Sec. 1.1.2. The interface of the oil towards the air usually flattens, far away from the wetting ridge. A minimal surface that fulfills such a property is the 'catenoid' which has the special property of a zero mean curvature, without being flat. This is possible because the curvature in the two main principal directions is equal in magnitude but opposite in prefactor, such that they cancel perfectly out[23]. In the total free energy functional, stated in Eq. (1.13), contributions from the PDMS oil are missing, and thus, the Youngs contact angle θ_Y is not applicable anymore. However, in the 'starved-limit' where PDMS oil infusion is scarce, the wetting ridge size becomes negligible compared to the drop size, Fig. 1.12b. In this scenario, a pseudo Young angle θ^S_{app} similar to the one in Eq. (1.14) can be defined [170] per

$$\gamma_l \cos\theta^S_{app} + \Upsilon^{\text{eff}}_{sl} - \Upsilon^{\text{eff}}_{s} = 0. \tag{1.27}$$

---

[22] A so-called 'Delaunay' surface, after their founder in 1841 [166].

[23] Sometimes the catenoid is referred to as the 'anti-sphere'.

The effective surface tensions of the solid have contributions from both, texture and PDMS oil and read

$$\Upsilon_s^{\text{eff}} = \Upsilon_s \alpha + \gamma_o (1-\alpha), \tag{1.28a}$$

$$\Upsilon_{sl}^{\text{eff}} = \Upsilon_{sl} \alpha + \gamma_{ow} (1-\alpha). \tag{1.28b}$$

In the starved limit, the shape of the wetting ridge is not only defined by the capillary equation system (1.26a)-(1.26c); when the oil film becomes very thin the film interfaces towards ambient and underlying solid start to interact with each other. Such interactions are characteristic of very thin films and are summarised in the 'disjoining pressure' framework. The interactions take place on a molecular level and can stem from van der Waals interactions, electrostatic attraction or repulsion, or steric forces [81]. The contributing forces to the disjoining pressure depend on the involved materials, which are the PDMS oil and the solid texture. In case of severe film starvation, the disjoining pressure needs to be considered within the total free energy functional, as well [171]. The consequence is that the oil interface assumes shapes, different from the catenoid [167].

In cases where the surface holds sufficient PDMS oil, the contact angle defined in Eq. (1.27) breaks down. The wetting ridge (as part of the underlying surface) obtains sizes that are no longer negligible, compared with the drop size. Hence, the underlying surface undergoes severe deformations and cannot be considered to be flat anymore. The shared oil-water interface of the ridge contributes now significantly to the total energy functional. Now, it becomes challenging to define a baseline from where to measure the angle, as the wetting ridge hides the footprint of the drop. In practice, apparent contact angles are utilized, which are defined as the angle of the drop at the Neumann point to the horizontal plane. The apparent angle derives from θ_{app}^S [172] per

$$\cos\theta_{app} = \cos\theta_{app}^S + \frac{h_f}{r}, \tag{1.29}$$

where h_f is the height of the wetting ridge. h_f typically depends on the film thickness of the PDMS oil film.

1.3.1.3 Thin Oil Film Cloak

The Neumann configuration defined by the balance in Eq. (1.24) requires a negative spreading coefficient S for the surface tensions γ_o, γ_w, and γ_{ow}. As all three interfaces are liquid, their surface tension is easily accessible with direct measurements and their values are listed in Tab. 1.2.

Notably, for these surface tension values, the spreading coefficient is $S \approx 7 - 16 > 0$, and thus, the PDMS oil tends to spread on top of the water drop [67]. The PDMS engulfs the drop with a thin layer. This behavior is called 'cloaking', and significantly changes the wetting picture. Due to the cloak, the surface energy of the drop cap changes, affecting the total free energy functional and

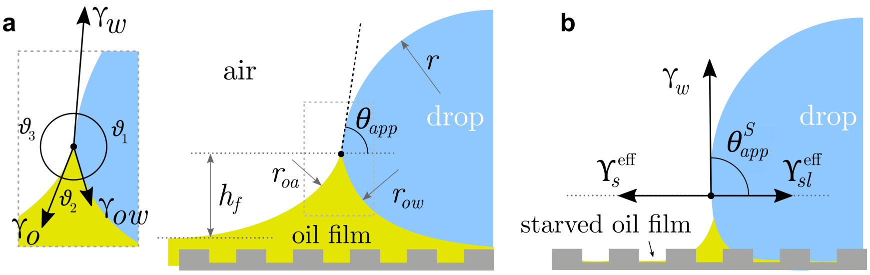

Figure 1.12: Wetting ridge and Neumann configuration. **a)** Excess PDMS oil film. The wetting ridge height h_f depends on the amount of excess film thickness. Due to the large oil meniscus, the apparent contact angle θ_{app} can be used to characterize the wetting interactions of water, oil, and texture. The surface tension of γ_o, γ_{ow}, and γ_w form a vector balance at the Neuman point. **b** starved PDMS oil film. This wetting configuration is characterized by a pseudo-Young equation, where the surface is considered to be effectively flat with surface tensions Υ_s^{eff} and $\Upsilon_{sl}^{\text{eff}}$.

Table 1.2: Interfacial tension between water-air, oil-air, and oil-water interface. Differences in the values can stem from differing PDMS molecular weight ($770-48000$ g/mol) and measurement errors.

Interface		Surface Tension [mN/m]
water-air	γ_w	72 (self-measured)
oil-air	γ_o	40 [173], 38 [174]
oil-water	γ_{ow}	$18-22$ [174], 21 [173], 25 [175]

consequently the wetting affinity of the drop and the contact angle, respectively. A cloaking layer of PDMS oil makes the Neumann configuration less obvious.

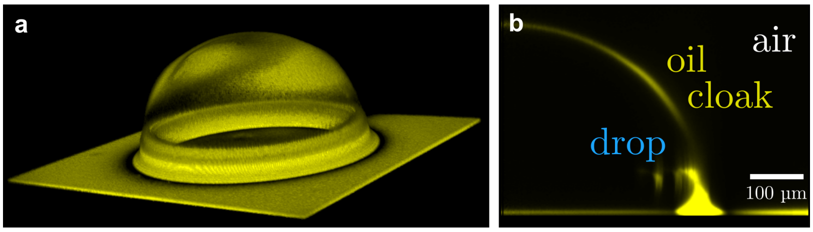

Figure 1.13: .Sessile drop on lubricated surface, cloaked by PDMS oil. **a)** Three-dimensional view of PDMS oil on the drop, obtained by laser scanning confocal microscopy. **b)** Side view of the angular averaged 3D stack. Reproduced from Badr et al. [176] with the permission of the American Chemical Society

Naively, the surface tension γ_c of the cloaked surface sums effectively up from two interfaces (water-oil and oil-air) that replace the uncloaked surface (water-air), *i.e.*

$$\gamma_c = \gamma_{ow} + \gamma_o. \tag{1.30}$$

However, the concepts of surface tension and surface energy, introduced in Sec. 1.1.1, consider shared surfaces of two bulk phases. Surface tension and energy result from excess energy that at some length (vicinity) around the surface and decays towards the bulk phases. The length (or the vicinity) in which the excess energy decays is also reflected in the stress isotropy, Fig. 1.2. Following this reasoning, γ_c is only correctly reflected in Eq. (1.30) when the cloaking layer is thick enough and the surface tension as 'bulk-properties' γ_{ow} and γ_o are applicable. However, the layer might be substantially thinner, especially upon cloak formation. In this case, the surface tension of each interface assumes adjusted 'thin film' values, *i.e.*, γ_{ow}^{Σ}, and γ_o^{Σ}. The two interfaces (water-oil and oil-ambient) of the thin cloak layer start to interact with each other *via* the disjoining pressure which yields additional, stabilizing stress contributions. The cloaked surface tension in this 'thin film' states computes therefore [177] with

$$\gamma_c = \gamma_{ow}^{\Sigma} + \gamma_o^{\Sigma} + \int_{h_c} \Pi(h_c) dz, \tag{1.31}$$

where h_c is the cloak layer thickness, $\Pi(h_c)$ is the disjoining pressure, and z is the coordinate, normal to the interface. Utilizing a Gibbs-Duhem formalism at the thin film, the useful relation between the film height h, the disjoining pressure $\Pi(h)$, and the thin-film surface tension becomes accessible per

$$\frac{\partial \gamma_{ow}^{\Sigma}}{\partial h_c} + \frac{\partial \gamma_o^{\Sigma}}{\partial h_c} = -\Pi(h_c). \tag{1.32}$$

The dependency on the film height can be obtained by integrating Eq. (1.32). The integration bounds can be readily found with the bounded limits (for $h_c \to \infty$) of the disjoining pressure and the bulk surface tension. With these limits

$$\lim_{h_c \to \infty} \Pi = 0, \tag{1.33a}$$

$$\lim_{h_c \to \infty} \gamma^{\Sigma} = \gamma. \tag{1.33b}$$

the integration within the bounds $[h_c, \infty)$ gives

$$(\gamma_{ow}^{\Sigma} - \gamma_{ow}) + (\gamma_o^{\Sigma} - \gamma_o) = -\int_{\infty}^{h_c} \Pi(h_c) dh_c. \tag{1.34}$$

Combining Eq. (1.31) and (1.34) yields the relation between the surface tension of the cloak in dependence of the bulk surface tensions of water-oil and oil-ambient interface and the film thickness [177–179]

$$\gamma_c = \gamma_{ow} + \gamma_o + \Pi(h_c)h_c - \int_{\infty}^{h_c} \Pi(h_c) dh_c. \tag{1.35}$$

For $h_c \to \infty$, the disjoining pressure vanishes [cf. Eq. (1.33a)] and Eq. (1.30) is recovered.

The formation of the cloak is a transient process, associated with time scales of the oils rooting in viscous or diffusive oil transport from the surface to the drop cap. Hence, the temporal evolution of the cloak formation can be measured: experimentally, this has been illustrated with pendant drop measurements, where drops hang on PDMS oil-infused surfaces [25]. In these experiments, the surface tension of the hanging drop (38 μl) changed from the characteristic $\gamma_{wa} = 72$ mN/m to $\gamma_c \approx 64$ mN/m after more than 25 minutes. Besides oil parameters (such as viscosity), the drop size also factors in the cloak formation time [180]. The coupling in Eq. (1.31) between γ_c and h_c indicates that one is a proxy for the other. Hence, the temporal evolution of γ_c may be linked to the gradual increase of the cloak thickness. Note, that $\gamma_{wo} + \gamma_o \approx 64$ mN/m, Tab. 1.2, indicating that the cloak reached a bulk-like thickness for $t \to \infty$.

1.3.1.4 Drop Mobility and Ridge Dissipation

The wetting ridge influences how drops move on the surface. The hydrodynamics, *i.e.*, the viscous shear flow in the wetting ridge causes dissipation that exceeds the contact line dissipation at the contact line (cf. Section 1.1.4). If the oil is very viscous, the drop mobility is significantly hampered [181]. As the wetting ridge dissipation governs the overall sliding friction, drops with very viscous liquids are much more mobile, compared to on non-lubricated surfaces [47].

The accumulated PDMS oil in the wetting ridge has major implications for the durability of the coating: the accumulated oil in the ridge is dragged along by sliding drops, gradually depleting the surface. As a workaround, porous textures with smaller and smaller pore sizes were proposed to oppose the depletion by strong capillary retention [145]. The thermodynamically driven oil cloaking - and consequently coating drainage - can only be prevented by tuning the surface chemistry, accordingly [144]. Overall, the issue of oil depletion still constitutes the strongest drawback of the steady long-term operability of PDMS oil coatings. Meanwhile, it is not clear if this drawback can eventually be overcome.

1.3.2 PDMS Elastomer Coatings

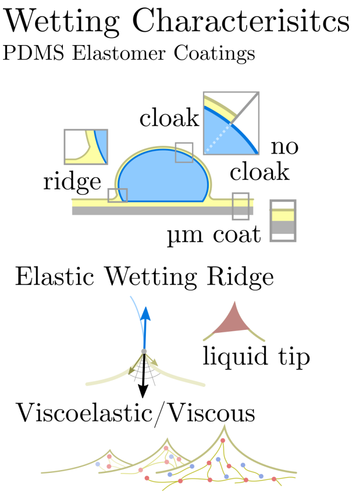

Crosslinking the PDMS chains creates an elastomer network that can withstand deformations. Therefore, elastomer coatings retain their structure better then oil coatings improving coating durability. However, the network structure can impose friction, more complex and higher in magnitude than mere viscous dissipation.

Generally, crosslinks that reticulate the chains can be either physical or chemical [182]. Physical crosslinks form when the PDMS chains are long enough (*i.e.*, their molecular weight is large enough) to facilitate entanglements. Much shorter chains can be crosslinked with the addition of a chemical agent. Such an agent comprises silicones with reactive side groups (e.g. methylhydrogensiloxane[24])

---

[24] Chem. struct. $(HCH_3)SiO$

and a platinum catalyst to drive the reaction[183]. As discussed previously, the PDMS chains require termination with reactive end groups, such as vinyl- or hydroxyl groups. In a hydrosilylation reaction, the crosslinker backbone is covalently linked to the end-group of the PDMS chain [184]. Other derivatives of the synthesis exist where e.g. the vinyl group is incorporated in the PDMS backbone or other kinds of cross-linking agents are utilized [183, 185–187]. Every crosslinking reaction (independent of precise formulation) strives to overcome the 'gel point'. The gel point is met when a critical amount of the crosslink reactions proceeded and the PDMS loses the fluidity [188]. PDMS above the gel point is non-fusible even above the glass transition temperature of the linear (uncrosslinked) PDMS chain. PDMS below the gel point can be dissolved in a range of solvents (e.g. hexane or toluene [137]), however, crossing the gel point implies that PDMS is not dissolvable any longer. Mechanically, the crossing of the gel point is reflected in an abrupt increase of the viscosity and the emergence of elasticity [185]. The mechanical properties (viscosity and elasticity) are good indicators to characterize the crosslinked PDMS. Such mechanical properties typically relate kinematic deformations of the material (*i.e.*, shear, strain, and their rates) to stresses. Their interdependence is governed by 'constitutive' or 'material' laws. The molecular structure, both chemically[25] and physically[26], factor in the exact nature of these laws. In practice, these properties are accessible through rheological measurements where the material is excited by kinematic actions (displacement and their rates) and the measurement of their mechanical stress responses. Note, that even under optimal stoichiometric conditions[27], not all reactive chains crosslink to the network but some remain free [137]. The free chains alter the material rheology and have strong implications for wetting. The free chains can accumulate in the wetting ridge [189], separate from the network [190, 191], cause cloaking [192] and affect static and dynamic wetting [1, 2, 193].

1.3.2.1 Elastic Wetting Ridges

Wetting ridges occur on elastomeric surfaces, too [72]. However, the mechanisms that govern the 'elastic' wetting ridge are different from the pure liquid ones. Capillary forces around the perimeter of a wetting drop induce mechanical stress in the PDMS material. Consequently, the material around the three-phase contact line deforms, and a wetting ridge forms, similar to the liquid one in Sec. 1.3.1.2. In addition to the surface tension of the coating, the elasticity of the network bulk contributes to the ridge geometry. Depending on the bulk stiffness, wetting ridges on elastomers grow up to a couple of tens of microns. With the steady improvement of optical techniques, elastic wetting ridges were resolved with an increasing level of detail. Such modern state-of-the-art techniques are e.g., interferometry, x-ray microscopy, and laser scanning confocal microscopy [72, 194–196], Fig. 1.14.

---

[25] What is the chemical substance and how does it interact on a molecular level?
[26] How is the structural makeup (e.g. crosslinked, confined, stretched, etc.) of the material?
[27] Ratio between chemical agent and reactive chains.

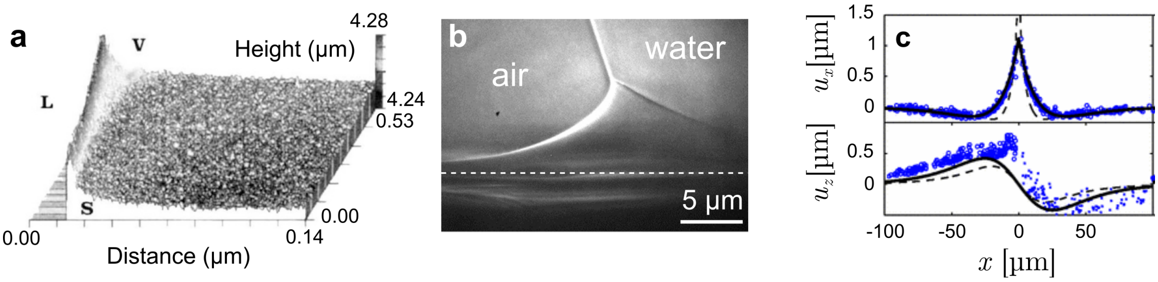

Figure 1.14: Elastocapillary wetting ridge induced by liquid drops on soft silicone surface. Different microscopy techniques and computational methods. a) Wetting ridge on silicone elastomer gel (630 kPa) visualized via scanning interferometric microscopy. **b)** Wetting ridge on a softer silicone gel (3 kPa) are larger. Visualized by X-ray microscopy. **c)** Horizontal and vertical displacement of silicone gel, induced by wetting drop. Visualized by confocal microscopy. Reproduced from references and with the permission of **a)** Carré et al. [72], **b)** Park et al. [194], and **c)** Jerison et al. [196].

The shape of the elastic wetting ridge can be found by balancing the bulk elasticity and the surface stress of the network to the imposed surface tension of the water drop at the three-phase contact line. The surface tension of the water γ_w pulls on the surface, acting like a point load on the PDMS material. In a simple picture, this can be viewed as a load-spring system, where the displacement (*i.e.*, the size of the wetting ridge $\delta_{e,\mathrm{I}}$ [197, 198]) scales with the load γ_w and inversely, with the stiffness η_0

$$\delta_{e,\mathrm{I}} = \frac{\gamma_w}{\eta_0}. \tag{1.36}$$

As PDMS is hydrophobic, the surface tension is angled at $\theta \approx 90° - 110°$ [131, 199–203] to the surface, Fig 1.8b. Hence, the magnitude of the point load is rather given by $\gamma_w \sin\theta$. The linear relation between the material stiffness (or rather the inverse of it, *i.e.*, its compliance) has been confirmed experimentally [72]. Exact solutions of the elastic wetting ridge can be obtained within the linear elastic framework [204–210], Fig. 1.15. The governing equations comprise momentum conservation, constitutive material laws, and boundary conditions that attribute to the contacting drop (cf. Appendix A.2). The local stress tensor in the PDMS coating is

$$\boldsymbol{\sigma} = -p\boldsymbol{I} + \boldsymbol{\tau}, \tag{1.37}$$

where p is the isotropic pressure and $\boldsymbol{\tau}$ is the internal stress. In the linear elastic framework $\boldsymbol{\tau}$ is linked to the displacement $\vec{u}$ by the constitutive law of Eq. (A.8). In equilibrium and without external force fields, $\boldsymbol{\sigma}$ balances *via* the Cauchy momentum equation [211]

$$\nabla \cdot \boldsymbol{\sigma} = 0. \tag{1.38}$$

The PDMS coating has an initial film thickness of h_0. To map the localized stresses, the material coordinates $\vec{x} = [x_1, x_2, x_3]^T$ are introduced that follow the deformations. The radial symmetric of the drop reduces the problem to only two dimensions. The circular drop suggests the transition to polar coordinates. However, the radius of macroscopic drops ($\mathcal{O} \approx 10^{-3}$ m) is much larger than the width of the wetting ridge ($\mathcal{O} \approx 10^{-6}$ m). Hence, the in-plane curvature becomes negligible and two-dimensional Cartesian coordinates are applicable, $\vec{x} = [x_1, x_2]^T$, with x_1 being the horizontal and x_2 the vertical component. At $x_2 = 0$ the film meets the drop and imposes the traction force

$$\vec{f} = \gamma_w \left\{ \cos\theta \vec{t} + \sin\theta \vec{n} \right\} \delta\left(x_1 - x_{\mathrm{cl}}\right). \tag{1.39}$$

where x_{cl} is the location of the three-phase contact line and $\delta(x - x_{\mathrm{cl}})$ is the Dirac delta. $\vec{n}$ and $\vec{t}$ are the normal and tangential vectors of the PDMS surface at $x_2 = 0$. The stress boundary condition at the film surface reads

$$\Upsilon_{\mathrm{e}} \left(\nabla \cdot \vec{n}\right) \vec{n} - \boldsymbol{\sigma} \vec{n} + \vec{f} = 0. \tag{1.40}$$

Υ_{e} is considered to be symmetric around x_{cl}, which is not fulfilled for water-air-PDMS ($\Upsilon_{el} \approx$ 40 mN/m and $\Upsilon_e \approx 20$ mN/m). However, in principle Eq. (1.40) can be adjusted with Heaviside functions to produce unsymmetrical solutions. Solutions of this system of equations (and variations) showed that the competition between the bulk elasticity η_0 and the capillary point load $\gamma_w \sin\theta$ produces shapes that are comparable with experimental measurements [194].
The mere consideration of these two interlayers produces a singularity at the contact point of the load. Here, the surface stress of the network material Υ_e regularizes this singularity by opposing the deformation with plastic stresses [209, 212]. The length scale at which the surface stress-regularization emerges is

$$\delta_{e,\mathrm{II}} = \frac{\Upsilon_e}{\eta_0}. \tag{1.41}$$

When the wetting drop induces an elastic wetting ridge where $\mathcal{O}(\delta_{e,\mathrm{I}})$ is below $\mathcal{O}(\delta_{e,\mathrm{II}})$ the Neumann configuration [Eq. (1.24)] is recovered. The ratio of the two elastic length scales demarcates the two limits in which the stress can be treated (cf. Appendix A.2):

$$\frac{\delta_{e,\mathrm{I}}}{\delta_{e,\mathrm{II}}} = \frac{2\gamma_w}{\Upsilon_e} = \begin{cases} \ll 1 & \text{Neumann-limit,} \\ \gg 1 & \text{bulk elasticity-limit.} \end{cases} \tag{1.42}$$

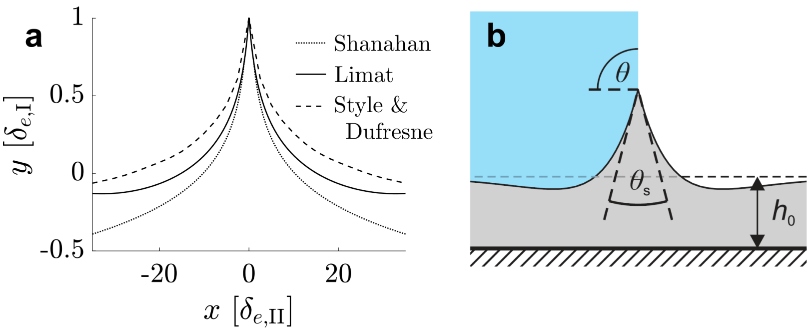

Figure 1.15: Elastic wetting ridge. **a)** Shape profiles calculated with linear elastic theory by Shanahan [204], Limat [208], and Style & Dufresne [209]. x-axis was normalized by $\delta_{e,\mathrm{II}}$ and y-axis by $\delta_{e,\mathrm{I}}$. Shanahan solution diverges around $|x| < 1$, as no surface stresses regularize the elastic bulk stress. In this region, the profile is cut. Limat utilizes Fourier transformations while Style & Dufresne use Hankel transformations for the governing linear stress balance. **b)** Finite element calculation of wetting ridge using linear elasticity [89]. θ is the apparent contact angle between the drop and the (horizontal) surface, θ_s is the solid contact angle that describes the opening angle of the elastic wetting ridge and h_0 is the coating thickness. Here, the coating thickness is comparable to the wetting ridge. This leads to coating dimpling around the wetting ridge. **b)** Reproduced from [89] with the permission of the Royal Society of Chemistry.

1.3.2.2 Solvent Separation

In PDMS gels with standard crosslinking procedure[28], around $5-\%$wt of the polymer chains remain free, and can be considered as a liquid solvent inside the crosslinked scaffold [137, 213]. The free chains travel to the surface and cause lubrication [193]. This makes the (swollen) elastomer[29] technically to a liquid-infused surface on which contaminants (such as water) hardly stick [52]. The free oil molecules accumulate around the three-phase contact line of the contacting drop [180] and cloak the drop [192] (cf. Section 1.3.1.3). In PDMS coatings with large amounts of liquid solvent, the microscopic zones of pure liquid solvent were observed, at the tip of the wetting ridge [190, 191]. The free PDMS influences the mobility of the drop [214] as the makeup of the wetting ridge directly factors into the dissipation mechanics, per Eq. (1.43). Experimentally, this has been observed with contact angle measurements [2], sliding experiments with free [193], and forced wetting [1]. In cases where the free PDMS undergoes such phase separation within the wetting ridge, and cloaks the drop, a more complex framework is required to map the dissipation during drop sliding, which is yet to be developed.

1.3.2.3 Complex Ridge Dissipation

The elastic wetting ridge influences drop motion, too, like their purely liquid counterparts. As the drop moves over an elastic surface, the wetting ridges reorganize that invokes dissipation

---

[28] E.g. Sylgard-184 PDMS

[29] A crosslinked polymer matrix, swollen with a solvent is also often referred to as a 'gel'.

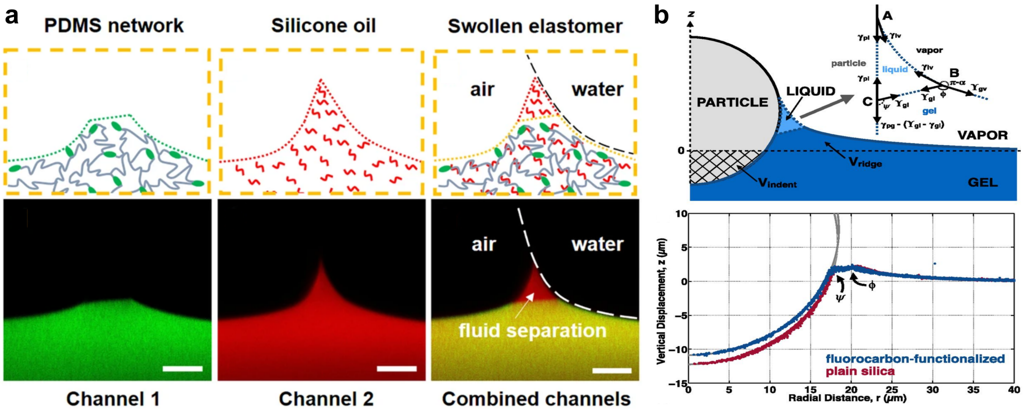

Figure 1.16: Phase separation of unbound, liquid PDMS at the tip of the elastic wetting ridge. **a)** Laser scanning confocal microscope image. Two fluorescent dyes with different emission spectra were added to the PDMS network (green) and the liquid PDMS (Red). Red-shifted perylene monoimide (PMI) with a fluorescence emission peak at ≈ 680 nm is covalently added to the PDMS network. The liquid PDMS (silicone oil, 4.8 mPa s) is mixed with fluorescein dye (emission peak at ≈ 512 nm). **b)** Phase separated wetting ridge around the contact line of a glass sphere. The PDMS surface is covered with fluorescing nanoparticles (≈ 50 nm) that resolve the surface of the PDMS network. In network does not form a sharp tip at the contact zone, indicating that the liquid PDMS phase separated from the network. Reproduced from and with the permission of **a)** Cai et al. [191] Nature Publishing Group, and **b)** Jensen et al. [190] National Academy of Sciences.

$$P_{\text{diss}} = \int_{V_e} \boldsymbol{\sigma} : \dot{\boldsymbol{\epsilon}} dV, \tag{1.43}$$

where V_e is the volume of the elastic wetting ridge[30]. The dissipation mechanics, however, typically show complex viscoelastic rheology (the local stress tensor $\boldsymbol{\sigma}$ can hold complex rheology, cf. Fig. A.1) and cannot be described by viscosity only [215]. To understand and tune drop dynamics on PDMS elastomers, it is important to find the shape of the wetting ridge and couple it to the material rheology. This yields the friction that builds up during drop sliding. The thickness of the coating affects the shape of the wetting ridge when the length scales of both become comparable [210, 216]. Coating material that accumulates in the elastic wetting ridge cannot be replenished. Thus, the coating dimples around the wetting ridge in a lack of coating material, Fig.1.15b. Very thin coatings also limit the size of the wetting ridge as the material is confined (or attached) to an underlying surface. The ridge geometry is in addition to $\delta_{e,\text{I}}$ and $\delta_{e,\text{II}}$ governed by the thin height h_0. The friction that builds up in the wetting ridge is consequently reduced, as the total dissipation volume, V_e decreases [217].

---

[30] The product $\boldsymbol{\sigma} : \dot{\boldsymbol{\epsilon}} = \sigma_{ik}\dot{\epsilon}_{ik}$ produces a scalar.

1.3.3 PDMS Chain Coatings

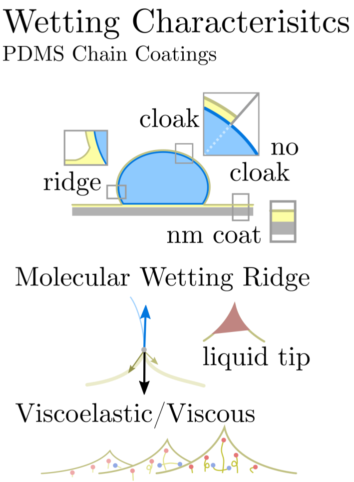

The linear PDMS chains can be grafted directly to a surface forming a layer of 'PDMS brushes' [218]. PDMS brush coatings are extremely thin and reach only tens of nanometers in height. The chains are grafted to anchor sites on the surface. The top chain end, however, remains free. Due to the low glass transition temperature and the large bond angle between Si – O in the polymer backbone ($\approx 150°$ [219]), the chains have a very low torsional resistance and maintain flexibility. This leads to excellent lubrication properties, low contact friction and high drop mobility. Such anchor sites are typically hydroxyl groups that can be added by chemical treatment. Many metal oxides (e.g. SiO_2, TiO_2, Al_2O_3, NiO) form hydroxyl groups naturally from ambient water vapour [220]. PDMS chains are formed either by adding sub-unit after sub-unit ('grafting from') or by adding an already polymerized chain ('grafting to') [221–223]. The surface chemistry of elastomeric and brush coatings is much alike. Thus, both surface types show similar wetting behavior with comparable contact angles on a macroscopic level, Fig. 1.4. However, the reticulations of the chains in the two coatings are quite different. PDMS chains can occur in a stretched or a collapsed state, depending on the affinity to the surrounding solvent [224]. A contacting aqueous drop leads to brush collapse due to the H_2O repulsiveness of PDMS. Drops of organic liquid invoke chain stretching as both components interact well. While the advancing and receding angles follow the expected tendency (high for water, low for organic liquid) the contact angle hysteresis is intriguingly low, for both liquids [135]. This is usually explained by the high flexibility of the chains; the high Si – O bond angle causes low rotational energy around the bonds (3.3 kJ/mol) - e.g. lower then between carbon-carbon bonds (13.8 kJ/mol) that occur in organic polymers, such as polyethylene glycol [225]. Thus, grafted chains can rotate relatively freely, which reduces contact friction [226] and the contact angle hysteresis $\Delta\theta$ is consequently relatively low. For this, PDMS brush-coated surfaces are attributed with the feature 'liquid-like', in resemblance to the lubrication of oil-coated surfaces. However, $\Delta\theta$ does depend on the grafting density and on the chain length (*i.e.*, the molecular weight) where experiments suggest that there is an optimum configuration [220].

1.3.3.1 Molecular Wetting Ridge

A wetting ridge on a brush-coated surface is theoretically possible: chains may stretch around the contact line, or uncrafted chains migrate freely to the contact line. Because of the nanometric dimensions of the brush coating, a direct (experimental) observation is lacking. Theoretical calculations -

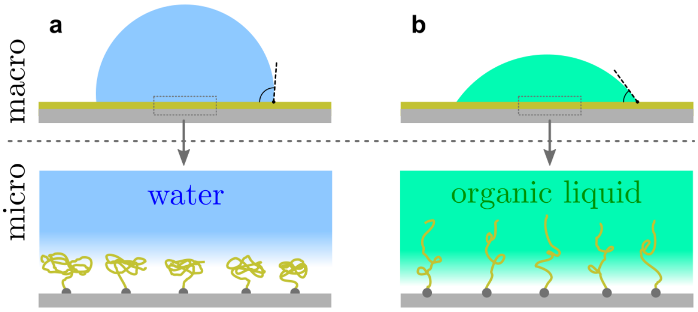

Figure 1.17: Wetting of PDMS brushes with **a)** water with high contact angles and collapsed brushes, and **b)** organic liquids with low contact angles and stretched brushes. The contact angle hysteresis for both liquids is low.

both on a molecular level and in a mean-field framework - clearly show the formation of a wetting ridge [176, 227–229].

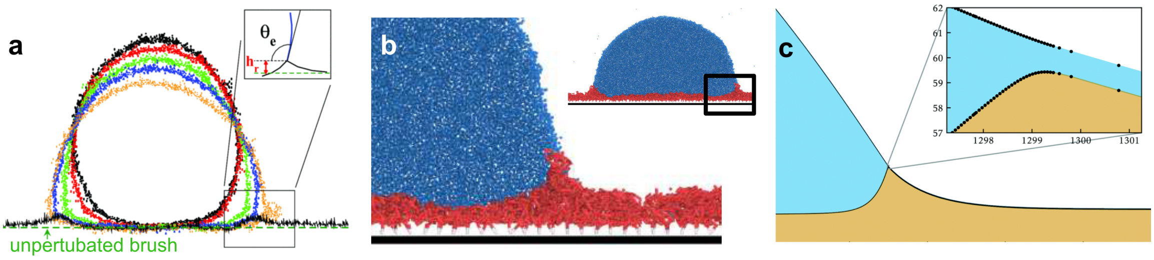

Figure 1.18: Formation of the wetting ridge on molecular thin brush coatings obtained by models increasing scale from **a)** to **c)**. **a)** Molecular dynamics simulation of polymeric brush with polymeric drop. **b)** Dissipative particle dynamic simulation of drop on brush surface. **c)** Gradient dynamics of free energy mean field model. The wetting drop utilizes a precursor model generating a very thin aqueous film on the surface (inset). Reproduced from and with the permission of **a)** Léonforte [227] American Institute of Physics, **b)** Badr et al. [176] American Chemical Society, and **c)** Henkel et al. [229] Royal Society of Chemistry

The molecular wetting ridge is, again, a result of the interplay of the capillary forces induced by the wetting drop and the material response of the coating. However, the motivation of the linear elasticity framework from a mechanical point of view is less obvious as the length scales are much smaller. Deformations occur (at most) over the length of a chain (collapsed to stretched) in contrast to networks that undergo deformations at scales of the crosslink node spacing. Further, the chain configuration introduces isotropy as the chains are not laterally reticulated. Therefore, the deformation of chain coatings is usually considered in a thermodynamic framework of the individual polymer chains. The restoring force on the molecular chain level originates from entropy [230]. Stretched chains have less conformational states. Thus, the entropy is low. This state is undesirable for the brush. It strives to increase the possible conformations and maximize its entropy by recovering the unstretched state [231, 232]. Noteworthy, the thermodynamic consideration recovers a linear relation between the deformation and the restoring force. A mobile drop sliding over the surface

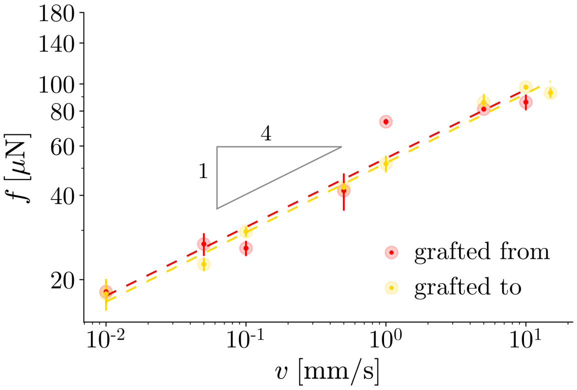

Figure 1.19: Force measurements of sliding water drops (10 μl) at sliding speeds between $v = 10$ m/s and 10 mm/s on glass surfaces (SiO_2) coated with PDMS brushes. Additional hydroxyl groups were added by oxygen plasma cleaning (cf. e.g. [25]). PDMS brushes were added by 'grafting to' (yellow) using vapor deposition [223] and 'grafting to' using 6000 g/mol PDMS chains [222]. Dashed line is the best arithmetic fit of measurement data.

reorganizes the ridge constantly. While low, the contact angle hysteresis is not zero; therefore, this is not a symmetric process: the differing capillary force at the advancing and receding side leads to a non-zero net force as the drop moves. The force that builds up during sliding was measured with a drop friction force instrument [99]. This force scales with the drop speed approximately with $f \sim v^{1/4}$, Fig 1.19. While preliminary, these measurements have some important implications: as the synthesis appears to not affect the friction force, the grafting density and chain length may not play such a significant role. However, rigorous investigations are still lacking and decisive conclusions should not be drawn at this stage.

1.3.3.2 Free Chains and Loops

Similar to elastomeric PDMS, not all chains are grafted to the surface. Depending on the synthesis method, grafting density, and chain length some chains will remain free. Free chains act as a liquid lubricant and decrease the contact angle hysteresis [222]. In simulations, the free chains accumulated in the microscopic wetting ridge and migrated on top of the air-exposed surface of the drop (*i.e.*, cloaking cf. Section 1.3.1.3) [176]. PDMS chains may also not be grafted at a single site and assume the linear topology; if the chain is large enough, the chain can form loops on the surface with more than one attachment site [233]. Such brush topologies affect the adhesion and the friction of the coating [234, 235] and ultimately their (dynamic) wetting behavior [236].

1.3.4 Coating Comparison

For self-cleaning applications, all three coating types strive to provide high drop mobility (low sliding friction) with lasting surface structure. As discussed in Sec. 1.3.1.4, 1.3.2.3, and 1.3.3 accumulated coating material in the wetting ridge is the main cause of dissipation during drop sliding. The different fabric of the coatings yields a coating-specific ridge dissipation which makes the drop mobility unique on each coating.

The different reticulations of the fabric do also affect the durability of each coating. PDMS oil coatings lie loosely on a substrate. Only the underlying texture stabilizes the PDMS oil (cf. 1.3.1.1). Hence, their retention is much lower than elastomer or chain coatings. PDMS chain coatings are more durable. The chains are well attached to the surface while the free ends remain free and flexibile, which provides lubrication properties, even without a liquid lubricant. However, the nano-size of the coating does not provide much 'healing' material once the coating abrades. The bulky structure of PDMS elastomers provides large amounts of bulk material and can therefore easily 'self-heal'. The presence of free chains in the elastomer network, however, is critical to maintain low sliding friction and upon depletion, drops experience much larger sliding friction.

The level of difficulty for the coating process varies for the different materials. Creating PDMS oil coats without a micro-/nanometric support scaffold is straightforward. Many surfaces can be quickly fictionalized by simply spreading PDMS oil on the surface. The process is similarly straightforward for PDMS elastomer coating, but only if no special requirements regarding the coating thickness exist. The 'grafting-from' technique for PDMS chain coatings is the most elaborate process. Typically, the 'chemical-vapor-deposition' (CVD) process is utilized which requires controlled atmosphere conditions, and sometimes toxic chemicals (e.g. trichlorosilane). However, this method allows the coating of very small/delicate structures which is not possible with either oil or elastomer coatings.

This shows that each of the coating types has advantages and disadvantages. Understanding their fabrication and the wetting mechanism is crucial to decide which coating is the most appropriate for a given application while maintaining long-lasting coating functionality. The main features of the three coatings is finally compared in Tab. 1.3.

Table 1.3: Comparison map between different PDMS coatings.

	PDMS oil coating	PDMS elastomer coating	PDMS chain coating
thickness	nm, μm, mm	nm, μm, mm	nm
ridge	liquid	elastic/liquid	elastic/liquid
dissipation	viscous	viscous/ viscoelastic	viscous/ viscoelastic
cloaking	inevitable	possible	possible
synthesis	easy/ hard (with scaffold)	easy/medium	easy ('grafting to') hard ('grafting from')
retention	capillary/spreading interactions	crosslinked network	grafting sites

Chapter 2

Synthesis

2.1 Separation of Free Chains in Elastomers

PDMS network coatings were considered to be dry, viscoelastic materials [204–206, 208, 209, 237]. This, however, is an incomplete picture: free (liquid) chains reside inside the network (e.g. for standard Sylgard 184 PDMS around 5 %wt [137]), and accumulate in the static wetting ridge [190, 191], cf. Sec. 1.3.2.2. First clues regarding dynamic wetting with macroscopic tools (camera, goniometer) [2, 193] and with interferometric measurements of the ridge relaxation [214] showed that the free chains decrease contact friction but lead to lubrication degradation over time. However, direct observation of the free chain accumulation in the wetting ridge under dynamic wetting conditions is still lacking. Detailed information on the reorganization of the chains is critical to assess the functionality and durability of the coat.

In *Phase Separation in Wetting Ridges of Sliding Drops on Soft and Swollen Surfaces* [1] the wetting ridges on soft and swollen elastomers during forced wetting are investigated with laser scanning confocal microscopy. The free and crosslinked chains are fluorescently labeled which enables discrimination between the phases. This directly resolves the network and free chains temporally and spatially around the three-phase contact zone during wetting. Water drops are slid on the surface of lightly crosslinked PDMS surfaces (60:1, weight ratio crosslinker to PDMS chains), swollen with silicone oil (ranging from 10× to 16× of the 'dry network volume'). The study finds that the two phases (oil and network) separated to a differing degree, depending on the sliding speed and the amount of swollen oil. A diffusion-advection model that considers the chemical potential in the respective phases is developed

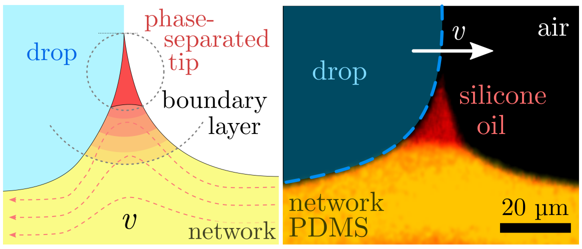

and validated with experimental data. The model helps to explain I) the degree of phase separation, and II) the mobility of the silicone oil in the PDMS network.

- **Functionality**. Network and oil phases have differing constitutive material laws (network: viscoelastic; oil: viscous). While the friction on oil with low viscosity can significantly reduce the overall friction during sliding. This study shows the coupling between the drop sliding speed and the degree of swelling to the degree of phase separation. In particular, it is shown that at slow sliding speeds the separation of purely liquid material around the wetting ridge is severe. This implies that most of the dissipation is viscously leading to low overall dissipation during drop sliding.
- **Durability**. The detrimental consequence of phase separation is that the separated material is entrained by the sliding drop, and upon drop departure is depleted from the surface. A sufficiently large number of wetting drops can permanently deplete the network and render it dry. Due to acquired knowledge about the coupling between separation and speed, surface depletion can be suppressed by tuning the drop speed, enabling surface durability.

2.1.1 Overarching Relevance

The material fabric in the wetting ridge governs the dissipation of the wetting ridge (cf. Sec. 1.3.1.4, 1.3.2.3, and 1.3.3.1). Hence, these observations will help to understand how and where dissipation within the wetting ridge acts. A purely liquid tip that comprises low molecular oil (*i.e.*, oligomers) behaves as a Newtonian fluid. The dissipation should therefore follow a linear relation per Eq. (A.9). The underlying swollen network, however, exhibits more complex rheology and is captured by viscoelastic dissipation [Eq. (A.14)]. The mapping of the sliding speed to the separation height shows also that the overall relaxation spectrum of the wetting ridge is not constant for the sliding speed. The separation has a material-specific relaxation time that depends on the network/crosslink density and the number of free polymer chains. This time scale competes with the sliding speed, resulting in a separation suppression. This cascades to a change in the material fabric and therefore a speed dependency for the appropriate dissipation functional. Drop mobility becomes a function of the sliding speed. While previous studies mostly focused on idealized soft surfaces that are either purely solid or liquid, this investigation pushes observations and models more toward real elastomers, that comprise both, liquid and solid phases.

2.2 Adaptive Wetting of Elastomeric Coatings

The contact angle hysteresis $\Delta\theta$ is classically considered to be a consequence of chemical inhomogeneity or surface roughness (cf. Sec. 1.1.4). Recently, another origin of $\Delta\theta$ was discussed in the framework of 'adaptive wetting' where the substrate adapts locally to the wetting drop [33, 66].

These adaptations have a mechanistic (e.g. diffusion/swelling, molecular orientation, charge formation) dependent relaxation time. The contact time of a moving drop is different at the rear and the front end of the drop; hence, the degree of adaptation differs. This gives rise to differing solid surface tensions, and hence an adaptation induced $\Delta\theta$. For PDMS it is not clear if adaptations play a role, if yes, which mechanisms are at play and on what time scales they operate. As contact angle hysteresis induces capillary forces that act laterally to the sliding drop [cf. Eq. (1.20)], PDMS adaptions link directly to the drop mobility.

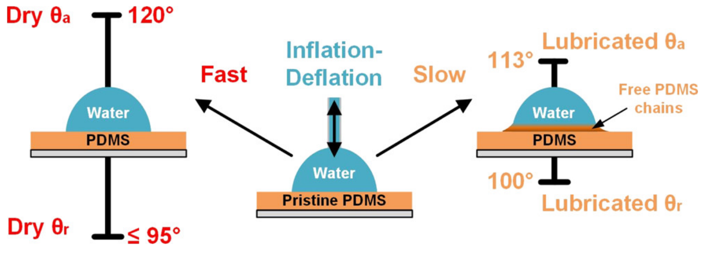

In *Adaptive Wetting of Polydimethylsiloxane* [2], PDMS adaptations are verified by goniometric contact angle measurements. For this, the advancing (θ_a) and receding (θ_r) are measured on drops that are de- and inflated on crosslinked polydimethylsiloxane surfaces, holding different amounts of free chains. The free chain amount is varied during synthesis. The standard synthesis procedure of Sylgard 184 (1:10, crosslinker to PDMS chains by weight) produces 'pristine' coatings with 5 %wt free chain content. Adding 8 %wt of silicone oil (2000 g/mol) during the synthesis creates 'lubricated' coatings. Immersing the pristine coatings for 24 h in toluene (a good solvent that swells the network), removes nearly all free chains and creates a 'dry' coating. On the pristine coatings, two values for $\Delta\theta = \theta_a - \theta_r$ were measured: a low one of $\approx 10°$, and a larger one. This is surprising since classically only a single value of $\Delta\theta$ characterizes a surface. The classical $\Delta\theta$ behavior is recovered on the lubricated elastomer coatings ($\theta \approx 10°$) or dry elastomer coatings ($\theta \approx 35°$). On pristine elastomer coatings, $\Delta\theta$ lies in between these two values. θ_a/θ_r on pristine coatings resembles the contact angles on the lubricated coating for low de-/inflation rates. Increasing the rates lead to a transition of θ_a/θ_r values, resembling the one on dry coatings. Hence, the degree of transition depends on the de-/infaltion rate. This transition is associated with surface adaptation: Upon drop contact, free oligomers migrate to the drop and create surface lubrication. The process is linked to first-order kinetics, which was previously proposed, theoretically [33, 66].

- **Functionality**. The contact angle hysteresis adaptations have direct consequences on the surface drop mobility. On pristine PDMS coatings adaptation is mostly suppressed on the advancing side for contact line speeds $> 50\ \mu$m/s (or capillary numbers $> 6 \times 10^{-7}$). The contact angle hysteresis is significantly suppressed for slow-moving drops. Hence, to maintain high drop mobility, it is advantageous to move slowly.

- **Durability**. When sufficient drops are moved over the surface, the free chains are gradually depleted over time. The study shows, that the adaptation speed is $\approx 5\mu m/s$. Contact lines that move slightly faster than this speed will reduce surface degradation.

2.2.1 Overarching Relevance

This study demonstrates how the molecular fabric of the PDMS surface close to the wetting zone influences the macroscopic shape and the contact angle hysteresis. The contact angle hysteresis $\Delta\theta$ can be utilized to gauge the force that builds up between a sliding drop and the underlying surface [cf. Sec. 1.1.4 and Eq. (1.20)]. Depending on the sliding speed of the drop, the capillary force between the drop and PDMS surface adapts. Understanding the adaptions enables minimizing the lateral capillary force and increasing drop mobility.

2.3 Water Transfer in (moving) PDMS

Water and PDMS interact very weakly, leading to partial wetting of water drops (cf. Sec. 1.1.3). The miscibility of water in PDMS, however, is relatively moderate ($\approx$ 770 ppm), and the diffusive mobility of water in PDMS ($\approx 2 \times 10^{-9}$ m^2/s) resembles liquid-liquid diffusion. The solubility and mobility of water in PDMS are usually investigated in setups, where bulk phases (water and PDMS) are stationary and share an interface [140, 238]. However, it is unclear what happens when the two bulk phases move relative against each other (which is the case for sliding drops). How does the movement affect the transfer from the water bulk into the PDMS bulk?

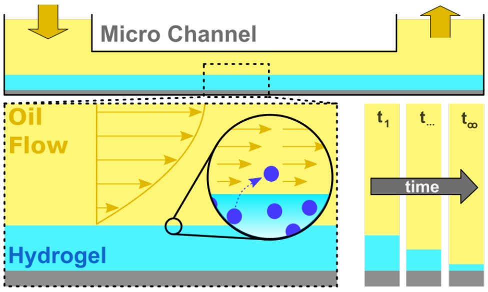

In *Linear Shrinkage of Hydrogel Coatings Exposed to Flow: Interplay Between Dissolution of Water and Advective Transport* [3] the dissolution of water in PDMS oil is investigated under the consideration of a relative sliding motion between the two phases. For this, a swollen hydrogel is exposed to a shearing (PDMS) silicone oil flow. The hydrogel is coated (thickness ≈ 5 μm) to the bottom of a microfluidic channel. Fluorescently dyed water swells the hydrogel to a thickness of up to 150 μm. 'Dry' silicone oil (*i.e.*, with zero water load) is steadily streamed over the hydrogel at flow rates ranging between $0.48-4.8$ ml/min. This leads to a gradual shrinkage of the hydrogel to its original height after 10 hours. Water migrates from the gel to the silicone oil and is entrained along. Computational fluid dynamics simulation reproduces the experimental findings and illustrates that the shared interface between oil and water is in a non-equilibrium. This implies a non-saturated interface and the requirement of a kinematic flux condition (Neumann boundary condition) at the shared interface. Physically, this flux condition roots in the energy barrier that water molecules need to overcome to migrate from the hydrogel to the oil phase. Utilizing the experimentally measured dehydration rates of the hydrogel, the results from simulations, and Kramer's theory that describes a diffusive barrier crossing, the energy barrier is determined to be $20-21\ \mathrm{k_bT}$, with k_B being the Boltzmann constant and T the ambient temperature.

2.3.1 Overarching Relevance

Wetting of water and silicone surfaces is facilitated by their weak mixing interaction that provides phase coexistence, cf. Sec. 1.3. However, the degree of water saturation in PDMS is not zero but around 770 ppm. Imbibing water may change the surface chemistry and hence, the surface energies, leading to differing wetting behavior (cf. Secs. 1.1.1, 1.1.2, and 1.1.4). When drops slide faster than $5.3mm/s$, the shared interface is in a non-equilibrium which significantly reduces water transport into PDMS. Further, this has consequences for the formation (or deformation) of water on PDMS coatings via phase change, such as condensation and evaporation: water can nucleate in silicone oil, drastically reducing the energy penalty; it can condense through a thin layer of silicone oil cloak and maintain condensation growth; or -on longer time scales - it may cause dehydration of aqueous environments.

2.4 Condensation and Frost on Oil Coatings

PDMS oil coatings showed promising frost repellency; a feature that is important for a range of applications (e.g. power lines, antennas, cryogenic equipment) [50]. The frost, however, drains on the oil lubricant [118, 239] which can lead to oil depletion and surface malfunction. The formation of condensation frosting is a transient process; the dynamic coupling between the oil and the condensation frosting process is unclear. This lack of insight needs to be cleared to overcome the depletion drawback.

In *How Frost Forms and Grows on Lubricated Micro- and Nanostructured Surfaces* [4] silicone oil-infused surfaces are cooled down to sub-zero temperatures (−12 to −22 °C) and exposed to humid atmospheres. This initiates condensation frosting (cf. Sec. 1.2) with the onset of condensation of liquid drops, the subsequent freezing of the liquid conden-

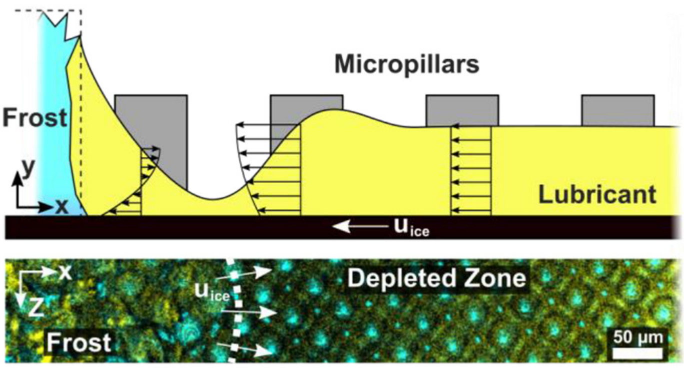

sate, and eventual frost propagation. The surface is structured with micro-post, regularly distributed on the surface. The fluorescently labeled PDMS lubricant sits in between the post-interstices. The lubricant on the surface is temporally and spatially monitored in course of condensation frosting by laser scanning confocal microscopy. A strong, dynamical coupling between the lubricant and the water during the respective condensation frosting stages is observed. In the condensation stage, water reliably condenses on top of the micro-posts. Due to the formation of oil-wetting ridges around the condensed drops (cf. Sec. 1.3.1.2), the lubricant depletes from the interstices. Upon frosting, the spiky structure of the frost leads to oil wicking into the frost patch (analogous to oil infusion, Sec. 1.3.1.1) and more oil depletion into the interstices. The suction of the oil into the porous frost structure evokes an oil flow from the micro-post interstices. While the suction into the oil is governed by the porosity of the frost and the affinity between frost and oil, the oil flow is governed by the surface tension and the viscosity of the oil. Both - oil flow and suction pressure - are affected by the porosity of the micro-post structure. The oil flow is modeled with thin film equations, that derive as an asymptotic limit from the Navier-Stokes equations. The (non-linear) thin film equations were implemented in (custom-written) numerical solvers. This generates the surface profile of the oil that is driven ahead of the propagating frost front. The numerically calculated profiles are verified by the experimentally measured profiles. This study gives the understanding under which frosting conditions oil depletes from the surface: frost propagation speed and frost dendrite morphology. Tuning the surface parameters (oil viscosity and texture porosity) can effectively reduce oil depletion.

- **Functionality**. Condensing drops experience low contact friction due to lubrication. Mobile drops can be rapidly removed from the surface (e.g. with a slight surface tilt) before they freeze and form frost clusters. Even when surface ice forms, the contact adhesion is low [51]. Thus, ice can be easily removed from the surface, too.
- **Durability**. The presence of oil lubricant conditions high drop mobility and low contact adhesion. Condensation frosting couples with the migration of oil. The coating durability is, hence, directly linked to the retention of oil during condensation frosting.

2.4.1 Overarching Relevance

Surfaces impregnated with PDMS silicone oil (a so-called 'lubricant') can create frost-repellency and remove surface contaminates. These features are rooted in lubrication: frost or its liquid drop precursors, experiences little sliding friction, and is rapidly removed from the surface. However, for lubrication to work, the presence of silicone oil on the surface is necessary and it is not obvious how frost and the lubricant interact, cf. Sec. 1.3.1. This study investigates the coupling between silicone oil infusion and frost formation. The governing parameters for lubricant depletion during frosting are determined that derive guidelines to avoid depletion.

2.5 Frost Formation and Propagation on Oil Coatings

The performance of PDMS oil coatings for anti-frosting is linked to the dynamics (*i.e.*, speed and mode) of condensation frosting [4]. While the formation of condensation frosting on dry surfaces is relatively well-understood [115, 240], a (dynamic) picture on oil-lubricated surfaces is missing.

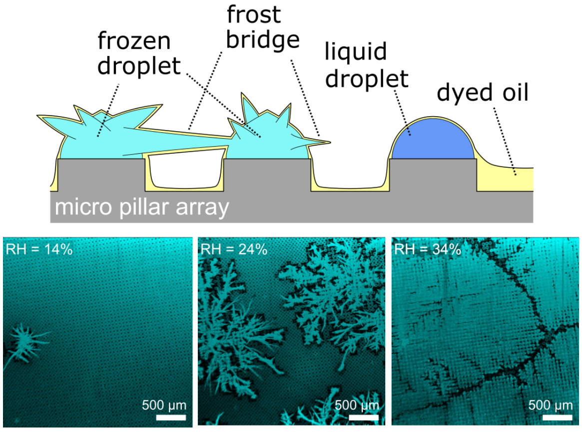

In *Frost Spreading and Pattern Formation on Microstructured Surfaces* [5] the formation and propagation of frost are investigated on lubricant-infused surfaces under a range of ambient conditions (various surface temperatures and relative humidity). Condensation frosting is characterized by a two-step process where water initially condenses as liquid droplets and subsequently freezes and propagates as continuous frost patches. The formation and propagation of frost on silicone oil-infused surfaces are affected by the presence of the oil. This stems from the strong wetting interactions between water and oil: water forms wetting ridges and cloaking layers around droplets and wicks into the porous frost structure. Micro-post textures are utilized to retain the oil on the surface and to foster regular drop condensation. Droplets tend to nucleate on top of the micro-posts as the micro-texture is hydrophilized by chemical treatment. The silicone oil is labeled with a fluorophore marker that enhances the contrast between frost, and surface. Frosting on the surface is temporally resolved with laser-induced fluorescence microscopy. By a variety of environmental frosting conditions (surface temperature and relative humidity), different modes of frost propagation were monitored. In very humid conditions, frost grows as a bulky structure with relatively smooth patch perimeters. In this regime, plenty of droplets with large volumes condense, supplying the subsequent frost propagation with a sufficient amount of liquid reservoir in form of drops. The propagation of the frost patch is a combination of diffusion through air and silicone oil during frost-bridge growth and drop-freezing upon contact. The combination of these two modes whereas the second is much faster than the former yields a relatively fast frost patch propagation. When the humidity is decreased, not all drops join the frost patch but some completely evaporate, leaving dry spots behind. This leads to a fractal frost patch structure where the propagation is around 30% slower. In very dry conditions water condenses sparsely on the surface leading to starved frost propagation of only single, small spiky structures. The silicone oil that surrounds water in liquid or solid states hampers the water diffusion, as the H_2O mobility is decreased by ≈ 4 orders of magnitude in silicone oil, compared to in the air. However, the water-surrounding silicone oil films are never too tick (from drop-cloaking layers around ≈ 10 nm to frost-wicking films around 10 μm).

Therefore, the overall diffusion resistance is not completely suppressed. The effect of the silicone oil on the diffusive mass transport is illustrated in a resistor model that accounts for the diffusive mobility in silicone and air, respectively. This shows that the presence of silicone oil on frozen drops becomes significant, when the drops are small; which is the case in course of condensation. Colder surface temperatures lead to an increased frost patch nucleation density. When the surface temperature falls below −40 °C the frost patch density approaches the limit of the micro-post density of the surface. This study shows how silicone oil and ambient conditions can tune the speed and mode of frost propagation. The experimental findings are supported by a diffusion model that elaborates on the influence of silicone oil as a diffusion damper. The frost structures are analyzed in terms of their fractal dimension which unravels that for high relative humidity frost propagates in a 'ballistic limit' where all liquid drops join the frost patch to a 'diffusion-limited-aggregate' at lower humidity that reassembles random-walker propagation.

- **Durability**. The fractal structure of frost depletes silicone oil-infused surfaces by wicking. The formation and propagation (topography/speed) are critical coupling parameters for oil depletion. Therefore studying how ambient conditions affect the formation and propagation of frost is key to circumventing lubricant depletion and determining suitable operation conditions for the use of PDMS oil coatings for anti-frosting applications.

2.5.1 Overarching Relevance

The diffusive transport of water in PDMS is relevant to understand how phase-change-induced wetting interactions take place on PDMS surfaces (condensation, evaporation, frosting). This model system illustrates how much PDMS shields the diffusive transport of water. Utilizing the propagation of the silicone oil-covered frost gives clues about the thickness of the silicone oil film on water. Studying the nature of this film becomes important as it influences wetting (cf. Sec. 1.3.1.3). This film may vary between ≈ 10 nm − 10 μm from drop-cloaking layers to frost-wicking films.

Appendix A

Appendix

A.1 Continuum Mechanics in the Wetting Ridges

Crosslinked PDMS forms a tethered network with elasticity, which is characteristic of solid material. Mechanically, this implies that the crosslinked network can withstand strain by building up internal stresses. To get an understanding of these stress-strain relationships, I start to introduce the kinematics (shear, strain) of the body within a mathematical framework [241–243]. Strain is defined as the deformation that the material undergoes. Consider a reference configuration where each point of the undeformed body is localized by $\vec{x}$. When the body undergoes some arbitrary deformation, each point from the initial localization $\vec{x}$ is displaced to a deformed configuration $\vec{x}'$ by

$$\vec{u} = \vec{x}' - \vec{x}. \tag{A.1}$$

Alternatively, the underfomerd configuration can be mapped to the deformed one with the 'deformation gradient' $\boldsymbol{F} = d\vec{x}'/d\vec{x}$, as

$$d\vec{x}' = \boldsymbol{F} d\vec{x}. \tag{A.2}$$

Strain quantifies how much relative deformation a body underwent. The strain can be quantified in normal or lateral directions. Therefore, the full strain at each point of the deformed body is characterized by a second-order tensor, $\boldsymbol{\epsilon}$. The strain in the normal directions sits on the main diagonal while the lateral strain (*i.e.*, shear) sits on the off-diagonal elements of $\boldsymbol{\epsilon}$. Generally, the strain tensor is expressed with the deformation gradient

$$\boldsymbol{\epsilon} = \frac{1}{2}\left(\boldsymbol{F}\boldsymbol{F}^T - 1\right), \tag{A.3}$$

or in index notation[1]

---

[1] ϵ_{ij} denotes the index notation, where e.g. $\vec{x} = x_i = [x_1, x_2, x_3]^T$ denotes the three spatial directions.

$$\epsilon_{ij} = \frac{1}{2}\left(\frac{\partial u_i}{\partial x_j} + \frac{\partial u_j}{\partial x_i} + \frac{\partial u_k}{\partial x_k}\frac{\partial u_i}{\partial x_j}\right). \tag{A.4}$$

The strain tensor Eq. (A.4) in this form is also known as the Cauchy strain tensor. Good intuition for this tensor can be developed by considering only small deformations[2]. In this approximation, the last (nonlinear) term in Eq. (A.4) vanishes. Within this approximation, the normal strain descriptively shows extensions and retractions per

$$\epsilon_{ii} = \frac{du_i}{dx_i}. \tag{A.5}$$

For lateral strain (*i.e.*, shear) the tensor measures the opening angle between an undeformed and a deformed line

$$\epsilon_{ij} = \frac{1}{2}\left(\frac{du_i}{dx_j} + \frac{du_j}{dx_i}\right),\ i \neq j. \tag{A.6}$$

The strain rate is now easily accessible by finding the time derivative of the strain tensor

$$\dot{\epsilon}_{ij} = \frac{d\epsilon_{ij}}{dt}. \tag{A.7}$$

The material stress of elastic materials is associated with the strain. Within a linearized framework, stress and strain are related with coefficients attributing to the (macroscopic) stiffness E and the ratio to the lateral strain ν (Poisson's ratio)[3]. A linear, so-called 'Hookean' relationship [244] is then

$$\boldsymbol{\tau} = \frac{E}{1+\nu}\left(\boldsymbol{\epsilon} + \frac{\nu}{1-2\nu}\mathrm{tr}(\boldsymbol{\epsilon})\boldsymbol{I}\right), \tag{A.8}$$

where $\boldsymbol{I}$ denotes the identity matrix. Stress-strain relationships are characteristic of solid materials and are features that emerge upon cross-linking of PDMS. A similar (linear) relation exists for fluids. However, fluids are fundamentally different from solids. Mechanically, this becomes evident considering a finite imposed shear on a fluid body. The fluid body rearranges freely under the imposed stress, while a solid body builds up non-zero internal stress. However, while undergoing the deformation, fluids build up frictional (viscous) stresses, as the fluid molecules shear against each other. This viscous stress (in its simplest form) is linearly related to the shear rate with the viscous coefficient (viscosity, η) by

$$\boldsymbol{\tau} = \eta\dot{\boldsymbol{\epsilon}}. \tag{A.9}$$

---

[2] As only deformations of a material point to a locally near one need to be small, the 'small deformation' assumption is still valid even for large body deformations.

[3] For incomprssible materials $\nu = 0.5$.

Fluids that follow such a linear behavior are 'Newtonian fluids'[4]. Many solids and fluids are more complex in their stress responses. Their elastic and viscous coefficients can depend on the kinematics $(\boldsymbol{\epsilon}, \dot{\boldsymbol{\epsilon}})$. Gels for example, exhibit a stress saturation after sufficient deformation ('neo-Hookean' behaviour [245]). Polymer chains in melts may align in course of increasing stress, leading to shear-thinning viscous stress. Alternatively, polymers (or sufficiently concentrated suspension particles) may interlock at higher shear rates, resulting in a shear-thickening effect. Fig. A.1b qualitatively illustrates the constitutive relation of the different materials.

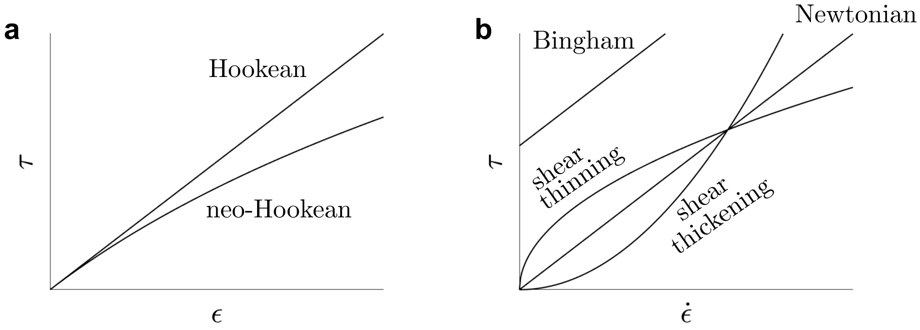

Figure A.1: Qualitative constitutive relations of different **a)** solid and **b)** liquid materials.

Polymer melts above the glass transition temperature are fluids. However, sufficiently long polymer chains can entangle. Such entanglements can build up internal (elastic) stresses when their chains are stretched. Note, that the viscous property is not immediately lost, as soon as such entanglements take place. The transition is gradual and the polymer exhibit both, elastic and viscous features over a large range of polymer chain lengths and several entanglements. Their material property is, hence, characterized as 'viscoelastic'. Similarly to the entanglement transition, chemical crosslinks evoke also viscoelasticity in elastomers. Viscoelastic behavior can be illustrated by considering a finite stretch on an elastomer. Immediately after imposing the stretch, the material answers with elastic stresses. Thereafter, the polymers start to rearrange ('creep') and gradually break down the internal stresses. The reorganization is accompanied by internal friction as polymers shear against each other. This is the viscous component of the material. After some time, the polymer chains adapted to the stretch such that no internal stresses prevail any longer. This example shows that the material behaves differently at different time scales: at short times, the material reacts as an elastic solid while at long times it starts to creep and reacts as a fluid. A simple constitutive relation that reflects this behavior is the Maxwell model [246],

$$\boldsymbol{\tau} + \lambda_1 \dot{\boldsymbol{\tau}} = \eta_0 \dot{\boldsymbol{\epsilon}}. \tag{A.10}$$

Here, λ_1 is the relaxation time which is the time needed to dissipate the internal stresses and η_0 is the shear modulus, reflecting microscopic stiffness. It is also the limiting time scale that separates

---

[4] E.g., water, low molecular weight polymers, many organic liquids, etc.

the material behavior from elastic ($t \ll \lambda_1$) to viscous ($t \gg \lambda_1$). Within intermediate timescales around λ_1, both response contributions need to be considered. η_0 and λ_1 depend on the specific polymer properties, such as length and chemical structure. Many polymers are not mono-disperse[5] but comprise polymers of differing lengths and molecules. Therefore, polymers are not characterized by one but many relaxation times (λ_k) and shear moduli (η_k). Each of these time and stiffness scales yield a kinematic relations between each $\boldsymbol{\tau}_k$ and $\boldsymbol{\epsilon}_k$, such as Eq. (A.10). Under the linearity assumption, these equations can be superposed and the total stress sums up to

$$\boldsymbol{\tau} = \sum_{k=1}^{\infty} \boldsymbol{\tau}_k. \tag{A.11}$$

The total stress evolution over time $\boldsymbol{\tau}(t)$ can be found by integrating Eq. (A.10), employing the condition of zero stress at $t \to \infty$. This yields

$$\boldsymbol{\tau}(t) = -\int_{-\infty}^{t} \left[\sum_{k=1}^{\infty} \frac{\eta_k}{\lambda_k} e^{-\frac{t-t'}{\lambda_k}} \right] \dot{\boldsymbol{\epsilon}}(t') dt' \tag{A.12}$$

the coefficient within the brackets in the integral reflects the material properties. It is the 'response function' or 'relaxation modulus' of the material and is written compactly as

$$\Psi(t-t') = -\sum_{k=1}^{\infty} \frac{\eta_k}{\lambda_k} e^{-\frac{t-t'}{\lambda_k}}. \tag{A.13}$$

The response function encodes the entire relaxation spectrum of the polymer. Now, the stress can be conveniently expressed as

$$\boldsymbol{\tau}(t) = \int_{-\infty}^{t} \Psi(t-t') \dot{\boldsymbol{\epsilon}}(t') dt'. \tag{A.14}$$

Transforming Eq. (A.10) into the frequency domain gives another perspective of the relaxation modulus and allows the introduction of the 'complex modulus'. In frequency space, the kinematic ratio becomes

$$\frac{\boldsymbol{\tau}_k(\omega)}{\boldsymbol{\epsilon}_k(\omega)} = \eta_k \left[\frac{\omega^2 + \lambda_k i\omega}{1 + \omega^2 \lambda_k^2} \right] = G'_k(\omega) + iG''_k(\omega). \tag{A.15}$$

with the storage modulus $G' = \sum_{k=1}^{\infty} G'_k(\omega)$ and the loss modulus $G'' = \sum_{k=1}^{\infty} G''_k(\omega)$. The complex modulus is

$$G^*(\omega) = G'(\omega) + iG''(\omega), \tag{A.16}$$

The complex modulus is also obtained directly from the response function by employing

$$G^*(\omega) = i\omega \int_{0}^{\infty} \Psi(\xi) e^{-i\omega\xi} d\xi. \tag{A.17}$$

---

[5] Homogeneous polymer chains of the same length and chemical makeup.

The complex, rate dependent modulus is a useful tool in practice, as many measurements are based on the oscillatory shear (e.g. $\epsilon_{12}(t) = \hat{\epsilon}\cos[\omega t]$) of the material and measuring the stress responds ($\tau_{12}(t) = \hat{\tau}\cos[\omega t + \delta]$). Their ratio is then a straightforward computation and yields the complex modulus. The phase shift δ of the stress response can be found from the ratio of the loss and the storage modulus

$$\frac{G''}{G'} = \tan\delta. \tag{A.18}$$

The phase shift is a good indicator to gauge whether the material behaves more like a liquid or like a solid:

$$\delta = \begin{cases} \ll \pi/4 & \text{solid-like behaviour} \\ \gg \pi/4 & \text{liquid-like behaviour.} \end{cases} \tag{A.19}$$

Another frequently used rheological model for the relaxation of elastomers is the Chasset-Thirion model which describes the complex modulus as

$$G^*(\omega) = \eta_0 \left[1 + (i\lambda\omega)^n\right]. \tag{A.20}$$

In this picture, there is one dominating timescale λ that governs the elastomer relaxation. The rheological exponent n indicates the steepness of the crossover between solid-like and viscoelastic-like behaviour, Fig. A.2b.

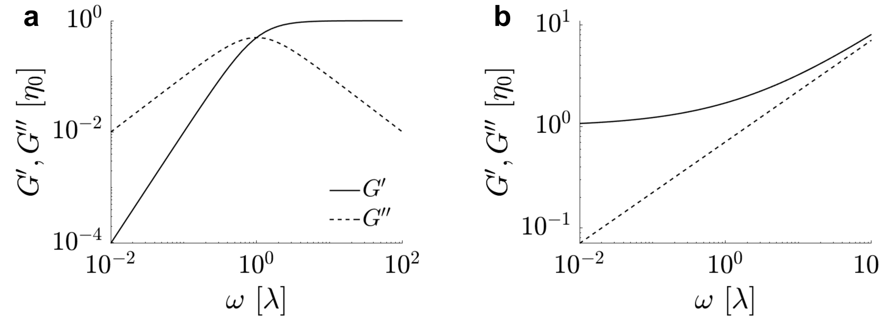

Figure A.2: G' (solid line) and G'' (dashed line) responds (normalized by η_0) to oscillatory shear ω (normalized by λ) of **a)** Maxwell material and **b)** Chasset-Thirion material.

A.2 Elastic Ridge Profile

When liquid drops come in contact with elastic PDMS networks, the network material is pulled upwards as a consequence of the drops surface tension. Here, I demonstrate a derivations for the (linear) elastic wetting ridge using Fourier transformations of the horizontal space component. The procedure was introduced by Limat et al. [208]. It starts by considering the stress tensor in the elastic network bulk

$$\boldsymbol{\sigma} = p\boldsymbol{I} + \boldsymbol{\tau}. \tag{A.21}$$

The momentum conservation assumes the form of a Cauchy equation. In steady state, the equation reads.

$$\nabla \cdot \boldsymbol{\sigma} = 0. \tag{A.22}$$

A Cartesian coordinate system at the surface of the PDMS network is introduced. Further, the radial symmetry of the drop is exploited that reduces the problem to only two dimensions. As discussed in Section 1.3.2.1, the radius of the drop is sufficiently large, which justifies a Cartesian coordinate system, *i.e.* curvature effects can be disregarded. This gives the set of coordinates $\vec{x} = [x_1, x_2]^T$, where x_1 is the horizontal and x_2 is the vertical component. $\vec{x}$ are material coordinates and follow the defromations of the network. At $x_2 = 0$ the drop imposes the point load (traction force)

$$\vec{f} = \gamma_w \left\{ \cos\theta \vec{t} + \sin\theta \vec{n} \right\} \delta\left(x_1 - x_{\text{cl}}\right), \tag{A.23}$$

where x_{cl} is the location of the three-phase contact line and $\delta(x - x_{\text{cl}})$ is the Dirac delta. $\vec{n}$ and $\vec{t}$ are the normal and tangential vectors of the PDMS surface at $x_2 = 0$. The stress boundary condition at at the film surface reads

$$\Upsilon_{\text{e}} \left(\nabla \cdot \vec{n}\right) \vec{n} - \boldsymbol{\sigma}\vec{n} + \vec{f} = 0, \tag{A.24}$$

where Υ_{e} is the solid surface stress of the PDMS film at $x_2 = 0$. The vertical displacement at $x_2 = 0$ is the curve yields the surface profile that corresponds to the profile of the elastic wetting ridge

$$\zeta(x_1) = u_2(x_1, x_2 = 0). \tag{A.25}$$

The normal vector is then $\vec{n} = [\zeta'/\sqrt{(1+\zeta'^2)}, 1/\sqrt{(1+\zeta'^2)}]^T$. At $x_2 = h_0$ the film is attached which prohibits displacements such that, here the appropriate boundary condition reads

$$\vec{u} = 0. \tag{A.26}$$

Eqs. (A.21)-(A.26) together with (A.8) form the system of equations that govern the shape of the elastic wetting ridge. To find a solution, the effective stream function $\psi(\vec{x})$ [**zhao˙geometrical˙2018a**, 208] is introduced as

$$\frac{\partial \psi}{\partial x_2} \equiv -u_1, \tag{A.27a}$$

$$\frac{\partial \psi}{\partial x_1} \equiv u_2, \tag{A.27b}$$

is introduced. Combining Eqs. (A.8), (A.22), and (A.27) and applying the curl operation ($\nabla\times$) yield the biharmonic equation

$$\nabla^4 \psi = \frac{\partial^4 \psi}{\partial^4 x_1} + 2\frac{\partial^4 \psi}{\partial^2 x_1 \partial^2 x_2} + \frac{\partial^4 \psi}{\partial^4 x_2} = 0. \tag{A.28}$$

The horizontal space component x_1 of Eq. is transformed into frequency space, yielding

$$q^4 \tilde{\psi} + 2q^2 \frac{\partial^2 \tilde{\psi}}{\partial^2 x_2} + \frac{\partial^4 \tilde{\psi}}{\partial^4 x_2} = 0, \tag{A.29}$$

with $\tilde{\psi}$ being the Fourier transform of ψ,

$$\tilde{\psi}\left(q, x_2\right) = \int_{-\infty}^{\infty} \psi\left(x_1, x_2\right) e^{-iqx_1} dx_1, \tag{A.30}$$

and q being the wave number. The general solution of Eq. (A.29) regarding x_2 can be obtained by quadruple integration

$$\tilde{\psi}\left(q, x_2\right) = C_1 e^{qx_2} + C_2 e^{-qx_2} + C_3 x_2 e^{qx_2} + C_4 x_2 e^{-qx_2}. \tag{A.31}$$

The integration constants $C_1 - C_4$ are specified by the boundary conditions Eqs. (A.24) and (A.26). The conditions in the frequency domain are

$$2\eta_0 iq \frac{\partial \tilde{\psi}}{\partial x_2} - \frac{\eta_0 i}{q} \left(\frac{\partial^3 \tilde{\psi}}{\partial x_2^3} - q^2 \frac{\tilde{\psi}}{\partial x_2} \right) = \tilde{f}_1(q) - \Upsilon_e ik^3\tilde{}(q), \tag{A.32a}$$

$$\eta_0 \left(-q^2 \tilde{\psi} + \frac{\partial^2 \tilde{\psi}}{\partial x_2^2} \right) = \tilde{f}_2(q), \tag{A.32b}$$

at $x_2 = 0$, and

$$\frac{\partial \tilde{\psi}}{\partial x_2} = 0, \tag{A.33a}$$

$$\tilde{\psi} = 0, \tag{A.33b}$$

at $x_2 = h_0$. Imposing boundary conditions (A.32) and (A.33) on Eq. (A.31) yields the ridge profile, in frequency space

$$\tilde{\zeta}\left(q\right) = Q(q)^{-1} \left(\tilde{f}_2 - i\tilde{f}_1 \frac{2h_0^2 q^2}{\sinh\left(2h_0 q\right) - 2h_0 q} \right), \tag{A.34}$$

where $Q(q)$ is the material responds. This can be viewed as a generalized spring constant

$$Q(q) = \frac{\Upsilon_e}{q^2 + \frac{\eta_0}{\Upsilon_e} K(q)^{-1}}, \tag{A.35}$$

and

$$K(q) = \frac{1}{2q} \left(\frac{\sinh(2h_0 q) - 2h_0 q}{2h_0^2 q^2 + \cosh(2h_0 q) + 1} \right). \tag{A.36}$$

If the film thickness h_0 exceeds the size of the wetting ridge $\mathcal{O}(h_0) \gg \mathcal{O}(\zeta)$, the complex spring constant converges to

$$\lim_{h_0/\zeta \to \infty} Q(q) = Q_\infty(q) = \frac{\Upsilon_e}{q^2 + 2q\frac{\eta_0}{\Upsilon_e}}. \tag{A.37}$$

In this thick film limit, the material response depends on the wavelength (or length scale) of the surface perturbation. When the perturbation wavelength is $\mathcal{O}(q) \ll 2\eta_0/\Upsilon_e$ the material responds dominantly with the solid surface tension Υ_e. In this limit, the force balance is similar to the Neumann configuration (cf. Section 1.3.1.2) [89]. When $\mathcal{O}(q) \gg 2\eta_0/\Upsilon_e$, bulk elasticity η_0 become important and factor into the ridge geometry [209]. Still, the solid surface tension is required as a (theoretical) ridge that is solely governed by bulk elasticity divergence at the tip where the point load attacks [204, 208]. Note, that the crossover is at $\delta_{e,\mathrm{II}}$. From a molecular perspective, elastic bulk contribution start to matter as soon as the perturbation length falls below a length scale at which elastic forces start to act [204, 208, 212]

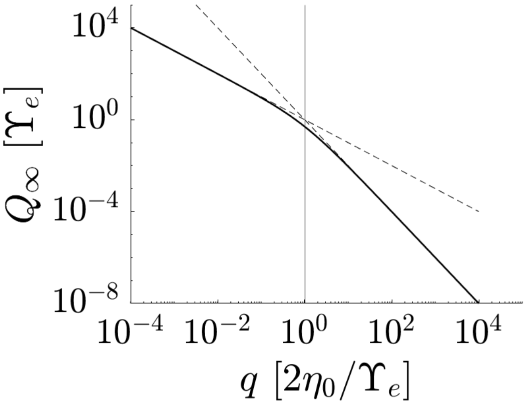

Figure A.3: Stiffness of generalized spring constant for thick coatings ($h_0 \to \infty$). For wetting ridges of the size $\mathcal{O}(\zeta) < \Upsilon_e/2\eta_0$ Q_∞ is stiff and responds mostly *via* the surface tension stiffness Υ_e. For $\mathcal{O}(\zeta) > \Upsilon_e/2\eta_0$, bulk elasticity contributes to Q_∞.

Bibliography

1. Hauer, L., Cai, Z., Vollmer, D. & Pham, J. T. *Phase Separation in Wetting Ridges of Sliding Drops on Soft and Swollen Surfaces* Aug. 2022. arXiv: `2208.11177 [cond-mat]`.
2. Wong, W. S. Y. *et al.* Adaptive Wetting of Polydimethylsiloxane. *Langmuir* **36,** 7236–7245. ISSN: 0743-7463 (July 2020).
3. Baumli, P. *et al.* Linear Shrinkage of Hydrogel Coatings Exposed to Flow: Interplay Between Dissolution of Water and Advective Transport. *Soft Matter* **18,** 365–371. ISSN: 1744-6848 (Jan. 2022).
4. Hauer, L. *et al.* How Frost Forms and Grows on Lubricated Micro- and Nanostructured Surfaces. *ACS Nano* **15,** 4658–4668. ISSN: 1936-0851, 1936-086X (Mar. 2021).
5. Hauer, L., Wong, W. S. Y., Sharifi-Aghili, A., Kondic, L. & Vollmer, D. Frost Spreading and Pattern Formation on Microstructured Surfaces. *Phys. Rev. E* **104,** 044901 (Oct. 2021).
6. Hamilton, W. J. & Seely, M. K. Fog Basking by the Namib Desert Beetle, Onymacris Unguicularis. *Nature* **262,** 284–285. ISSN: 0028-0836, 1476-4687 (July 1976).
7. Zheng, Y. *et al.* Directional Water Collection on Wetted Spider Silk. *Nature* **463,** 640–643. ISSN: 0028-0836, 1476-4687 (Feb. 2010).
8. Ju, J. *et al.* A Multi-Structural and Multi-Functional Integrated Fog Collection System in Cactus. *Nat. Commun.* **3,** 1247. ISSN: 2041-1723 (Jan. 2012).
9. Ebner, M., Miranda, T. & Roth-Nebelsick, A. Efficient Fog Harvesting by Stipagrostis Sabulicola (Namib Dune Bushman Grass). *J. Arid Environ.* **75,** 524–531. ISSN: 01401963 (June 2011).
10. Lord, J. *et al.* Global Potential for Harvesting Drinking Water from Air Using Solar Energy. *Nature* **598,** 611–617. ISSN: 0028-0836, 1476-4687 (Oct. 2021).
11. Liu, X., Beysens, D. & Bourouina, T. Water Harvesting from Air: Current Passive Approaches and Outlook. *ACS Mater. Lett.* **4,** 1003–1024. ISSN: 2639-4979, 2639-4979 (May 2022).
12. Fujishima, A. & Zhang, X. Titanium Dioxide Photocatalysis: Present Situation and Future Approaches. *C. R. Chim.* **9,** 750–760. ISSN: 16310748 (May 2006).
13. Thiele, U., Velarde, M. G. & Neuffer, K. Dewetting: Film Rupture by Nucleation in the Spinodal Regime. *Phys. Rev. Lett.* **87,** 016104. ISSN: 0031-9007, 1079-7114 (June 2001).
14. Maas, J. H., Fleer, G. J., Leermakers, F. A. M. & Cohen Stuart, M. A. Wetting of a Polymer Brush by a Chemically Identical Polymer Melt: Phase Diagram and Film Stability. *Langmuir* **18,** 8871–8880. ISSN: 0743-7463, 1520-5827 (Nov. 2002).
15. Liu, P., Huang, X., Zhou, R. & Berne, B. J. Observation of a Dewetting Transition in the Collapse of the Melittin Tetramer. *Nature* **437,** 159–162. ISSN: 0028-0836, 1476-4687 (Sept. 2005).
16. Hua, L., Huang, X., Liu, P., Zhou, R. & Berne, B. J. Nanoscale Dewetting Transition in Protein Complex Folding. *J. Phys. Chem. B* **111,** 9069–9077. ISSN: 1520-6106, 1520-5207 (Aug. 2007).
17. Young, T. III. An Essay on the Cohesion of Fluids. *Phil. Trans. R. Soc.* **95,** 65–87. ISSN: 0261-0523, 2053-9223 (Dec. 1805).

18. de Gennes, P. G. Wetting: Statics and Dynamics. *Rev. Mod. Phys.* **57,** 827–863. ISSN: 0034-6861 (July 1985).

19. *Surface Science Techniques* (eds Bracco, G. & Holst, B.) ISBN: 978-3-642-34242-4 978-3-642-34243-1 (Berlin, Heidelberg, 2013).

20. Lafuma, A. & Quéré, D. Superhydrophobic States. *Nat. Mater.* **2,** 457–460. ISSN: 1476-1122, 1476-4660 (July 2003).

21. Marmur, A. The Lotus Effect: Superhydrophobicity and Metastability. *Langmuir* **20,** 3517–3519. ISSN: 0743-7463, 1520-5827 (Apr. 2004).

22. Mognetti, B. M., Kusumaatmaja, H. & Yeomans, J. M. Drop Dynamics on Hydrophobic and Superhydrophobic Surfaces. *Faraday Discuss.* **146,** 153. ISSN: 1359-6640, 1364-5498 (2010).

23. Backholm, M. *et al.* Water Droplet Friction and Rolling Dynamics on Superhydrophobic Surfaces. *Commun. Mater.* **1,** 64. ISSN: 2662-4443 (Dec. 2020).

24. Barthlott, W. & Neinhuis, C. Purity of the Sacred Lotus, or Escape from Contamination in Biological Surfaces. *Planta* **202,** 1–8. ISSN: 0032-0935, 1432-2048 (Apr. 1997).

25. Naga, A. *et al.* How a Water Drop Removes a Particle from a Hydrophobic Surface. *Soft Matter* **17,** 1746–1755. ISSN: 1744-683X, 1744-6848 (2021).

26. Truesdell, R., Mammoli, A., Vorobieff, P., van Swol, F. & Brinker, C. J. Drag Reduction on a Patterned Superhydrophobic Surface. *Phys. Rev. Lett.* **97,** 044504. ISSN: 0031-9007, 1079-7114 (July 2006).

27. Zhu, J., Hsu, C.-M., Yu, Z., Fan, S. & Cui, Y. Nanodome Solar Cells with Efficient Light Management and Self-Cleaning. *Nano Lett.* **10,** 1979–1984. ISSN: 1530-6984, 1530-6992 (June 2010).

28. Deng, B. *et al.* Laundering Durability of Superhydrophobic Cotton Fabric. *Adv. Mater.* **22,** 5473–5477. ISSN: 1521-4095 (2010).

29. Park, Y.-B., Im, H., Im, M. & Choi, Y.-K. Self-Cleaning Effect of Highly Water-Repellent Microshell Structures for Solar Cell Applications. *J. Mater. Chem.* **21,** 633–636. ISSN: 0959-9428, 1364-5501 (2011).

30. Pernites, R. B. *et al.* Tunable Protein and Bacterial Cell Adsorption on Colloidally Templated Superhydrophobic Polythiophene Films. *Chem. Mater.* **24,** 870–880. ISSN: 0897-4756, 1520-5002 (Mar. 2012).

31. Darmanin, T. & Guittard, F. Recent Advances in the Potential Applications of Bioinspired Superhydrophobic Materials. *J. Mater. Chem. A* **2,** 16319–16359. ISSN: 2050-7488, 2050-7496 (2014).

32. Geyer, F. *et al.* When and How Self-Cleaning of Superhydrophobic Surfaces Works. *Sci. Adv.* **6,** eaaw9727. ISSN: 2375-2548 (Jan. 2020).

33. Butt, H.-J., Berger, R., Steffen, W., Vollmer, D. & Weber, S. A. L. Adaptive Wetting—Adaptation in Wetting. *Langmuir* **34,** 11292–11304. ISSN: 0743-7463 (Sept. 2018).

34. Bhowmick, A. K. *Current Topics in Elastomers Research* ISBN: 978-1-4200-0718-3 (Boca Raton, FL, May 2008).

35. Griffith, L. G. Polymeric Biomaterials. *Acta Mater.* **48,** 263–277. ISSN: 1359-6454 (Jan. 2000).

36. Yoda, R. Elastomers for Biomedical Applications. *J. Biomater. Sci. Polym. Ed.* **9,** 561–626. ISSN: 0920-5063, 1568-5624 (Jan. 1998).

37. Lim, J. A., Liu, F., Ferdous, S., Muthukumar, M. & Briseno, A. L. Polymer Semiconductor Crystals. *Materials Today* **13,** 14–24. ISSN: 1369-7021 (May 2010).

38. Greenham, N. C. & Friend, R. H. in *Solid State Physics* (eds Ehrenreich, H. & Spaepen, F.) 1–149 (Jan. 1996).

39. Lalia, B. S., Kochkodan, V., Hashaikeh, R. & Hilal, N. A Review on Membrane Fabrication: Structure, Properties and Performance Relationship. *Desalination* **326,** 77–95. ISSN: 0011-9164 (Oct. 2013).

40. Eduok, U., Faye, O. & Szpunar, J. Recent Developments and Applications of Protective Silicone Coatings: A Review of PDMS Functional Materials. *Prog. Org. Coat.* **111,** 124–163. ISSN: 03009440 (Oct. 2017).

41. Golovin, K., Dhyani, A., Thouless, M. D. & Tuteja, A. Low–Interfacial Toughness Materials for Effective Large-Scale Deicing. *Science* **364,** 371–375. ISSN: 0036-8075, 1095-9203 (Apr. 2019).

42. Hu, P., Xie, Q., Ma, C. & Zhang, G. Silicone-Based Fouling-Release Coatings for Marine Antifouling. *Langmuir* **36,** 2170–2183. ISSN: 0743-7463 (Mar. 2020).

43. Klein, J., Perahia, D. & Warburg, S. Forces Between Polymer-Bearing Surfaces Undergoing Shear. *Nature* **352,** 143–145. ISSN: 0028-0836, 1476-4687 (July 1991).

44. Klein, J. Shear, Friction, and Lubrication Forces Between Polymer-Bearing Surfaces. *Annu. Rev. Mater. Sci.* **26,** 581–612. ISSN: 0084-6600 (Aug. 1996).

45. Kreer, T. Polymer-Brush Lubrication: A Review of Recent Theoretical Advances. *Soft Matter* **12,** 3479–3501. ISSN: 1744-683X, 1744-6848 (2016).

46. Klein, J. Repair or Replacement–A Joint Perspective. *Science* **323,** 47–48. ISSN: 0036-8075, 1095-9203 (Jan. 2009).

47. Solomon, B. R., Khalil, K. S. & Varanasi, K. K. Drag Reduction Using Lubricant-Impregnated Surfaces in Viscous Laminar Flow. *Langmuir* **30,** 10970–10976. ISSN: 0743-7463 (Sept. 2014).

48. Lee, T., Charrault, E. & Neto, C. Interfacial Slip on Rough, Patterned and Soft Surfaces: A Review of Experiments and Simulations. *Adv. Colloid Interface Sci.* **210,** 21–38. ISSN: 00018686 (Aug. 2014).

49. Subramanyam, S. B., Rykaczewski, K. & Varanasi, K. K. Ice Adhesion on Lubricant-Impregnated Textured Surfaces. *Langmuir* **29,** 13414–13418. ISSN: 0743-7463, 1520-5827 (Nov. 2013).

50. Kim, P. *et al.* Liquid-Infused Nanostructured Surfaces with Extreme Anti-Ice and Anti-Frost Performance. *ACS Nano* **6,** 6569–6577. ISSN: 1936-0851 (Aug. 2012).

51. Wong, W. S. Y. *et al.* Capillary Balancing: Designing Frost-Resistant Lubricant-Infused Surfaces. *Nano Lett.* **20,** 8508–8515. ISSN: 1530-6984 (Dec. 2020).

52. Amini, S. *et al.* Preventing Mussel Adhesion Using Lubricant-Infused Materials. *Science* **357,** 668–673. ISSN: 0036-8075, 1095-9203 (Aug. 2017).

53. Epstein, A. K., Wong, T.-S., Belisle, R. A., Boggs, E. M. & Aizenberg, J. Liquid-Infused Structured Surfaces with Exceptional Anti-Biofouling Performance. *Proc. Natl. Acad. Sci. U.S.A.* **109,** 13182–13187. ISSN: 0027-8424, 1091-6490 (Aug. 2012).

54. Leslie, D. C. *et al.* A Bioinspired Omniphobic Surface Coating on Medical Devices Prevents Thrombosis and Biofouling. *Nat. Biotechnol.* **32,** 1134–1140. ISSN: 1087-0156, 1546-1696 (Nov. 2014).

55. Chen, J. *et al.* An Immobilized Liquid Interface Prevents Device Associated Bacterial Infection in Vivo. *Biomaterials* **113,** 80–92. ISSN: 01429612 (Jan. 2017).

56. Lavielle, N., Asker, D. & Hatton, B. D. Lubrication Dynamics of Swollen Silicones to Limit Long Term Fouling and Microbial Biofilms. *Soft Matter* **17,** 936–946. ISSN: 1744-683X, 1744-6848 (2021).

57. Armugam, A. *et al.* Broad Spectrum Antimicrobial PDMS-based Biomaterial for Catheter Fabrication. *Biomater Res* **25,** 33. ISSN: 2055-7124 (Dec. 2021).

58. Sokuler, M. *et al.* The Softer the Better: Fast Condensation on Soft Surfaces. *Langmuir* **26,** 1544–1547. ISSN: 0743-7463 (Feb. 2010).

59. Xiao, R., Miljkovic, N., Enright, R. & Wang, E. N. Immersion Condensation on Oil-Infused Heterogeneous Surfaces for Enhanced Heat Transfer. *Sci. Rep.* **3,** 1988. ISSN: 2045-2322 (Electronic) 2045-2322 (Linking) (2013).

60. Cho, H. J., Preston, D. J., Zhu, Y. & Wang, E. N. Nanoengineered Materials for Liquid–Vapour Phase-Change Heat Transfer. *Nat. Rev. Mater.* **2,** 16092. ISSN: 2058-8437 (Feb. 2017).

61. Lee, J. N., Jiang, X., Ryan, D. & Whitesides, G. M. Compatibility of Mammalian Cells on Surfaces of Poly(Dimethylsiloxane). *Langmuir* **20,** 11684–11691. ISSN: 0743-7463, 1520-5827 (Dec. 2004).

62. Sotiri, I. *et al.* Tunability of Liquid-Infused Silicone Materials for Biointerfaces. *Biointerphases* **13,** 06D401. ISSN: 1934-8630, 1559-4106 (Dec. 2018).

63. Schubotz, S. *et al.* Memory Effects in Polymer Brushes Showing Co-Nonsolvency Effects. *Adv. Colloid Interface Sci.* **294,** 102442. ISSN: 00018686 (Aug. 2021).

64. Li, X. *et al.* Adaptation of a Styrene–Acrylic Acid Copolymer Surface to Water. *Langmuir* **37,** 1571–1577. ISSN: 0743-7463 (Feb. 2021).

65. Wong, W. S. Y. & Vollmer, D. Effervescence-Inspired Self-Healing Plastrons for Long-Term Immersion Stability. *Adv. Funct. Mater.* **32,** 2107831. ISSN: 1616-3028 (2022).

66. Kleingartner, J. A., Lee, H., Rubner, M. F., McKinley, G. H. & Cohen, R. E. Exploring the Kinetics of Switchable Polymer Surfaces with Dynamic Tensiometry. *Soft Matter* **9,** 6080. ISSN: 1744-683X, 1744-6848 (2013).

67. Bergeron, V. & Langevin, D. Monolayer Spreading of Polydimethylsiloxane Oil on Surfactant Solutions. *Phys. Rev. Lett.* **76,** 3152–3155. ISSN: 0031-9007, 1079-7114 (Apr. 1996).

68. Mahadevan, L., Adda-Bedia, M. & Pomeau, Y. Four-Phase Merging in Sessile Compound Drops. *J. Fluid Mech.* **451,** 411–420. ISSN: 0022-1120, 1469-7645 (Jan. 2002).

69. Kreder, M. J. *et al.* Film Dynamics and Lubricant Depletion by Droplets Moving on Lubricated Surfaces. *Phys. Rev. X* **8,** 031053. ISSN: 2160-3308 (Sept. 2018).

70. Berry, M. V. Simple Fluids Near Rigid Solids: Statistical Mechanics of Density and Contact Angle. *J. Phys. A: Math. Nucl. Gen.* **7,** 231–245. ISSN: 0301-0015 (Jan. 1974).

71. Herring, A. R. & Henderson, J. R. Simulation Study of the Disjoining Pressure Profile Through a Three-Phase Contact Line. *J. Chem. Phys.* **132,** 084702. ISSN: 0021-9606, 1089-7690 (Feb. 2010).

72. Carré, A., Gastel, J.-C. & Shanahan, M. E. R. Viscoelastic Effects in the Spreading of Liquids. *Nature* **379,** 432–434. ISSN: 0028-0836, 1476-4687 (Feb. 1996).

73. Clanet, C. & Quéré, D. Onset of Menisci. *J. Fluid Mech.* **460,** 131–149. ISSN: 1469-7645, 0022-1120 (June 2002).

74. Park, S. J., Bostwick, J. B., Andrade, V. D. & Je, J. H. Self-Spreading of the Wetting Ridge During Stick-Slip on a Viscoelastic Surface. *Soft Matter* **13,** 8331–8336. ISSN: 1744-6848 (Nov. 2017).

75. Bico, J., Reyssat, E. & Roman, B. Elastocapillarity: When Surface Tension Deforms Elastic Solids. *Annu. Rev. Fluid Mech.* **50,** 629–659 (Jan. 2018).

76. Chaplin, M. F. Water: Its Importance to Life. *Biochem. Mol. Biol. Educ.* **29,** 54–59. ISSN: 1470-8175 (Mar. 2001).

77. Lewicki, P. P. Water as the Determinant of Food Engineering Properties. a Review. *J. Food Eng. Food Processing and Technology - Selected Papers from the 15th CHISA Congress* **61,** 483–495. ISSN: 0260-8774 (Mar. 2004).

78. Mays, L. W. *Water Resources Engineering* Second. ISBN: 978-0-470-46064-1 (Tempe, AZ, June 2010).

79. Al-Ghouti, M. A., Al-Kaabi, M. A., Ashfaq, M. Y. & Da'na, D. A. Produced Water Characteristics, Treatment and Reuse: A Review. *J. Water Process. Eng.* **28,** 222–239. ISSN: 2214-7144 (Apr. 2019).
80. Butts, M. *et al.* in *Kirk-Othmer Encyclopedia of Chemical Technology* (2002). ISBN: 978-0-471-23896-6.
81. Butt, H.-J. & Kappl, M. *Surface and Interfacial Forces* Second. ISBN: 978-3-527-34165-8 (Weinheim, Germany, June 2018).
82. Rowlinson, J. S. & Widom, B. *Molecular Theory of Capillarity* 1st. ISBN: 978-0-486-42544-3 (Oxford and New York, 1982).
83. Nagata, Y., Ohto, T., Backus, E. H. G. & Bonn, M. Molecular Modeling of Water Interfaces: From Molecular Spectroscopy to Thermodynamics. *J. Phys. Chem. B* **120,** 3785–3796. ISSN: 1520-6106 (Apr. 2016).
84. Stauffer, C. E. The Measurement of Surface Tension by the Pendant Drop Technique. *J. Phys. Chem.* **69,** 1933–1938. ISSN: 0022-3654 (June 1965).
85. Style, R. W., Jagota, A., Hui, C.-Y. & Dufresne, E. R. Elastocapillarity: Surface Tension and the Mechanics of Soft Solids. *Annu. Rev. Condens. Matter Phys.* **8,** 99–118. ISSN: 1947-5454, 1947-5462 (Mar. 2017).
86. Shuttleworth, R. The Surface Tension of Solids. *Proc. Phys. Soc. A* **63,** 444–457. ISSN: 0370-1298 (May 1950).
87. Andreotti, B. & Snoeijer, J. H. Soft Wetting and the Shuttleworth Effect, at the Crossroads Between Thermodynamics and Mechanics. *EPL* **113,** 66001. ISSN: 0295-5075 (Apr. 2016).
88. Snoeijer, J. H., Rolley, E. & Andreotti, B. Paradox of Contact Angle Selection on Stretched Soft Solids. *Phys. Rev. Lett.* **121,** 068003. ISSN: 0031-9007, 1079-7114 (Aug. 2018).
89. Van Gorcum, M., Karpitschka, S., Andreotti, B. & Snoeijer, J. H. Spreading on Viscoelastic Solids: Are Contact Angles Selected by Neumann's Law? *Soft Matter* **16,** 1306–1322. ISSN: 1744-6848 (Feb. 2020).
90. Smith-Mannschott, K. *et al.* Droplets Sit and Slide Anisotropically on Soft, Stretched Substrates. *Phys. Rev. Lett.* **126,** 158004. ISSN: 0031-9007, 1079-7114 (Apr. 2021).
91. Dupré, A. *Theorie mecanique de la chaleur* (1869).
92. Marquis de Laplace, P. S. *Traité de mécanique céleste* (Paris, France, 1805).
93. Furmidge, C. Studies at Phase Interfaces. I. The Sliding of Liquid Drops on Solid Surfaces and a Theory for Spray Retention. *Journal of Colloid Science* **17,** 309–324. ISSN: 00958522 (Apr. 1962).
94. Dussan V., E. B. On the Ability of Drops or Bubbles to Stick to Non-Horizontal Surfaces of Solids. Part 2. Small Drops or Bubbles Having Contact Angles of Arbitrary Size. *J. Fluid Mech.* **151,** 1. ISSN: 0022-1120, 1469-7645 (Feb. 1985).
95. Tadmor, R. Approaches in Wetting Phenomena. *Soft Matter* **7,** 1577–1580. ISSN: 1744-6848 (Feb. 2011).
96. Dussan V., E. B. On the Ability of Drops to Stick to Surfaces of Solids. Part 3. the Influences of the Motion of the Surrounding Fluid on Dislodging Drops. *J. Fluid Mech.* **174,** 381–397. ISSN: 0022-1120, 1469-7645 (Jan. 1987).
97. Extrand, C. W. & Gent, A. N. Retention of Liquid Drops by Solid Surfaces. *J. Colloid Interface Sci.* **138,** 431–442. ISSN: 0021-9797 (Sept. 1990).
98. ElSherbini, A. I. & Jacobi, A. M. Retention Forces and Contact Angles for Critical Liquid Drops on Non-Horizontal Surfaces. *J. Colloid Interface Sci.* **299,** 841–849. ISSN: 0021-9797 (July 2006).
99. Gao, N. *et al.* How Drops Start Sliding Over Solid Surfaces. *Nat. Phys.* **14,** 191–196. ISSN: 1745-2481 (Feb. 2018).

100. Blake, T. D. & Haynes, J. M. Kinetics of Liquidliquid Displacement. *J. Colloid Interface Sci.* **30,** 421–423. ISSN: 0021-9797 (July 1969).

101. Blake, T. D. The Physics of Moving Wetting Lines. *J. Colloid Interface Sci.* **299,** 1–13. ISSN: 0021-9797 (July 2006).

102. Stetten, A. Z., Golovko, D. S., Weber, S. A. L. & Butt, H.-J. Slide Electrification: Charging of Surfaces by Moving Water Drops. *Soft Matter* **15,** 8667–8679. ISSN: 1744-683X, 1744-6848 (2019).

103. Li, X. *et al.* Spontaneous Charging Affects the Motion of Sliding Drops. *Nat. Phys.* **18,** 713–719. ISSN: 1745-2481 (June 2022).

104. Beysens, D. The Formation of Dew. *Atmos. Res.* **39,** 215–237. ISSN: 0169-8095 (Oct. 1995).

105. Kashchiev, D. *Nucleation* 1st. ISBN: 978-0-08-053783-2 (Oxford, UK, Feb. 2000).

106. Pruppacher, H. R. & Klett, J. D. in *Microphysics of Clouds and Precipitation* Second, 191–209 (New York, Boston, Dordrecht, London, Moscow, 2004).

107. Butt, H.-J., Graf, K. & Kappl, M. in *Physics and Chemistry of Interfaces* 3rd, 6 (Weinheim, Germany, Apr. 2013). ISBN: 978-3-527-41216-7.

108. Liu, X. Y. Heterogeneous Nucleation or Homogeneous Nucleation? *J. Chem. Phys.* **112,** 9949–9955. ISSN: 0021-9606 (June 2000).

109. Verdaguer, A., Sacha, G. M., Bluhm, H. & Salmeron, M. Molecular Structure of Water at Interfaces: Wetting at the Nanometer Scale. *Chem. Rev.* **106,** 1478–1510. ISSN: 0009-2665 (Apr. 2006).

110. Kalikmanov, V. *Nucleation Theory* 1st (Heidelberg, 2013).

111. Nath, S. & Boreyko, J. B. On Localized Vapor Pressure Gradients Governing Condensation and Frost Phenomena. *Langmuir* **32,** 8350–8365. ISSN: 0743-7463 (Aug. 2016).

112. Schmidt, E., Schurig, W. & Sellschopp, W. Versuche über die Kondensation von Wasserdampf in Film- und Tropfenform. *Technische Mechanik und Thermodynamik* **1,** 53–63. ISSN: 1434-0860 (Feb. 1930).

113. Rose, J. W. Dropwise Condensation Theory and Experiment: A Review. *Proc. Inst. Mech. Eng. A* **216,** 115–128. ISSN: 0957-6509 (Jan. 2002).

114. Chen, C.-H. *et al.* Dropwise Condensation on Superhydrophobic Surfaces with Two-Tier Roughness. *Appl. Phys. Lett.* **90,** 173108. ISSN: 0003-6951 (Apr. 2007).

115. Nath, S., Ahmadi, S. F. & Boreyko, J. B. A Review of Condensation Frosting. *Nanoscale Microscale Thermophys. Eng.* **21,** 81–101. ISSN: 1556-7265, 1556-7273 (Apr. 2017).

116. Kreder, M. J., Alvarenga, J., Kim, P. & Aizenberg, J. Design of Anti-Icing Surfaces: Smooth, Textured or Slippery? *Nat. Rev. Mater.* **1,** 15003. ISSN: 2058-8437 (Jan. 2016).

117. Golovin, K. *et al.* Designing Durable Icephobic Surfaces. *Sci. Adv.* **2,** e1501496. ISSN: 2375-2548 (Mar. 2016).

118. Witt, K. E., Ahmadi, S. F. & Boreyko, J. B. Ice Wicking. *Phys. Rev. Fluids* **4,** 024002 (Feb. 2019).

119. Chavoshani, A., Hashemi, M., Mehdi Amin, M. & Ameta, S. C. in *Micropollutants and Challenges: Emerging in the Aquatic Environments and Treatment Processes* 1st, 119 (Amsterdam, Netherlands ; Kidlington, Oxford ; Cambridge, MA, 2020). ISBN: 978-0-12-818612-1.

120. Maitz, M. Applications of Synthetic Polymers in Clinical Medicine. *Biosurface and Biotribology* **1,** 161–176. ISSN: 24054518 (Sept. 2015).

121. Sta Apolónia *et al.* Study of Pdms Characterization and Its Applications in Biomedicine: A Review. *JMEB* **4,** 1–9. ISSN: 2456219X (Aug. 2019).

122. Moretto, H.-H., Schulze, M. & Wagner, G. in *Ullmann's Encyclopedia of Industrial Chemistry* (ed Wiley-VCH Verlag GmbH & Co. KGaA) 682 (Weinheim, Germany, June 2000). ISBN: 978-3-527-30673-2.

123. Chung, H. U. *et al.* Skin-Interfaced Biosensors for Advanced Wireless Physiological Monitoring in Neonatal and Pediatric Intensive-Care Units. *Nat. Med.* **26,** 418–429. ISSN: 1078-8956, 1546-170X (Mar. 2020).

124. Kim, S. *et al.* Soft, Skin-Interfaced Microfluidic Systems with Integrated Immunoassays, Fluorometric Sensors, and Impedance Measurement Capabilities. *Proc. Natl. Acad. Sci. U.S.A.* **117,** 27906–27915. ISSN: 0027-8424, 1091-6490 (Nov. 2020).

125. Xia, Y. & Whitesides, G. M. Soft Lithography. *Angew. Chem. Int. Ed.* **37,** 550–575. ISSN: 1433-7851, 1521-3773 (Mar. 1998).

126. Ozbolat, V. *et al.* 3D Printing of PDMS Improves Its Mechanical and Cell Adhesion Properties. *ACS Biomater. Sci. Eng.* **4,** 682–693 (Feb. 2018).

127. Morbioli, G. G., Speller, N. C. & Stockton, A. M. A Practical Guide to Rapid-Prototyping of PDMS-Based Microfluidic Devices: A Tutorial. *Anal. Chim. Acta* **1135,** 150–174. ISSN: 0003-2670 (Oct. 2020).

128. Volkov, A. in *Encyclopedia of Membranes* (eds Drioli, E. & Giorno, L.) 1–2 (Berlin, Heidelberg, 2015). ISBN: 978-3-642-40872-4.

129. Gutekunst, S. B., Grabosch, C., Kovalev, A., Gorb, S. N. & Selhuber-Unkel, C. Influence of the PDMS Substrate Stiffness on the Adhesion of Acanthamoeba Castellanii. *Beilstein J. Nanotechnol.* **5,** 1393–1398. ISSN: 2190-4286 (Aug. 2014).

130. Johnston, I. D., McCluskey, D. K., Tan, C. K. L. & Tracey, M. C. Mechanical Characterization of Bulk Sylgard 184 for Microfluidics and Microengineering. *J. Micromech. Microeng.* **24,** 035017. ISSN: 0960-1317, 1361-6439 (Mar. 2014).

131. Seghir, R. & Arscott, S. Extended PDMS Stiffness Range for Flexible Systems. *Sens. Actuators A: Phys.* **230,** 33–39. ISSN: 09244247 (July 2015).

132. Style, R. W. *et al.* Stiffening Solids with Liquid Inclusions. *Nature Phys* **11,** 82–87. ISSN: 1745-2473, 1745-2481 (Jan. 2015).

133. Masterton, S. & Ahearne, M. Influence of Polydimethylsiloxane Substrate Stiffness on Corneal Epithelial Cells. *R. Soc. open sci.* **6,** 191796. ISSN: 2054-5703 (Dec. 2019).

134. Gelest. *Conventional Silicone Fluids* https://technical.gelest.com/brochures/silicone-fluids/conventional-silicone-fluids/.

135. Wooh, S. & Vollmer, D. Silicone Brushes: Omniphobic Surfaces with Low Sliding Angles. *Angew. Chem. Int. Ed.* **55,** 6822–6824. ISSN: 1521-3773 (2016).

136. Noll, W. in *Chemistry and Technology of Silicones* 1st, 8 (24/28 Oval Road, London NW1, 1968). ISBN: 978-0-323-14140-6.

137. Lee, J. N., Park, C. & Whitesides, G. M. Solvent Compatibility of Poly(Dimethylsiloxane)-Based Microfluidic Devices. *Anal. Chem.* **75,** 6544–6554. ISSN: 0003-2700, 1520-6882 (Dec. 2003).

138. Tamai, Y., Tanaka, H. & Nakanishi, K. Molecular Simulation of Permeation of Small Penetrants through Membranes. 2. Solubilities. *Macromolecules* **28,** 2544–2554. ISSN: 0024-9297, 1520-5835 (Mar. 1995).

139. Watson, J. & Baron, M. The Behaviour of Water in Poly(Dimethylsiloxane). *J. Membr. Sci.* **110,** 47–57. ISSN: 03767388 (Feb. 1996).

140. Harley, S. J., Glascoe, E. A. & Maxwell, R. S. Thermodynamic Study on Dynamic Water Vapor Sorption in Sylgard-184. *J. Phys. Chem. B* **116,** 14183–14190. ISSN: 1520-6106, 1520-5207 (Dec. 2012).

141. Seiwert, J., Clanet, C. & Quéré, D. Coating of a Textured Solid. *J. Fluid Mech.* **669,** 55–63. ISSN: 0022-1120, 1469-7645 (Feb. 2011).

142. Wong, T.-S. *et al.* Bioinspired Self-Repairing Slippery Surfaces with Pressure-Stable Omniphobicity. *Nature* **477,** 443–447. ISSN: 0028-0836, 1476-4687 (Sept. 2011).

143. Owen, M. J. Why Silicones Behave Funny. *Chemtech* **11,** 288–292 (1981).

144. Smith, J. D. *et al.* Droplet Mobility on Lubricant-Impregnated Surfaces. *Soft Matter* **9,** 1772–1780. ISSN: 1744-683X, 1744-6848 (2013).

145. Kim, P., Kreder, M. J., Alvarenga, J. & Aizenberg, J. Hierarchical or Not? Effect of the Length Scale and Hierarchy of the Surface Roughness on Omniphobicity of Lubricant-Infused Substrates. *Nano Lett.* **13,** 1793–1799. ISSN: 1530-6984, 1530-6992 (Apr. 2013).

146. Lafuma, A. & Quéré, D. Slippery Pre-Suffused Surfaces. *EPL* **96,** 56001. ISSN: 0295-5075, 1286-4854 (Dec. 2011).

147. Bohn, H. F. & Federle, W. Insect Aquaplaning: Nepenthes Pitcher Plants Capture Prey with the Peristome, a Fully Wettable Water-Lubricated Anisotropic Surface. *Proc. Natl. Acad. Sci. U.S.A.* **101,** 14138–14143. ISSN: 0027-8424 (Sept. 2004).

148. Villegas, M., Zhang, Y., Abu Jarad, N., Soleymani, L. & Didar, T. F. Liquid-Infused Surfaces: A Review of Theory, Design, and Applications. *ACS Nano* **13,** 8517–8536. ISSN: 1936-0851 (Aug. 2019).

149. Baumli, P. *et al.* The Challenge of Lubricant-Replenishment on Lubricant-Impregnated Surfaces. *Adv. Colloid Interface Sci.* **287,** 102329. ISSN: 00018686 (Jan. 2021).

150. Zhang, P., Lin, L., Zang, D., Guo, X. & Liu, M. Designing Bioinspired Anti-Biofouling Surfaces Based on a Superwettability Strategy. *Small* **13,** 1503334. ISSN: 16136810 (Jan. 2017).

151. Wang, C. & Guo, Z. A Comparison between Superhydrophobic Surfaces (SHS) and Slippery Liquid-Infused Porous Surfaces (SLIPS) in Application. *Nanoscale* **12,** 22398–22424. ISSN: 2040-3364, 2040-3372 (2020).

152. Shirtcliffe, N. J. *et al.* The Use of High Aspect Ratio Photoresist (SU-8) for Super-Hydrophobic Pattern Prototyping. *J. Micromech. Microeng.* **14,** 1384–1389. ISSN: 0960-1317 (July 2004).

153. Ware, C. S. *et al.* Marine Antifouling Behavior of Lubricant-Infused Nanowrinkled Polymeric Surfaces. *ACS Appl. Mater. Interfaces* **10,** 4173–4182. ISSN: 1944-8244 (Jan. 2018).

154. Doll, K. *et al.* Development of Laser-Structured Liquid-Infused Titanium with Strong Biofilm-Repellent Properties. *ACS Appl. Mater. Interfaces* **9,** 9359–9368. ISSN: 1944-8244 (Mar. 2017).

155. Wang, J., Li, Q., Knoll, W. & Jonas, U. Preparation of Multilayered Trimodal Colloid Crystals and Binary Inverse Opals. *J. Am. Chem. Soc.* **128,** 15606–15607. ISSN: 0002-7863 (Dec. 2006).

156. Wei, C., Zhang, G., Zhang, Q., Zhan, X. & Chen, F. Silicone Oil-Infused Slippery Surfaces Based on Sol–Gel Process-Induced Nanocomposite Coatings: A Facile Approach to Highly Stable Bioinspired Surface for Biofouling Resistance. *ACS Appl. Mater. Interfaces* **8,** 34810–34819. ISSN: 1944-8244 (Dec. 2016).

157. Sunny, S., Vogel, N., Howell, C., Vu, T. L. & Aizenberg, J. Lubricant-Infused Nanoparticulate Coatings Assembled by Layer-by-Layer Deposition. *Adv. Funct. Mater.* **24,** 6658–6667. ISSN: 1616-3028 (2014).

158. Schellenberger, F. *et al.* Direct Observation of Drops on Slippery Lubricant-Infused Surfaces. *Soft Matter* **11,** 7617–7626. ISSN: 1744-683X, 1744-6848 (2015).

159. Bico, J., Tordeux, C. & Quéré, D. Rough Wetting. *EPL* **55,** 214. ISSN: 0295-5075 (July 2001).

160. Whitaker, S. Flow in Porous Media I: A Theoretical Derivation of Darcy's Law. *Transp Porous Med* **1,** 3–25. ISSN: 1573-1634 (Mar. 1986).

161. Lucas, R. Ueber Das Zeitgesetz Des Kapillaren Aufstiegs Von Flüssigkeiten. *Kolloid-Zeitschrift* **23,** 15–22. ISSN: 1435-1536 (July 1918).

162. Washburn, E. W. The Dynamics of Capillary Flow. *Phys. Rev.* **17,** 273–283. ISSN: 0031-899X (Mar. 1921).

163. Ishino, C., Reyssat, M., Reyssat, E., Okumura, K. & Quéré, D. Wicking Within Forests of Micropillars. *EPL* **79,** 56005. ISSN: 0295-5075, 1286-4854 (Sept. 2007).

164. Ponomarenko, A., Quéré, D. & Clanet, C. A Universal Law for Capillary Rise in Corners. *J. Fluid Mech.* **666,** 146–154. ISSN: 0022-1120, 1469-7645 (Jan. 2011).

165. Charlton, J. J., Lavrik, N., Bradshaw, J. A. & Sepaniak, M. J. Wicking Nanopillar Arrays with Dual Roughness for Selective Transport and Fluorescence Measurements. *ACS Appl. Mater. Interfaces* **6,** 17894–17901. ISSN: 1944-8244 (Oct. 2014).

166. Delaunay, C. Sur la surface de révolution dont la courbure moyenne est constante. *Journal de Mathématiques Pures et Appliquées,* 309–314. ISSN: 0021-7874 (1841).

167. Gunjan, M. R., Kumar, A. & Raj, R. Droplets on Lubricant-Infused Surfaces: Combination of Constant Mean Curvature Interfaces with Neumann Triangle Boundary Conditions. *Langmuir* **36,** 2974–2983. ISSN: 0743-7463 (Mar. 2020).

168. Lopez, F. J. & Ros, A. Complete Minimal Surfaces with Index One and Stable Constant Mean Curvature Surfaces. *Commentarii Mathematici Helvetici* **64,** 34–43. ISSN: 0010-2571, 1420-8946 (Dec. 1989).

169. Meeks, W. & Pérez, J. The Classical Theory of Minimal Surfaces. *Bull. Amer. Math. Soc.* **48,** 325–407. ISSN: 0273-0979, 1088-9485 (July 2011).

170. Semprebon, C., McHale, G. & Kusumaatmaja, H. Apparent Contact Angle and Contact Angle Hysteresis on Liquid Infused Surfaces. *Soft Matter* **13,** 101–110. ISSN: 1744-6848 (Dec. 2016).

171. Tress, M. *et al.* Shape of a Sessile Drop on a Flat Surface Covered with a Liquid Film. *Soft Matter* **13,** 3760–3767. ISSN: 1744-6848 (May 2017).

172. Semprebon, C., Sadullah, M. S., McHale, G. & Kusumaatmaja, H. Apparent Contact Angle of Drops on Liquid Infused Surfaces: Geometric Interpretation. *Soft Matter* **17,** 9553–9559. ISSN: 1744-6848 (Nov. 2021).

173. Barca, F., Caporossi, T. & Rizzo, S. Silicone Oil: Different Physical Proprieties and Clinical Applications. *Biomed. Res. Int.* **2014,** 1–7. ISSN: 2314-6133, 2314-6141 (2014).

174. Teisala, H. *et al.* Wetting Over Pre-Existing Liquid Films. *Phys. Rev. Fluids* **3,** 084002 (Aug. 2018).

175. Toor, A., Lamb, S., Helms, B. A. & Russell, T. P. Reconfigurable Microfluidic Droplets Stabilized by Nanoparticle Surfactants. *ACS Nano* **12,** 2365–2372. ISSN: 1936-0851 (Mar. 2018).

176. Badr, R. G. M., Hauer, L., Vollmer, D. & Schmid, F. Cloaking Transition of Droplets on Lubricated Brushes. *J. Phys. Chem. B* **126,** 7047–7058. ISSN: 1520-6106 (Sept. 2022).

177. Platikanov, D. & Exerowa, D. in *Fundamentals of Interface and Colloid Science* 6.1–6.91 (2005). ISBN: 978-0-12-460530-5.

178. Hadjiiski, A., Tcholakova, S., Ivanov, I. B., Gurkov, T. D. & Leonard, E. F. Gentle Film Trapping Technique with Application to Drop Entry Measurements. *Langmuir* **18,** 127–138. ISSN: 0743-7463 (Jan. 2002).

179. Gunjan, M. R., Kumar, A. & Raj, R. Cloaked Droplets on Lubricant-Infused Surfaces: Union of Constant Mean Curvature Interfaces Dictated by Thin-Film Tension. *Langmuir* **37,** 6601–6612. ISSN: 0743-7463 (June 2021).

180. Hourlier-Fargette, A., Dervaux, J., Antkowiak, A. & Neukirch, S. Extraction of Silicone Uncrosslinked Chains at Air–Water–Polydimethylsiloxane Triple Lines. *Langmuir* **34,** 12244–12250. ISSN: 0743-7463 (Oct. 2018).

181. Keiser, A., Baumli, P., Vollmer, D. & Quéré, D. Universality of Friction Laws on Liquid-Infused Materials. *Phys. Rev. Fluids* **5,** 014005 (Jan. 2020).

182. Dollase, T., Spiess, H. W., Gottlieb, M. & Yerushalmi-Rozen, R. Crystallization of PDMS: The Effect of Physical and Chemical Crosslinks. *EPL* **60,** 390. ISSN: 0295-5075 (Nov. 2002).

183. Adam, M., Lairez, D., Karpasas, M. & Gottlieb, M. Static and Dynamic Properties of Cross-Linked Poly(Dimethylsiloxane) Pregel Clusters. *Macromolecules* **30,** 5920–5929. ISSN: 0024-9297 (Sept. 1997).

184. Bogdan, M., Hieronim, M., Cezary, P. & Piotr, P. *Hydrosilylation* (eds Bogdan, M. & Janis, M.) (Berlin).

185. Chambon, F. & Winter, H. H. Stopping of Crosslinking Reaction in a PDMS Polymer at the Gel Point. *Polym. Bull.* **13,** 499–503. ISSN: 1436-2449 (June 1985).

186. Mani, S., Cassagnau, P., Bousmina, M. & Chaumont, P. Cross-Linking Control of PDMS Rubber at High Temperatures Using TEMPO Nitroxide. *Macromolecules* **42,** 8460–8467. ISSN: 0024-9297 (Nov. 2009).

187. Chassé, W., Lang, M., Sommer, J.-U. & Saalwächter, K. Cross-Link Density Estimation of PDMS Networks with Precise Consideration of Networks Defects. *Macromolecules* **45,** 899–912. ISSN: 0024-9297 (Jan. 2012).

188. Flory, P. J. in *Principles of Polymer Chemistry* 1st, 47 (Ithaca, New York, 1953). ISBN: 978-0-8014-0134-3.

189. Flapper, M. M., Pandey, A., Karpitschka, S. & Snoeijer, J. H. *Reversal of Solvent Migration in Poroelastic Folds* Sept. 2022. arXiv: `2209.00887 [cond-mat]`.

190. Jensen, K. E. *et al.* Wetting and Phase Separation in Soft Adhesion. *Proc. Natl. Acad. Sci. U.S.A.* **112,** 14490–14494 (Nov. 2015).

191. Cai, Z., Skabeev, A., Morozova, S. & Pham, J. T. Fluid Separation and Network Deformation in Wetting of Soft and Swollen Surfaces. *Commun. Mater.* **2,** 1–11. ISSN: 2662-4443 (Feb. 2021).

192. Sharma, C. S. *et al.* Enhanced Condensation on Soft Materials through Bulk Lubricant Infusion. *Adv. Funct. Mater.* **32,** 2109633. ISSN: 1616-3028 (2022).

193. Hourlier-Fargette, A., Antkowiak, A., Chateauminois, A. & Neukirch, S. Role of Uncrosslinked Chains in Droplets Dynamics on Silicone Elastomers. *Soft Matter* **13,** 3484–3491. ISSN: 1744-6848 (May 2017).

194. Park, S. J. *et al.* Visualization of Asymmetric Wetting Ridges on Soft Solids with X-Ray Microscopy. *Nat. Commun.* **5,** 4369. ISSN: 2041-1723 (Sept. 2014).

195. Gerber, J., Lendenmann, T., Eghlidi, H., Schutzius, T. M. & Poulikakos, D. Wetting Transitions in Droplet Drying on Soft Materials. *Nat. Commun.* **10,** 4776. ISSN: 2041-1723 (Oct. 2019).

196. Jerison, E. R., Xu, Y., Wilen, L. A. & Dufresne, E. R. Deformation of an Elastic Substrate by a Three-Phase Contact Line. *Phys. Rev. Lett.* **106,** 186103 (May 2011).

197. Roman, B. & Bico, J. Elasto-Capillarity: Deforming an Elastic Structure with a Liquid Droplet. *J. Phys. Condens. Matter* **22,** 493101. ISSN: 0953-8984 (Nov. 2010).

198. Mora, S., Phou, T., Fromental, J.-M., Pismen, L. M. & Pomeau, Y. Capillarity Driven Instability of a Soft Solid. *Phys. Rev. Lett.* **105,** 214301 (Nov. 2010).

199. Mata, A., Fleischman, A. J. & Roy, S. Characterization of Polydimethylsiloxane (PDMS) Properties for Biomedical Micro/Nanosystems. *Biomed. Microdevices* **7,** 281–293. ISSN: 1572-8781 (Dec. 2005).

200. Haubert, K., Drier, T. & Beebe, D. PDMS Bonding by Means of a Portable, Low-Cost Corona System. *Lab Chip* **6,** 1548–1549. ISSN: 1473-0189 (Nov. 2006).

201. Kim, H. T. & Jeong, O. C. PDMS Surface Modification Using Atmospheric Pressure Plasma. *Microelectron. Eng. Proceedings of the 36th International Conference on Micro- and Nano-Engineering (MNE)* **88,** 2281–2285. ISSN: 0167-9317 (Aug. 2011).

202. Qiu, W., Sun, X., Wu, C., Hjort, K. & Wu, Z. A Contact Angle Study of the Interaction between Embedded Amphiphilic Molecules and the PDMS Matrix in an Aqueous Environment. *Micromachines* **5,** 515–527. ISSN: 2072-666X (Aug. 2014).

203. Ruben, B. *et al.* Oxygen Plasma Treatments of Polydimethylsiloxane Surfaces: Effect of the Atomic Oxygen on Capillary Flow in the Microchannels. *Micro Nano Lett.* **12,** 754–757. ISSN: 1750-0443, 1750-0443 (Oct. 2017).

204. Shanahan, M. E. R. The Influence of Solid Micro-Deformation on Contact Angle Equilibrium. *J. Phys. D: Appl. Phys.* **20,** 945–950. ISSN: 0022-3727 (July 1987).

205. Shanahan, M. E. R. & Carre, A. Viscoelastic Dissipation in Wetting and Adhesion Phenomena. *Langmuir* **11,** 1396–1402. ISSN: 0743-7463 (Apr. 1995).

206. Long, D., Ajdari, A. & Leibler, L. Static and Dynamic Wetting Properties of Thin Rubber Films. *Langmuir* **12,** 5221–5230. ISSN: 0743-7463 (Jan. 1996).

207. Xu, Y. *et al.* Imaging In-Plane and Normal Stresses near an Interface Crack Using Traction Force Microscopy. *Proc. Natl. Acad. Sci. U.S.A.* **107,** 14964–14967. ISSN: 0027-8424, 1091-6490 (Aug. 2010).

208. Limat, L. Straight Contact Lines on a Soft, Incompressible Solid. *Eur. Phys. J. E* **35,** 134. ISSN: 1292-8941, 1292-895X (Dec. 2012).

209. Style, R. W. & Dufresne, E. R. Static Wetting on Deformable Substrates, from Liquids to Soft Solids. *Soft Matter* **8,** 7177–7184. ISSN: 1744-6848 (June 2012).

210. Zhao, M. *et al.* Geometrical Control of Dissipation During the Spreading of Liquids on Soft Solids. *Proc. Natl. Acad. Sci. U.S.A.* **115,** 1748–1753 (Feb. 2018).

211. Irgens, F. in *Continuum Mechanics* 1st, 54–58 (Berlin, 2008). ISBN: 978-3-540-74297-5.

212. Marchand, A., Das, S., Snoeijer, J. H. & Andreotti, B. Contact Angles on a Soft Solid: From Young's Law to Neumann's Law. *Phys. Rev. Lett.* **109,** 236101 (Dec. 2012).

213. Regehr, K. J. *et al.* Biological Implications of Polydimethylsiloxane-Based Microfluidic Cell Culture. *Lab Chip* **9,** 2132–2139. ISSN: 1473-0189 (Aug. 2009).

214. Xu, Q., Wilen, L. A., Jensen, K. E., Style, R. W. & Dufresne, E. R. Viscoelastic and Poroelastic Relaxations of Soft Solid Surfaces. *Phys. Rev. Lett.* **125,** 238002. ISSN: 0031-9007, 1079-7114 (Nov. 2020).

215. Chasset, R. & Thirion, P. in *Proceedings of the Conference on Physics of Non-Crystalline Solids* (Amsterdam, 1965).

216. Pericet-Camara, R. *et al.* Solid-Supported Thin Elastomer Films Deformed by Microdrops. *Soft Matter* **5,** 3611–3617. ISSN: 1744-6848 (Sept. 2009).

217. Khattak, H. K., Karpitschka, S., Snoeijer, J. H. & Dalnoki-Veress, K. Direct Force Measurement of Microscopic Droplets Pulled along Soft Surfaces. *Nat. Commun.* **13,** 4436. ISSN: 2041-1723 (July 2022).

218. Milner, S. T. Polymer Brushes. *Science* **251,** 905–914. ISSN: 0036-8075, 1095-9203 (Feb. 1991).

219. Weinhold, F. & West, R. The Nature of the Silicon–Oxygen Bond. *Organometallics* **30,** 5815–5824. ISSN: 0276-7333 (Nov. 2011).

220. Krumpfer, J. W. & McCarthy, T. J. Rediscovering Silicones: "Unreactive" Silicones React with Inorganic Surfaces. *Langmuir* **27,** 11514–11519. ISSN: 0743-7463 (Sept. 2011).

221. Wang, L. & McCarthy, T. J. Covalently Attached Liquids: Instant Omniphobic Surfaces with Unprecedented Repellency. *Angew. Chem. Int. Ed.* **55,** 244–248. ISSN: 1521-3773 (2016).

222. Teisala, H., Baumli, P., Weber, S. A. L., Vollmer, D. & Butt, H.-J. Grafting Silicone at Room Temperature—a Transparent, Scratch-resistant Nonstick Molecular Coating. *Langmuir* **36,** 4416–4431. ISSN: 0743-7463, 1520-5827 (Apr. 2020).

223. Liu, J. *et al.* One-Step Synthesis of a Durable and Liquid-Repellent Poly(Dimethylsiloxane) Coating. *Adv. Mater.* **33,** 2100237. ISSN: 1521-4095 (2021).

224. Binder, K. & Milchev, A. Polymer Brushes on Flat and Curved Surfaces: How Computer Simulations Can Help to Test Theories and to Interpret Experiments. *J. Polym. Sci. B Polym. Phys.* **50,** 1515–1555. ISSN: 08876266 (Nov. 2012).

225. Colas, A. Silicones: Preparation, Properties and Performance. *Dow corning, life sciences* (2005).

226. Krumpfer, J. W. & McCarthy, T. J. Contact Angle Hysteresis: A Different View and a Trivial Recipe for Low Hysteresis Hydrophobic Surfaces. *Faraday Discuss.* **146,** 103–111. ISSN: 1364-5498 (July 2010).

227. Léonforte, F. & Müller, M. Statics of Polymer Droplets on Deformable Surfaces. *J. Chem. Phys.* **135,** 214703. ISSN: 0021-9606 (Dec. 2011).

228. Thiele, U. & Hartmann, S. Gradient Dynamics Model for Drops Spreading on Polymer Brushes. *Eur. Phys. J. Spec. Top.* **229,** 1819–1832. ISSN: 1951-6401 (Sept. 2020).

229. Henkel, C., Snoeijer, J. H. & Thiele, U. Gradient-Dynamics Model for Liquid Drops on Elastic Substrates. *Soft Matter* **17,** 10359–10375. ISSN: 1744-683X, 1744-6848 (2021).

230. Milner, S. T., Witten, T. A. & Cates, M. E. Theory of the Grafted Polymer Brush. *Macromolecules* **21,** 2610–2619. ISSN: 0024-9297 (Aug. 1988).

231. Alexander, S. Adsorption of Chain Molecules with a Polar Head a Scaling Description. *J. Phys. France* **38,** 983–987. ISSN: 0302-0738, 2777-3396 (Aug. 1977).

232. de Gennes, P. G. Conformations of Polymers Attached to an Interface. *Macromolecules* **13,** 1069–1075. ISSN: 0024-9297 (Sept. 1980).

233. Benetti, E. M. *et al.* Loops and Cycles at Surfaces: The Unique Properties of Topological Polymer Brushes. *Chem. Eur. J.* **23,** 12433–12442. ISSN: 09476539 (Sept. 2017).

234. Léger, L., Raphaël, E. & Hervet, H. in *Polymers in Confined Environments* (eds Granick, S. *et al.*) 185–225 (Berlin, Heidelberg, 1999). ISBN: 978-3-540-69711-4.

235. Casoli, A., Brendlé, M., Schultz, J., Auroy, P. & Reiter, G. Friction Induced by Grafted Polymeric Chains. *Langmuir* **17,** 388–398. ISSN: 0743-7463 (Jan. 2001).

236. Coppée, S., Gabriele, S., Jonas, A. M., Jestin, J. & Damman, P. Influence of Chain Interdiffusion Between Immiscible Polymers on Dewetting Dynamics. *Soft Matter* **7,** 9951–9955. ISSN: 1744-6848 (Oct. 2011).

237. Karpitschka, S. *et al.* Droplets Move Over Viscoelastic Substrates by Surfing a Ridge. *Nat. Commun.* **6,** 7891. ISSN: 2041-1723 (Aug. 2015).

238. Tamai, Y., Tanaka, H. & Nakanishi, K. Molecular Simulation of Permeation of Small Penetrants through Membranes. 1. Diffusion Coefficients. *Macromolecules* **27,** 4498–4508. ISSN: 0024-9297, 1520-5835 (Aug. 1994).

239. Rykaczewski, K., Anand, S., Subramanyam, S. B. & Varanasi, K. K. Mechanism of Frost Formation on Lubricant-Impregnated Surfaces. *Langmuir* **29,** 5230–5238. ISSN: 0743-7463 (Apr. 2013).

240. Guadarrama-Cetina, J., Mongruel, A., González-Viñas, W. & Beysens, D. Percolation-Induced Frost Formation. *EPL* **101,** 16009. ISSN: 0295-5075 (Jan. 2013).

241. Landau, L. & Lifshitz, E. in *Theory of Elasticity* 3rd, 1–37 (Oxford, 1986). ISBN: 978-0-08-057069-3.

242. Haupt, P. in *Continuum Mechanics and Theory of Materials* (ed Haupt, P.) Second, 7–74 (Berlin, Heidelberg, 2002). ISBN: 978-3-662-04775-0.

243. Ogden, R. W. in *Non-Linear Elastic Deformations* 1st, 83–120 (Mineola, New York, 1997). ISBN: 978-0-486-69648-5.

244. Hooke, R. *Lectures de Potentia Restitutiva, Or of Spring Explaining the Power of Springing Bodies* (1678).

245. Rivlin, R. S. Large Elastic Deformations of Isotropic Materials IV. Further Developments of the General Theory. *Phil. Trans. R. Soc. Lond. A* **241,** 379–397. ISSN: 0080-4614, 2054-0272 (Oct. 1948).

246. Maxwell, J. C. IV. On the Dynamical Theory of Gases. *Phil. Trans. R. Soc.* **157,** 49–88. ISSN: 0261-0523, 2053-9223 (Dec. 1867).

Appendix B

Appended Published Articles

B.1 Phase Separation in Wetting Ridges of Sliding Drops on Soft and Swollen Surfaces

Lukas Hauer†, Zhuoyun Cai†, Artem Skabeev, Doris Vollmer, Jonathan T. Pham, Physical Review Letters 130, no. 5 (2023): 058205.

† equal contribution

Abstract

Drops in contact with swollen, elastomeric substrates can induce a capillary-mediated phase separation in wetting ridges. Using laser scanning confocal microscopy, we visualize phase separation of oligomeric silicone oil from a crosslinked silicone network during steady-state sliding of water drops. We find an inverse relationship between the oil tip height and the drop sliding speed, which is rationalized by competing transport timescales of oil molecules: separation rate and drop-advection speed. Separation rates in highly swollen networks are as fast as diffusion in pure melts.

Introduction

Classically, wetting is characterized by the Young-Dupré contact angle at the three-phase-contact line of a drop on a substrate [1]. However, when the underlying substrate is a liquid or a soft solid, this angle does not suffice because of an out-of-plane ridge formation [2–4]. A 'wetting ridge' emerges due to the drop surface tension, which pulls on the substrate and deforms it upwards [5–14]. On pure liquid substrates, the ridge geometry is solely governed by capillarity, while on soft solid substrates, elastic contributions add to the ridge geometry [15–17]. The Neumann angles consider force balances not only in the horizontal but also in the vertical direction [18], and can help recover a better description of the wetting situation [19–21].

Although wetting of pure liquid or soft solid substrates are typically treated as two distinct cases, many soft substrates have features of both [22–26]. For example, crosslinked polymeric substrates are often swollen with unbound, free molecules (e.g. oligomers in elastomers or water in hydrogels); this leads to a complex combination of liquid and solid behaviors. Recently, it has been shown that ridges on swollen, lightly crosslinked elastomers do not necessarily comprise a homogeneous phase. Unbound molecules phase-separate at the tip of the ridge, forming a region of pure liquid [27–29]. However, these have been mostly considered in static drops.

In dynamic wetting conditions, the ridge is highly relevant: Friction that builds up during drop sliding dissipates mostly in the ridge [30–33]. Hence, the shape and material makeup of the wetting ridge are central components to determine drop movement. For soft, swollen elastomers, the presence of free molecules is likely to alter the drop dynamics [34–37]. Yet, it is not well understood how drop sliding speed couples to phase separation, how sliding-induced separation is related to the swelling ratio of the underlying network, and what time scales govern the separation mechanism.

In this Letter, we investigate wetting ridges on soft polydimethylsiloxane (PDMS) substrates, swollen with silicone oil (liquid oligomers), during steady-state sliding of water drops. The network and oil are dyed with individual fluorescence markers, enabling independent visualization of each phase by laser scanning confocal microscopy (LSCM). Cross-sectional views of the moving wetting ridge yield their shape and the spatial distribution of network and oil phases in the ridge. For highly swollen networks, the extent of phase separation depends on the sliding speed of the drop, which is suppressed at fast sliding speeds. However, no phase separation is observed on less swollen substrates, even for slower moving drops. From images of the speed-dependent wetting ridge, we extract the mobility of phase separating oil that approaches values of free melt diffusion (up to 0.4 μm^2/ms).

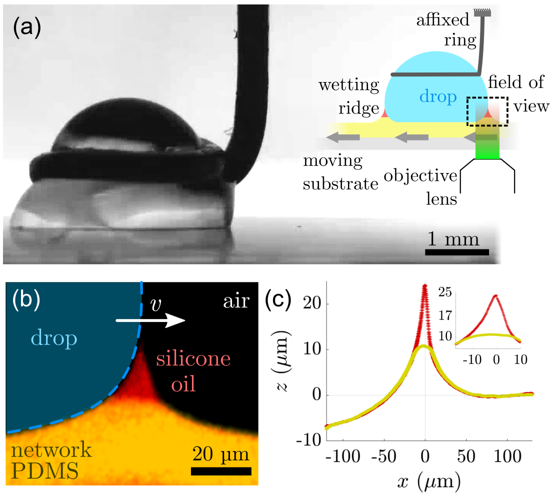

Figure B.1: Drop sliding set-up and wetting ridge visualization. (a) Macroscopic side view of affixed drop, sliding at 5 μm/s on a swollen PDMS network ($Q = 14.5$). Substrate moves left while drop is stationary. Inset, set-up schematic. (b) Temporal averaged ($n = 158$) LSCM image of a phase-separated wetting ridge. PDMS network and silicone oil are dyed separately with fluorescence markers with different emission spectra. Red shows silicone oil and orange shows swollen PDMS network. (c) Extracted interfaces of silicone oil (red points) and PDMS network (yellow points). Inset, blown up section of the phase-separated zone in the wetting ridge. Standard errors are smaller than symbol size.

Results and Discussion

Material system

Soft PDMS networks (Young's modulus $E \approx 3 - 5$ kPa) with different amounts of swelling agent (*i.e.*, swelling ratio $Q = V_{\text{swollen}}/V_{\text{dry}}$) were manufactured and placed on glass slides (synthesis, rheology, and pore pressure Π given in Supplemental Material [1]. Q ranges from 7.5 ($\Pi \approx 7.5$ kPa) to near saturation (i.e., fully swollen, saturated $Q = 16.5$, $\Pi \approx 1.2$ kPa). PDMS networks were initially cleaned of uncrosslinked material followed by reswelling with silicone oil having well-defined low molecular weight (770 g/mol, Gelest). The substrate thickness is ≈ 100 μm, sufficiently large to not interfere with the wetting ridge while still allowing for clear confocal imaging [39].

Phase-separated wetting ridge of dynamic drops

The swollen PDMS networks are mounted on a motorized linear stage over a confocal microscope (Leica SP8). An 8 μl water drop (large enough to neglect evaporation but small enough to facilitate easy sliding) is then placed on the substrate. Upon deposition, there is an initial dwell time, in which an annular wetting ridge forms at the three-phase contact line. A metal ring (diameter ≈ 2.5 mm) is fixed 1 mm above the substrate and holds the drop in position while the stage moves at constant speeds ($5 - 800$ μm/s), Fig. B.1(a). This generates a relative sliding motion between the drop and

---

[1] See Supplemental Material and [38])

substrate, while the drop remains fixed in the laboratory frame for imaging. The drop is positioned such that the advancing contact zone lies in the confocal field of view, which spans 250 × 62 μm^2. While the drop is brought up to its set-point speed, the system shows transient startup dynamics; however, this regime of motion lies outside the scope of our current study on steady-state dynamics. In steady-state, the wetting ridge assumes a near-constant shape at a stationary position within the field of view, even during long sliding times ($>$ 200 s). We note that the wetting ridge shape does not depend on the dwell time of the drop prior to sliding. On rare occasions, the ridge deviates from its stationary position due to contact line pinning, likely stemming from surface impurities or contamination [40–42]. Images are taken 1.6× per second, which enables resolving these motions. This fast recording, however, brings higher signal noise with it - a drawback that we overcome by aligning each image by the tip of the ridge, followed by averaging, Supporting Information [2].

To illustrate the core features of the moving, phase-separated wetting ridge, we first slide drops over a swollen substrate ($Q = 14.5$) at a speed of 5 μm/s . We start recording images $20 - 30$ s after the onset of sliding, when no more variations are observed in the ridge shape. The dynamic wetting ridge is recorded for $\approx$ 18.5 s. This gives $n = 158$ images that yield a crisp reconstruction of the averaged wetting zone, Fig. B.1(b). The wetting ridge clearly shows two phases of (i) swollen, network PDMS (orange) and (ii) pure liquid silicone oil (red). While the network height is only slightly elevated, the silicone oil forms a sharp tip. Extracting the interfaces of each phase reveals more quantifiable detail, Fig. B.1(c). The small relative errors of the temporally accumulated data indicates that indeed, the ridge is in a steady-state. At $x = 0$, the wetting ridge has its highest point. At $|x| \gg 0$, interfacial profiles of the two phases (red and yellow) align. At $x \ll 0$, the PDMS network profile is dented due to the Laplace pressure in the drop acting on the substrate. The network and the silicone oil are well separated between $-15\ \mu\text{m} \lesssim x \lesssim 8\ \mu\text{m}$, Fig. B.1(c) inset. Within this range, the ridge profile is asymmetric with more silicone oil towards the drop ($x < 0$). Additionally, in the separated region, the network profile bends into the oil phase. The positive curvature of the network profile indicates an over-pressure inside the network PDMS with respect to the oil phase. At $x = 0$, phase-separation is strongest with a separation height of more than 10 μm.

Sliding speed and swelling ratio variation

Next, we vary the sliding speed ($v = 5-800\ \mu$m/s) and the substrate swelling ratio ($Q = 7.5-16$, near saturation).The ridge profiles of silicone oil are shown in Fig. B.2(a) for $Q = 16$ at various sliding speeds, together with the network profiles in the inset. The corresponding averaged LSCM images at the slow and fast speeds are shown in the top row. The highest ridge ($\approx$ 35 μm) forms at low sliding speed (5 μm/s, dark blue). Increasing v gradually decreases the ridge height. The smallest recorded

---

[2] See Supplemental Material for details for LSCM image processing and source codes.

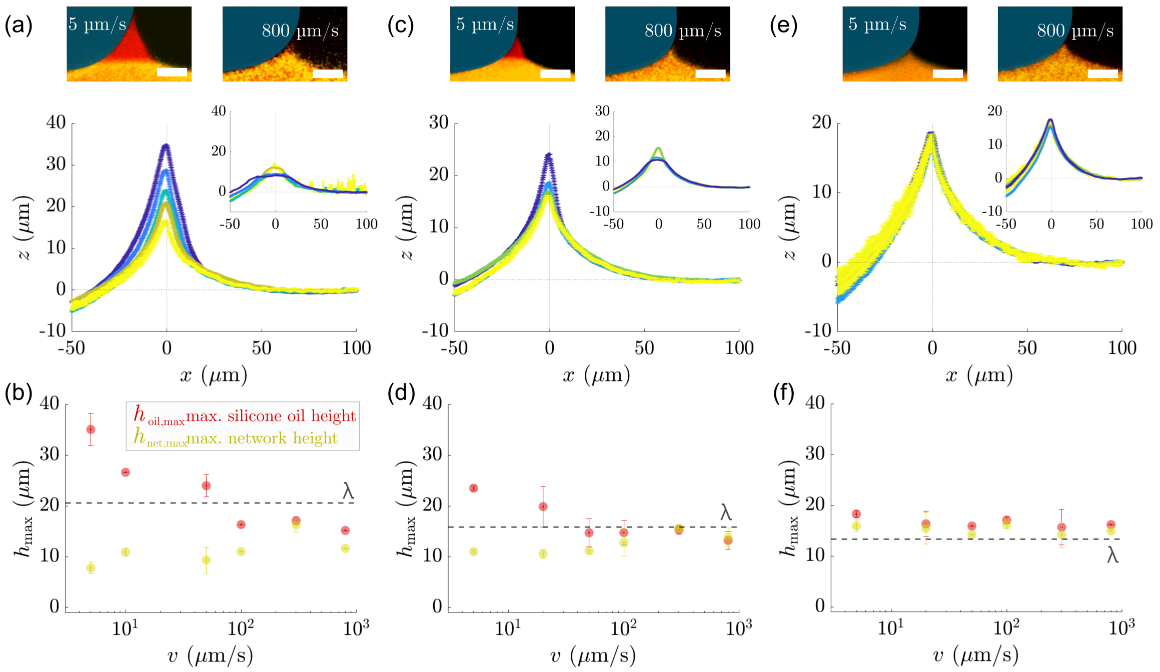

Figure B.2: Dynamic wetting ridge shape for different sliding speeds and swelling ratios (a), (b) $Q = 16$, (c), (d) $Q = 14.5$, (e), (f) $Q = 10$. (a), (c), (e) Dynamic ridge profiles of liquid silicone oil (and network PDMS as insets). (a), (c) For silicone oil, the ridge height gradually decreases for increasing drop speed, $v = 5, 10, 50, 100, 300, 800$ μm/s. Top row images are representative LSCM images for $v = 5$ μm/s and $v = 800$ μm/s (scale bar 20 μm). (b), (d), (f) Maximum height of dynamic ridges of silicone oil (red) and network PDMS (yellow). Data shows average of min. $n = 3$ repetitions together with standard deviations. Dashed lines mark dynamic elastocapillary height $\lambda \sim \gamma \sin\theta_{\mathrm{adv}}/E$, which are (b) 21 μm ($E \approx 3$ kPa) (d) 16 μm ($E \approx 3.9$ kPa) (f) 13 μm ($E \approx 4.8$ kPa).

ridge is less than 20 μm at $v = 800$ μm/s (light yellow). This height-speed relationship is inverted for the network profile, *i.e.*, the network rises with increasing speed. However, the sensitivity of the network height to v is not as pronounced as for the silicone oil tip height, Fig. B.2(b). With increasing speed, the decrease in maximum oil height $h_{\mathrm{oil,max}}$ (red circles) is much steeper than the increase in maximum network height $h_{\mathrm{net,max}}$ (yellow circles). For $v > 100$ μm/s, the height difference between $h_{\mathrm{oil,max}}$ and $h_{\mathrm{net,max}}$ is only $1 - 3$ μm. For substrates swollen to a lesser extent ($Q = 14.5$), we observe smaller ridge heights (≈ 25 μm for $v = 5$ μm/s) and narrower widths compared to the saturated ($Q = 16$) substrate, Fig. B.2(c)-(d). The less swollen substrate also has a less sensitive height-speed dependency. For $v > 100$ μm/s, the silicone oil does not clearly separate. When substrates are swollen even less to $Q = 10$, phase separation is not visible in our images; within experimental accuracy, all ridges collapse to the same shape, independent of sliding speed *i.e.*, $h_{\mathrm{oil,max}} \approx h_{\mathrm{net,max}}$, Fig. B.2(e). The maximum ridge height reaches about 15 μm for all speeds tested. These results illustrate that sliding speed and swelling ratio are critical factors that govern phase separation in dynamic wetting.

To obtain a mechanical picture of the (separated) ridge, we now relate the network height to the acting force. The network PDMS is (visco)elastic and adapts its shape to imposed stresses. Therefore, $h_{\mathrm{net,max}}$ is a proxy for the force f, acting on the material [43] per

$$h_{\mathrm{net,max}} \sim f/E, \tag{B.1}$$

where E is the Young's modulus of the swollen network [29]. In cases without phase separation, the force is imposed at a singular point by the capillary action of the drop,

$$f \sim \gamma \sin\theta_{\mathrm{adv}}, \tag{B.2}$$

where γ is the drop surface tension and θ_{adv} the advancing contact angle. Hence, $h_{\mathrm{net,max}}$ should coincide with the advancing elastocapillary length

$$\lambda \sim \gamma \sin\theta_{\mathrm{adv}}/E. \tag{B.3}$$

Swollen PDMS has an advancing contact angle of $\theta_{\mathrm{adv}} \approx 105°$ [44]. Liquid silicone oil tends to cloak aqueous drops and consequently lowers γ from 72 mN/m to 64 mN/m [45, 46]. When no phase separation is detected, λ and $h_{\mathrm{net,max}}$ coincide within experimental margin, Fig. B.2(b),(d) and (f) dashed line. Discrepancies may arise from small measurement errors of E and from the omission of the geometrical prefactors [47]. For substrates of $Q > 10$, the transition to suppressed phase separation happens at speeds around $v > 100$ μm/s. On $Q \leq 10$, $h_{\mathrm{oil,max}} \approx h_{\mathrm{net,max}}$ for all v, indicating that phase separation is mostly suppressed - although a very thin layer that is not visible likely exists. For $Q = 16$ and 14.5, $h_{\mathrm{net,max}}$ decreases with decreasing speeds. The height-speed trend inverses for $h_{\mathrm{oil,max}}$. This indicates a coupling between $h_{\mathrm{oil,max}}$ and $h_{\mathrm{net,max}}$: In cases of phase separation, the normal force acting on the network relaxes from the initial capillary-induced force, Eq. (B.2), over the region of phase separation. Alternatively, $h_{\mathrm{net,max}}$ may also change due to altered material composition (*i.e.*, E) in the network ridge when phases separate. However, we expect that the material composition in the network remains largely unaffected by variations in v, due to the large reservoir of silicone oil in the bulk.

Dynamic separation height

The size of the separated liquid tip $h_{\mathrm{sep}} = h_{\mathrm{oil,max}} - h_{\mathrm{net,max}}$ ranges between $h_{\mathrm{sep,0}}$ at $v = 0$ down to 0 for $v \to \infty$, Fig. B.3(a). The initial separation height becomes visible for $Q > 8$ and becomes more pronounced for larger Q, Fig. B.3(a) inset. Physically, the separation is driven by differing chemical potentials in the tip μ_{tip} and in the bulk network μ_{net}. As the tip is purely liquid, μ_{tip} is governed by the internal tip pressure. The liquid tip pressure changes with the interfacial curvature (Laplace pressure), and thus, also changes with h_{sep}. μ_{net} depends on the pore pressure, and therefore on Q. The dashed line in the inset of Fig. B.3(a) shows $h_{\mathrm{sep,0}}$, solely balanced by the pore pressure

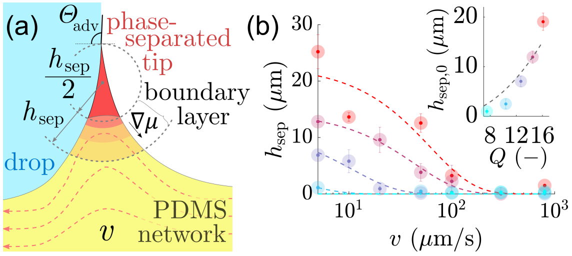

Figure B.3: Separation of liquid, silicone oil. (a) Separation height h_{sep} versus v, for $Q = 16$ (cherry red), $Q = 14.5$ (bordeaux), $Q = 12.7$ (dark blue), $Q = 10$ (blue), and $Q = 7.5$ (turquoise). Dashed lines show exponential relaxation per Eq. (B.6). Inset, measured $h_{\mathrm{sep},0}$ at zero speed for different Q. The dashed line shows $h_{\mathrm{sep},0}$, when the balance Eq. (B.4) is met. (b) Competing transport mechanisms of phase separating, silicone oil molecules induced by $\nabla\mu$ and sliding speed v. The boundary layer where $\nabla\mu \neq 0$ penetrates $\approx h_{\mathrm{sep}}/2$ into the network bulk.

which shows reasonable overlay to the data at zero speed, Supplemental Material [3]. The potential difference invokes the oil flux from the network to the tip, $j_{\mathrm{diff}} = -m\nabla\mu$, where m is the flux mobility. Given the poroelastic nature of the flux [48–51], the mobility can be thought of as a Darcy type, $m = k/\eta\Omega^2$, where k is the network permeability, $\eta = 4.6$ mPa s the viscosity, and $\Omega = 840$ mL/mol the molar volume of the low molecular weight silicone oil [52]. The region under the tip, where $\nabla\mu \neq 0$, resembles a diffusive boundary layer, which has a size $\approx h_{\mathrm{sep}}/2$, Fig. B.3(b). In equilibrium, the tip separates to $h_{\mathrm{sep},0}$ (Fig. B.3(a) inset) and the chemical potentials balance

$$\mu_{\mathrm{tip}}\left(h_{\mathrm{sep},0}\right) = \mu_{\mathrm{net}}\left(Q\right). \tag{B.4}$$

$h_{\mathrm{sep},0}$ is reached after a time given by $\tau^* = h^2_{\mathrm{sep},0}/4m$. The equilibrium values τ^* and $h_{\mathrm{sep},0}/2$ allow us to construct an equilibration speed $v^* = h_{\mathrm{sep},0}/2\tau^*$.

When the drop is brought into sliding motion, an advective flux builds up in the reference frame of the ridge, $j_{\mathrm{adv}} = \Omega v$, which superposes j_{diff}. This hinders the full static equilibration of the tip as the region underneath the tip is constantly refreshed. At constant sliding motion, however, a steady-state exists. This steady-state is only possible when the two fluxes balance,

$$j_{\mathrm{diff}} = j_{\mathrm{adv}}. \tag{B.5}$$

Additional fluxes from the cloaking layer or an oil precursor on the network surface may contribute. However, the interfacial area between these fluxes and the tip subceeds the ones from j_{diff} and j_{adv} by a few orders of magnitude and are therefore comparatively minor; hence, these are neglected in our description. When the sliding speed is sufficiently large, the advective flux can fully suppress separation. We condense the flux balance [Eq. (B.5)] and the equilibrium condition [Eq. (B.4)] into a steady-state 'balance model' (cf. SI [4] for full derivations). The model

---

[3] See Supplemental Material for the pore pressure determination.

[4] See Supplemental Material for detailed model derivations

estimates the speed-dependent separation height; the dashed-dotted line in Fig. B.4(a) shows the renormalized model estimate. To compare our data with the balance model, we extract v^* from our data by calculating the correlation speed of the measured $h_{\text{sep}}(v)$ using the correlation function $\text{corr}\left\{h_{\text{sep}}, h_{\text{sep},0}\right\}$, SI [5]. We find that the normalized speed-correlation function is well represented by a decaying exponential:

$$\text{corr}\left\{h_{\text{sep}}, h_{\text{sep},0}\right\} \approx h_{\text{sep}}\left(v\right)/h_{\text{sep},0} \approx e^{-v/v^*}. \tag{B.6}$$

Renormalization of the height and speed as $h_{\text{sep}}/h_{\text{sep},0}$ and v/v^* collapses the data onto the exponential relaxation curve, Fig. B.4(a). The balance model recovers the experimentally observed separation (and the exponential relaxation) for $v \to 0$ and $v \to \infty$, Fig B.4(a) dashed-dotted line. For $v/v^* < 1$, the modeled separation is underestimated while for $v/v^* > 1$ it is slightly overestimated. These deviations may stem from h_{sep}-dependent, elastic contributions to μ_{net} in the boundary layer. Additionally, the omission of geometrical factors may introduce further uncertainties.

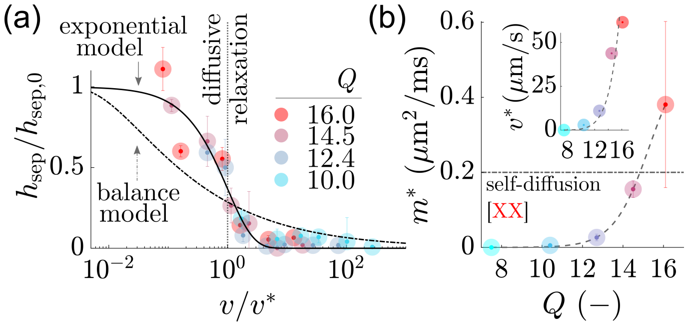

Figure B.4: Separation dynamics and mobilities. (a) Normalized tip height $h_{\text{sep}}/h_{\text{sep},0}$ against normalized sliding speed v/v^* (colored circled). Dashed line: balance model; and solid line: exponential relaxation. (b) Measured mobility m^* against Q. Horizontal line is the mobility of self-diffusion [53]. Inset shows extracted correlation speed v^*. Dashed lines indicate trends and error bars correspond to fitted root-square-mean error.

The extracted heights and speeds produce an effective mobility $m^* = v^* h_{\text{sep},0}/2$ of the separating oil. Consequently, m^* is only measurable when a tip separates; that is, the mobility is $m^* \approx 0$ for $Q \leq 10$, Fig. B.4(b). For $Q > 10$, m^* increases with Q. At high Q, $\mathcal{O}\left(m^*\right) = 10^{-10}$ m^2/s, which is close to the mobilities of self diffusing (low Ω) PDMS molecules in melts [53], Fig. B.4(b) horizontal line. The increasing m^* at higher Q can be explained by considering the network structure: When more oil is swollen into the network, the pores of the network (*i.e.*, mesh size) are expanded [54]. When molecules travel through the expanded pores, the imposed friction from the immobilized (crosslinked) network is reduced. This is reflected in higher permeability values k, and hence, a higher Darcy mobility. At a given prevailing chemical potential gradient, combined with an inherent excess in available oil molecules, high swelling ratios lead to faster molecular fluxes, and ultimately,

---

[5] See Supplemental Material presentation of speed-correlation function and exponential relaxation.

to faster and larger ridge formations. Eventually, the imposed friction in strongly expanded networks stems dominantly from internal molecular friction, since the interactions with the immobile network become negligible. Hence at a high swelling ratio, our data suggests a crossover from a Darcy transport to melt diffusion.

Conclusion

In summary, the competition of drop advection and molecular flux governs the degree of phase separation in wetting ridges of moving drops. Understanding phase separation should offer guidelines for controlling drop dynamics. Notably, phase separation is locally triggered by the (weak) singularity of the three-phase contact line. Whether phase separation occurs spontaneously or requires some threshold effort remains an open and relevant question for wetting on soft substrates.

Acknowledgements

We thank Rodrique Badr, Abhinav Naga, Friederike Schmid, and William S. Y. Wong for discussions. This research is supported by the US National Science Foundation through award number 2043732 (Z.C., J.T.P.), German Research Foundation (DFG) with the Priority Programme 2171 (L.H., D.V.).

References

1. Young, T. III. An Essay on the Cohesion of Fluids. *Phil. Trans. R. Soc.* **95,** 65–87. ISSN: 0261-0523, 2053-9223 (Dec. 1805).
2. Yuk, S. H. & Jhon, M. S. Contact Angles on Deformable Solids. *J. Colloid Interface Sci.* **110,** 252–257. ISSN: 0021-9797 (Mar. 1986).
3. Schellenberger, F. *et al.* Direct Observation of Drops on Slippery Lubricant-Infused Surfaces. *Soft Matter* **11,** 7617–7626. ISSN: 1744-683X, 1744-6848 (2015).
4. Semprebon, C., McHale, G. & Kusumaatmaja, H. Apparent Contact Angle and Contact Angle Hysteresis on Liquid Infused Surfaces. *Soft Matter* **13,** 101–110. ISSN: 1744-6848 (Dec. 2016).
5. Carré, A., Gastel, J.-C. & Shanahan, M. E. R. Viscoelastic Effects in the Spreading of Liquids. *Nature* **379,** 432–434. ISSN: 0028-0836, 1476-4687 (Feb. 1996).
6. Chaudhuri, K. & Pham, J. T. Temperature-Dependent Soft Wetting on Amorphous, Uncrosslinked Polymer Surfaces. *Soft Matter* **18,** 3698–3704. ISSN: 1744-6848 (May 2022).
7. Saiz, E., Tomsia, A. & Cannon, R. Ridging Effects on Wetting and Spreading of Liquids on Solids. *Acta Materialia* **46,** 2349–2361. ISSN: 13596454 (Apr. 1998).
8. Clanet, C. & Quéré, D. Onset of Menisci. *J. Fluid Mech.* **460,** 131–149. ISSN: 1469-7645, 0022-1120 (June 2002).
9. Léonforte, F. & Müller, M. Statics of Polymer Droplets on Deformable Surfaces. *J. Chem. Phys.* **135,** 214703. ISSN: 0021-9606 (Dec. 2011).
10. Park, S. J., Bostwick, J. B., Andrade, V. D. & Je, J. H. Self-Spreading of the Wetting Ridge During Stick-Slip on a Viscoelastic Surface. *Soft Matter* **13,** 8331–8336. ISSN: 1744-6848 (Nov. 2017).

11. Gerber, J., Lendenmann, T., Eghlidi, H., Schutzius, T. M. & Poulikakos, D. Wetting Transitions in Droplet Drying on Soft Materials. *Nat. Commun.* **10,** 4776. ISSN: 2041-1723 (Oct. 2019).

12. Masurel, R., Roché, M., Limat, L., Ionescu, I. & Dervaux, J. Elastocapillary Ridge as a Noninteger Disclination. *Phys. Rev. Lett.* **122,** 248004 (June 2019).

13. Andreotti, B. & Snoeijer, J. H. Statics and Dynamics of Soft Wetting. *Annu. Rev. Fluid Mech.* **52,** 285–308 (2020).

14. Dai, Z. & Vella, D. Droplets on Lubricated Surfaces: The Slow Dynamics of Skirt Formation. *Phys. Rev. Fluids* **7,** 054003. ISSN: 2469-990X (May 2022).

15. Mora, S., Phou, T., Fromental, J.-M., Pismen, L. M. & Pomeau, Y. Capillarity Driven Instability of a Soft Solid. *Phys. Rev. Lett.* **105,** 214301 (Nov. 2010).

16. Jerison, E. R., Xu, Y., Wilen, L. A. & Dufresne, E. R. Deformation of an Elastic Substrate by a Three-Phase Contact Line. *Phys. Rev. Lett.* **106,** 186103 (May 2011).

17. Bico, J., Reyssat, E. & Roman, B. Elastocapillarity: When Surface Tension Deforms Elastic Solids. *Annu. Rev. Fluid Mech.* **50,** 629–659 (Jan. 2018).

18. Neumann, A. W., Good, R. J., Hope, C. J. & Sejpal, M. An Equation-of-State Approach to Determine Surface Tensions of Low-Energy Solids from Contact Angles. *J. Colloid Interface Sci.* **49,** 291–304. ISSN: 0021-9797 (Nov. 1974).

19. Marchand, A., Das, S., Snoeijer, J. H. & Andreotti, B. Contact Angles on a Soft Solid: From Young's Law to Neumann's Law. *Phys. Rev. Lett.* **109,** 236101 (Dec. 2012).

20. Cao, Z. & Dobrynin, A. V. Polymeric Droplets on Soft Surfaces: From Neumann's Triangle to Young's Law. *Macromolecules* **48,** 443–451. ISSN: 0024-9297 (Jan. 2015).

21. Van Gorcum, M., Karpitschka, S., Andreotti, B. & Snoeijer, J. H. Spreading on Viscoelastic Solids: Are Contact Angles Selected by Neumann's Law? *Soft Matter* **16,** 1306–1322. ISSN: 1744-6848 (Feb. 2020).

22. Tanaka, T. Gels. *Sci. Am.* **244,** 124-S–17. ISSN: 0036-8733 (1981).

23. Tanaka, T. *et al.* Mechanical Instability of Gels at the Phase Transition. *Nature* **325,** 796–798. ISSN: 1476-4687 (Feb. 1987).

24. Lee, J. N., Park, C. & Whitesides, G. M. Solvent Compatibility of Poly(Dimethylsiloxane)-Based Microfluidic Devices. *Anal. Chem.* **75,** 6544–6554. ISSN: 0003-2700, 1520-6882 (Dec. 2003).

25. Chan, E. P. & Crosby, A. J. Fabricating Microlens Arrays by Surface Wrinkling. *Advanced Materials* **18,** 3238–3242. ISSN: 1521-4095 (2006).

26. Chan, E. P., Smith, E. J., Hayward, R. C. & Crosby, A. J. Surface Wrinkles for Smart Adhesion. *Advanced Materials* **20,** 711–716. ISSN: 1521-4095 (2008).

27. Jensen, K. E. *et al.* Wetting and Phase Separation in Soft Adhesion. *Proc. Natl. Acad. Sci. U.S.A.* **112,** 14490–14494 (Nov. 2015).

28. Pham, J. T., Schellenberger, F., Kappl, M. & Butt, H.-J. From Elasticity to Capillarity in Soft Materials Indentation. *Phys. Rev. Mater.* **1,** 015602 (June 2017).

29. Cai, Z., Skabeev, A., Morozova, S. & Pham, J. T. Fluid Separation and Network Deformation in Wetting of Soft and Swollen Surfaces. *Commun. Mater.* **2,** 1–11. ISSN: 2662-4443 (Feb. 2021).

30. Shanahan, M. E. R. & Carre, A. Viscoelastic Dissipation in Wetting and Adhesion Phenomena. *Langmuir* **11,** 1396–1402. ISSN: 0743-7463 (Apr. 1995).

31. Long, D., Ajdari, A. & Leibler, L. Static and Dynamic Wetting Properties of Thin Rubber Films. *Langmuir* **12,** 5221–5230. ISSN: 0743-7463 (Jan. 1996).

32. Karpitschka, S. *et al.* Droplets Move Over Viscoelastic Substrates by Surfing a Ridge. *Nat. Commun.* **6,** 7891. ISSN: 2041-1723 (Aug. 2015).

33. Zhao, M. *et al.* Geometrical Control of Dissipation During the Spreading of Liquids on Soft Solids. *Proc. Natl. Acad. Sci. U.S.A.* **115,** 1748–1753 (Feb. 2018).
34. Hourlier-Fargette, A., Antkowiak, A., Chateauminois, A. & Neukirch, S. Role of Uncrosslinked Chains in Droplets Dynamics on Silicone Elastomers. *Soft Matter* **13,** 3484–3491. ISSN: 1744-6848 (May 2017).
35. Zhao, M. *et al.* Growth and Relaxation of a Ridge on a Soft Poroelastic Substrate. *Soft Matter* **14,** 61–72. ISSN: 1744-683X, 1744-6848 (2018).
36. Wong, W. S. Y. *et al.* Adaptive Wetting of Polydimethylsiloxane. *Langmuir* **36,** 7236–7245. ISSN: 0743-7463 (July 2020).
37. Xu, Q., Wilen, L. A., Jensen, K. E., Style, R. W. & Dufresne, E. R. Viscoelastic and Poroelastic Relaxations of Soft Solid Surfaces. *Phys. Rev. Lett.* **125,** 238002. ISSN: 0031-9007, 1079-7114 (Nov. 2020).
38. Glover, J. D., McLaughlin, C. E., McFarland, M. K. & Pham, J. T. Extracting Uncrosslinked Material from Low Modulus Sylgard 184 and the Effect on Mechanical Properties. *J. Polym. Sci.* **58,** 343–351. ISSN: 2642-4169 (2020).
39. Khattak, H. K., Karpitschka, S., Snoeijer, J. H. & Dalnoki-Veress, K. Direct Force Measurement of Microscopic Droplets Pulled along Soft Surfaces. *Nat. Commun.* **13,** 4436. ISSN: 2041-1723 (July 2022).
40. Forsberg, P. S. H., Priest, C., Brinkmann, M., Sedev, R. & Ralston, J. Contact Line Pinning on Microstructured Surfaces for Liquids in the Wenzel State. *Langmuir* **26,** 860–865. ISSN: 0743-7463 (Jan. 2010).
41. Kajiya, T. *et al.* Advancing Liquid Contact Line on Visco-Elastic Gel Substrates: Stick-Slip Vs. Continuous Motions. *Soft Matter* **9,** 454–461. ISSN: 1744-683X, 1744-6848 (2013).
42. Lhermerout, R. & Davitt, K. Controlled Defects to Link Wetting Properties to Surface Heterogeneity. *Soft Matter* **14,** 8643–8650. ISSN: 1744-683X, 1744-6848 (2018).
43. Roman, B. & Bico, J. Elasto-Capillarity: Deforming an Elastic Structure with a Liquid Droplet. *J. Phys. Condens. Matter* **22,** 493101. ISSN: 0953-8984 (Nov. 2010).
44. Cai, Z. & Pham, J. T. How Swelling, Cross-Linking, and Aging Affect Drop Pinning on Lubricant-Infused, Low Modulus Elastomers. *ACS Appl. Polym. Mater.* **4,** 3013–3022 (May 2022).
45. Hourlier-Fargette, A., Dervaux, J., Antkowiak, A. & Neukirch, S. Extraction of Silicone Uncrosslinked Chains at Air–Water–Polydimethylsiloxane Triple Lines. *Langmuir* **34,** 12244–12250. ISSN: 0743-7463 (Oct. 2018).
46. Naga, A. *et al.* How a Water Drop Removes a Particle from a Hydrophobic Surface. *Soft Matter* **17,** 1746–1755. ISSN: 1744-683X, 1744-6848 (2021).
47. Style, R. W. & Dufresne, E. R. Static Wetting on Deformable Substrates, from Liquids to Soft Solids. *Soft Matter* **8,** 7177–7184. ISSN: 1744-6848 (June 2012).
48. Biot, M. A. General Theory of Three-Dimensional Consolidation. *J. Appl. Phys.* **12,** 155–164. ISSN: 0021-8979 (Feb. 1941).
49. Hu, Y., Zhao, X., Vlassak, J. J. & Suo, Z. Using Indentation to Characterize the Poroelasticity of Gels. *Appl. Phys. Lett.* **96,** 121904. ISSN: 0003-6951 (Mar. 2010).
50. Berman, J. D. *et al.* Singular Dynamics in the Failure of Soft Adhesive Contacts. *Soft Matter* **15,** 1327–1334. ISSN: 1744-683X, 1744-6848 (2019).
51. Flapper, M. M., Pandey, A., Karpitschka, S. & Snoeijer, J. H. *Reversal of Solvent Migration in Poroelastic Folds* Sept. 2022. arXiv: `2209.00887 [cond-mat]`.
52. . *Polydimethylsiloxane, Trimethylsiloxy Terminated, 5 Cst* https://www.gelest.com/product/DMS-T05/.

53. McCall, D. W. & Huggins, C. M. Self-Diffusion in Linear Polydimethyl Siloxane Liquids. *Appl. Phys. Lett.* **7,** 153–154. ISSN: 0003-6951 (Sept. 1965).
54. Saalwächter, K. & Seiffert, S. Dynamics-Based Assessment of Nanoscopic Polymer-Network Mesh Structures and Their Defects. *Soft Matter* **14,** 1976–1991 (2018).
55. Huggins, M. L. Solutions of Long Chain Compounds. *J. Chem. Phys.* **9,** 440–440. ISSN: 0021-9606 (May 1941).
56. Flory, P. J. Thermodynamics of High Polymer Solutions. *J. Chem. Phys.* **9,** 660–660. ISSN: 0021-9606 (Aug. 1941).
57. Daniel, D., Timonen, J. V. I., Li, R., Velling, S. J. & Aizenberg, J. Oleoplaning Droplets on Lubricated Surfaces. *Nat. Phys.* **13,** 1020–1025. ISSN: 1745-2481 (Oct. 2017).
58. Kreder, M. J. *et al.* Film Dynamics and Lubricant Depletion by Droplets Moving on Lubricated Surfaces. *Phys. Rev. X* **8,** 031053. ISSN: 2160-3308 (Sept. 2018).
59. Gunjan, M. R., Kumar, A. & Raj, R. Cloaked Droplets on Lubricant-Infused Surfaces: Union of Constant Mean Curvature Interfaces Dictated by Thin-Film Tension. *Langmuir* **37,** 6601–6612. ISSN: 0743-7463 (June 2021).

Supplemental Material

Interfial profile extraction

LSCM images were recorded at a rate of 1.6 fps. Raw images were processed via a custom-written Matlab script [6]. Images were preconditioned by renormalizing the 8bit grayscale with 1% over saturation. To remove photon noise, we applied a wiener filter together with a gaussian filter on the images. The preconditioning step ends with image binarization, utilizing an otsu-threshold. All functions are part of the Matlab Image Processing Toolbox (Version 11.2). The interface profiles of each phase h_{oil} and h_{net} are extracted by finding the location where binary pixel values switch from 1 to 0. Each profile at time t_i is vectorized as $\boldsymbol{x}_{\text{profile,i}} = [x, h(x)]$. The maximal height of each profile, is discerned as the tip of the ridge, with location $\boldsymbol{x}_{\text{ridge,i}} = [\text{argmax}(h), \max(h)]$. Now, each profile is re-centered, according to

$$\tilde{\boldsymbol{x}}_{\text{profile,i}} = \boldsymbol{x}_{\text{profile,i}} - \boldsymbol{x}_{\text{ridge,i}}. \tag{B.7}$$

Thereafter, ridge profiles are temporally averaged to obtain profiles, as plotted in Fig 2. Similarly, LSCM images are processed, Fig. B.5.

Preparation of swollen polydimethylsiloxane substrates

PDMS networks (Sylgard 184, Dow) are prepared by mixing 60:1 base to crosslinking agent by weight. For visualization, we add fluorescein O,O'-diacrylate (Sigma-Aldrich) that covalently binds to network molecules. The mixture is spin-coated onto glass slides pre-coated with a sacrificial layer (polymmethylmethacrylate), creating ≈ 100 μm thick substrates. The substrates are cured at 65° C for 48 hours. Thereafter, the network is cleaned of uncrosslinked molecules via an extraction method

---

[6] source code available at https://github.com/st4cc0/LSCM-2-phase-ridge-extraction.git

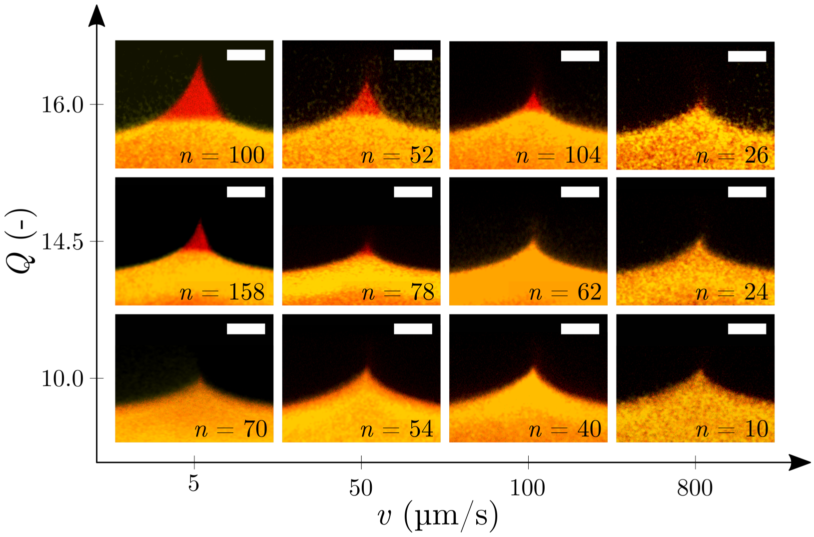

Figure B.5: Temporal averaged LSCM micrographs of the advancing wetting ridges of soft PDMS. Ridges are shown at different swelling ratios Q and speeds v. Orange crosslinked PDMS network, red marks liquid oligomers. Number n of frames for each temporal average in the bottom right corner. Top right scale bar is 20 μm.

[38]. Briefly, the cured samples are cut to 1×0.5 cm^2 rectangles. The substrates are then placed on the surface of a deionized water bath. Hexane (≈ 200 ml) is poured on top to wash the PDMS substrate, such that uncrosslinked PDMS chains diffuse into the hexane. The hexane layer is renewed daily for one week. This gives a washed ('dry') PDMS substrate of which we measure the area A_{dry}. Inert, low molecular weight, liquid silicone oil (5 cSt/770 g/mol, Gelest) is premixed with red-shifted perylene monoimide (PMI) dye and added directly onto the dry PDMS substrate. Note that we renounced on dying the water drop with a third marker in order to reduce overlapping fluorescence spectra and photon noise in the system. As a drawback, direct measurments of the contact angle with confocal microscopy is not straight forward. The silicone oil is allowed to distribute homogeneously in the network over the course of one week. The area A of the swollen substrates is used to determine the swelling ratio, defined as $Q = (A/A_{\mathrm{dry}})^{3/2}$. The swollen substrates are placed onto a glass slide for drop sliding experiments.

Rheology and relaxation of swollen elastomers

The relaxation of the swollen elastomer was obtained by small amplitude oscillatory rheometer measurements (TA Instruments Discovery HR-2). We measured the frequency (ω) dependent complex modulus $G(\omega) = G'(\omega) + iG''(\omega)$, with the storage and the loss moduli, G' and G'', respectively. The measurement data were fitted to the Chasset-Thirion model

$$G(\omega) = G_0 \left[1 + (\tau_s \omega i)^n\right]. \tag{B.8}$$

Here, G_0 is the zero angle modulus, τ_s the relaxation time, and n the rheological exponent. We measured substrates swollen to $Q = 16, 15.4, 11.5$, and 6.2, Fig. B.6. The extracted model parameters are listed in Tab. SB.1.

Table B.1: Fitted rheological parameters.

Q	G_0 (Pa)	τ_s (s)	n
1.0	4450	1.1	0.35
6.2	1800	1.0E-07	0.24
11.4	1600	3.8E-08	0.24
14.5	1350	8.2E-09	0.22
16.3	900	8.3E-09	0.20

To estimate how important the viscoelastic relaxations within the ridge are during drop sliding, we compare the sliding speeds v with the viscoelastic relaxation speed in the wetting ridge. The important length scale of the viscoelastic wetting ridge is the solid viscoelastic length scale

$$\lambda_s \sim \frac{\Upsilon_s + \Upsilon_{sl}}{G_0}, \tag{B.9}$$

where $\Upsilon_s \approx 40$ mN/m and $\Upsilon_{sl} \approx 20$ mN/m are approximated as the solid surface tension between the PDMS-air and the PDMS-liquid interface, respectively. We estimate a solid Capillary number

$$\mathrm{Ca}_s = \frac{vG_0}{\tau_s(\Upsilon_s + \Upsilon_{sl})}. \tag{B.10}$$

Comparing Ca_s over the range of investigated sliding speeds ($5-800$ μm/s), shows that $Ca_s \ll 1$, Fig. B.6(e). This indicates that viscoelastic perturbations relax much faster than the contact line. By also looking at the fully extracted, dry polymer network, where no oil exists, the capillary numbers approach those where viscoelasticity may play a role.

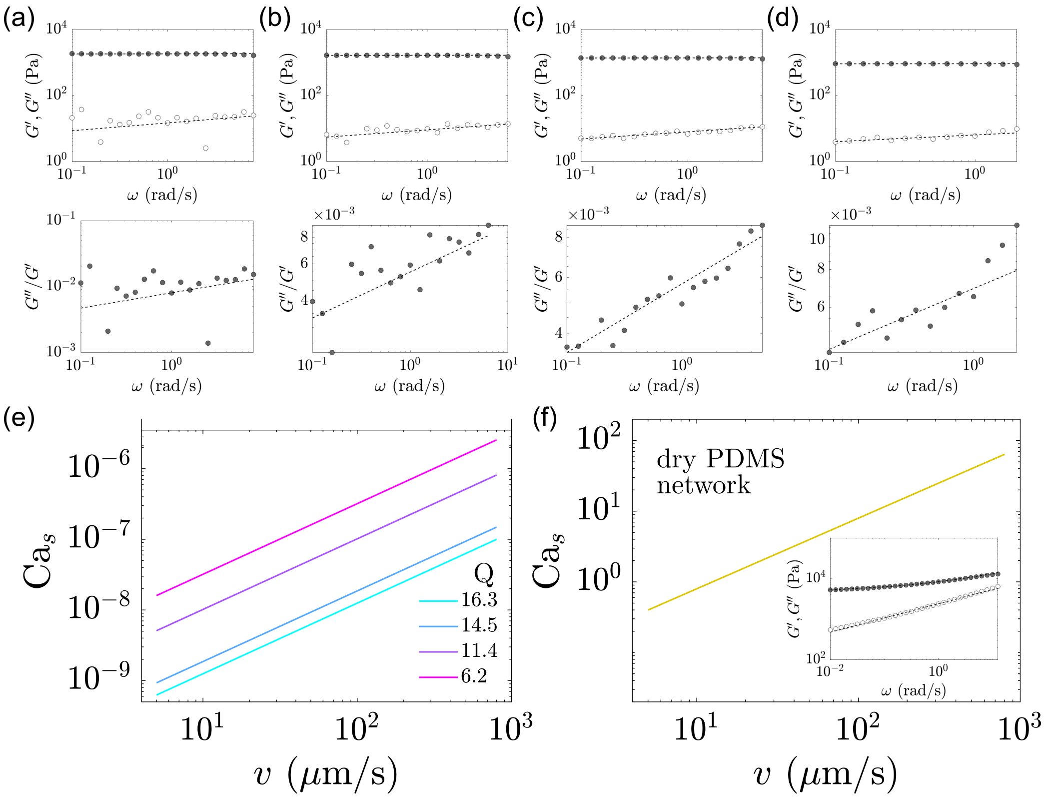

Figure B.6: Relaxation of swollen elastomers. Top; measurements of storage and loss moduli, G' (closed symbols) G'' (open symbols) and bottom: G''/G' for (a) $Q = 6.2$, (b) $Q = 11.5$, (c) $Q = 14.5$, and (d) $Q = 16$. Dashed lines correspond to fitted complex modulus Eq. (B.8). (e) Solid capillary number Ca_s length against sliding speed v for elastomers, swollen to $Q = 16-6.2$. (f) Solid capillary number for dry PDMS network. Inset, G' and G'' sweep for dry PDMS.

Pore Pressure

Based on the Flory Huggins relation [55, 56] for mixing of liquid solvents into cross-linked polymer networks, we compute the pore pressure Π of the swollen PDMS network as

$$\Pi(\phi) = -\frac{k_B T N_a}{\Omega}\left[\log\left(1-\phi\right) + \phi + \chi\phi^2\right]. \tag{B.11}$$

Here, k_B, T, N_a, and Ω are the Boltzmann constant, the ambient temperature, Avogadro's constant, and the molar volume of the PDMS oligomers, respectively [7]. ϕ corresponds to the volume fraction of the PDMS network and is related to the swelling ratio per $\phi = 1/Q$. χ denotes the Flory Huggins interaction parameter that was previously estimated to be around $\chi \approx 0.44$ [29]. For the investigated swelling ratios ($7.5 - 16$) the pore pressure lies between $\Pi(Q = 7.5) \approx 7.5$ kPa and $\Pi(Q = 16) \approx 1.3$ kPa, Fig. B.7.

---

[7] $k_B = 1.380649 \times 10^{-23}$ J/K, $T = 393$ K, $N_a = 6.02214076 \times 10^{23}$ 1/mol, $\Omega = 840 \times 10^{-6}$ m^3/mol

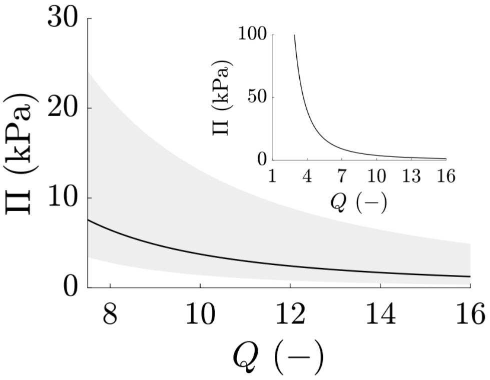

Figure B.7: Pore pressure for PDMS networks, swollen to different amounts of swelling rations. Gray area demarcates ranges of $\chi = 0.2 - 0.5$.

Oil transport to separated tip

The phase-separated tip interfaces towards various fluxes that supply and drain the tip with oil Fig. B.8. Here, we consider four fluxes that are provided by 1) the diffusive transport due to the chemical potential difference [j_{diff}], 2) the advective transport from the network bulk due to drop sliding [j_{adv}], 3) oil transport from a possible oil precursor at the network-air interface [j_{pre}], and 4) oil transport from the cloaking layer on the drop [j_{cloak}]. The mass balance at the ridge reads

$$\frac{dM}{dt} + \sum \int_{A_i} j_i dS = 0. \tag{B.12}$$

Here, the sum accounts for all fluxes j_i, integrated over their respective interfaces A_i, where the interfaces are measured per unit depth. The mass of the separated tip is $M = \rho \alpha h_{\text{sep}}^2$, where ρ is the density of the oil, h_{sep} is the separation height and α is a geometrical coefficient that we approximate as unity. Further, we assume constant flux over the interfaces, such that the mass balance reads

$$\rho \frac{dh_{\text{sep}}^2}{dt} + j_{\text{diff}} A_{\text{diff}} + j_{\text{adv}} A_{\text{adv}} + j_{\text{pre}} A_{\text{pre}} + j_{\text{cloak}} A_{\text{cloak}} = 0 \tag{B.13}$$

The diffusive flux is driven by the chemical potential gradient,

$$j_{\text{diff}} = -\frac{m}{RT} \nabla \mu. \tag{B.14}$$

The advective flux, driven by the sliding speed v is

$$j_{\text{adv}} = \rho v. \tag{B.15}$$

The transport from the precursor is also driven by the sliding speed v, as the wetting ridge moves along the surface and picks up the precursor. Hence, the resulting flux is $j_{\text{pre}} = -\rho v$. Oil transported by the cloaking layer is an entrainment effect of the rolling water molecules of the drop.

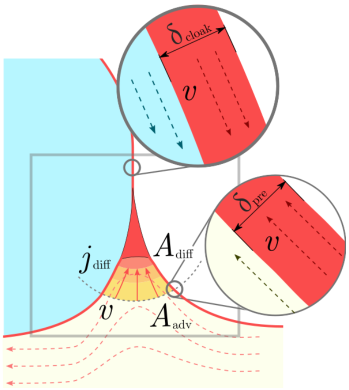

Figure B.8: Mainly 4 fluxes [$j_\text{diff}, j_\text{adv}, j_\text{pre}, j_\text{cloak}$] interface the tip. j_cloak forms due to the flow in the moving drop. The interfacial areas, $A_\text{diff}, A_\text{adv}$ and $A_\text{pre}, A_\text{cloak}$ are separated by 2 to 4 orders of magnitude.

As the water moves from the rear end to the front end, the thin cloaking layer is transported on the drop interfaces towards the wetting ridge. The transport of the cloaking layer is thus governed by the speed of the rolling water molecules at the interface of the drop cap. This speed is very close to the sliding speed, and therefore, the transport is $j_\text{cloak} \approx -\rho v$.

In terms of the areas, the diffusive flux crosses over the interface $A_\text{diff} = h_\text{sep}$, since the ratio of the tip width and its height is approximated as $\alpha \approx 1$. The advective flux is transported over the boundary layer height, that is $A_\text{adv} = \frac{h_\text{sep}}{2}$ (cf. Fig 3b, main text). The thickness of the precursor and the cloak are δ_pre and δ_cloak, respectively. Hence, the mass balance becomes

$$2\rho h_\text{sep}\frac{dh_\text{sep}}{dt} + v\rho\left(\frac{h_\text{sep}}{2} - \delta_\text{pre} - \delta_\text{cloak}\right) - h_\text{sep}\frac{m}{RT}\nabla\mu = 0. \tag{B.16}$$

The precursor and the cloak are stabilized by Hamaker interactions that start to become significant when their layer thickness is in the order of $\mathcal{O}(\delta_\text{pre}) \approx \mathcal{O}(\delta_\text{cloak}) \approx 10^{-9} - 10^{-8}$ m [57–59]. The separation height (in steady state) is in the order of $\mathcal{O}(h_\text{sep}) \approx 10^{-6} - 10^{-5}$ m, as observed in our experiments. Since the separation height is orders larger than the thickness of the potential cloak or precursor layers, the fluxes from the precursor and the cloak are negligible and the flux balance becomes

$$2\rho\frac{dh_\text{sep}}{dt} + \frac{v\rho}{2} - \frac{m}{RT}\nabla\mu = 0. \tag{B.17}$$

Kinematic limit

In a steady state when all time derivatives vanish, the mass balance is

$$\frac{v\rho}{2} = \frac{m}{RT}\nabla\mu. \tag{B.18}$$

The gradient of the chemical potential decays over the boundary layer and scales therefore as $\nabla\mu \sim \frac{\Delta\mu}{h_{\text{sep}}}$. This yields a scaling between the speed and the separation height as

$$h_{\text{sep}} \sim \frac{1}{v}. \tag{B.19}$$

At finite $\Delta\mu$ (and independent of the magnitude), the separation height is fully suppressed at $v \to \infty$, as reflected in Eq. (B.19). This behavior stems from the simple flux balance between j_{adv} and j_{diff} and coincides with our experimental observations. As the suppression of the separation height is governed by the speed v, we term this the 'kinematic limit' of the separation height. While for $v \to \infty$ Eq. (B.19) recovers reasonably the experimental observations and gives a physical explanation for the h_{sep} suppression at high speeds. However, we also find a singularity for h_{sep} at $v \to 0$. This behavior contradicts our experimental data. Hence, we need to adjust the model, accordingly.

Regularized model

The cause for $h_{\text{sep}} \to \infty$ at $v \to 0$ roots in the constant chemical potential which means a constant driving force for the phases to separate. When no advection opposes the diffusive flux this results in an unbound separation of the liquid, and thus, a separation height, growing to infinity. This, however, contradicts observations from the experiment, where the phase-separated tip reaches finite size, even when the drop is sessile [29]. Therefore, the chemical potential within the liquid tip is not constant but needs to change with the tip size. This becomes evident as the chemical potential inside the tip is related to the internal pressure, per

$$\mu_{\text{sep}} = p\Omega. \tag{B.20}$$

Due to the excessive oil reservoir swollen in the network, we assume a constant chemical potential within the network bulk, far away from the liquid tip

$$\mu_{\text{net}} = \text{const}. \tag{B.21}$$

The tip internal pressure changes with the curvatures of the liquid interfaces (towards air and the drop). This curvature reduces during tip growth. The curvatures and the internal pressure are related *via* the Laplace pressure

$$p = -\frac{\gamma_{\text{oil}}}{h_{\text{sep}}}. \tag{B.22}$$

The surface tension of the liquid PDMS is $\gamma_{\text{oil}} = 20$ mN/m. The radius of curvature is approximated with the tip height (again, with the approximation that the geometric mapping between curvature and tip height is unity). The chemical potential difference between the separated ridge and network is thus

$$\Delta\mu(h_{\mathrm{sep}}) = \mu_{\mathrm{net}} - \mu_{\mathrm{tip}} = \mu_{\mathrm{net}} + \Omega \frac{\gamma_{\mathrm{oil}}}{h_{\mathrm{sep}}}, \tag{B.23}$$

and gradually decays as the tip grows. When the drop is not moving ($v = 0$), the equilibrium height is found at $\Delta\mu(h_{\mathrm{sep},0}) = 0$. The evolution of the zero-speed tip is

$$\frac{dh_{\mathrm{sep}}}{dt} = \frac{m}{RT} \frac{\mu_{\mathrm{net}} + \Omega \frac{\gamma_{\mathrm{oil}}}{h_{\mathrm{sep}}}}{h_{\mathrm{sep}}}, \tag{B.24}$$

where we omit geometrical prefactors. The equilibrium height is reached around the characteristic diffusion time

$$\tau^* = h_{\mathrm{sep},0}^2/4m, \tag{B.25}$$

or by the characteristic diffusive speed

$$v^* = 2m/h_{\mathrm{sep},0}. \tag{B.26}$$

To obtain the separation height shifted from equilibrium during drop sliding, we transform the time (as a measure for the non-equilibrium) in the evolution equation (B.24) with

$$t = h_{\mathrm{sep},0}/v. \tag{B.27}$$

We nondimensionalize the separation height with

$$H \equiv h_{\mathrm{sep}}/h_{\mathrm{sep},0}, \tag{B.28}$$

and the speed with

$$V \equiv v h_{\mathrm{sep},0}/m = v/v^*. \tag{B.29}$$

After the transformation, nondimensionalization, and reorganization of Eq. (B.24), we obtain the ordinary differential equation (ODE)

$$\frac{dH}{dV^{-1}} = \frac{c_0 + Hc_1}{H^2}, \tag{B.30}$$

with the coefficients

$$c_0 = \frac{\Omega}{RT} \frac{\gamma_{\mathrm{oil}}}{h_{\mathrm{sep},0}}, \quad c_1 = \frac{\mu_{\mathrm{net}}}{RT}. \tag{B.31}$$

This ODE has the closed-form solution

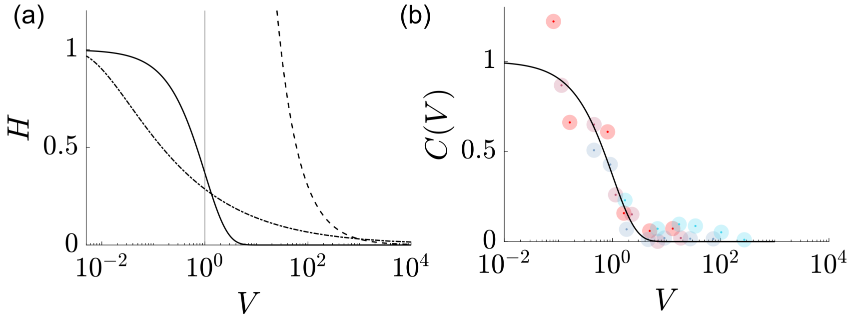

Figure B.9: (a) Nondimensionalized dynamic separation height $H = h_{\text{sep}}/h_{\text{sep},0}$ versus nondimensionalized $V = v/v^*$. The dashed line corresponds to the kinematic limit with zero-speed singularity. Solid and dot-dashed lines correspond to regularized models that generate finite separation heights even at speeds, slower than v^*. Vertical line corresponds to $V = 0$, *i.e.* the ridge growth rate. Dot-dashed line corresponds to model equation (B.32) with parameters $c_0 = c_1 = 10^{-2}$. (b) Speed-correlation values between measured h_{sep} and $h_{\text{sep},0}$. Solid lines in (a) and (b) correspond to exponential relaxation.

$$V^{-1} = \frac{c_0^2}{c_1^3}\log\left(1+\frac{c_1}{c_0}H\right) + \frac{H}{2c_1^2}\left(c_1 H - 2c_0\right) \tag{B.32}$$

Here, we enforced the condition $H(V \to \infty) = 0$, based on experimental observations. The coefficients c_0 and c_1 give the order of magnitude of the nondimensionalized chemical potentials in the network and the liquid tip. Introducing characteristic values yield $\mathcal{O}(c_0) \approx \mathcal{O}(c_1) \approx 10^{-2}$. Plotting H against V shows that the height, indeed, assumes finite values for speeds below the characteristic ridge growth time at zero speed, Fig. B.9.

Speed correlation and exponential relaxation

To compare our data with the presented models, we extract the characteristic scales (v^* and $h_{\text{sep},0}$) to rescale the data accordingly [per Eqs. (B.28) and (B.29)]. For this we consider the speed-correlation function $C(V)$ of the equilibrium height $h_{\text{sep},0}$ with the separation heights during drop sliding, $h_{\text{sep}}(v)$ with

$$C(V) = \frac{\operatorname{cov}\left(h_{\text{sep}}, h_{\text{sep},0}\right)}{\operatorname{cov}\left(h_{\text{sep},0}, h_{\text{sep},0}\right)}, \tag{B.33}$$

where cov is the covariance. The speed-correlation values at various V for our measured h_{sep} is plotted in Fig. B.9b. The correlation function shows exponential relaxation speed $V = 1$ ($v = v^*$). We express

$$C(V) \approx h_{\text{sep}}/h_{\text{sep},0} \approx e^{-V}. \tag{B.34}$$

Utilizing this trend for a speed-dependent relaxation of the tip height, we use the relation of

$$h_{\mathrm{sep}}(v) = h_{\mathrm{sep},0} e^{-v/v^*}, \tag{B.35}$$

with dimensional units. Comparing the exponential relaxation with Eq. (B.32) shows that the characteristic speed v^* and the equilibrium separation height $h_{\mathrm{sep},0}$ are reasonably recovered, Fig SB.9. This motivates the extraction [*via* fitting of Eq. (B.35)] of the effective mobility m^* and the separation height at zero speed $h_{\mathrm{sep},0}$ from our experimental data. To improve the quality of the fits, we introduce the parameter $\Delta h_{\mathrm{sep},0}$ to allow for non-zero relaxations at higher speeds

$$h_{\mathrm{sep}}(v) = h_{\mathrm{sep},0} - \Delta h_{\mathrm{sep},0} \left(1 - e^{-v/v^*}\right). \tag{B.36}$$

This parameter, however, is non-physical but artificial, stemming from an insufficient fitting range of the sliding speeds. When $h_{\mathrm{sep},0} \approx \Delta h_{\mathrm{sep},0}$, the speed range is sufficiently large. This criterion is met in our experiments, Tab. B.2.

Table B.2: Fitted parameters from regularized Eq. (4), main text. ϵ is the fitted root-square-mean error.

Q	$h_{\mathrm{sep},0}$ (μm)	$\epsilon[h_{\mathrm{sep},0}]$ (μm)	$\Delta h_{\mathrm{sep},0}$ (μm)	v^* μm/s	$\epsilon[v^*]$ μm/s
16.1	24.8	3.2	22.7	61.5	1.0
14.5	14.2	0.5	14.5	43.8	0.1
12.7	9.6	0.6	11.6	11.0	0.2
10.4	7.3	0.3	6.1	2.9	0.0
7.5	3.5	0.4	3.3	0.1	0.0

B.2 Adaptive Wetting of Polydimethylsiloxane

William SY Wong, Lukas Hauer, Abhinav Naga, Anke Kaltbeitzel, Philipp Baumli, Rüdiger Berger, Maria D 'Acunzi, Doris Vollmer, and Hans-Jürgen Butt, Langmuir 36, no. 26 (2020): 7236-7245.

Abstract

To better understand the wetting of cross-linked polydimethylsiloxane (PDMS), we measured advancing and receding contact angles of sessile water drops on cross-linked PDMS as a function of contact line velocity (up to 100 μm/s). Three types of samples were investigated: Pristine PDMS, PDMS where oligomers were removed by toluene treatment, and PDMS with an enriched concentration of oligomers. Depending on the velocity of advancing contact lines and the contact time with water, different modes of wetting were observed. One with a relatively low contact angle hysteresis ($\Delta\theta \approx 10°$) and one with a much larger hysteresis. We attribute the low hysteresis state, called the lubricated state, to the enrichment of free oligomers at the water-PDMS interface. The kinetics of the transition to the lubricated state can be described by adaptation theory. PDMS adapts to the presence of water by an enrichment of free oligomers at the interface and a correlated reduction in interfacial tension.

Introduction

The wetting of polydimethylsiloxane (PDMS) by water has been widely studied. One reason for this interest is the application of PDMS in e.g. household sanitary environment or as electric insulator. Though the material is hydrophobic with contact angles of the order of 90°, cross-linked PDMS can take up to ≈ 30 mM water in contact with water. Water molecules diffuse with a diffusion coefficient of 2.5×10^{-9} m^2/s which is of the same order of magnitude as the self-diffusion coefficient of water [1, 2]. Despite the fact that the wetting of PDMS has been studied intensely, reported advancing and receding contact angles vary significantly depending on the specific preparation, pretreatment, contact time with water and velocity of the advancing or receding contact lines. The aim of this paper is to better understand dynamic advancing, θ_a, and receding contact angles, θ_r, on cross-linked PDMS surfaces. How do θ_a and θ_r depend on the velocity of the advancing and receding contact line and how do the functions $\theta_a(v)$ and $\theta_r(v)$ adapt to the exposure to water?

In general, contact angles depend on how fast the contact line moves. The two most well-known descriptions of dynamic contact angles are the hydrodynamic and molecular dynamic theories [3–5]. Hydrodynamic models explain the velocity dependence of advancing contact angle by assuming that viscous dissipation caused by flow within the corner in front of the moving contact line dominates. The shear stress in the wetting ridge diverges upon approaching the contact line. This divergence can be circumvented by defining a lower cut-off length, typically of molecular size. In this microscopic regime, slip between the solid and liquid is allowed. Molecular kinetic theory assumes that the motion of the contact line is governed by the dynamics of the molecules in the close vicinity of the three-phase contact region, *i.e.*, the region where the surface, liquid and gas phases meet.3 The driving force for the contact line to move is an out-of-equilibrium surface tension; γ_{LV} $(\cos\theta^0 - \cos\theta)$ where γ_{LV} is the liquid-air interfacial tension, θ^0 the equilibrium and θ is the dynamic contact angle [6]. Thermally activated adsorption/desorption processes of the molecules occur at the advancing/receding side of a moving drop. The velocity dependent contact angles are modelled in terms of the "jumping" distance and frequency, two parameters depending on the system's inherent cohesive and adhesive forces [7]. Both hydrodynamic and MKT models are often able to reproduce measured dynamic contact angles [8]. However, the fitting parameters sometimes do not to fit realistic expectations, *i.e.*, the lower cut-off length can be far below one Angstrom or the jumping frequencies can be surprisingly high or low. In particular, both theories do not predict significant changes in contact angle for capillary numbers below 10^{-4} [6, 9–11]; the capillary number is the velocity of the contact line v multiplied with its viscosity and divided by the surface tension of the liquid, γ: $\mathrm{Ca} = \eta v/\gamma$. Lately, another model was proposed, taking into account a wetting-induced adaptation of surface energies, so-termed adaptive wetting [12]. In the case of cross-linked PDMS, there is already experimental evidence for adaptation. When PDMS is hydrophilized e.g. by exposing it to corona discharge or an oxidizing plasma, it recovers its hydrophocity when aging in air for few hours or days [13]. Aging in water does not recover hydrophobicity [2, 14]. This recovery is explained by the diffusion of residual silicone oligomers which are not cross-linked and which remain in the PDMS [15, 16].

Here, contact angles are measured optically while volumes of sessile drops were increased and decreased. The sessile drop method is the most common method to determine contact angles. As it turns out, the accessible contact line velocities are susceptible to adaptation of cross-linked PDMS to water. Instead of well-defined dynamic advancing and receding contact angles, PDMS shows two advancing angles at constant inflation rate and a minimum during receding, depending on the pre-exposure to water.

Methods

Synthesis of Test Surfaces

Three types of PDMS surfaces were studied. The PDMS was either used as prepared (pristine PDMS, still containing $4-5$ wt% free chains), “dry” (free chains were removed by washing with toluene and drying) or “lubricated” (adding 8 wt% free PDMS chains).

Pristine PDMS was prepared by crosslinked Sylgard 184 PDMS, mixed with a $1:10$ weight ratio (1 g : 10 g) of crosslinker-to-vinyldimethylsiloxane respectively, in a 20 ml vial stirred at ca. 60 rpm, for 2 minutes. The base (part A) contained dimethyl siloxane, dimethylvinyl terminated, dimethylvinylated and trimethylated silica, tetra(trimethoxysiloxy) silane, and ethyl benzene. Volatile organic content (VOC): 8 g/L. The curing agent (part B) contained dimethyl, methylhydrogen siloxane, dimethyl siloxane, dimethylvinyl terminated, dimethylvinylated and trimethylated silica, tetramethyl tetravinyl cyclotetra siloxane, and ethyl benzene. This is a 3-component system that includes a base, curing agent and a catalyst. The third component, which is part of the curing agent, comprises of a metal-centered catalyst that promotes crosslinking. This is a platinum complex which promotes a hydrosilylation reaction between the methylhydrogen siloxane and the terminal vinyl groups in the curing agent and the base formulation respectively [17]. 170 μm thick glass slides were rinsed with ethanol and exposed to an oxygen plasma (0.4 bars) for 5 minutes at 300 W (Femto, Diener Electronic, Germany). After spin-coating the crosslinker-vinyldimethylsiloxane mixture (1000 rounds/min for 60 s, ramped up in 15 s), samples were cured in a heated oven at 60 °C for 18 hours. The PDMS coatings had a thickness of ≈ 60 μm as measured by cross-section analysis in SEM. The magnification error of an SEM can range from $5-10\%$, and this reported thickness should be taken within an order of the reported magnitude.

Dry PDMS surfaces were obtained by soaking the as-prepared pristine PDMS samples in excess toluene (1 glass slide, 2×6 cm^2 at 60 μm thickness in 100 ml toluene) for 24 hours. Oligomers in the eluent were analyzed by chromatography; see below. The washed samples were then dried in vacuum at 1 mbar for 72 hours. The saturation vapor pressure of toluene is 37.5 mbar, and the lower-than-saturation pressure applied for an extended time should thus be sufficient for solvent extraction. The amount of free oligomers was determined by weighing samples before and after PDMS extraction. Free oligomers were extracted from within the PDMS matrix, accounting to between $4-5\%$ by weight.

Lubricated PDMS samples were prepared as pristine PDMS, except that we added 8 wt% unreactive PDMS oligomers ($M_w = 2000$ g/mol, $\nu = 20$ cSt, methyl-terminated, Aldrich) during the blending of crosslinkers and vinyldimethylsiloxane monomers. The molar mass of oligomers added was aligned to the molecular weight of the free oligomers in pristine PDMS, Figure B.16. The “dry” and “lubricated” PDMS surfaces serve as benchmarks for understanding the dry-to-lubricated adaptive nature of pristine PDMS.

Gel Permeation Chromatography

GPC experiments were performed using an Agilent Technologies 1260 instrument consisting of a pump, autosampler and column oven. As eluent, toluene was used. A column set consisting of 3 columns: SDV 106 Å, SDV 104 Åand SDV 500Å(PSS Standards Service GmbH, Mainz, Germany), all of 300 × 8 mm and 10 μm average particle size were used at a flow rate of 1.0 ml/min and a column temperature of 30 °C. The injection volume was 100 μl. Detection was accomplished with a RI detector (Agilent Technologies). In order to reproduce the measurement each sample was injected twice. Data acquisition and evaluation was performed using PSS WINGPC UniChrom (PSS Polymer Standards Service GmbH, Mainz, Germany). Calibration was carried out by using the universal calibration method with polystyrene standards provided by PSS Polymer Standards Service GmbH (Mainz, Germany) and the Mark-Houwink coefficients for PDMS in toluene.

Wetting and Contact Angle Analysis

Dynamic contact angle measurements were performed in the sessile drop configuration under variable volumetric flow rates. Fitting of dynamic contact angles and contact line displacements were performed using the automated program provided by the manufacturer: SCA20, Dataphysics. We have made use of the “Sessile Drop - Needle In Algorithm”, with dynamic contact angles fitted via an ellipse. The ellipse-fitting method was chosen due to its accuracy in determining contact angles within our operating range (90° to 120°) and drop volume (5 to 25 μl). All data (including controls) were analyzed using this method for consistency. Readers should be aware of potential differences in measured contact angles with the use of different fitting methods (ellipse, tangent, Young-Laplace etc.) in order to avoid misinterpretation [18–21]. To ensure defined flow rates, a homebuilt nanometric pump was specifically designed, with a range of flow rates between 50 nL/s and 2 μl/s (Methods, Supporting Information). We inserted a bent needle (fluoro-treated) from the back of the drop to minimize needle induced asymmetric distortions of the drop shape during inflating or deflating [22]. As a result, the left and right contact angles perfectly overlaid. The repeatability of the experiments was verified at least 3 times on independent experiments, with two contact angles measured during each run (6 data measurements per graph). Errors in measurements typically fall within ±1° and are smaller than the symbol sizes in the figures. All experiments were performed with an initial drop size of ca. 2.5 μl; we chose a minimal starting volume to avoid evaporation effects between drop formation and start of the inflation. The initial 0.5 μl needed to reach 3.0 μl allows the drop to achieve its maximum dynamic advancing contact angle. Typically, we truncated all graphs from 3.0 μl onwards to remove the minute differences that were induced by human inputs from 2.5 μl to 3.0 μl.

Velocity and displacement analysis

At this junction, it is instructive to discuss how the contact line velocity is related to the flow rate. As the volume of the drop was increased/decreased at a constant volumetric rate, ($\dot{V}$), the contact line velocity, v, was not constant. At constant contact angle it scales with $v \sim V^{-2/3}\dot{V}$. When increasing/decreasing the drop volume, the contact line velocity decreases/increases (Figure B.17). Deviations from this scaling are caused by changes in contact angle. Experimentally, the velocities determined were based on actual video-measurements. We are able to automatically measure the displacement of the contact line based on the videos, which can then be step-wise evaluated as velocity-volume plots. A range of absolute v do exist throughout the entire inflation-deflation cycle. However, we chose to evaluate averages, $\bar{v}$ selected over both advancing and receding segments of the contact line velocity profiles. These were abstracted while considering 1) Similar drop volumes, 2) Excluding sharp velocity fluctuations and 3) Averages over at least 3 μl. The mean contact line velocity $\bar{v}$ was determined by averaging the advancing ($<$ 500 nL/s) or receding ($\geq$ 500 nL/s) velocities in the velocity-volume graphs (without jumps in velocity that are induced by contact angle variations). Error bars presented in average contact line velocity represent deviations within one inflation-deflation cycle. Notably, $\bar{v}$ did not change significantly between inflating and deflating unless the contact line was temporally pinned.

In this work, the key variable is either more appropriately represented as velocity or displacement. A displacement analysis experiences lesser noise, but the former is integrated better into the adaptive wetting equations that we will later describe. In addition, volume, as presented is one typical representation in these dynamic contact angle measurements. The contact-angle/volume and contact-angle/velocity-displacement data will be presented in either the main manuscript or the supporting information. These are the experimentally accessible datasets. To convert these into an improved intuition for contact time, we convert these to contact line velocities.

Results and Discussion

Dry and Lubricated PDMS

Dry and lubricated PDMS represent the two limiting cases. On a dry PDMS surface (Figure B.10a, red squares), the advancing contact angle observed during inflation is $\theta_a = 119 - 120°$ (dashed red line) at a slow volumetric inflation-deflation (50 nL/s). During deflation, the contact line was pinned. As a result, the contact angle dropped continuously until a volume of 4 μl was reached. After depinning, the contact angle decreased with a reduced slope and reached a value of 87° at a volume of 3 μl. On a lubricated PDMS surface (Figure B.10a, yellow circles), the contact line advanced at a lower angle (θ_a110°). When decreasing the volume of the water drop, the contact line first pinned. The contact angle linearly decreased until it reached 104° (dashed yellow line). Decreasing the volume even further, the contact line depinned and receded at a constant contact angle of $\theta_r = 104°$ at ≈ 7.5 μl. Then, θ_r only slightly decreased until it reached a value of $\theta_r = 101°$ at a volume of 43 μl.

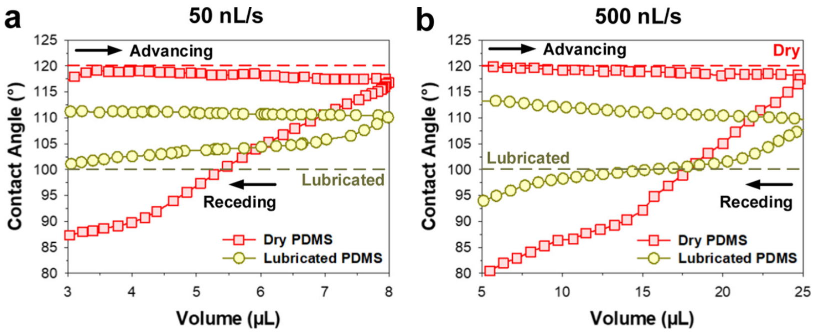

Figure B.10: Contact angle of water on dry and lubricated PDMS at low and high contact line velocity. a) Contact angles measured at low flow rates (50 nL/s correspond to an average contact line velocity of $3 - 4$ μm/s). b) Contact angles observed at high flow rates (500 nL/s correspond to an average contact line velocity of 30 μm/s). Three separate readings were taken; only representative curves are presented for clarity. The standard errors are typically around 1° between repeat experiments performed on the same day. The 60 μm thick PDMS films were fabricated on 170 μm glass cover slips.

Contact angle hysteresis, $\theta = \theta_a - \theta_r$ on the lubricated PDMS, $\Delta\theta_L = 10° \pm 1°$ was much lower than on dry PDMS $\Delta\theta_D = 32° \pm 3°$. We attribute the reduced contact angle hysteresis to an enrichment of oligomers near the PDMS/water interface. The presence of excess liquid oligomers leads to lower contact angle hysteresis, as expected of a highly mobile liquid-like interface [23]. In contrast to the lubricated state on slippery liquid-infused porous surfaces (SLIPS) [24], no free layer (> 100 nm) of lubricant exists on PDMS (Figure B.18). They are primarily soft elastomeric surfaces that experiences a reorganization of surface chemistry (and energy) upon wetting. The reason for slight change in the receding contact angle of the lubricated PDMS is less clear and we can only speculate.

To observe dynamic changes of contact angles at higher flow rates (500 nL/s vs. 50 nL/s), we needed to increase the maximum drop volume from 8 μl to 25 μl to expand the domain of observation. On dry and lubricated PDMS (Figure B.10b), the wetting behaviors were qualitatively similar to the ones observed at slower inflation/deflation rates. Dry PDMS showed an advancing plateau θ_a of $119 - 120°$ (dashed red line). While deflating, the contact angle decreased linearly until the contact line depinned at $V = 15$ μl, $\theta_r = 90°$. Continuing to decrease the volume resulted in a further decrease of the contact angle, though with a lower slope. On lubricated PDMS, the advancing contact angle θ_a slightly decreased from 112° to 110° when increasing the volume to 25 μl. Then the contact line was pinned until the volume was decreased to $\theta_r \approx 20$ μl. Between 20 μl and 10 μl the receding angle was $\theta_r \approx 100°$.Again, contact angle hysteresis was greatly reduced on lubricated PDMS, indicative of the presence of a mobile liquid-like interface. Thus, advancing and receding contact angles on dry PDMS is qualitatively similar irrespective on contact line velocity. The same holds for lubricated PDMS.

Pristine PDMS

At low inflation rate (50 nL/s), the contact line begins to advance at an angle $\theta_a = 119°$ (Figure B.11a). However, it decreased to $\theta_a = 113°$ when the drop volume exceeded 4 μl and stayed almost constant up to the maximum volume of 8 μl. The transition between both plateaus was accompanied by a non-monotonous change of the contact line velocity (Figure B.19, Figure B.11c,e). The contact line velocity increased from approximately 4 μm/s to 6 μm/s during the transition followed by a decrease to 3.2 ± 0.4 μm/s. The presence of the transition does not depend on the initial drop size. We interpret the changes in θ_a from 119 to 113° by a reorganization and migration of oligomers from the pristine PDMS matrix to the solid-liquid interface. Notably, pristine PDMS contains a significant concentration of free oligomers (measured here at $4 - 5$ % by weight), in alignment with previous investigations [25, 26]. Upon wetting of the PDMS with water, the interface adapts from a dry to a lubricated state. This is evident from the decreasing contact angle hysteresis after the transitions, which hints of liquid-like surface lubrication (Figure B.10). During wetting adaptation, the migration of oligomers is sufficiently fast to influence the contact line during its advancing motion. Thus, the moving contact line first interacts with a “dry state” before later interacting with a “lubricated-state”.

This “lubricated-state” persists throughout the receding cycle. After expanding the drop to 8 μl, the volume was decreased at the same rate of 50 nL/s. The linear decrease of the contact angle before reaching a volume of 6.6 μl was due to contact line pinning (Movie M1). The contact line then started to move at an almost constant contact angle of 105°. Such a high receding contact angle is interpreted as the presence of a “lubricated-state” (Figure B.10). This hints that the PDMS surface dynamically adapts to the presence of the water drop. This adaptation accounts for the transition

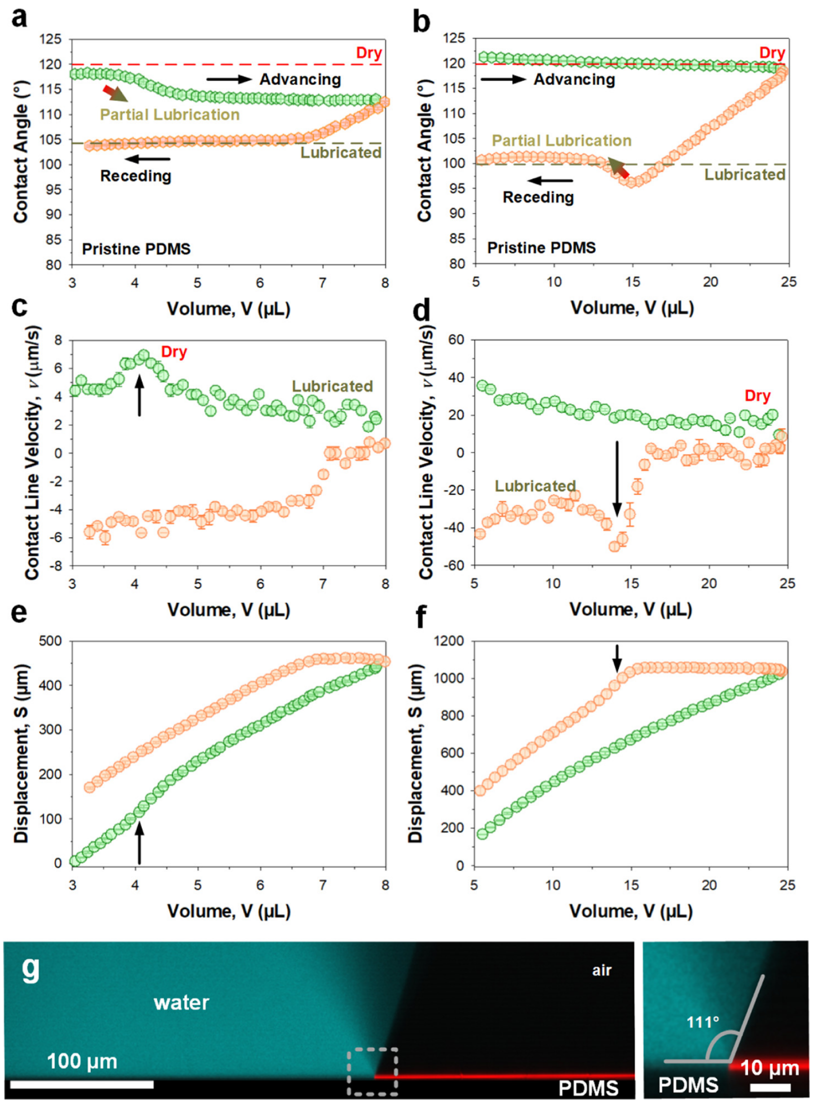

Figure B.11: Contact angle of water on pristine PDMS at low and high contact line velocity. a) Contact angle measured for a low flow rate (50 nL/s, corresponding to an average contact line velocity of 4 μm/s). b) Contact angles measured at high flow rates (500 nL/s, average contact line velocity of 30 μm/s). Whereas the advancing contact angles almost remain constant, the receding angles pass through a minimum. c,d) Contact line velocities during drop inflation-deflation experiments for flow rates of 50 and 500 nL/s, respectively. These contact line velocities are derivatives of the video-captured contact line displacements, which were recorded at low (e, 50 nL/s) and high (f, 500 nL/s) flow rates of drop inflation (green) and deflation (orange). Green symbols – Advancing cycle. Orange symbols – Receding cycle. g) Confocal microscopy imaging (XZ plane) of a liquid drop of water, cyan (dyed with ATTO 488, 10 μg/ml) on PDMS with a magnified inset. Reflection signal colored in red.

between a higher dry θ_a of $119-120°$ to a lower lubricated θ_a of 113° as observed in Figure B.11a,c,e. Thereafter, the drop recedes on a lubricated state. Pristine PDMS shows a different behavior at a high inflation rate (500 nL/s), corresponding to high mean contact line velocity ($\bar{v} = 30$ μm/s). Throughout the entire volumetric expansion, θ_a remained high at $119-120°$ (Figure B.11b,d,f), similar to the dry state, Figure B.10. On the receding part, the contact angles resemble those of water in contact with dry PDMS until a volume of 15 μl, reaching a minimum contact angle of 95°. This was followed by a rise in receded θ_r that plateaus at 100°, akin to lubricated PDMS, Figure B.10. This close matching of the respective contact angles for pristine PDMS (Figure B.11) with those for dry PDMS (Figure B.10) hints that the surface remained in its dry state during inflation and during the initial receding phase. After the drop volume decreased below 15 μl, the drop experienced a lubricated surface. Despite the evidence of so-termed "lubrication", these surfaces should not be confused with standard SLIPS surfaces as no visible wetting ridges (up to 1 μm in resolution) can be discerned (Figure B.11g).

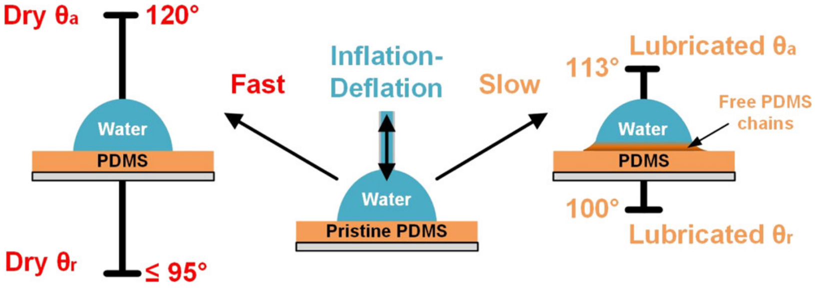

Figure B.12: Sketch of dependence of the contact angle of pristine PDMS on the inflation/deflation rate. At high inflation/deflation rates (> 500 nL/s), the advancing (θ_a) / receding (θ_r) contact angles resemble those on PDMS not containing free oligomers (dry). At low inflation/deflation rates, the advancing/receding contact angles resemble those on lubricated PDMS (free PDMS chains are not to scale).

At high deflation rates, depinning is characteristically accompanied by a peak in the contact line velocity (Figure B.11d) caused by pinning. The peak increases with the flow rate, most likely due to the reduced time to adapt and transition to the lubricated state. Thus, pristine PDMS displays both wetting states within a single measurement cycle. In summary, for low inflation rates (Figure B.11a,c,e) a sufficient amount of oligomers have a chance to migrate towards the PDMS/water interface, which leads to lubrication during the inflation cycle (starting at ≈ 4.5 μl). For high flow rates (Figure B.11b,d,f) the contact line advances and recedes quickly ($\bar{v} = 30$ μm/s), which leads to lubrication only during the receding part (starting at 15 μl). The occurrence of lubrication is time- and contact- dependent. Therefore: depending on the relative contact line velocity, the lubrication transition can occur within either the advancing/receding cycle. Therefore, we have a dry state with $\theta_a = 120°$, $\theta_r \leq 95°$ and a lubricated state with $\theta_a = 113°$, $\theta_r \approx 100°$ (Figure B.12).

In the PDMS represented in Figure B.12, we schematized the lubricated state (not to scale). PDMS represents an organogel that is partially infused with oligomers, though at low concentration. The concentration of the oligomers in the pristine state is homogenous, but can be enriched at the interface during wetting.

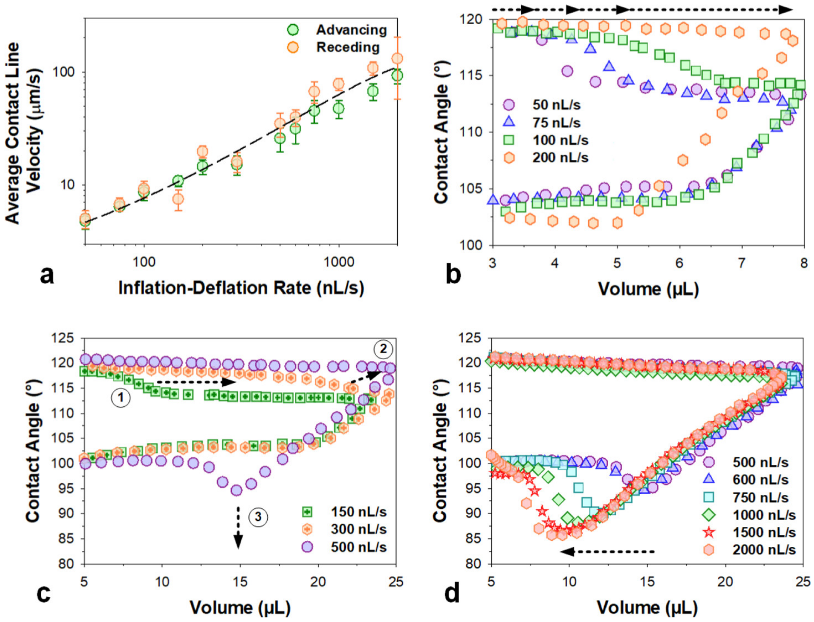

Figure B.13: Influence of contact line velocity (inflation/deflation rate) on dynamic wetting. a) Inflation-deflation rate $\dot{V}$ was used to directly control contact line velocity of the moving drop. The dashed line serves as a guide to the eye. b) Contact angles measured at flow rates of 50, 75, 100, and 200 nL/s. c) Increasing the maximal drop volume to 25 μl enabled observation of the spatial transitions within the advancing cycle up to a flow rate of 300 nL/s. A receding peak showed up at 500 nL/s. d) At 500, 1000, 1500, and 2000 nL/s, the receding peak occurred at receded drop volumes of 15, 12, 10, and 8 μl respectively.

Conditions for Adaptation-Induced Lubrication

In the following, we focus on pristine PDMS surfaces in order to provide a deeper insight towards its adaptation. By increasing the flow rate from 50 nL/s to 200 nL/s, the average contact line velocity increased from $\bar{v} = 4 \pm 1$ up to $\bar{v} = 14 \pm 2$ μm/s (Figure B.13a-b, Figure B.19). In all cases, an initial wetting plateau occured at $\approx 119 - 120°$. Then the advancing contact angle decreased to a value of $\approx 114°$, corresponding to the lubricated state. The end of the plateau is shifted to larger volumes with increasing flow rate. For a flow rate of 200 nL/s, this shift occurs at above 8 μl. At initial contact line velocities of $\gg 10$ μm/s, the contact line seems to advance faster than the rate at which the lubrication layer forms (Figure B.19). Here, the contact line advances only over the dry state. The receding contact angle plateaued between 104° (50 nL/s) and 102° (200 nL/s). Thus, before the contact line recedes, the surface is able to adapt. Thus, the contact line recedes through the lubricated state with a θ_r plateau at $\approx 103°$.

When we further increased the flow rate from 150 to 300 nL/s (and the observable drop volume to 25 μl), corresponding to $\bar{v} = 11 \pm 1$ to 15 ± 3 μm/s, the transition to the lubricated state in the advancing parts is even shifted to higher volumes (Figure B.13c, green squares and orange hexagons). We propose that, at higher inflation rates of 500 nL/s and higher, the contact line advances faster than the rate at which the lubrication layer can form. The hypothesis is further supported by the observation that at even higher contact line velocities, (Figure B.13d, 500 nL/s, $\bar{v} > 20\ \mu$m/s), no lubricated state was detected anymore during contact line advancement (Figure B.13d and Figure B.20). In fact, the surface does not completely adapt before commencing the receding cycle. Therefore, the drop begins to recede within its dry state. In contrast to flow rates up to 300 nL/s, where contact lines receded at contact angles of $101-104°$ ($V = 5\ \mu$l) in the lubricated state, the receding contact angle was initially pinned (Figure B.13c). The pinning delay is characteristic of a dry state interaction. Only after reaching a drop volume of 15 $\mu l, atapproximately 30-35 s of interaction and a contact angle of 95^\circ$ did the contact line depin. The receding cycle then continues in the lubricated state. θ_r rises and plateaus at 100°. This minimum in the receding contact angle persists throughout increments in volumetric flow rates and contact line velocities (Figure B.13d and Figure B.20). We tested it by varying $\dot{V}$ between 500 and 2000 nL/s for maximum drop volumes of 25 μl. When increasing the flow rate further, the receding contact angle follows the “dry” graph (Figure B.10) to even lower drop volumes (Figure B.13d) before the contact line started to move. For $\dot{V} = 2000$ nL/s the minimum of $\theta_r = 85°$ was reached at a volume as low as 10 μl. A continuously decreasing minimum was observed before finally rising to form the stable, lubricated 100° plateau (Figure B.13d). This transition was accompanied by an increase in contact line velocity (Figure B.20-6, Movie M2).

At our maximum inflation-deflation rate of 2000 nL/s, a second effect was observed: the receding contact angle increased from a final 97° to 101° in the last stages of deflation between $V = 7$ and 5 μl. This phenomenon was observed in all experiments, also on both sides of the symmetrical drop. We speculate that the flow rate is so high that the retracted drop still experiences elastic stress on its PDMS-water interface after the rapid retraction (almost 300 μm/s, Figure B.20). At this point, we would like to mention that the motion observed here is different to the stick-slip motion observed on very soft PDMS (Static shear modulus $G = 265$ Pa [27] vs 0.62 MPa here) before [28].

Pre-wetting and Formation of Lubrication Layer

This velocity-dependent change in contact angle raises two questions: Do oligomers cloak the water drop and reduce surface tension of water? Does the enrichment of free oligomers (lubricant) at the water-PDMS interface change the interfacial tension?

Three experiments were carried out to elucidate the presence of free PDMS at the water-air and the water-PDMS interface.

- To find out if oligomers adsorb to the water-air interface and reduce the surface tension of water, inflation-deflation cycles were measured with a single drop and re-used and re-deposited (up to 8 μl) over three separate spots on a pristine PDMS surface (Figure B.14a). The measurements fall on top of each other. Throughout all three cycles, the dry- (119°, dashed red line) and lubricated- (113°) states were present. Thus, no surface-active substance cloaks the test drop.

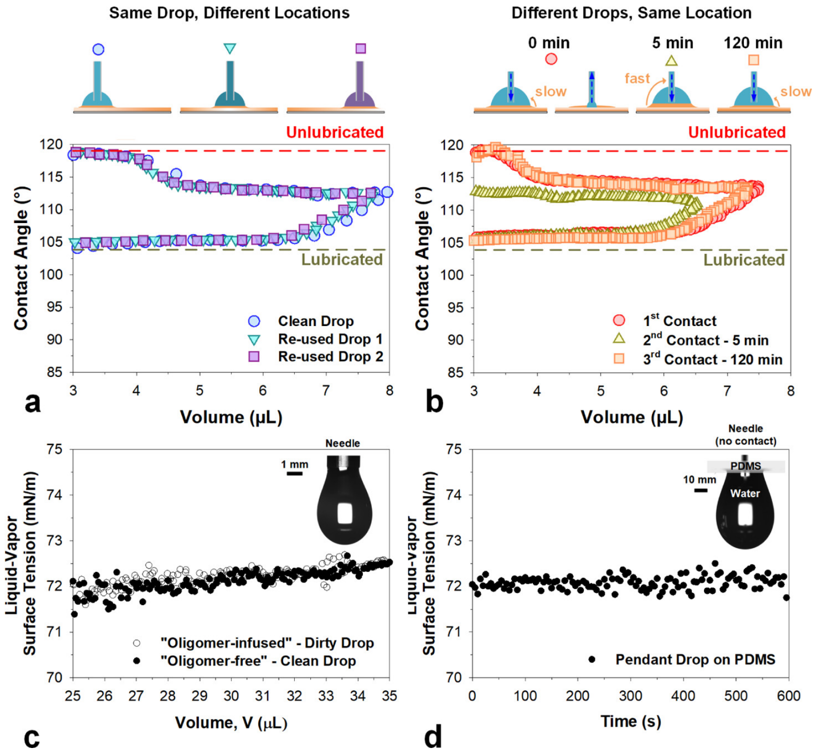

Figure B.14: Lubrication layer formation on pristine PDMS. a) The repeated use of a single drop over 3 cycles on fresh locations (circle, triangle and square) results in identical values for the contact angle during inflation and deflation. Flow rate: 50 nL/s. b) Water was inflated and successively deflated at an identical drop location. Time between measurements: 5 min between the first (circles) and second (triangle) measurement. 120 min between the second and third (square) measurement. Flow rate: 50 nL/s. The maximal volume decrease in the second cycle is attributed to evaporation losses ($1 - 2$ μl) during the waiting time (5 min). 120 min between the second and third (square) measurement. Flow rate: 50 nL/s. The first and third cycles are aligned for representation. c) A pendant drop of water was first tested up to 35 μl (Oligomer-free, clean) using the dynamic surface tension measurement technique. The same drop was deposited onto a PDMS surface for 2 minutes before being re-measured (Oligomer-infused, dirty). d) An alternate dynamic measurement of a pendant drop (directly on PDMS) was used to gauge if surface tension changes over a period of 10 minutes. Drops in a) and b) were removed and deposited using a hydrophobized needle nozzle. No sliding of the drop on the substrate took place. Every drop was cleanly (macroscopically) removed from the test surface between measurements. In c) and d), the drops were kept on the surfaces throughout the experiment.

- To gain further insight into the formation and decay of the lubricated state, we placed fresh water drops on a specific spot on pristine PDMS (Figure B.14b). The first inflation/deflation cycle revealed the normal dry-to-lubricated transition (Figure B.14b, red circles). Then the drop was removed. A second fresh drop was placed at the same spot after 5 min. The second cycle only showed the lubricated plateau (Figure B.14b, yellow triangles). The presence of the water drop enriches oligomers at the interface during contact [24, 29, 30]. This lubrication layer does not depart with the water drop during deflation. When, however, waiting for 120 min before placing the next drop, a third cycle demonstrated full dry-to-lubricated transition and a recovered dry state (Figure B.14b, orange squares). This indicates that oligomers slowly diffuse back into the polymer matrix when exposed to an ambient environment, thus going back to the dry state.

- This result was verified using a modified pendant drop measurement. A drop of water (30 μl) was deposited upside down on a pristine PDMS surface. The drop shape, hence surface tension was continuously measured over 10 min and the shape was evaluated using the Laplace equation. The surface tension did not change from its initial $72-73$ mN/m (Figure B.14c,d) over this entire duration.

Why does the presence of water enrich oligomers at the solid-liquid interface? The migration of oligomers towards the water-PDMS interface can arise because of two effects. First, a mechanical stress exerted at the contact line balancing the surface tension of the liquid, inducing an effective under-pressure [31] and sucking up oligomers. Second, it is energetically favorable for oligomers to enrich at the water-PDMS interface. The first is a contact line effect while the second is a contact area effect.

For the contact line effect: Forces exerted by the liquid contact line on the solid have a normal component of $\gamma_{LV} \sin\theta^0$, where θ^0 is the actual contact angle. For a θ^0 of 90°, this represents a force per unit line of $72-73$ mN/m [32]. Assuming that the force is distributed over an effective width of 10 nm [33], the force per unit area exerted on the PDMS underneath is 7.2 MPa. As the contact line moves over PDMS, it is hypothesized to pull out oligomers during travel. As a first approximation, the amount of liquid oligomer extracted from the PDMS matrix at a given position is inversely proportional to the contact line velocity.

One key explanation for the decreasing advancing contact angle upon adaptation is a spontaneous enrichment of oligomers at the water-PDMS interface. Such an enrichment is likely, considering that unreacted end-groups of pristine PDMS are composed of asymmetrical $C = C$ bonds with CH_2 tails. Such differently terminated PDMS oligomers of varying chain lengths may possess different effective surface energies under specific orientation [34]. Shorter chain lengths also experience greater influence from terminal groups. Thus, if oligomers saturate at the interface, they can form a PDMS surface with lower interfacial tension ($\gamma_{SL}^{\mathrm{lub}}$) during wetting-induced lubrication. During this reversible enrichment process (also termed adaptation), we observe 2 distinct timescales: 1) adaptation time and 2) relaxation time. The relaxation time needed for returning to its original pristine state far exceeds the adaptation time (typically by 2 orders of magnitude). The coexistence of 2 timescales hints strongly at the occurrence of adaptation instead of mechanically-driven viscoelastic dissipation which is governed by only one response time [35]. Essentially, these observations cannot be explained by a viscoelastic energy dissipation in the PDMS alone, because the viscoelastic properties of the PDMS do not depend on the presence of water.

Wetting Adaptation Theory

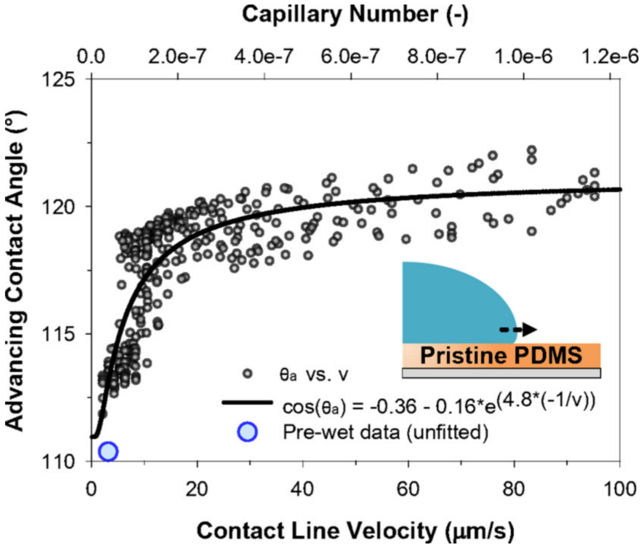

Figure B.15: Advancing contact angle versus mean contact line velocity measured for water on pristine PDMS. Experimental contact angles (symbols) were fitted with equation (4). An experiment involving a pre-wetted spot (unfitted) is highlighted as a blue, marked data point for reference. Fits were achieved using all individually measured contact line velocities and contact angles collated from experimental data. The advancing adaptation velocities, v_{SL} is 4.7 μm/s. For reference, the capillary number has been included in the alternate x-axis.

To check whether dynamic contact angles can be described by the adaptive wetting model, data obtained from instantaneous velocity - and - dynamic advancing contact angles were fitted [12]. The adaptation model is based on the assumption that surfaces spontaneously change their material properties under the presence of wetting liquids [4, 6, 8, 36, 37], giving rise to variations in interfacial tensions. These changes in interfacial chemistry influence the dynamics of contact lines and thus the dependence of the contact angles on velocity. As a first approach, wetting adaptation can be treated by first order kinetics: $\gamma_i = \gamma_i^{\infty} + \Delta\gamma_i e^{-t/\tau_i}$. γ_i stands for the respective liquid-solid γ_LS, solid-vapor γ_{SV} and liquid-air γ_L interfacial tension [12]. τ_i is the characteristic relaxation time of the adaptive process. This implies exponentially relaxing interfacial tensions [12]. Implementing the adapted interfacial tensions into Young's equation $\gamma_{LV} \cos\theta = \gamma_{SV} - \gamma_{SL}$ gives rise to velocity-dependent advancing (θ_a) and receding contact angles (θ_r).

We fitted our entire dataset of advancing contact angles vs. contact line velocities. Advancing (θ_a) contact angles and the corresponding instantaneous contact line velocities (v_a) were determined from dynamic wetting experiments. From the advancing curves, local contact line velocities were taken from the entire contact angle domain (plateaus and transitions). The experimental data set consists of θ_a of $110 - 123°$ and a respective instantaneous advancing velocities v_a of $3 - 100$ μm/s (Figure B.15). When water is in contact with PDMS, the instantaneous interfacial tension is denoted by $\gamma_{SL}(t)$. We assume that water contact enriches oligomers at the interface, thus decreasing interfacial tension to a new equilibrium value γ_{SL}^{∞}. Assuming first order kinetics this relaxation can be described by:

$$\gamma_{SL}(t) = \gamma_{SL}^{\infty} - \Delta\gamma_{SL} e^{-t/\tau_{SL}}. \tag{B.37}$$

Here, τ_{SL} characterizes the adaptation time for the enrichment of oligomers at the interface. $\Delta\gamma_{SL} = \gamma_{SL}^{0} - \gamma_{SL}^{\infty}$ is the change of the solid-liquid interfacial energy. In the case of wetting-induced lubrication, it can also be represented as $\Delta\gamma_{SL} = \gamma_{SL}^{\text{dry}} - \gamma_{SL}^{\text{lub}}$. The force balance leading to Young's equation is relevant only for a width l_{SL} around the contact line (also called peripheral length). Thus, the relevant interfacial tension can be expressed as:

$$\gamma_{SL}(v) = \gamma_{SL}^{\infty} - \Delta\gamma_{SL} e^{-v_{SL}/v}. \tag{B.38}$$

Here, v is the actual contact line velocity while $v_{SL} = l_{SL}/\tau_{SL}$ characterizes the adaptation velocity of the solid-liquid interface. The characteristic adaptation velocity, v_{SL}, represents the critical contact line velocity needed for transitioning from the dry- to the lubricated- states. During infinitely slow steady state advancement of the contact line, Young's equation is:

$$\gamma_{LV}^{\infty} \cos\theta_a^{\infty} = \gamma_{SV}^{\infty} - \gamma_{SL}^{\infty}. \tag{B.39}$$

To consider adaptation, we replace γ_{SL}^{∞} by the actual interfacial tension given by expression (B.38). This leads to an expression for the velocity dependent advancing contact angle θ_a:

$$\cos\theta_a = \cos\theta_a^{\infty} - \frac{\Delta\gamma_{SL}}{\gamma_{LV}^{\infty}} e^{-v_{SL}/v}. \tag{B.40}$$

Experimental advancing contact angles could be fitted with equation (B.40), as outlined in Figure B.15. We fitted Eq (B.40), assuming that $\theta_a^{\infty} = 110°$, *i.e.*, $\cos\theta_a^{\infty} = -0.36$. Both datasets containing averaged and instantaneous contact line velocities were analyzed. For the interfacial tension of water, we used γ_{LV}^{∞} is 72 mN/m. This allows us to obtain the adaptation velocity $v_{SL} = 4.7$ μm/s and the adaptation induced change of the PDMS-water interfacial tension, $\Delta\gamma_{SL} = +11.5 \pm 1.0$ mN/m. The obtained adaptation velocity is close to what we estimated from the contact line velocities at low inflation velocities in Figure B.11. If the contact line velocity is significantly faster than 4.7 μm/s (≥ 200 nL/s at > 10 μm/s), adaptation is too slow and the contact line advances in its unadapted state. An adaptation velocity of 4.7 μm/s corresponds to an adaptation time of $\tau_{SL} = 2.1$ ms, assuming an adaptation length of $l_{SL} = 10$ nm. Assuming an adaptation length of $l_{SL} = 100$ nm leads to an adaptation time of $\tau_{SL} = 21$ ms. It could be speculated whether diffusion of water into the PDMS bulk cause wetting adaptation. However, the fast diffusion of water in PDMS, 2×10^{-9} m^2/s, should result in adaptation times within a few nanoseconds, *i.e.*, a few orders of magnitude faster than what is observed experimentally. The value of the adaptation velocity may thus depend sensitively on the concentration and size of remaining oligomers in the PDMS matrix. Thus is likely to depend on the preparation and history of the sample.

In the adaptation model, contact with a wetting drop induces exponential relaxation of interfacial tension (solid-liquid). During receding, we should have an analogous effect. The "solid" adaptation velocity v_S may be different from the "solid-liquid" adaptation velocity v_{SL}. However, because of contact line pinning, it is unclear whether the high contact line velocities after depinning are caused by adaptation, by slip or by a combination of both. Therefore, we did not fit data from the receding curves. To check whether dynamic contact angles can be also described by conventional hydrodynamic (Cox-Voinov) and molecular-kinetic (MKT) models, we fitted our data sets using both theories. As far as we know, hydrodynamic theory cannot account for the wetting-induced lubrication transition. For instance, fitting our data with the Cox-Voinov model results in invalid values as it is typically utilized for high capillary numbers (Supporting Information, Figure B.22).4,5 We also tested our results against molecular kinetic theory [38, 39], yielding values under a comparatively poor fit for the friction coefficient of 74 μNs/mm^2. With an assumed hopping distance of 1 nm, the hopping frequency is 55 kHz (Supporting Information, Figure B.23). An alternative recently proposed by Perrin et. al. described a unified model including both hydrodynamics and thermal activation over defects [40, 41]. The main difference between adaptive wetting and the approach in Perrin et al. lies in the understanding of defects. Perrin et al. assume that the defects do not change in course of the experiment and can be characterized by their height, width, distance and strength [40]. These parameters do not change due to the presence or absence of water. In contrast, adaptive wetting assumes that the substrate can change due to contact with the drop [12]. This implies that the presence of the sessile drop changes the height, width, distance and strength of a defect. Perrin's model was fitted over 4 parameters, and provided the fit parameters of a transitional capillary number of 1.7×10^{-6}, a defect spacing of 1 nm and a static contact angle of 125° (Supporting Information, Figure B.24). So far, these models were unable to provide reasonable results (physicality) for describing wetting-induced lubrication.

Conclusions

To describe wetting of pristine PDMS by water one needs to consider that the surface adapts. Dynamic advancing contact angles depend on velocity of the contact line. Receding contact angles depend on the time the surface had been in contact with water. For PDMS, results indicate that adaptation of the solid-liquid interface is caused by trapped oligomers in the polymer matrix that were pulled out from the PDMS matrix. The oligomers induce a reversible transformation from the dry to the lubricated wetting state. After the drop is removed, the oligomers slowly (several minutes) diffuse back into the bulk phase. This long residence time of oligomers would also explain why previous experiments were often difficult to interpret: Measured contact angles depend on the history of a sample. This scenario should be generic, *i.e.*, holds for all surfaces containing mobile molecules or containing dangling ends, particularly for soft polymeric solids. The presence of oligomers at the interface results in the formation of a PDMS surface with a net lower surface tension. Wetting adaptation may thus unveil previously unknown contributions to changes in dynamic contact angles and contact line hysteresis on chemically- and topologically- homogenous ideal surfaces.

Author Contributions

W.S.Y.W. and M.D. fabricated the surfaces. W.S.Y.W carried out the experiments and characterization unless otherwise stated below and wrote the manuscript. L.H and W.S.Y.W analyzed the system analytically to understand the phenomenon. A.N and A.K helped with data interpretation and confocal microscopy. W.S.Y.W., D.V. and H.J.B contributed to experimental planning, data analysis, and manuscript preparation. All authors reviewed and approved the manuscript.

Acknowledgements

This work was supported by the European Union's Horizon 2020 research and innovation program LubISS No. 722497 (W.W., A.N., P.B., D.V.), the ERC Advanced Grant No. 340391 "SUPRO" (H.-J.B., D.V.), the German Research Foundation (DFG, SPP2171: D.V., L.H., H.-J.B.) with the Collaborative Research Center 1194 (H.-J.B.). We thank A. Sharifi for technical support and F. Geyer, K. Hegner, H. Teisala, A. Saal, A. Stetten and especially S. Silge for stimulating discussions.

References

1. Barrie, J. A. & Machin, D. The Sorption and Diffusion of Water in Silicone Rubbers: Part I. Unfilled Rubbers. *J. Macromol. Sci. Phys.* **3,** 645–672. ISSN: 0022-2348, 1525-609X (Dec. 1969).
2. Watson, J. & Baron, M. The Behaviour of Water in Poly(Dimethylsiloxane). *J. Membr. Sci.* **110,** 47–57. ISSN: 03767388 (Feb. 1996).
3. Blake, T. D. The Physics of Moving Wetting Lines. *J. Colloid Interface Sci.* **299,** 1–13. ISSN: 0021-9797 (July 2006).
4. Snoeijer, J. H. & Andreotti, B. Moving Contact Lines: Scales, Regimes, and Dynamical Transitions. *Annu. Rev. Fluid Mech.* **45,** 269–292. ISSN: 0066-4189 (Jan. 2013).
5. Voinov, O. V. Hydrodynamics of Wetting. *Fluid Dyn.* **11,** 714–721. ISSN: 0015-4628, 1573-8507 (1977).
6. Blake, T. D. Forced Wetting of a Reactive Surface. *Adv. Colloid Interface Sci.* **179–182,** 22–28. ISSN: 0001-8686 (2012/11/01/).
7. Blake, T. D. & De Coninck, J. Dynamics of Wetting and Kramers' Theory. *Eur. Phys. J. Spec. Top.* **197,** 249–264. ISSN: 1951-6355, 1951-6401 (Aug. 2011).
8. Le Grand, N., Daerr, A. & Limat, L. Shape and Motion of Drops Sliding down an Inclined Plane. *J. Fluid Mech.* **541,** 293–315. ISSN: 0022-1120 (Oct. 2005).
9. Henrich, F. *et al.* Influence of Surfactants in Forced Dynamic Dewetting. *Soft Matter* **12,** 7782–7791. ISSN: 1744-683X, 1744-6848 (2016).

10. Petrov, J. G., Ralston, J., Schneemilch, M. & Hayes, R. A. Dynamics of Partial Wetting and Dewetting in Well-Defined Systems. *J. Phys. Chem. B* **107,** 1634–1645. ISSN: 1520-6106 (Feb. 2003).

11. Ralston, J., Popescu, M. & Sedev, R. Dynamics of Wetting from an Experimental Point of View. *Annu. Rev. Mater. Res.* **38,** 23–43. ISSN: 1531-7331 (Aug. 2008).

12. Butt, H.-J., Berger, R., Steffen, W., Vollmer, D. & Weber, S. A. L. Adaptive Wetting—Adaptation in Wetting. *Langmuir* **34,** 11292–11304. ISSN: 0743-7463 (Sept. 2018).

13. Gubanski, S. & Vlastos, A. Wettability of Naturally Aged Silicon and Epdm Composite Insulators. *IEEE Trans. Power Delivery* **5,** 1527–1535. ISSN: 08858977 (July 1990).

14. Morra, M. *et al.* On the Aging of Oxygen Plasma-Treated Polydimethylsiloxane Surfaces. *J. Colloid Interface Sci.* **137,** 11–24. ISSN: 0021-9797 (1990/06/01/).

15. Kim, J., Chaudhury, M. K. & Owen, M. J. Modeling Hydrophobic Recovery of Electrically Discharged Polydimethylsiloxane Elastomers. *J. Colloid Interface Sci.* **293,** 364–75. ISSN: 0021-9797 (Print) 0021-9797 (Linking) (Jan. 2006).

16. Eddington, D. T., Puccinelli, J. P. & Beebe, D. J. Thermal Aging and Reduced Hydrophobic Recovery of Polydimethylsiloxane. *Sens. Actuators B: Chem.* **114,** 170–172. ISSN: 0925-4005 (2006/03/30/).

17. Collins, A. M. in *Nanotechnology Cookbook* (ed Collins, A. M.) 205–253 (Oxford, 2012/01/01/). ISBN: 978-0-08-097172-8.

18. Korhonen, J. T., Huhtamäki, T., Ikkala, O. & Ras, R. H. A. Reliable Measurement of the Receding Contact Angle. *Langmuir* **29,** 3858–3863. ISSN: 0743-7463 (Mar. 2013).

19. Srinivasan, S., McKinley, G. H. & Cohen, R. E. Assessing the Accuracy of Contact Angle Measurements for Sessile Drops on Liquid-Repellent Surfaces. *Langmuir* **27,** 13582–13589. ISSN: 0743-7463, 1520-5827 (Nov. 2011).

20. Saad, S. M. I. & Neumann, A. W. Axisymmetric Drop Shape Analysis (ADSA): An Outline. *Adv. Colloid Interface Sci.* **238,** 62–87. ISSN: 0001-8686 (2016/12/01/).

21. Xu, Z. N. & Wang, S. Y. A Highly Accurate Dynamic Contact Angle Algorithm for Drops on Inclined Surface Based on Ellipse-Fitting. *Rev. Sci. Instrum.* **86,** 025104. ISSN: 0034-6748 (Feb. 2015).

22. Wong, W. S. Y. & Tricoli, A. Cassie-Levitated Droplets for Distortion-Free Low-Energy Solid–Liquid Interactions. *ACS Appl. Mater. Interfaces* **10,** 13999–14007. ISSN: 1944-8244, 1944-8252 (Apr. 2018).

23. Wang, L. & McCarthy, T. J. Covalently Attached Liquids: Instant Omniphobic Surfaces with Unprecedented Repellency. *Angew. Chem. Int. Ed.* **55,** 244–248. ISSN: 1521-3773 (2016).

24. Wong, T.-S. *et al.* Bioinspired Self-Repairing Slippery Surfaces with Pressure-Stable Omniphobicity. *Nature* **477,** 443–447. ISSN: 0028-0836, 1476-4687 (Sept. 2011).

25. Pham, J. T., Schellenberger, F., Kappl, M. & Butt, H.-J. From Elasticity to Capillarity in Soft Materials Indentation. *Phys. Rev. Mater.* **1,** 015602 (June 2017).

26. Whitesides, G. M. The Origins and the Future of Microfluidics. *Nature* **442,** 368–373. ISSN: 1476-4687 (Electronic) 0028-0836 (Linking) (July 2006).

27. van Gorcum, M., Andreotti, B., Snoeijer, J. H. & Karpitschka, S. Dynamic Solid Surface Tension Causes Droplet Pinning and Depinning. *Phys. Rev. Lett.* **121,** 208003 (11/16/ 2018).

28. Johnston, I. D., McCluskey, D. K., Tan, C. K. L. & Tracey, M. C. Mechanical Characterization of Bulk Sylgard 184 for Microfluidics and Microengineering. *J. Micromech. Microeng.* **24,** 035017. ISSN: 0960-1317, 1361-6439 (Mar. 2014).

29. Lafuma, A. & Quéré, D. Slippery Pre-Suffused Surfaces. *EPL* **96,** 56001. ISSN: 0295-5075, 1286-4854 (Dec. 2011).

30. Smith, J. D. *et al.* Droplet Mobility on Lubricant-Impregnated Surfaces. *Soft Matter* **9,** 1772–1780. ISSN: 1744-683X, 1744-6848 (2013).

31. Pericet-Cámara, R., Best, A., Butt, H.-J. & Bonaccurso, E. Effect of Capillary Pressure and Surface Tension on the Deformation of Elastic Surfaces by Sessile Liquid Microdrops: An Experimental Investigation. *Langmuir* **24,** 10565–10568. ISSN: 0743-7463, 1520-5827 (Oct. 2008).

32. Fernandez-Toledano, J. C., Blake, T. D., Lambert, P. & De Coninck, J. On the Cohesion of Fluids and Their Adhesion to Solids: Young's Equation at the Atomic Scale. *Adv. Colloid Interface Sci.* **245,** 102–107. ISSN: 1873-3727 (Electronic) 0001-8686 (Linking) (July 2017).

33. Butt, H.-J. *et al.* Design Principles for Superamphiphobic Surfaces. *Soft Matter* **9,** 418–428. ISSN: 1744-683X, 1744-6848 (2013).

34. Jalbert, C., Koberstein, J. T., Yilgor, I., Gallagher, P. & Krukonis, V. Molecular Weight Dependence and End-Group Effects on the Surface Tension of Poly(Dimethylsiloxane). *Macromolecules* **26,** 3069–3074. ISSN: 0024-9297, 1520-5835 (June 1993).

35. Karpitschka, S. *et al.* Droplets Move Over Viscoelastic Substrates by Surfing a Ridge. *Nat. Commun.* **6,** 7891. ISSN: 2041-1723 (Aug. 2015).

36. Eggers, J. Existence of Receding and Advancing Contact Lines. *Phys. Fluids* **17,** 082106. ISSN: 1070-6631 (Aug. 2005).

37. Hänni-Ciunel, K., Findenegg, G. H. & von Klitzing, R. Water Contact Angle On Polyelectrolyte-Coated Surfaces: Effects of Film Swelling and Droplet Evaporation. *Soft Materials* **5,** 61–73. ISSN: 1539-445X, 1539-4468 (Dec. 2007).

38. Ray, S., Sedev, R., Priest, C. & Ralston, J. Influence of the Work of Adhesion on the Dynamic Wetting of Chemically Heterogeneous Surfaces. *Langmuir* **24,** 13007–13012. ISSN: 0743-7463 (Nov. 2008).

39. Pilat, D. W. *et al.* Dynamic Measurement of the Force Required to Move a Liquid Drop on a Solid Surface. *Langmuir* **28,** 16812–16820. ISSN: 0743-7463, 1520-5827 (Dec. 2012).

40. Perrin, H., Lhermerout, R., Davitt, K., Rolley, E. & Andreotti, B. Thermally Activated Motion of a Contact Line Over Defects. *Soft Matter* **14,** 1581–1595. ISSN: 1744-683X (2018).

41. Perrin, H., Lhermerout, R., Davitt, K., Rolley, E. & Andreotti, B. Defects at the Nanoscale Impact Contact Line Motion at All Scales. *Phys. Rev. Lett.* **116,** 184502 (5/02/ 2016).

Supplementary Information

Supporting Figures

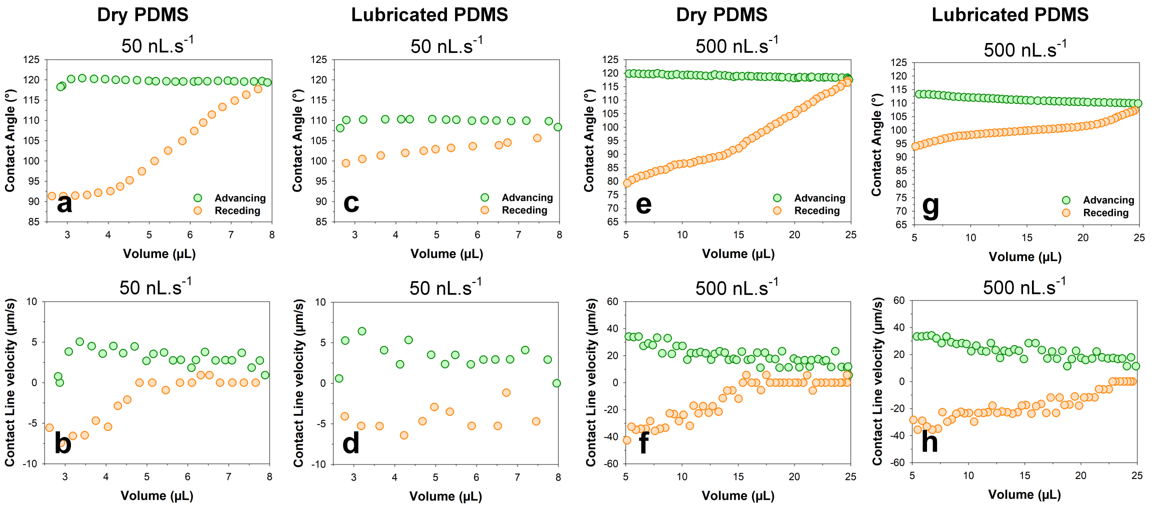

Figure B.16: Gel-permeation chromatography elution spectrums of normalized distributions vs. molar mass of components. a) Sylgard 184 Part I (uncrosslinked). b) Oligomers from crosslinked PDMS (1:10 w/w ratio). Cured at 80 °C for 2 hours. Samples were cut into 1 cm × 1 cm pieces and stirred in 40 ml toluene 3 days. Toluene-eluted samples are analyzed using GPC.

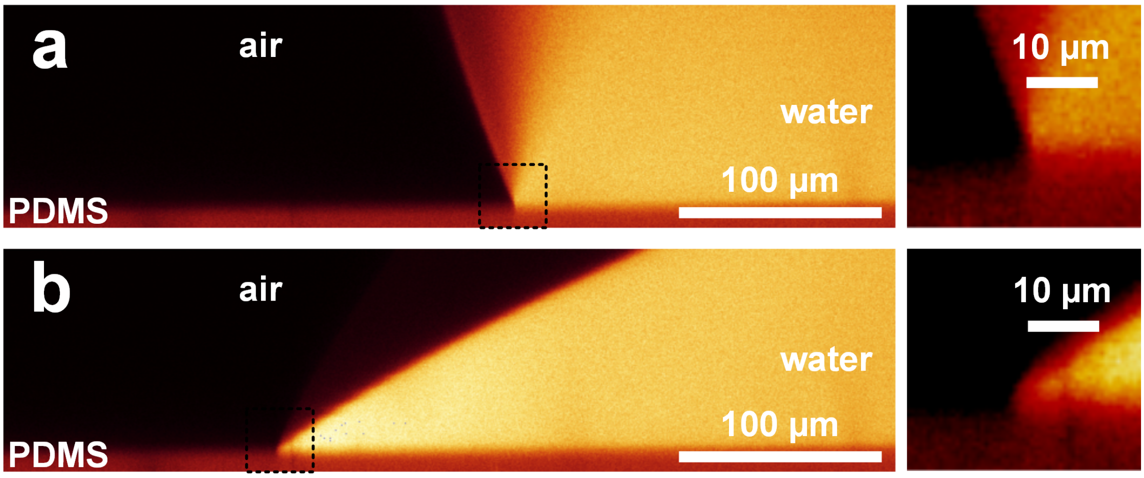

Figure B.17: Contact angle and contact line velocity plots at low- (50 nL/s) and high- (1000 nL/s) speed drop inflation-deflation experiments on dry and lubricated PDMS. Extremely high velocities of drop inflation-deflation experiments on pristine PDMS, up to 25 μl, did not recover distinctive advancing transitional lubrication peaks. a, c, e, g) A slight incline reached a maximum of ca. 123°, later decreasing to 117°. More interestingly, the growth and shift of a reversal peak continues with increasing drop volume inflation-deflation speeds, where it took place at originally at 500, 1000, and then 1500 nL/s respectively during the receding half-cycle at 15, 12, and 10 μl respectively. This persisted at ca. 10 μl at 2000 nL/s. b, d, f, h) During these peaks, distinct velocity variations were also noted to occur up to -300 μm/s. Contact line velocities were extracted from datasets for the fitting of adaptation theory.

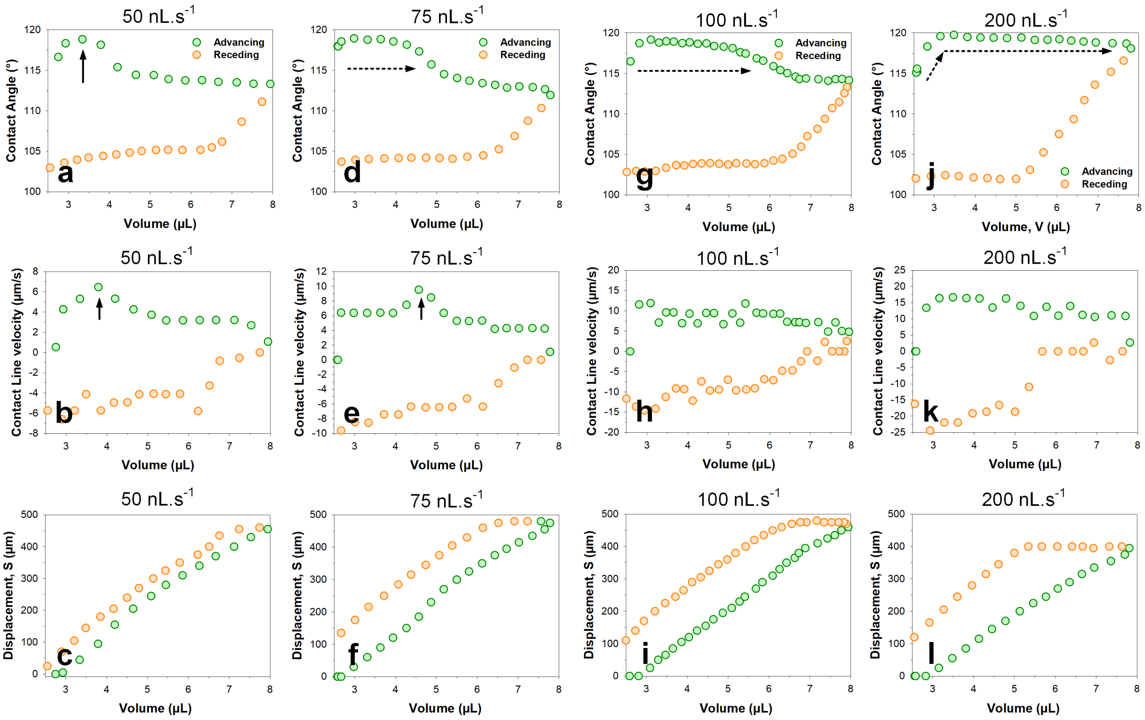

Figure B.18: The lack of a micrometric wetting ridge at the water-on-pristine PDMS contact line. An inverted laser scanning confocal microscope (Leica TCS SP8) was used to dynamically observe the contact line of a water drop (dyed with 10 μg/ml ATTO 488) on PDMS. The XZ scanning plane was used to illustrate how the surface experience a range of vastly different dynamic contact angles (high to low). No wetting ridges were detected, down to the resolution of ca. 1 μm.

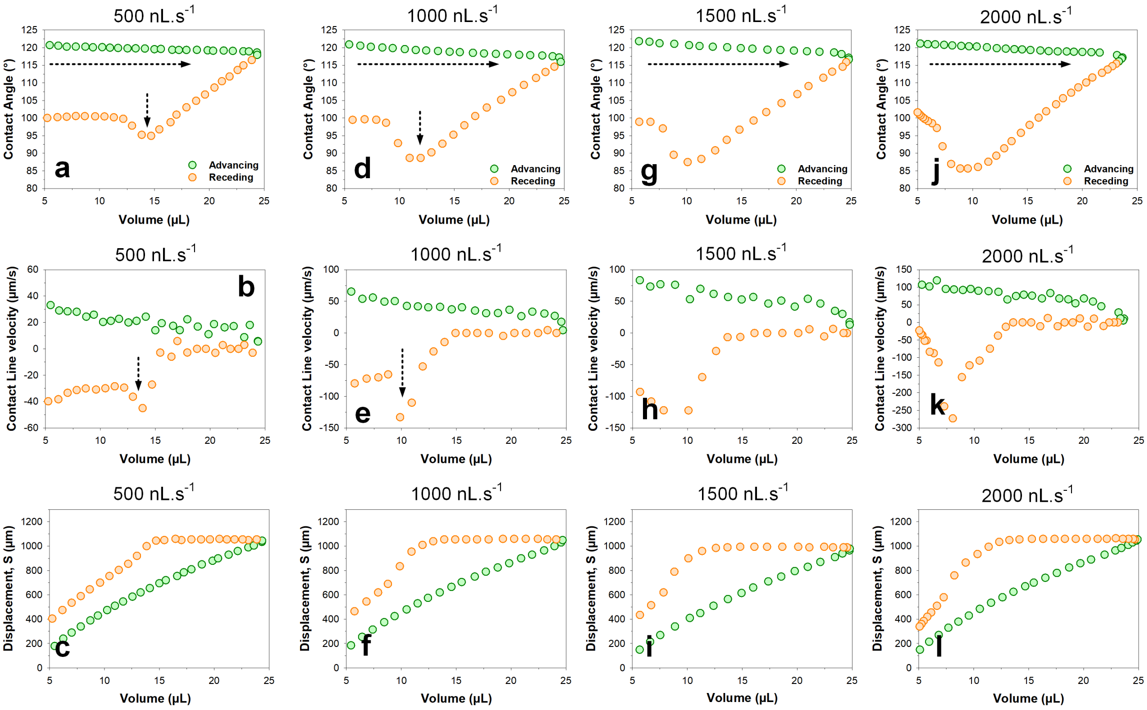

Figure B.19: Contact angle and contact line velocity plots at low-speed drop inflation-deflation experiments, presented in trend. Low speeds of drop inflation-deflation experiments on pristine PDMS above the $50 - 200$ nL/s limit results in diminishing peak-presence. Lubrication peaks are similar to those demonstrated at extremely slow velocities, appearing to occur with a ca. +5°, from an initial equilibrium of ca. a, d, g, j) $112/3 - 115°$ (due to receding parameters) up to 118°. A maximum "dry-equilibrium" contact angle of 120° was obtained, during which the loss of the "lubricated-equilibrium" at 112/3° occurred at 200 nL/s with a maximum drop size of 8 μl. b, e, h, k) Contact line velocities were extracted from datasets for the fitting of adaptation theory, per the raw datasets of c, f, i, l) contact line displacement datasets.

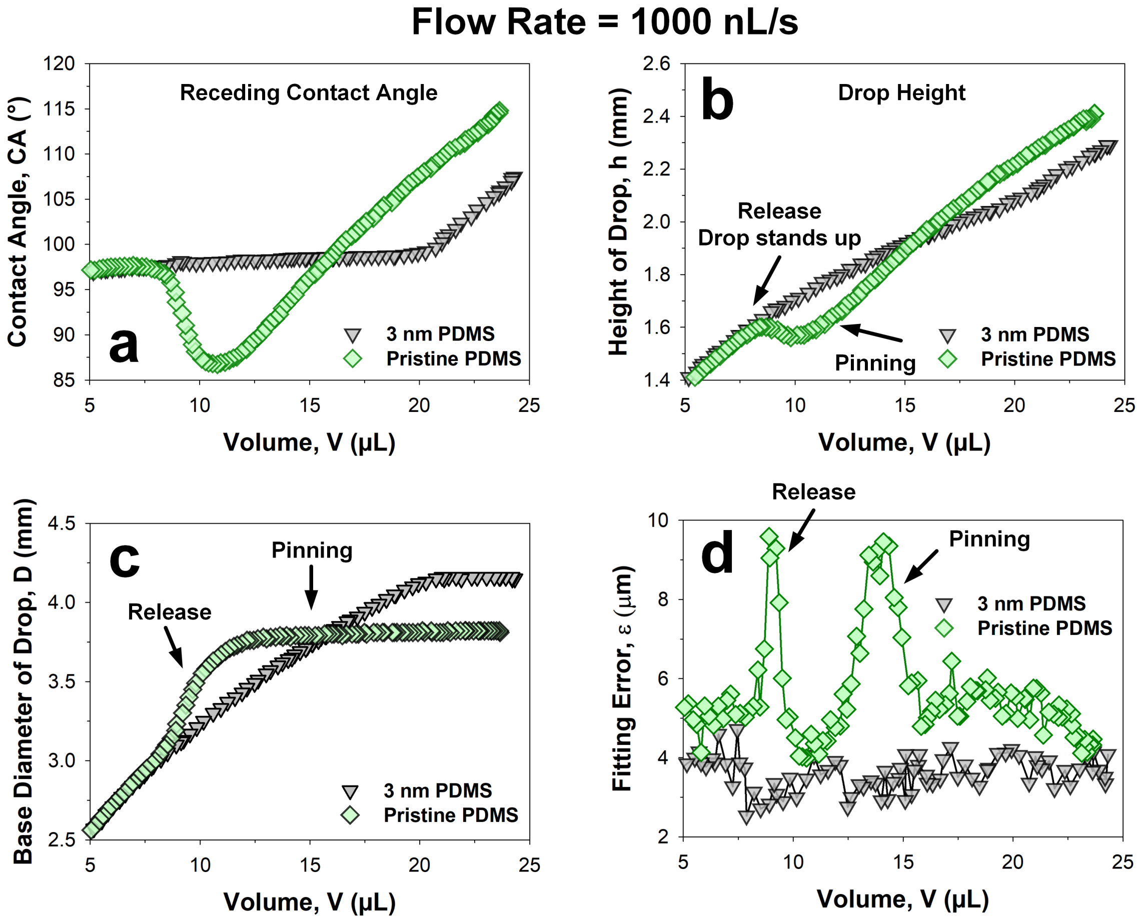

Figure B.20: Contact angle and contact line velocity plots at high-speed drop inflation-deflation experiments, presented in trend. Extremely high velocities of drop inflation-deflation experiments on pristine PDMS, up to 25 μl, did not recover distinctive advancing transitional lubrication peaks. a, d, g, j) A slight incline reached a maximum of ca. 123°, later decreasing to 117°. More interestingly, the growth and shift of a reversal peak continues with increasing drop volume inflation-deflation speeds, where it took place at originally at 500, 1000, and then 1500 nL/s respectively during the receding half-cycle at 15, 12 and 10 μl respectively. This persisted at ca. 10 μl at 2000 nL/s. b, e, h, k) During these peaks, distinct velocity variations were also noted to occur up to -300 μm/s. b, e, h, k) Contact line velocities were extracted from datasets for the fitting of adaptation theory, per the raw datasets of c, f, i, l) contact line displacement datasets.

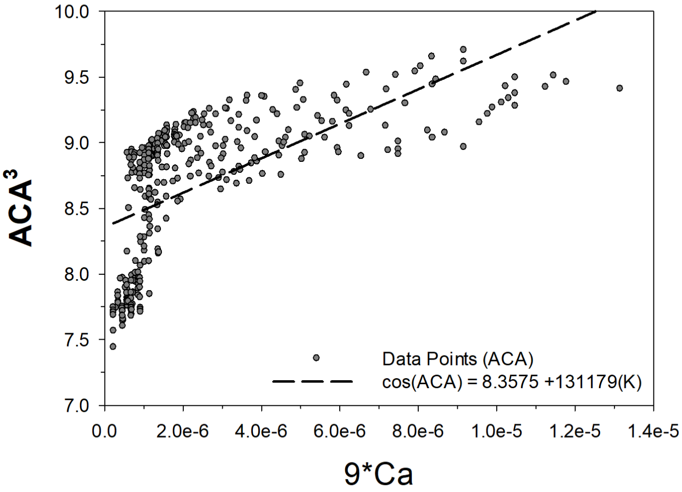

Figure B.21: Mechanism of drop pinning during receding half-cycle, compared between a nanometric thick 3 nm PDMS sample (green) with pristine PDMS sample (grey). a) The peak present in the receding contact angle is highlighted by a drop in the receding contact angle, followed by a rise and plateau, reaching the same value as thin 3 nm PDMS. b) The peak appears to arise from drop pinning, where the feet of the drop is pinned, giving rise to an temporal decrease in drop height. The pinned domains are later released, resulting in a sharp increase in drop height during relaxation. c) The pinning of the drop is evident from the invariance of drop's base diameter, compared to the peakless system, before a steep drop. d) These elements of drop profile distortions are reflected in the fitting error during drop profile analysis, with increase in errors during periods of pinning and release.

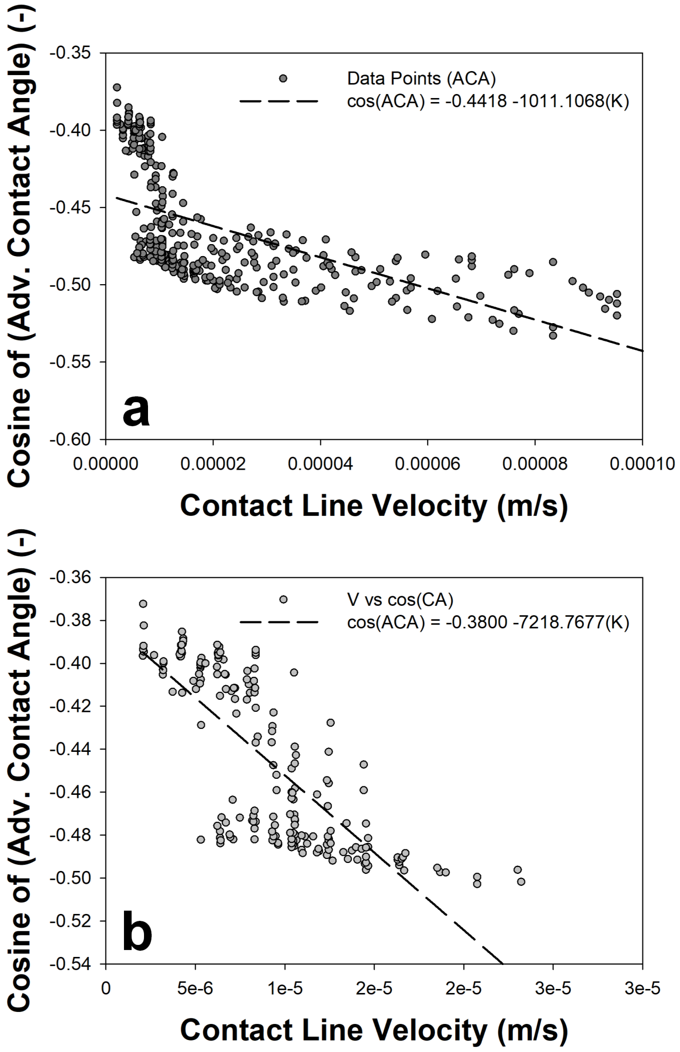

Figure B.22: Cox Voinov fit using hydrodynamics theory: $\theta^3 = \theta_e^3 - 9\mathrm{Ca}\log\frac{x}{l_{\mathrm{micro}}}$. Dataset from pristine PDMS was used. $\theta representsthedynamiccontactangle, hereoftenrepresentedas\theta_a$. θ_e represents the equilibrium contact angle and Ca represents the capillary number, $\eta v/\gamma$. $\frac{x}{l_{\mathrm{micro}}}$ represent the length scale over which the contact line is evaluated.The resulting fitting parameter of $\log\frac{x}{l_{\mathrm{micro}}} = 131179$ cannot be solved as $\frac{x}{l_{\mathrm{micro}}} \to \infty$.

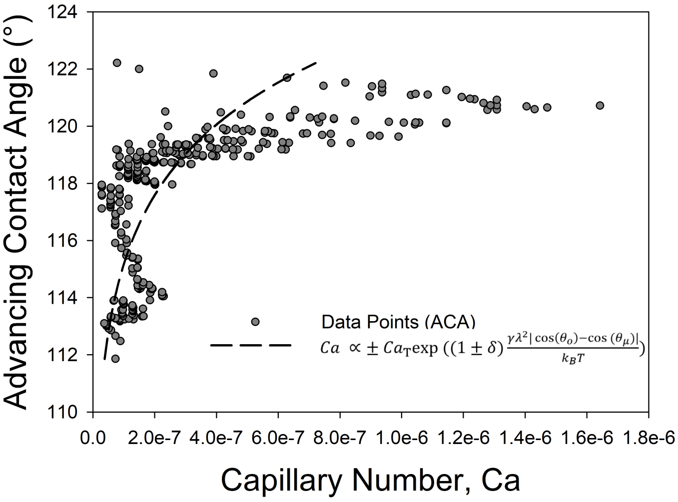

Figure B.23: Molecular-Kinetic fit using $\cos\theta_a(v) = \cos\theta_a(0) - \frac{v\zeta}{\gamma}$ hwere $\zeta = k_B T / K_0 \lambda^3$. $\theta_a(v)$ and $\theta_a(0)$ represents the actual and equilibrium contact angles while ζ is the friction coefficient, v is the contact line velocity, γ is the surface tension and $k_B T$ as the boltzmann constant and temperature respectively. Dataset from pristine PDMS was used. a) Fitting over the entire dry- and lubricated-domains and b) Fitting only over the lubricated domain. Assuming a regular hopping distance, K_0 of 1 nm, The respective fits gave rise to an average hopping frequency, λ of 55 kHz and 7.7 kHz in the overall and the lubricated domain respectively. The hopping frequency decreases in the lubricated domain.

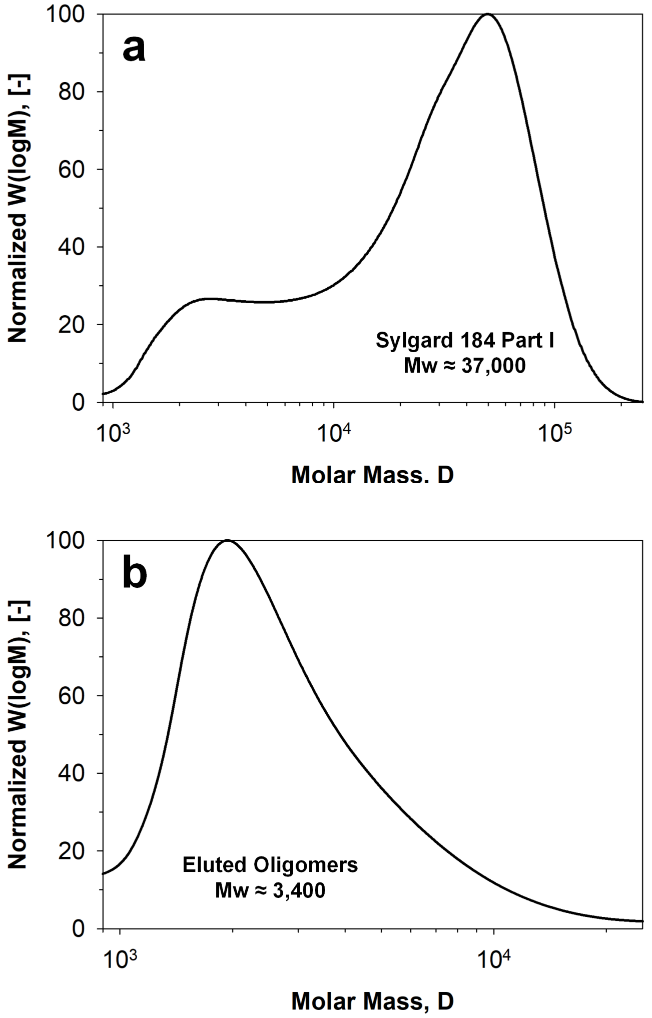

Figure B.24: A unified hydrodynamics and thermal activation based model proposed by Perrin et. al in Soft Matter 2018, 14, 1581. The model, $\mathrm{Ca} \sim \mathrm{Ca}_T \exp\left((1 \pm \delta)\frac{\gamma\lambda^2|\cos\theta_0 - \cos\theta_\mu|}{k_B T}\right)$, is fitted over 4 parameters: $\mathrm{Ca}_T, \delta, \lambda$, and θ_0. θ_μ is the reported contact angle while $k_B T$ as the boltzmann constant and temperature respectively. Ca represents the transitional capillary number, δ is the symmetry coefficient, λ is the distance between defects and θ_0 is the static contact angle. The fit results in the respective values of $\mathrm{Ca}_{\approx 1.7\times10^{-6}}$, $\delta \approx -0.0031$, $\lambda \approx 1$ nm, $\theta_0 \approx 2.19$ rad or 125°.

B.3 Linear Shrinkage of Hydrogel Coatings Exposed to Flow: Interplay between Dissolution of Water and Advective Transport

Philipp Baumli[†], Lukas Hauer[†], Emanuela Lorusso[†], Azadeh Sharifi Aghili, Katharina I. Hegner, Maria D'Acunzi, Jochen S. Gutmann, Burkhard Dünweg, and Doris Vollmer, Soft Matter 18, no. 2 (2022): 365-371.

[†] equal contribution

Abstract

We investigate the shrinkage of a surface-grafted water-swollen hydrogel under shear flows of oils by laser scanning confocal microscopy. Interestingly, external shear flows of oil lead to linear dehydration and shrinkage of the hydrogel for all investigated flow conditions irrespective of the chemical nature of the hydrogel. The reason is that the finite solubility of water in oil removes water from the hydrogel continuously by diffusion. The flow advects the water-rich oil, as demonstrated by numerical solutions of the underlying convection-diffusion equation. In line with this hypothesis, shear does not cause gel shrinkage for water-saturated oils or non-solvents. The solubility of water in the oil will tune the dehydration dynamics.

Introduction

Hydrogels are ubiquitous in our daily lives. Everyday applications range from jelly pudding and diapers to contact lenses and scaffolds in tissue engineering [1–4]. Hydrogels are three-dimensional networks of hydrophilic polymers formed by chemical (covalent) crosslinks or physical (noncovalent) crosslinks such as entanglements that provide physical and structural integrity [5, 6]. All hydrogels have in common that they can bind large amounts of water, even as much as 99% [7] Most hydrogels are based upon polyelectrolytes, where the macromolecules dissociate ions into the water.8, 9 These ions form a "gas" that wants to expand as much as possible [8, 9]. For electrostatic reasons, the oppositely charged polymer network then swells as well. Another class of hydrogels is based upon thermo-responsive macromolecules such as Poly-N-isopropylacrylamide (PNIPAm) [10–12]. For these hydrogels, the solubility is provided by an interplay between the polar groups and the geometrical match between the local structure of the macromolecule and the short-range structure of water [13–15]. Both mechanisms give rise to a strong water retention capacity, even maintained under mechanical loading conditions, such as squeezing (Fig B.25a) [16].

Therefore, there is wide interest in the stability of hydrogels [17]. So far, most investigations have focused on the response to changes in bulk thermodynamic parameters (such as temperature or salt concentration) [18–20]. Here we are investigating the interactions of the hydrogel with its surroundings upon subjecting the hydrogel to a steady fluid flow across its surface. The study of the transport of fluids across a hydrogel interface finds vital importance in the fields of water-remediation [21, 22] and bio-adhesion in the context of hydrogels used as implants or surgical devices [23–27]. Therefore, the transport and interactions of aqueous fluids across a hydrogel surface/interface are well studied. In contrast, the interactions and transport of non-polar fluids across a hydrogel surface/interface remain unexplored.

We investigate the stability with respect to a non-aqueous liquid that flows past the hydrogel. We find hydrogel shrinkage exclusively caused by the finite solubility of water in the flowing liquid. This even happens when the solubility is low, such as in the case of flowing oil. Here we find that the dehydration rate is correspondingly also very low. This gives rise to a decrease of the hydrogel volume that progresses linearly in time because the flow removes the dissolved water quickly. Interestingly, the dehydration rate seems to be governed only by the properties of the water-oil interface. The polymer component plays no role during the process, spanning roughly an order of magnitude in hydrogel volume. This is even true when comparing a polyelectrolyte gel (poly(acrylic acid), PAA) with a neutral thermoresponsive gel (PNIPAm). The purpose of the present paper is to substantiate this picture by reporting our experimental findings obtained by laser scanning confocal microscopy and the corresponding theoretical analysis based on numerical solutions of the convection-diffusion equation that governs the solute dynamics.

Materials and Methods

Materials

SU-8 photoresist was purchased from MicroChem Corp. Trichloro(octadecyl)silane (OTS, $>$ 90%), N-Isopropylacrylamide (NIPAm, 97%), acrylic acid (AA, 99%), N,N'-methylenebisacrylamide (NMBA, 99%), 2-Hydroxy-4-(2-hydroxyethoxy)-2-methylpropiophenone (Irgacure D-2959) and Allylamine (ALAm, $99,5\%$) were purchased from Sigma-Aldrich. The fluorescent dye was ATTO 488 NHS-ester (ATTO-TEC GmbH, Germany, diluted in MilliQ water, concentration: 1 μg/g). As lubricants, silicone oils (PDMS, Sigma-Aldrich, viscosity: 50 cSt and 500 cSt at 25 °C), mineral oil (Paragon Scientific Ltd., viscosity: 100 cSt at 20 °C), FluorinertTM FC-70® (Sigma-Aldrich, viscosity: 12 cSt), and olive oil (Bertolli®) were used. All chemicals were used as received. Epoxy resin flow cells (Sticky-Slide VI0.4) were ordered from ibidi GmbH (Germany). The individual channels are 0.5 mm high (including adhesive layer), 17 mm long, and 3.8 mm wide, which amount to a coverable area of 64.6 mm^2 per channel. Each channel has a volume of 32 µL. Alternatively, flow cells having a height of 0.1 mm, a length of 45 mm, a width of 5 mm, and a volume of 23L were used. The flow cells were connected to a peristaltic pump (Reglo-Analog MS4/8, Cole-Parmer GmbH) via polyvinyl chloride (PVC)-tubes (internal diameter = 1.42 mm, Novodirect GmbH Labor und Meßgeräte) and tightly sealing linkers. The fluorescent dye ATTO 488 NHS-ester offers excellent water solubility, strong absorption, high fluorescence quantum yield, and high photostability. The fluorescence is excited most efficiently in the range of 480 and 515 nm. The 488 nm line of an argon laser was used for excitation. The used dye concentrations did not change the interfacial tension of water as verified from interfacial tension measurements.

Preparation of Hydrogel Surfaces

To achieve a homogeneous binding of the hydrogel to a surface, it turned out that a microstructure facilitates the binding. The regular microstructured surface consisted of uniform arrays of cylindrical micropillars fabricated by photolithography using an epoxy-based negative photoresist (*i.e.*, SU-8) [28, 29]. SU-8 photoresist was spin-coated on oxygen plasma activated glass coverslips (10 min, 300 W) and soft baked (95 °C, 4 min) to evaporate the solvent and densify the deposited film. Illumination with UV-light (mercury lamp, 350 W, 30-35 s) through a photomask induced crosslinking within the exposed portions of the film. Subsequently, a post-exposure baking step (10 min at 65 °C; 2 min at 95 °C; 30 min at 65 °C) was performed to crosslink those areas selectively. The SU-8 micropillars arrays were coated with a hydrogel, Figure 1a, b. Double functional groups were first introduced onto the SU-8 photoresist-based micropillar array surface via a reaction involving allylamine (ALAm) [30, 31]. A 5%v/v solution of allylamine in water was prepared and put under stirring for 10 minutes. The thus-prepared solution was poured into a glass box containing the SU-8 micropillar arrays and left for 30 minutes. The amino-groups of ALAm react with the epoxy groups of SU-8 in an SN2-type reaction, thus exposing the allyl group to the surface. After 30 minutes, the samples were then extensively rinsed with water and left to dry. After the pre-modification, UV-induced radical photopolymerization was used to grow the hydrogel network on SU-8 micropillar arrays. For that purpose, 10%v/v aqueous solutions of NIPAm and AA were prepared by adding a 2%w/w nmBA, with respect to the monomer content, as the crosslinker. Finally, 20mg of Irgacure D-2959 as initiator was added to the solutions. The micropillar arrays were wetted with 1 ml of hydrogel solution. A glass slide was gently positioned onto the arrays forming a “sandwich structure” by doctor blading to spread the solution drop, avoiding the formation of bubbles. The arrays were placed under a UV lamp at a distance of 7.5 cm (6.0 mW/cm^2) and irradiated for 20 minutes. After polymerization, the glass slide was removed. The hydrogel formed had more affinity with the micropillars arrays; therefore, only this surface was coated. The thus-obtained hydrogel-functionalized micropillar arrays were washed with water and left to dry. Coating with an acrylic acid-based hydrogel solution establishes PAA-based hydrogel coatings. In contrast, an N-isopropylamide-based hydrogel solution establishes the PNIPAm hydrogels. Scanning Electron Microscopy (SEM) confirms the presence of a homogeneous hydrogel coating (Fig. B.29, Supporting Information).

Preparation of Water-Saturated Oil

12 ml of MilliQ water was added to 40 ml of 50 cSt silicone oil and stirred at 300 rpm for 72 h. The separation of saturated oil and excess water was performed with a separation funnel. The vessel was sealed during the experiments using paraffin tape.

Laser Scanning Confocal Microscopy (LSCM)

LSCM allows distinguishing the different fluid phases via fluorescent dyes, which is impossible when using a standard goniometer setup. An inverted laser scanning confocal microscope (LSCM, Leica TCS SP8 SMD) with a $40\times/1.11$ water immersion objective lens (Olympus) was employed to image the shrinkage, *i.e.*, dehydration of the hydrogel. The horizontal resolution was ≈ 500 nm, the vertical resolution was ≈ 1 μm, and the time span in-between successive images was 10 min – 30 min. Confocal image acquisition is a trade-off between image quality and imaging speed. For the data presented in Fig. B.26 and 4, the priority was on image quality. Hence, we only performed confocal imaging at one point along the flow channel. Image acquisition parameters like a long pixel dwell time (0.12ms), a high line average (8), a comparatively small scanning frequency (400 Hz), and a large field of view (291.19×291.19 μm^2 4096×4096 pixel^2) ensure optimal image quality, albeit slowing the image acquisition speed. These significant acquisition times render different imaging points along the flow channel (as done for the data presented in Fig. B.27) experimentally unfeasible. In Fig. B.27, the focus was on the comparison to the simulation results. Hence, the acquisition parameters of the confocal laser scanning microscopy imaging were optimized for faster imaging. The scanned areas in the cross-section images (xz-scans) were 291×146 μm^2 (512×256 pixel^2). The pixel dwell time was 1.2 μs. We employed a line average of 2. The scanning frequency was 600 Hz. The scanning frequency was 600 Hz. A line average of 8 was used to improve image quality. Acquired images of the hydrogel cross-section were evaluated with a custom-written MATLAB® routine. This yields an average height per cross-sectional image.

Scanning Electron Microscopy

The micropillar arrays were characterized via scanning electron microscopy (SEM) using a LEO 1530 Gemini scanning electron microscope (Zeiss, Germany). The samples were tilted (45°) to visualize a micropillar array best.

Model and Simulation

Water migrating from the hydrogel into the oil is transported [32] as

$$\partial_t c + \nabla \cdot (\boldsymbol{u}c - D\nabla c) = 0 \tag{B.41}$$

The concentration of water, c, follows the advective flow of the oil with the hydrodynamic velocity $\boldsymbol{u} = u_x \boldsymbol{e}_x + u_y \boldsymbol{e}_y$, while it diffuses into the bulk oil with a mobility which we estimate [33] as $D = 2 \times 10^{-9}$ m^2/s. The advective transport term in Eq. (B.41) is an essential part of the dehydration process. Without considering this term, water saturation would occur inside the channel within seconds to minutes, and no dehydration would occur after that. In order to solve Eq. (B.41), we search for $\boldsymbol{u}$, utilizing the momentum conservation in the (incompressible) bulk oil flow [34], namely

$$\rho \left(\partial_t \boldsymbol{u} + (\boldsymbol{u} \cdot \nabla)\, \boldsymbol{u}\right) + \nabla \cdot (p\boldsymbol{I} + \boldsymbol{\tau}) = 0. \tag{B.42}$$

Here, ρ and η are the density and the dynamic viscosity of the oil, respectively. Because the dilution of water is minor, we neglect any density changes in the oil phase. p is the hydrostatic pressure, $\boldsymbol{I}$ the identity matrix and $\boldsymbol{\tau}$ is the shear tensor, which we consider Newtonian without compression, such that it reads

$$\boldsymbol{\tau} = \eta \left(\nabla \boldsymbol{u} + (\nabla \boldsymbol{u})^T\right) \tag{B.43}$$

We do not consider any transient relaxations, such that the time derivatives in Equations (B.41) and (B.42) become zero. We use standard conditions on the domain-boundaries (*i.e.*, no-slip, no-flux cf. Fig. B.37 and Table B.3), except on the shared interface between hydrogel and oil. Here, we utilize a kinematic flux condition, which we discuss in the results and discussion.

We solve Equations (B.41) and (B.42), together with the boundary conditions (Fig. B.36, Table B.3, and Equation (B.47)) in the microchannel (microfluidic flow cell) numerically, utilizing the software package COMSOL Multiphysics® 5.5. For discretization, the finite element method is utilized (linear ansatz functions for mass conservation, $P2+P1$ elements with consistent stabilization for momentum conservation). The computation domain defined in Fig. B.37 was discretized with a structured, Cartesian mesh, holding 15132432 degrees of freedom. We added 1.5 mm to the inlet height to let the flow develop into a parabola. Mesh independence was verified by successively increasing the number of degrees of freedom until no variations in the solutions were observed. The equations were solved directly with the MUMPS solver [35].

Results and Discussion

We used a microfluidic flow cell with plastic side and top walls to investigate the hydrogels' flow-induced dehydration. The polymer-coated micropillars (Fig. B.25b) formed the base of the cell (Fig. B.25c). Next, the flow cell is filled with dyed MilliQ-water (blue) to induce polymer swelling, Fig. B.25d. After 30 minutes, a steady-state thickness of the swollen equilibrated hydrogel has been reached, and a flow of neat silicon oil (polydimethylsiloxane, PDMS) was applied, Fig. B.25e. Silicone oil offers the advantage of identical chemical characteristics over wide viscosity ranges. We monitored the swollen hydrogels' stability in situ under flow conditions utilizing an inverted laser scanning confocal microscope (LSCM, Fig. B.30). LSCM allows distinguishing different fluid phases via fluorescent dyes at concentrations sufficiently low that the dyes do not change the system´s constituents' interfacial properties.

Within the flow cell (height 500 μm), the flow profile of the oil is approximately parabolic through its depth and uniform through its width. The volumetric flow rates Q established through the flow channel using a peristaltic pump ranged from $Q = 0.48$ mm/min to 4.80.2 mm/min, which resulted in average flow velocities ranging from 5.3 mm/s to 532 mm/s. Image acquisition was performed in the middle of the horizontal flow cell with respect to the lateral direction parallel to the flow if not stated otherwise.

The height of the initial swelling (> 100 μm for PAA, > 50 μm for PNIPAm, Fig. B.26a, top, B.31a, B.32a) is much larger than the pillar height (black, $h = 10$ μm). The interface between the excess water and the water contained in the hydrogel causes a change in the emission intensity. The difference in light intensity may be attributed to different affinities of the hydrophilic dye to unbound and bound water within the hydrogel or to a shift of the dye's emission signal. The flow of silicone

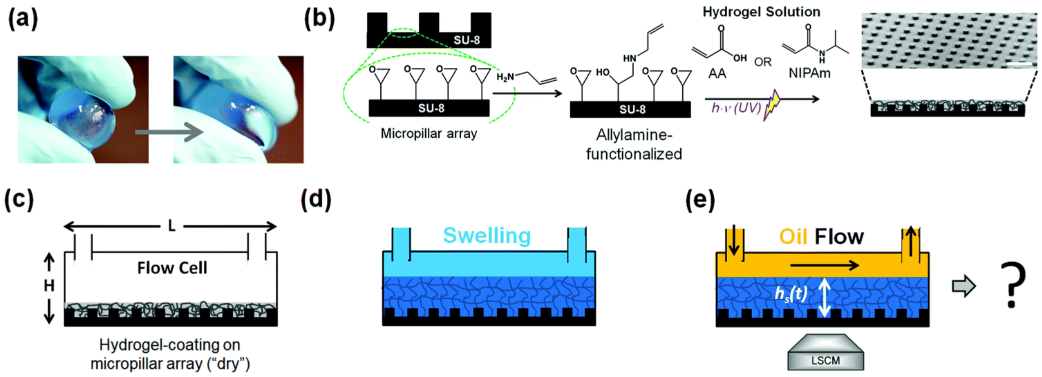

Figure B.25: Experimental approach. (a) The hydrogel beads prove resilient to squeezing and maintain the imbibed water. (b) Preparation of hydrogel coatings covalently attached to a micropillar array via allylamine-functionalization of SU-8 micropillar arrays. The micropillars had a diameter of 30 μm, a height of 10 μm, and a centre-to-centre distance of 60 μm, decorating a 170 μm thick glass coverslip as a substrate. (c) Hydrogel-coated micropillar arrays are contained in a microfluidic flow cell. (d) The hydrogel is swollen with MilliQ water containing fluorescent dye (Atto 488 NHS-Ester, 1 μg/g). This low concentration ensures that the interfacial tensions remain unmodified. (e) Shrinkage experiment: a flow of silicone oil (yellow) is applied across the hydrogel coating, which leads to shear stresses acting on the hydrogel coating. The evolution of the thickness height of the hydrogel coating above the substrate, $h_s(t)$, is monitored by laser scanning confocal microscopy (LSCM). Can the hydrogel be shrunk with shear flows of oil? And if so, how fast?

oil (black) leads to progressive shrinkage owed to dehydration of the hydrogel, *i.e.*, water depletion of the coating (Fig. B.26a, Fig. B.31b-k). As dehydration progresses, the remaining portions of the swollen hydrogel conform to the shape of the micropillar array (Fig. B.26a, bottom, Fig. B.31j-r). Eventually, the remaining swollen portions of the hydrogel reach a steady-state retention thickness, which remains unchanged as the oil flow continues (Fig. B.26a, bottom, Fig. B.31k-r).

The quantification of the hydrogel dehydration was performed by extracting the mean height $h_s(t)$ of the hydrogel coating above the substrate (averaged over at least 15 positions). The hydrogel coating thickness, *i.e.*, hydrogel shrinkage, progresses linearly with time (Fig. B.26b). Notably, a linear decrease in thickness is found for the polyelectrolyte PAA and the neutral PNIPAm-based hydrogel coatings (Fig. B.26b, Fig. B.31, B.32, and B.34). The shrinkage of the hydrogel coating progresses until the steady-state retention thickness is reached, which happens with a sharp transition (Fig. B.26b, inset) and is indicative of residual water content. At first glance, linear dehydration kinetics might be surprising and counterintuitive since hydrogels have been observed to undergo structural changes during dehydration [36, 37].

Regardless of the hydrogel coating and the flow characteristics that were considered experimentally (flow velocity and oil viscosity), the dehydration kinetics (represented by the slopes of the curve) hardly show any variations (Fig. B.26c), within experimental accuracy. We varied the Reynolds number $\mathrm{Re} = \rho v/\eta$ between 0.053 and 0.106. The maximum flow velocity v is set by the pump, the

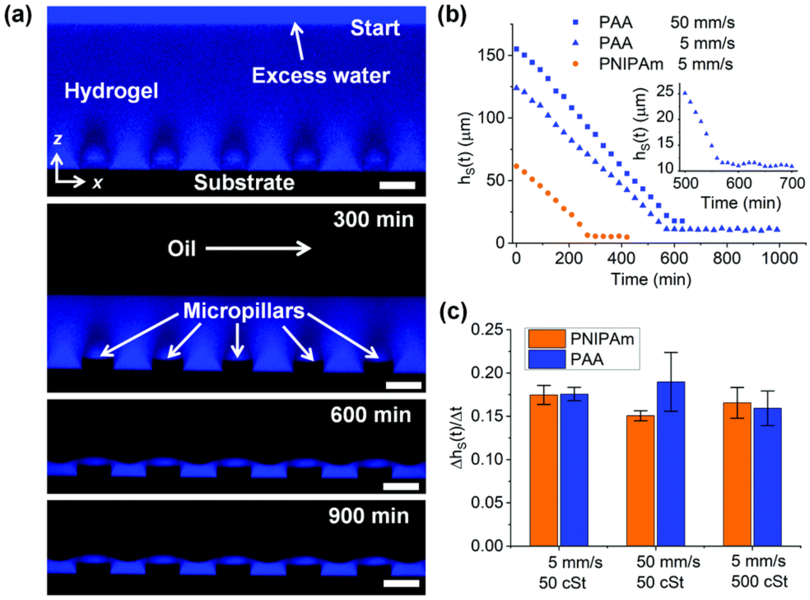

Figure B.26: Hydrogels encountering a shear flow of oil. (a) Time evolution of side view (xz-scan) laser scanning confocal images (40 × /1.1 water immersion objective) demonstrating dehydration of a hydrogel coating consisting of PAA (poly (acrylic acid)) on a micropillar array (consisting of photoresist SU-8). The image acquisition was performed exactly in the middle of the flow channel. The flow direction of oil is from left to right. The hydrogel coating is swollen with fluorescently labelled MilliQ-water. Dye (Atto-488 NHS-Ester) concentration: 1 μg/ml. The substrate and the micropillars appear black since they have not been dyed. Silicone oil (viscosity: 50 cSt, density: 0.96 g/ml, not dyed) is then continuously circulated over the hydrogel-coated micropillar array at a volumetric flow rate Q of 0.48 mm/min for 900 min. Pillar dimensions: diameter $d = 30$ μm, centre-to-centre spacing ("pitch") $p = 60$ μm, and pillar height $h = 10$ μm. All scale bars are 30 μm. (b) The mean height of hydrogels linearly decreases with time while silicone oil (50 cSt) is flowing over the hydrogel (solid blue squares: PAA, flow velocity 50 mm/s, $R^2 = 0.999$, solid blue triangles: PAA, flow velocity 5 mm/s, $R^2 = 0.999$, solid orange circles: PNIPAm, flow velocity 5 mm/s, $R^2 = 0.998$). R^2 denotes the coefficient of determination. The establishment of the retention thickness takes place sharply (inset). Flow velocities: 5 mm/s or 50 mm/s. The image acquisition was performed exactly in the middle of the flow channel. (c) The slope of the time evolution of the hydrogel thickness is constant for the investigated parameter range within experimental accuracy (blue: PAA, orange: PNIPAm). The image acquisition was performed exactly in the middle of the flow channel.

microfluidic flow cell, the channel height h, and the oil density ρ and viscosity η. For the considered Re, our experiments are in the Stokes limit, *i.e.*, the inertia terms in Eq. (B.42) are diminishingly small.

What causes the linear decrease of the thickness with time? One option would be that oil slowly and continuously shears off the water. However, in that case, the shrinkage rate should change with varying oil viscosity or flow velocity. Within the experimental resolution, we did not observe a dependence on velocity or viscosity. We also did not observe a flow-induced dissolution of arrays of discrete oil droplets [38].

To understand hydrogel shrinkage, it is important to keep in mind that silicone oil can take up around 30 mm of water [33]. Initially, the entering silicone oil is ‘dry’. The hydrogel contains a large amount of water. Hence, the chemical potential, characterized by an intensive free energy, is unbalanced in the two phases. This imbalance of chemical potential can be regarded as osmotic pressure acting on the water molecules. To equilibrate this imbalance, water migrates via diffusion from one phase (hydrogel) to the other (silicone oil) until the oil is saturated. This is feasible due to the mobility of water in silicone oil, quantified by the diffusivity18 of approximately $D = 2 \times 10^{-9}$ m^2/s for the investigated viscosities. Given the length scale of the channel height $h = 100$ μm, it can be expected that molecules diffuse in oil from the channel's bottom to its ceiling at a rate of $\tau_{\text{diff.}}^{-1} = D/h^2 \approx 0.2 s^{-1}$. Diffusion of water into oil relaxes the osmotic pressure (balancing the differing chemical potentials). Vice versa, oil enters the hydrogel as well; however, only to such an extremely low degree (< 1 ppm) that we neglect it [39]. The advective flow of the oil superposes diffusive transport of water molecules. The imposed oil flow of $v = 5$ mm/s creates a situation where the relaxation of the osmotic pressure becomes impossible: dry silicone oil enters the flow channel ($l = 53.2$ mm) at a rate of $\tau_{\text{adv.}}^{-1} = v/l \approx 0.1 s^{-1}$. In fact, the advective transport dominates over the diffusive transport, depicted by the Peclet number ($\mathrm{Pe} = vl/D = 1.33 \times 10^5$ to 5.32×10^6), which relates the two transport mechanisms to each other. Water molecules migrating from the hydrogel into the oil are entrained and quickly removed from the shared interface by the oil flow.

Therefore, the water concentration at the shared interface is unlikely to be in local equilibrium here, *i.e.*, the oil is unsaturated. In this state of imbalance, water molecules in the hydrogel and oil have differing standard enthalpies, which resembles the latent heat of an evaporation process. The differing enthalpy can be considered an energetic barrier at the shared interface, which holds the water molecules within the hydrogel. The free energetic barrier at the shared interface prevents the water molecules from spontaneous migration into the oil flow. We now assume that the escape of a water molecule may be viewed as an activated process, for which Kramers' theory can be applied [40]. According to this theory, the escape rate is

$$\tau^{-1} = \frac{D}{2\pi\sigma^2} \frac{\Delta U}{k_B T} \exp\left(-\frac{\Delta U}{k_B T}\right) \tag{B.44}$$

where ≈ 1 nm is the thickness of the shared interface, U is the energy barrier height over which water molecules have to diffuse, $k_B = 1.380 \times 10^{-23} J/K$ is the Boltzmann constant, and $T = 293$ K the ambient temperature. We determine the height of the barrier to be in the range of $20.3 - 21.3$ $k_B T$, (see Sec. B.3).

Starting from these assumptions, we conducted a finite element analysis (FEM, model and simulation) of the water distribution in the silicone oil, Fig. B.27a. The water concentration is low close to the inlet (yellow) and increases along the flow direction. We highlight four lines (I-IV) of constant

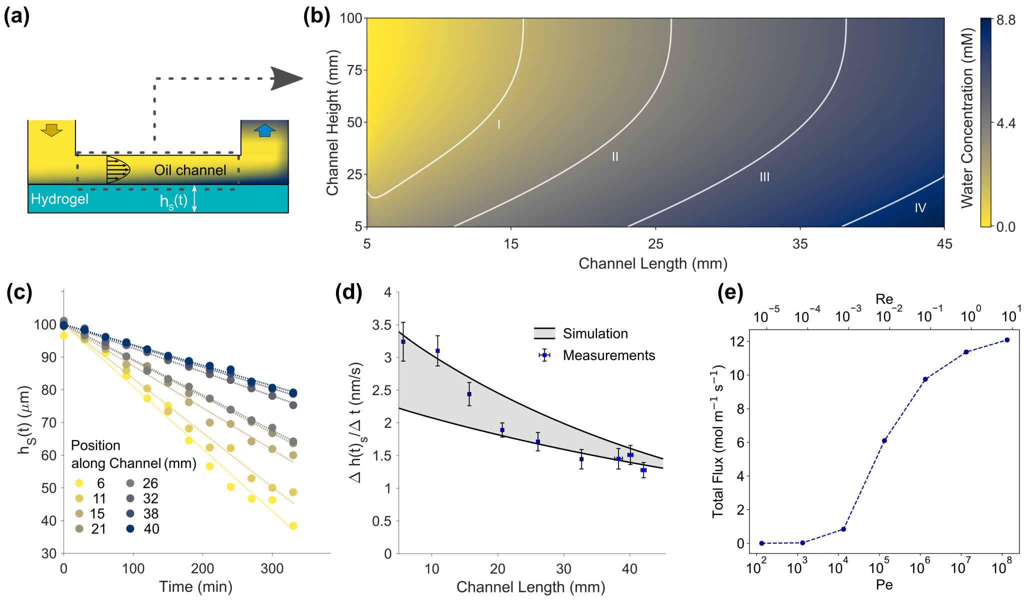

Figure B.27: Dehydration of the hydrogel by diffusion and advection. (a) Sketch of flow channel. Water diffuses into the oil at the shared hydrogel-oil interface. $h_S(t)$ is height of hydrogel. Dashed white box demarcates position shown in (b) Water concentration field in the oil between inlet and outlet, obtained by direct numerical simulation. The dry oil (yellow) enters the flow cell. The water concentration increases in the flow direction. The white lines I-IV correspond to water concentration in the oil of $2, 4, 6$, and 8 mm, respectively. (c) $h_S(t)$, evolution on 8 positions along the channel axis (channel height: 100 μm). The hydrogel thickness decreases more slowly in the downstream direction. The dotted lines are linear fits of the measurement data and help to guide the eye. (d) Slope of the time evolution of the hydrogel thickness, along the channel length/oil layer thickness. Solid lines represent results from simulation, while symbols represent the confocal microscopy measurements. The flow cells used for these experiments have a volume of $23L$, a height of $H = 100$ μm, a length of $L = 45$ mm, and a width of $W = 5.0$ mm. (e)Total water flux, integrated along the entire interface length. For all Pe and Re configurations, the free energy barrier was set to 20.3 k_BT.

water concentrations ($42, 4, 6$, and 8 mm, respectively) to visualize the increasing water concentration along the channel. Consequently, dehydration of the hydrogel progresses faster in the upstream direction. This is in line with experimental observations, Fig. B.35 and Fig. B.37. Water enriched oil (approx. 9 mm; however, not saturated) leaves the channel on the right-hand side. Considering the conservation of mass in the hydrogel, we can map the measured vertical hydrogel height to the depleting water flux. The grey area in Fig. B.27c marks the range of fluxes for the determined barrier heights. The overlaid data (blue squares) from experiments and simulation show excellent agreement, providing further support for these considerations. This picture considers the hydrogel's response as instantaneous because of the huge amount of swollen water. This implies neglecting any effects, such as e.g., elastic deformation (Fig. B.36). We expect that when the hydrogel is nearly fully depleted, these effects cause the sharp transition between the diffusion-advection-dominated regime and the steady-state retention thickness. To obtain insights into the dependency of flow condition and dehydration kinetics, we conduct simulations for Pe from 10^2 to 10^8, Fig. B.27e. Here, we show dehydration rates integrated along the channel length, shown in Fig. B.27b. The free energy barrier for these calculations was set to 20.3 $k_B T$. The dehydration rates plateaus in two regimes: for low Pe, *i.e.*, Pe $\ll 10^5$ the dehydration rate is diminishingly small. The oil in the microchannel flows at such low rates, that the entire channel interior saturates and the chemical potential difference between hydrogel and oil flow are close to zero. Water migration from hydrogel to oil phase becomes limited by the very weak oil flow. For Pe $\gg 10^5$, the oil migration levels around $11 mol m^{-1} s^{-1}$. This upper limit of oil migration is limited by the free energy barrier at the hydrogel interface. Only in-between those two plateaus, the dehydration rates depend on the Péclet number. Note, that taking the low free energy barrier (20.3 $k_B T$) leads to higher dehydration rates. Since we observe no variations of dehydration rates with different flow conditions in the experiments, we expect that the free energy barrier in the experiments is in fact higher, *i.e.*, more favoured towards the 21.3 $k_b T$ value.

To test the hypothesis that shrinkage is determined by the finite solubility of water in oil, we conducted experiments using water-saturated oil. Indeed, the thickness of the hydrogel remains unaltered beyond sample inhomogeneity (Fig. B.28a). In contrast, when conducting the shrinkage experiment with silicone oil, which is not water-saturated, one observes the already familiar linear shrinkage of the hydrogel coating. Therefore, shrinkage (dehydration) can be avoided by subjecting the swollen hydrogel to a shear flow of water-saturated oil. No observable water migration occurs from the water tethered in the hydrogel into the external oil phase.

To substantiate our findings further, we conducted the same shrinkage experiments with oils that are chemically different from silicone oil. Olive oil (Fig. B.28b, green hexagons), a mixture of fatty acids, shows linear shrinkage behaviour analogous to silicone oil. When conducting shrinkage experiments with mineral oil and FluorinertTM FC-70® (Perfluorotripentylamine, C15F33N), one observes a nonlinear shrinkage behaviour. The solubility of water in mineral oil (Fig. B.28b, black circles) is approximately 0.2 mm, which is two orders of magnitude smaller than the solubility of water in silicone oil (≈ 30 mm). Hence, water saturation occurs in the early stages of the shrinkage experiment, *i.e.*, after a much shorter time than shrinkage experiments conducted with silicone oil. When conducting shrinkage experiments with FluorinertTM FC-70®, the thickness of the hydrogel coating remains constant throughout the shrinkage experiment (Fig. B.28b, red squares). The extremely low solubility of water in FC-70®, which lies below 10 μm, explains this observation.

Conclusion

In summary, we have investigated the stability of hydrogels under shear flows of oil. We found experimentally that swollen hydrogels are linearly shrinking irrespective of the investigated flow velocity, oil viscosity, and the hydrogel's chemical nature. A gradient in the chemical potential between

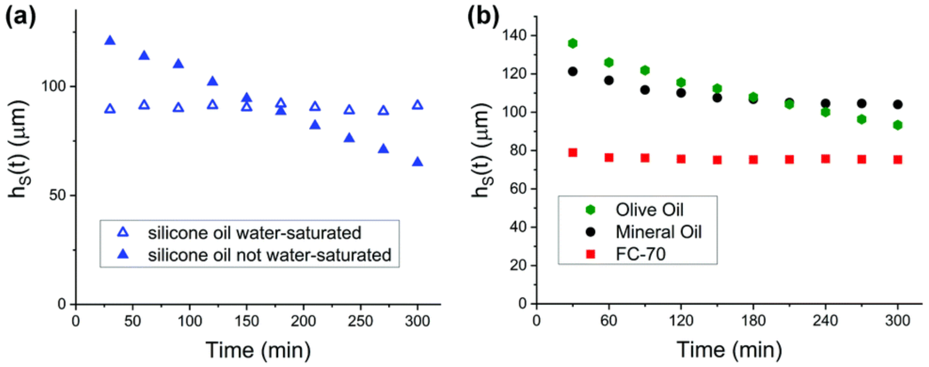

Figure B.28: Influence of water saturation. (a) Presence (solid triangles) or absence (open triangles) of shrinkage on swollen hydrogel coatings subjected to a shear-flow of neat and water-saturated silicone oil. (b) Olive oil (green hexagons) shows linear shrinkage behaviour analogous to silicone oil. For mineral oil (black circles) and the perfluorinated oil FluorinertTM FC-70®(red squares), the oil achieves water saturation early during the shrinkage experiment. Hence, the dehydration comes to a halt, translating into a constant thickness of the hydrogel coating.

the hydrogel and any surrounding phase gives diffusion as a dehydration mechanism. The hydrogel structure can continuously adjust to cope with a wide window of water concentrations without evoking significant thermodynamic changes. The chemical potential gradient vanishes when saturating the oil. In this case, the diffusion-driven dehydration is neutralized. This is confirmed by our control experiment working with water-saturated oils.

Numerical simulations revealed that the interplay between the diffusion of water into the oil phase and the advective transport of the oil is the underlying universal mechanism for the observed shrinkage behaviour. The only condition is that there is a time-scale separation, and the transition of the water into the flowing liquid is sufficiently slow. The finite yet non-vanishing solubility of water in oil proved central to explaining the observed phenomena. Our findings help to improve our understanding of the fundamental physics of hydrogels. The same depletion mechanism (among others) is expected for swollen organogels, which are frequently used as low adhesive surfaces.

Author Contributions

Philipp Baumli: Conceptualization, Methodology, Investigation, Visualization, Resources, Writing – Original Draft, Writing- Review Editing, Lukas Hauer: Software, Formal Analysis, Validation, Data Curation, Visualization, Writing – Original Draft, Writing- Review Editing, Emanuela Lorusso: Conceptualization, Methodology, Resources, Writing – Original Draft, Azadeh Sharifi Aghili: Resources, Investigation, Katharina, I. Hegner: Resources, Investigation, Maria D'Acunzi: Resources, Investigation, Jochen S. Gutmann: Supervision, Writing- Review Editing, Project Administration, Burkhard Dünweg: Supervision, Writing- Review Editing and Doris Vollmer: Supervision, Writing-

Review Editing, Project Administration, Funding Acquisition.

Acknowledgements

The authors acknowledge the funding received from the European Union's Horizon 2020 research and innovation program under the Marie Skłodowska-Curie grant agreement No 722497 (Innovative Training Network) ITN LubISS (P.B., E.L.), the support from a Swiss National Science Foundation (SNSF) Early Postdoc.Mobility fellowship under project number P2SKP2 191361 (P.B.), the Priority Programme SPP 2171 (D.V., L.H.) the Max Planck – Univ. Twente Center for Complex Fluid Dynamics (D.V.) and the Max Planck Graduate Center (MPGC) (K.I.H.). The authors thank Hans-Jürgen Butt, Lou Kondic, Detlef Lohse, Abhinav Naga, Harald Pleiner, Walter Richtering, Thomas Vilgis, and William S.Y. Wong for helpful and stimulating discussions. The authors are grateful to Anke Kaltbeitzel and Alexandre Laroche (Airbus) for assisting in confocal microscopy and photography.

References

1. Caló, E. & Khutoryanskiy, V. V. Biomedical Applications of Hydrogels: A Review of Patents and Commercial Products. *European Polymer Journal* **65,** 252–267. ISSN: 0014-3057 (2015/04/01/).
2. Lee, K. Y. & Mooney, D. J. Hydrogels for Tissue Engineering. *Chem. Rev.* **101,** 1869–1880. ISSN: 0009-2665, 1520-6890 (July 2001).
3. Guo, Y. *et al.* Hydrogels and Hydrogel-Derived Materials for Energy and Water Sustainability. *Chem. Rev.* **120,** 7642–7707. ISSN: 0009-2665, 1520-6890 (Aug. 2020).
4. Peppas, N. A., Hilt, J. Z., Khademhosseini, A. & Langer, R. Hydrogels in Biology and Medicine: From Molecular Principles to Bionanotechnology. *Adv. Mater.* **18,** 1345–1360. ISSN: 0935-9648, 1521-4095 (June 2006).
5. Tanaka, T. Gels. *Sci. Am.* **244,** 124-S–17. ISSN: 0036-8733 (1981).
6. Peppas, N. A., Huang, Y., Torres-Lugo, M., Ward, J. H. & Zhang, J. Physicochemical Foundations and Structural Design of Hydrogels in Medicine and Biology. *Annu. Rev. Biomed. Eng.* **2,** 9–29. ISSN: 1523-9829, 1545-4274 (Aug. 2000).
7. Flory, P. J. Statistical Mechanics of Swelling of Network Structures. *J. Chem. Phys.* **18,** 108–111. ISSN: 0021-9606, 1089-7690 (Jan. 1950).
8. Volk, N., Vollmer, D., Schmidt, M., Oppermann, W. & Huber, K. in *Polyelectrolytes with Defined Molecular Architecture II* (ed Schmidt, M.) 29–65 (2004).
9. Schmidt, M. *Polyelectrolytes with Defined Molecular Architecture I* ISBN: 978-3-540-00528-5 (2004).
10. Halperin, A., Kröger, M. & Winnik, F. M. Poly(N-isopropylacrylamide) Phase Diagrams: Fifty Years of Research. *Angewandte Chemie International Edition* **54,** 15342–15367. ISSN: 1433-7851 (2015).
11. Heskins, M. & Guillet, J. E. Solution Properties of Poly(N-isopropylacrylamide). *J. Macromol. Sci. A* **2,** 1441–1455. ISSN: 0022-233X (Dec. 1968).
12. Haq, M. A., Su, Y. & Wang, D. Mechanical Properties of PNIPAM Based Hydrogels: A Review. *Mater. Sci. Eng. C* **70,** 842–855. ISSN: 09284931 (Jan. 2017).

13. Tanaka, T. Collapse of Gels and the Critical Endpoint. *Phys. Rev. Lett.* **40,** 820–823. ISSN: 0031-9007 (Mar. 1978).

14. Hirotsu, S., Hirokawa, Y. & Tanaka, T. Volume-Phase Transitions of Ionized *N* -Isopropylacrylamide Gels. *J. Chem. Phys.* **87,** 1392–1395. ISSN: 0021-9606, 1089-7690 (July 1987).

15. Tamai, Y., Tanaka, H. & Nakanishi, K. Molecular Simulation of Permeation of Small Penetrants through Membranes. 1. Diffusion Coefficients. *Macromolecules* **27,** 4498–4508. ISSN: 0024-9297, 1520-5835 (Aug. 1994).

16. Meid, J. *et al.* Mechanical Properties of Temperature Sensitive Microgel/Polyacrylamide Composite Hydrogels—from Soft to Hard Fillers. *Soft Matter* **8,** 4254. ISSN: 1744-683X, 1744-6848 (2012).

17. Richtering, W. & Saunders, B. R. Gel Architectures and Their Complexity. *Soft Matter* **10,** 3695–3702. ISSN: 1744-683X, 1744-6848 (2014).

18. Takahashi, A., Kato, N. & Nagasawa, M. The Osmotic Pressure of Polyelectrolyte in Neutral Salt Solutions. *J. Phys. Chem.* **74,** 944–946. ISSN: 0022-3654, 1541-5740 (Feb. 1970).

19. Cai, S. & Suo, Z. Mechanics and Chemical Thermodynamics of Phase Transition in Temperature-Sensitive Hydrogels. *J. Mech. Phys. Solids* **59,** 2259–2278. ISSN: 00225096 (Nov. 2011).

20. Dalgicdir, C., Rodríguez-Ropero, F. & van der Vegt, N. F. A. Computational Calorimetry of PNIPAM Cononsolvency in Water/Methanol Mixtures. *J. Phys. Chem. B* **121,** 7741–7748. ISSN: 1520-6106 (Aug. 2017).

21. Hu, X.-S., Liang, R. & Sun, G. Super-Adsorbent Hydrogel for Removal of Methylene Blue Dye from Aqueous Solution. *J. Mater. Chem. A* **6,** 17612–17624. ISSN: 2050-7488, 2050-7496 (2018).

22. Pereira, A. G., Rodrigues, F. H., Paulino, A. T., Martins, A. F. & Fajardo, A. R. Recent Advances on Composite Hydrogels Designed for the Remediation of Dye-Contaminated Water and Wastewater: A Review. *Journal of Cleaner Production* **284,** 124703. ISSN: 09596526 (Feb. 2021).

23. Lutolf, M. P. *et al.* Synthetic Matrix Metalloproteinase-Sensitive Hydrogels for the Conduction of Tissue Regeneration: Engineering Cell-Invasion Characteristics. *Proc. Natl. Acad. Sci. U.S.A.* **100,** 5413–5418 (2003).

24. Lauto, A., Mawad, D. & Foster, L. J. R. Adhesive Biomaterials for Tissue Reconstruction. *J. Chem. Technol. Biotechnol.* **83,** 464–472. ISSN: 02682575, 10974660 (Apr. 2008).

25. Kim, K. D. & Wright, N. M. Polyethylene Glycol Hydrogel Spinal Sealant (DuraSeal Spinal Sealant) as an Adjunct to Sutured Dural Repair in the Spine: Results of a Prospective, Multicenter, Randomized Controlled Study. *Spine* **36,** 1906–1912. ISSN: 0362-2436 (Nov. 2011).

26. Mehdizadeh, M. & Yang, J. Design Strategies and Applications of Tissue Bioadhesives. *Macromolecular Bioscience* **13,** 271–288. ISSN: 1616-5187 (2013).

27. Michel, R. *et al.* Interfacial Fluid Transport Is a Key to Hydrogel Bioadhesion. *Proc. Natl. Acad. Sci. U.S.A.* **116,** 738–743 (2019).

28. Papadopoulos, P., Mammen, L., Deng, X., Vollmer, D. & Butt, H.-J. How Superhydrophobicity Breaks Down. *Proc. Natl. Acad. Sci. U.S.A.* **110,** 3254–3258 (2013).

29. Schellenberger, F. *et al.* Direct Observation of Drops on Slippery Lubricant-Infused Surfaces. *Soft Matter* **11,** 7617–7626. ISSN: 1744-683X, 1744-6848 (2015).

30. Chatterjee, S., Major, G. H., Lunt, B. M., Kaykhaii, M. & Linford, M. R. Polyallylamine as an Adhesion Promoter for SU-8 Photoresist. *Microsc. Microanal.* **22,** 964–970. ISSN: 1431-9276, 1435-8115 (Oct. 2016).

31. Zhu, Z., Chen, P., Liu, K. & Escobedo, C. A Versatile Bonding Method for PDMS and SU-8 and Its Application towards a Multifunctional Microfluidic Device. *Micromachines* **7,** 230. ISSN: 2072-666X (Dec. 2016).

32. Probstein, R. F. *Physicochemical Hydrodynamics: An Introduction* Second. ISBN: 978-0-471-72512-1 (2005).
33. Barrie, J. A. & Machin, D. The Sorption and Diffusion of Water in Silicone Rubbers. Part II. Filled Rubbers. *J. Macromol. Sci. Phys.* **3,** 673–692. ISSN: 0022-2348 (Dec. 1969).
34. Acheson, D. J. *Elementary Fluid Dynamics* 1st. ISBN: 978-0-19-859679-0 (1990).
35. Amestoy, P. R., Duff, I. S., L'Excellent, J.-Y. & Koster, J. *MUMPS: A General Purpose Distributed Memory Sparse Solver* in (eds Sørevik, T., Manne, F., Gebremedhin, A. H. & Moe, R.) (2001), 121–130. ISBN: 978-3-540-70734-9.
36. Kaklamani, G. *et al.* Anisotropic Dehydration of Hydrogel Surfaces. *Prog. Biomater.* **6,** 157–164. ISSN: 2194-0509, 2194-0517 (Dec. 2017).
37. Sekine, Y. & Ikeda-Fukazawa, T. Structural Changes of Water in a Hydrogel During Dehydration. *J. Chem. Phys.* **130,** 034501. ISSN: 0021-9606, 1089-7690 (Jan. 2009).
38. Bao, L. *et al.* Flow-Induced Dissolution of Femtoliter Surface Droplet Arrays. *Lab Chip* **18,** 1066–1074. ISSN: 1473-0197, 1473-0189 (2018).
39. Baumli, P. *et al.* Flow-Induced Long-Term Stable Slippery Surfaces. *Adv. Sci.,* 1900019. ISSN: 2198-3844, 2198-3844 (Apr. 2019).
40. Risken, H. in *The Fokker-Planck Equation: Methods of Solution and Applications* 63–95 (Berlin, Heidelberg, 1996). ISBN: 978-3-642-61544-3.
41. Jin, Y. *et al.* Thermally Tunable Dynamic and Static Elastic Properties of Hydrogel Due to Volumetric Phase Transition. *Polymers* **12,** 1462. ISSN: 2073-4360 (June 2020).
42. Takigawa, T., Yamawaki, T., Takahashi, K. & Masuda, T. Change in Young's Modulus of Poly(n-Isopropylacrylamide) Gels by Volume Phase Transition. *Polym. Gels Netw.* **5,** 585–589. ISSN: 0966-7822 (Apr. 1998).

Supplementary Information

Discussion on Free Energy Barrier

We assume that the escape of a water molecule may be viewed as an activated process, for which Kramers' theory can be applied [40]. According to this theory, the escape rate is

$$\tau^{-1} = \frac{\omega_{min}\omega_{max}}{2\pi\zeta} \exp\left(-\frac{\Delta U}{k_B T}\right) = \frac{D\omega_{min}\omega_{max}}{2\pi\ k_B T} \exp\left(-\frac{\Delta U}{k_B T}\right). \tag{B.45}$$

where k_B is the Boltzmann constant, T the absolute temperature, ΔU the barrier height, and ω_{min}^2 and ω_{max}^2 are the spring constants describing the harmonic expansion of the barrier potential at the minimum and the maximum, respectively. ζ is the molecule's friction coefficient, which is related to its (tracer) diffusion coefficient D via the Einstein relation $D = k_B T/\zeta$. Furthermore, we assume that for D we can take the tracer diffusion coefficient for water at room temperature, $D \approx 2.3$ nm^2/ns. Furthermore, we assume that the spring constants may be roughly estimated as:

$$\omega_{min}^2 = \omega_{max}^2 = \frac{\Delta U}{\sigma^2} \tag{B.46}$$

where σ is the thickness of the oil-water interface, assumed to take the value 1 nm. We thus arrive at

$$\tau^{-1} = \frac{D}{2\pi\sigma^2} \frac{\Delta U}{k_B T} \exp\left(-\frac{\Delta U}{k_B T}\right) \tag{B.47}$$

From the experimentally measured shrinkage rate and the density of water we may estimate the escape rate as roughly $5s^{-1}$. Inserting numbers, we find

$$\frac{\Delta U}{k_B T} \exp\left(-\frac{\Delta U}{k_B T}\right) = 1.3 \times 10^{-9}. \tag{B.48}$$

which we may view as a nonlinear equation for $\frac{\Delta U}{k_B T}$. The equation has two solutions, which may be found numerically, and the physically reasonable one is the larger value, $\frac{\Delta U}{k_B T} \approx 21$. In other words, the small shrinkage rate may be explained in terms of a barrier height of order 20 $k_B T$20, which we feel is not unreasonable.

Supplementary Figures

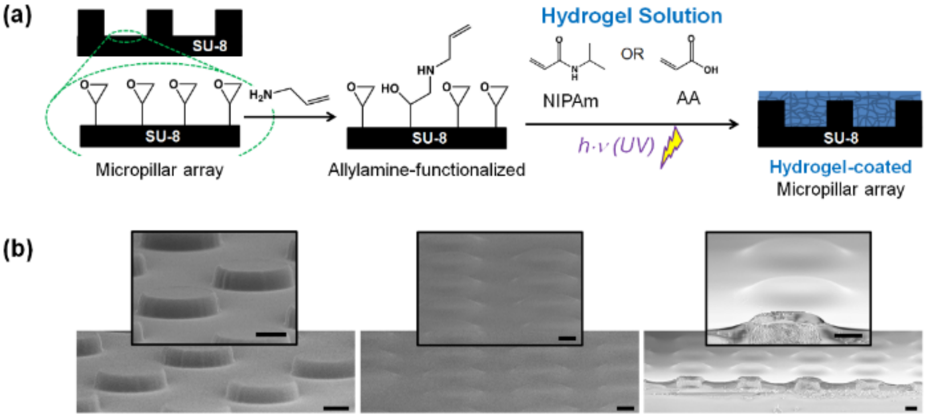

Figure B.29: Sample preparation a) Preparation of Hydrogel Coating on SU-8 photoresist-based micropillar arrays (pillar diameter: 30 μm,centre-to-centre spacing: 60 μm, Pillar height: 10 μm. The hydrogel solution consisting of either N-isopropylamide (NIPAm) or acrylic acid (AA) monomers, initiator, and crosslinker is applied via doctor blading, followed by UV-illumination (Methods). b) SEM images (Methods) of neat unfunctionalized micropillars (left), pillar array coated with hydrogel, dry state (middle), and the cross-section through hydrogel coating (right). All scale bars are 10 μm.

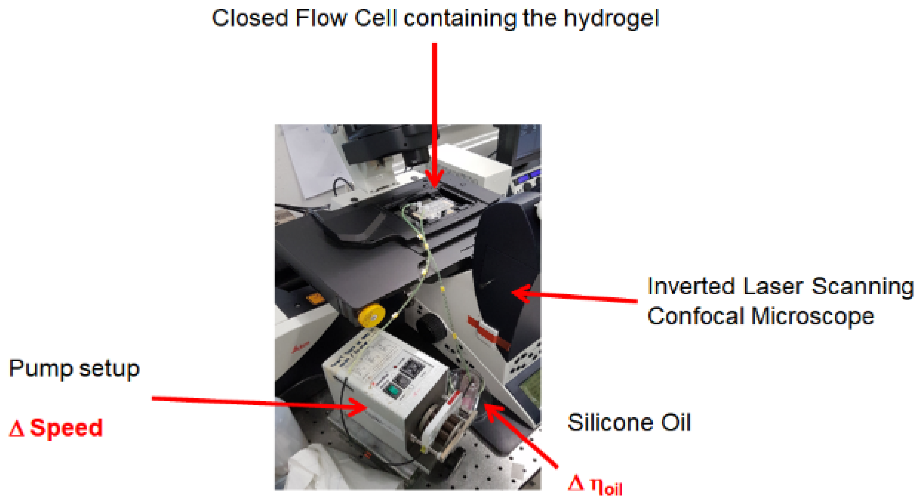

Figure B.30: Experimental setup. The key components are the inverted laser scanning confocal microscope (Leica TCS SP8 SMD), the pump, and the hydrogel coatings in flow cells. The system is not open to the atmosphere. The vials containing the oil and the flow cells are sealed with paraffin tape.

Table B.3: Boundary conditions on Ω_{oil} . Boundaries $W_1 - W_8$ demarcate the computational domain. $\boldsymbol{n}$ and $\boldsymbol{t}$ are the boundaries normal and tangential vectors, respectively. The kinematic flux on W_4 resembles the determined free energy barrier [Eq. (B.47)] and is linearized with respect to c, with $j_0 = 0.1 - 0.16$ mmol/sm^2 and $j_1 = 10 - 18$ μm/s. This takes into account that an increased water concentration in the oil gives rise to a reduced thermodynamic driving force, thus reducing the flux.

Boundary	Boundary Type (Momentum)	Boundary Condition	Boundary Type (Mass)	Boundary Condition
W_1	constant inflow	$u_x = 5$ mm/s $u_y = 0$	no normal diffusion	$\nabla c \cdot \boldsymbol{n} = 0$
W_2	no-slip	$u_x = u_y = 0$	no flux	$\boldsymbol{j} = 0$
W_3	no-slip	$u_x = u_y = 0$	no flux	$\boldsymbol{j} = 0$
W_4	no-slip	$u_x = u_y = 0$	kinematic flux	$\boldsymbol{j} \cdot \boldsymbol{n} = j_0 - j_1 c$
W_5	no-slip	$u_x = u_y = 0$	no flux	$\boldsymbol{j} = 0$
W_6	no-slip	$u_x = u_y = 0$	no flux	$\boldsymbol{j} = 0$
W_7	no-slip	$u_x = u_y = 0$	no flux	$\boldsymbol{j} = 0$
W_8	no normal stress; no lateral flow	$\boldsymbol{n}^T \cdot \boldsymbol{\tau} \boldsymbol{n} = 0$ $u_y = 0$	no normal diffusion	$\nabla c \cdot \boldsymbol{n} = 0$

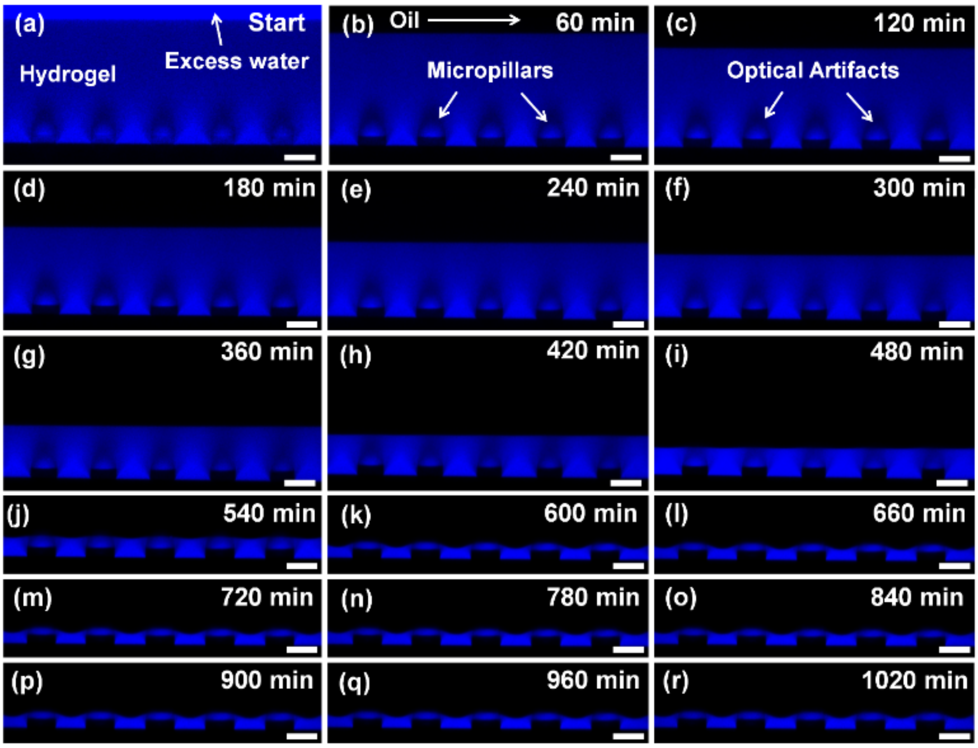

Figure B.31: Linear Shrinkage of PAA-Hydrogels with Oil Flows. Time evolution of side view (xz-scan) laser scanning confocal images (40x/1.1 water immersion objective lens) demonstrating progressive dehydration of a hydrogel coating consisting of PAA on a micropillar array (based on SU-8) due to the flow of oil across the coating (flow direction from left to right). The time series consists of images acquired in the fluorescence channel. Only the water (blue) in the hydrogel was dyed using a fluorescent dye (ATTO 488 NHS-Ester, concentration: 1 μg/g). The dye concentration is sufficiently low not to change the interfacial tension. Image acquisition was performed in the middle of the flow channel using a line average of 8 and a scanning frequency of 600 Hz. a) Initially, the hydrogel coating is swollen with fluorescently labelled MilliQ-water and let to equilibrate for 30 min. b-j) Silicone oil (viscosity: 50 cSt, density: 0.96 g/ml) is then continuously circulated over the hydrogel-coated micropillar array at an average flow velocity of 5.3 mm/s. The continuous flow leads to progressive dehydration, *i.e.*, shrinkage, of the hydrogel, evidenced by the decreasing thickness of the fluorescence emission signal detected, representing the thinning of the hydrogel coating. The water leaving the hydrogel coating moves too fast to be monitored. Hence, only the water remaining within the hydrogel contributes to detected fluorescence. k - r) Eventually, the hydrogel reaches a steady-state thickness, which remains unchanged although oil continues to circulate continuously over the hydrogel coating. Pillar dimensions: diameter $d = 30$ μm, centre-to-centre spacing $p = 60$ μm, and pillar height $h = 10$ μm. All scale bars are 30 μm.

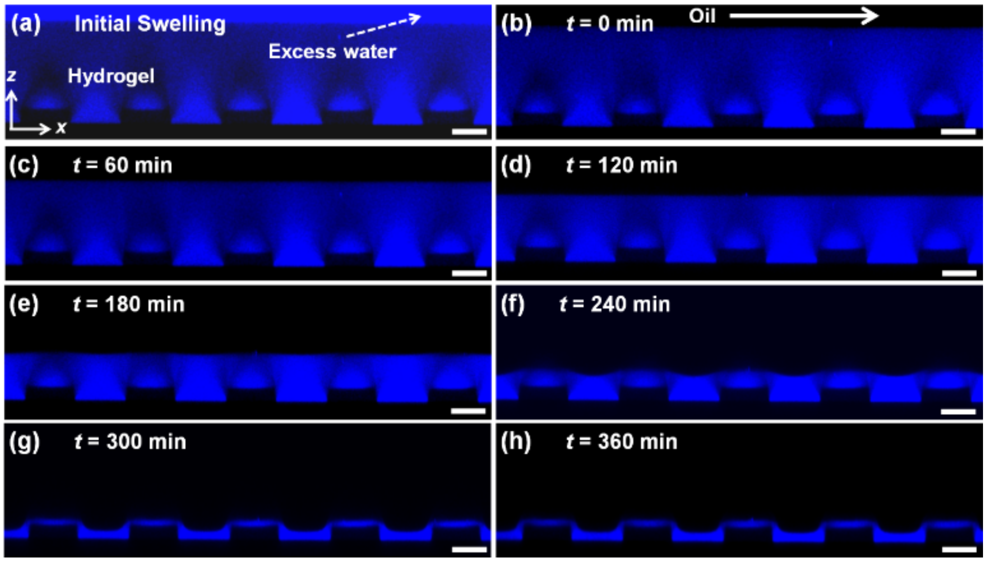

Figure B.32: Linear Shrinkage of PNIPAm-Hydrogels with Oil Flows. Time evolution of side view (xz-scan) laser scanning confocal images (40 × /1.1 water immersion objective lens) demonstrating progressive dehydration of a hydrogel coating consisting of PNIPAm with 20% crosslinking density on a micropillar array due to the flow of oil across the coating (flow direction from left to right). The time series consists of images acquired in the fluorescence channel. Only the water (blue) in the hydrogel was dyed using a fluorescent dye (ATTO 488 NHS-Ester, concentration: 1 μg/g). The dye concentration is sufficiently low not to change the interfacial tension. Image acquisition was performed in the middle of the flow channel using a line average of 8 and a scanning frequency of 600 Hz. a) Initially, the hydrogel coating is swollen with fluorescently labelled MilliQ-water and let to equilibrate for 30 min. b-g) Silicone oil (viscosity: 50 cSt, density: 0.96 g/ml) is then continuously circulated over the hydrogel-coated micropillar array at an average flow velocity of 5.3 mm/s. The continuous flow leads to progressive dehydration, *i.e.*, shrinkage, of the hydrogel, evidenced by the decreasing thickness of the fluorescence emission signal detected, representing the thinning of the hydrogel coating. The water leaving the hydrogel coating moves too fast to be monitored. Hence, only the water remaining within the hydrogel contributes to detected fluorescence. g, h) Eventually, the hydrogel reaches a steady-state thickness, which remains unchanged although oil continues to circulate continuously over the hydrogel coating. Pillar dimensions: diameter $d = 30$ μm, centre-to-centre spacing $p = 60$ μm, and pillar height $h = 10$ μm. All scale bars are 20 μm.

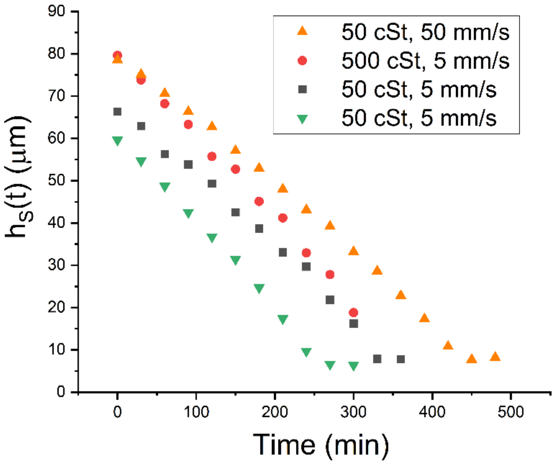

Figure B.33: Representative shrinkage experiments conducted on PNIPAm-based hydrogel coating subjected to a shear flow of silicone oil. Time evolution of the height of the hydrogel coating above the substrate. Summarizing the shrinkage experiments for the PNIPAm-based hydrogel, it appears that neither changing the flow velocity (5 mm/s – 50 mm/s) nor varying the oil viscosity (50–500 cSt) strongly affects hydrogel dehydration. Linear shrinkage behavior is evidenced by linear regression. Orange up triangle: $R^2 = 0.9972$, red solid circle: $R^2 = 0.9954$, black solid squares: $R^2 = 0.9912$, green down triangle: $R^2 = 0.9972$.

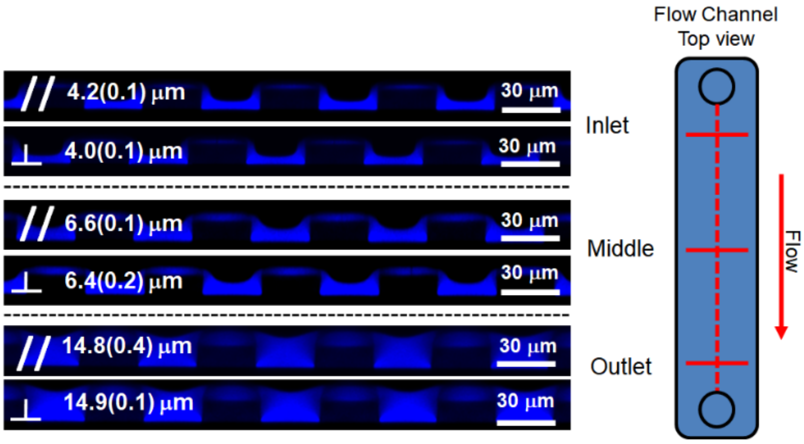

Figure B.34: Progress of shrinkage parallel and perpendicular to the flow direction. Situation of PNIPAm-based hydrogel subjected to a shear flow of 500 cSt silicone oil with an average flow velocity of 10 mm/s after 5 hours. The progress of dehydration close to the inlet is faster than close to the outlet (top view of flow channel on the right). Dehydration slows down in the downstream direction for the same lateral positions (perpendicular to the flow direction).

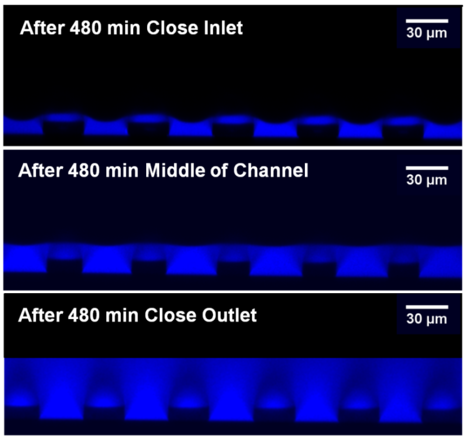

Figure B.35: Progress of shrinkage for PAA-based hydrogels. The progress of dehydration close to the inlet is faster than close to the outlet. After running the shrinkage experiment for 8 hours (480 min, Figure 2a), the shrinkage is more advanced close to the inlet than close to the outlet of the flow channel. Close to the inlet, the thickness of the hydrogel coating measured above the substrate amounts to 8.8 μm. In contrast, in the middle of the flow channel and close to the outlet of the flow channel, the obtained thicknesses of the hydrogel coating amounted to 21 μm and 48.4 μm, respectively.

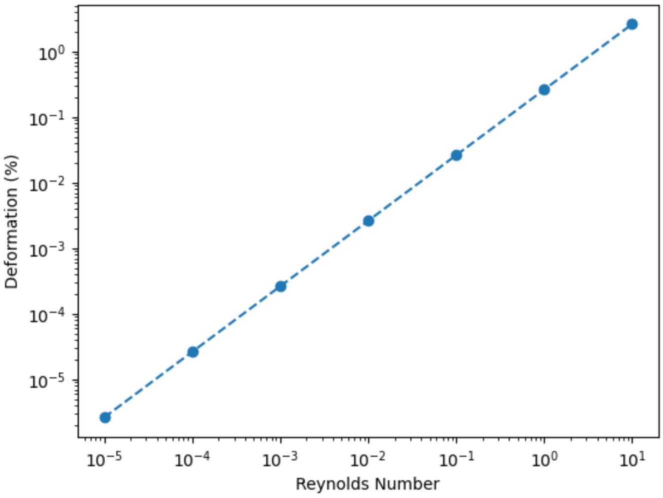

Figure B.36: Hydrogels normal deformation for different Reynolds numbers. At experimental flow conditions (Re $\approx 10^{-2}$) yields a deformation $\epsilon = \tau E/2(1+\nu)$ of around 0.02%. Here, $E \approx 10^5 Pa$ and ≈ 0.46 resembles the Youngs modulus and the Poisson ratio, respectively [41, 42].

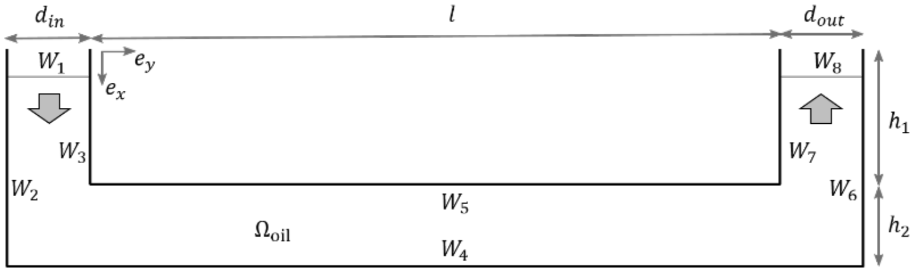

Figure B.37: Computational Domain. The oil is introduced into the domain Ω_{oil} on the left-hand side at W_1 and exits at W_8. $\boldsymbol{e}_x$ and $\boldsymbol{e}_y$ are the unit vectors in x and y direction. The inlet and the outlet have the same width $d_{\text{in}} = d_{\text{out}} = 3.8$ mm and a height of $h_1 = 0.9$ mm. The flow channel is $l = 53.2$ mm long and $h_2 = 0.1$ mm high. To close the set of partial differential equations (B.41) and (B.42) in the computational domain accurately describing the experimental situation, we define boundary conditions on $W_1 - W_8$ in Table B.3

B.4 How Frost Forms and Grows on Lubricated Micro- and Nanostructured Surfaces

Copyright

Lukas Hauer†, William SY Wong†, Valentina Donadei, Katharina I. Hegner, Lou Kondic, and Doris Vollmer ACS Nano 15, no. 3 (2021): 4658-4668.

† equal contribution

Abstract

Frost is ubiquitously observed in nature whenever warmer and more humid air encounters colder than melting point surfaces (e.g. morning dew frosting). However, frost formation is problematic as it damages infrastructure, roads, crops and efficient operation of industrial equipment (*i.e.* heat exchangers, cooling fins). While Lubricant Infused Surfaces (LIS) offer promising anti-frosting properties, underlying mechanisms of frost formation and its consequential effect on frost-to-surface dynamics remain elusive. Here, we monitor the dynamics of condensation-frosting on micro- and hierarchically structured surfaces (the latter combines micro- with nano- features) infused with lubricant, temporally and spatially resolved using Laser Scanning Confocal Microscopy. The growth dynamics of water droplets differs for micro- and hierarchically structured surfaces, by hindered drop-coalescence on the hierarchical ones. However, the growth and propagation of frost dendrites follows the same scaling on both surface types. Frost propagation is accompanied by a reorganization of the lubricant thin film. We numerically quantify the experimentally observed flow profile using an asymptotic long-wave model. Our results reveal that lubricant reorganization is governed by two distinct driving mechanisms, namely: 1) Frost propagation speed and 2) Frost dendrite morphology. These in-depth insights into the coupling between lubricant flow and frost formation/propagation enable improved control over frosting by adjusting design and features of the surface.

Introduction

Water is widely available in the atmosphere and in the environment. The interplay between the chemical properties of water and the thermal conditions of our planet results in the formation of clouds, rain or frost [1, 2]. Despite the ubiquitous nature of frost, understanding and controlling its formation [3] and propagation [4, 5] still poses several challenges. Control of frosting is relevant for a range of industries: In the energy [6], transportation [7] or telecommunication [8] sectors, frost constitutes serious hazards when it forms on critical components of machines and devices, causing them to fail. To control frosting, a strong momentum of research in anti-icing technology [9–11] was recently generated. Surfaces which passively avoid, repel or retard frost or ice formation were designed [12–15]. Lubricant infused surfaces (LIS) were shown to resist frost formation more efficiently compared to dry micro-/nanostructured or flat, chemically functionalized variants [15]. Lubricant infused porous surfaces are characterized by solid three dimensional structures, infused with a liquid lubricant [16, 17]. The lubricant renders the surface slippery, resulting in a high mobility of contacting liquids. Capillary forces retain lubricants within the surface by virtue of the porous, structured geometry [18]. During condensation-frosting however, the lubricant in the porous structure of LIS appears to reorganize, leading to depletion of the structure [19, 20]. Aiming to gain insight in the underlying dynamics, here, we monitor and model lubricant reorganization and frost propagation dynamics (space- and time- resolved) on micro- and hierarchically (combining micro- with nanofeatures) structured surfaces under moderately low subzero temperatures (-12 ° to -22 °C). Despite widespread occurrence of frost, the understanding of its formation and growth particularly on LIS remains elusive. The reasons are multi-fold: Insights into frosting are hampered by poor optical contrast between frost and lubricant and by the non-equilibrium nature of frost formation, that involves multiple time and length scales. Mathematical modelling of the involved non-equilibrium processes requires the description of freezing, dendrite-growth, propagation of frost bridges and lubricant flow in mutual interplay. The first clue of lubricant reorganization was obtained by focused ion beam and scanning electron microscopy, revealing that frozen water droplets on LIS are covered by a thin layer of lubricant [19]. However, none of these techniques and investigations allow for insights into the coupled evolution of both frost and lubricant. To reach better insight, we have developed a setup that enables the in-situ monitoring of lubricant reorganization and frost formation using Laser Scanning Confocal Microscopy. Such a setup allows to discriminate between frost and lubricant. In particular, our setup provides the spatially and temporally resolved data of the formation and growth of frost, accompanied by quantifiable lubricant reorganization. The summary of our findings is that analogously to frost propagation on dry surfaces, frost bridges [4, 21] form. A strong capillary pressure inside the frost structure induces lubricant flow during condensation-frosting. Three-dimensional surface mapping by quantitative confocal microscopy provides a time-resolved evolution of lubricant during frosting. We then utilize a long-wave approximation [22] to model the experimentally quantified lubricant reorganization during the transient process of frost formation and propagation. We derive and solve the governing equations numerically to predict the height profile of the lubricant. The experimental data and numerical predictions for lubricant reorganization on micro- and hierarchically structured surfaces show excellent agreement. Notably, we find that lubricant reorganization and depletion is primarily affected by the frost propagation speed and dendritic frost geometry.

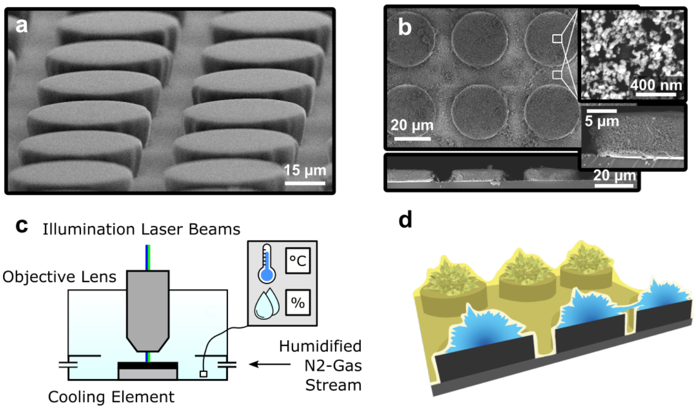

Figure B.38: Condensation-frosting on lubricated micro- and hierarchically structured surfaces. a) Scanning Electron Microscope (SEM) image of the plain micropillar surface. The pillars have a diameter of 30 μm, a height of 10 μm, with a separation distance of 10 μm. b) SEM images of hierarchical structure consisting of the micropillar array coated with silica nanoparticles on the entire surface. Highly magnified image (top right) of the particle coating show that individual particles have diameters of less than 50 nm. The entire surface is evenly coated with nanoparticles, while the microstructure is retained (bottom). c) Experimental set-up: The surface is mounted on the cooling element and monitored through an objective lens (2.5×, 10×, 100×). A green (532 nm) and a blue (473 nm) laser are used to illuminate the sample. A humidified carrier gas (nitrogen) is introduced into the chamber. During the experiment, the temperature and humidity in the far field are recorded. d) Schematics of condensation-frosting (blue) on the infused (yellow) micro-pillar substrate.

Results and Discussion

Condensation-frosting on lubricated micro- and hierarchically structured surfaces is temporally and spatially resolved by Laser Scanning Confocal Microscopy (LSCM). As model surfaces (approximately 5 cm^2 large), we use regularly spaced micropillar arrays (square orientation), Fig B.38. To analyse the influence of nanoroughness on condensation-frosting, lubricant distribution is monitored on bare micro (Fig B.38a) and hierarchically structured surfaces, characterized by both micro and nanoscopic features. Here, the hierarchical structure is facilitated by coating the micropillar arrays with a thin layer of silica nanoparticles, Fig B.38b. The cylindrical micropillars are fabricated by photolithography using an epoxy-based photoresist (SU-8, cf. Methods). Two variants of functionalized silica nanoparticles (amine- and epoxy-groups) are then deposited in a 'layer-by-layer' method, via a two-step-dip-coating procedure (cf. Methods). This creates a thin, homogenous nanoparticle coating of approximately 1 μm thickness on the micropillar array. The average roughness on top of the micropillars increased from 3.4 ± 0.3 nm to 35.1 ± 1.7 nm, after the nanoparticle coat was added, Fig B.43. We then infuse the surfaces with 2 μl of fluorescence marked silicone oil (viscosity, $\eta_{\mathrm{SiOil}} = 194$ mPa s) as a lubricant. After leaving the surface overnight homogeneous lubricant distribution in the pillars' interstices (approximately 10 μm height) with a thin layer on top of each pillar (below 1 μm) is verified by confocal microscopy. The LIS is placed on a cooling element in a sealed (frosting) cell and directly monitored simultaneously using a custom-built confocal microscope (Fig B.38c, Fig B.44, Methods). We cool down the surfaces to set-point temperatures below the atmospheric freezing point of water (Fig B.45) in a dry atmosphere ($<$ 4% relative humidity, RH) which were then held constant for 10 minutes. To trigger condensation-frosting, Fig B.38d, we flow a humidified nitrogen carrier gas (30% RH at 18.1 ± 0.6 ° C, Fig B.46, Methods) for 30 seconds into the cell. Thereafter, the cell is sealed. The long working distance of all objective lenses ($100 \times /0.80:\ 2$ mm; $10 \times /0.4:\ 3.1$ mm, $2.5 \times /0.07:\ 9$ mm) provides sufficient space between lens and sample to ensure evenly distributed humidity around the sample substrate. The laser illumination is noninvasive and does not interfere with the observed processes on the sample substrate, cf. SI S1.

Condensation on Microstructured LIS

Approximately 10 seconds after introducing the stream of humidified nitrogen into the frosting chamber, the formation of distinct and individual droplets on micropillar tops become visible (dark spheroids), Fig B.39a-b. Vertical cross-sectioning through the surface shows condensed droplets wrapped in lubricant and the accompanied depletion of lubricant between the micropillars, Fig B.39a. A 3D image reveals that the droplets (dark spots) are formed on top of the micropillars, Fig B.39b. The thin lubricant film on top of the micropillars is permeated easily by atmospheric water-vapour molecules via diffusion ($D_{\mathrm{W/SiOil}} = 2 \times 10^{-9}$ m^2/s) and accumulates at the micropillar-lubricant interface due to the finite solubility of water in silicone oil of up to 40 mM [23]. Here, stable nucleation sites for condensation are most likely due to sufficiently low energy sinks at this location (cf. Sec. B.4) [24–26]. After nucleation, the droplets grow in size and soon become visible under the microscope: Droplets appear as dark spheroids, surrounded by lubricant (yellow), Fig B.39a-b. At the contact line where the droplet, lubricant and air meet, the surface stresses of the respective phases fulfil a force balance [27]. The vertical component of the droplet surface stress promotes the formation of annular wetting ridges [28] of silicone oil around condensing water droplets. Due to a positive spreading parameter [29], $S = \gamma_{sv} - (\gamma_{sl} + \gamma_{lv}) \approx 12$ mN/m [14], silicone oil spreads on water, leading to completely cloaked [30, 31] droplet-air interfaces by lubricant. The lubricant layer around each droplet (ridge and cloak) slightly retards coalescence [32]. However, when the droplets grow, the layer thins until it becomes unstable and disintegrates, leading to coalescence. Eventually, only one single droplet (diameter $\approx 30\ \mu$m) remains on top of each micropillar, Fig B.39c.

Condensation on Hierarchical LIS

While the initial emergence of femtoliter droplets was similar on both surface types, the consecutive droplets-growth-phase deviates on hierarchically structured surfaces. The separating lubricant layer around droplets appears to be more stable. On hierarchically structured surfaces, not a single droplet but multiple sessile droplets remain on top of each pillar, Fig B.39d. The increased surface roughness introduces pinning sites for the droplets, leading to delayed coalescence. Hence, the nanoparticle coat prevents the coalescence of condensate droplets into a single one. To quantify the migration of lubricant during condensation, we monitor the film height in the array's interstices, i.e. in a square domain of $40\ \mu\text{m} \times 40\ \mu\text{m}$, containing 4 half micro-pillars (field of observation), Fig B.39e inset. The lubricant height h is evaluated at n=128 spots along the observed length (inset, dashed line) while the temporal resolution is 0.2 frames per second. The time dependence of the average height, $\langle h \rangle = 1/n \sum_i h_i(t)$, is shown for micro- (Fig B.39e) and hierarchically structured (Fig B.39f) surfaces, respectively. For micro structured surfaces, the average lubricant height depletes according to a square root behaviour, $\langle h \rangle = t^{-1/2}$ Fig B.39e, from the initial average height, $h_0 \approx 10$ mum within the first 100 seconds. The approximate square root scaling of $\langle h \rangle(t)$ is independent of substrate temperature and field of observation. We rationalize lubricant depletion in the micropillars' interstices by the formation of wetting ridges and cloaking of the condensing droplets. The direct correlation between condensation and depletion is supported by the square root scaling of the latter, which is similar for diffusion-controlled condensation (Eq (B.54), Methods). Furthermore, the depletion rate is proportional to the set-point temperature of the substrate (viz. Fig B.39e), which again, is typical for diffusion-controlled condensation, where supersaturation (or here undercooling) determines the magnitude of the condensation rate. For hierarchically structured surfaces, the depletion dynamics changes slightly: While lubricant height evolutions show a similar dependence between set-point temperature and depletion rate (cf. Fig B.39e) lubricant depletion deviates from the square root behaviour, Fig B.39f. We speculate that the delayed coalescence accompanied by a large number of smaller droplets causes the altered depletion dynamics. It should be noted that the wetting properties of the surface affects the location of preferred droplet nucleation, the number and size of condensed droplets25 and therefore frost formation and propagation.

Mesoscopic Frost Formation and Propagation

At the sub-zero surface temperatures, prolonged exposure eventually results in frosting of condensate droplets. We observe formation and propagation of the lubricant covered frost patches with a lower magnification objective (2.5×), providing a wider field of observation, Fig B.40a-b. Placing the

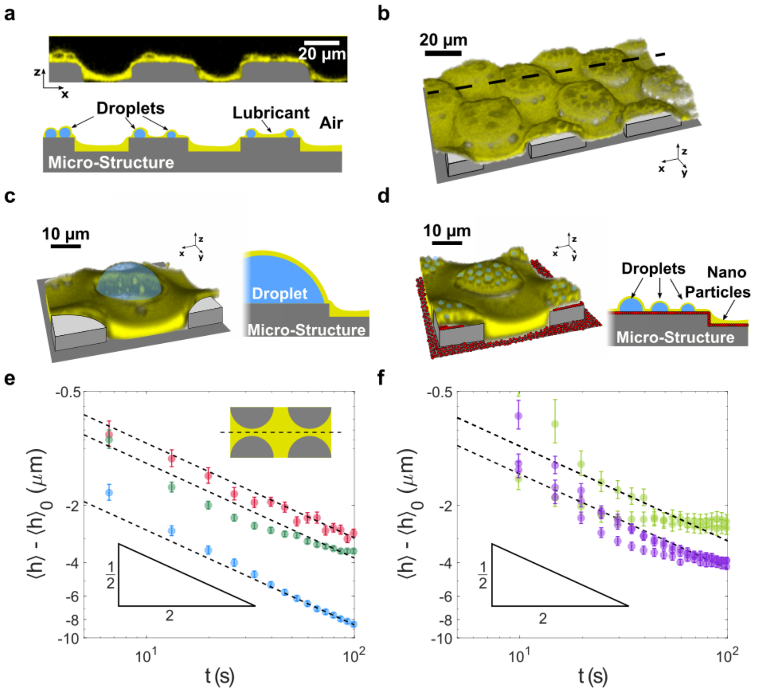

Figure B.39: Condensation of water droplets on lubricant infused, micro- and hierarchically structured surfaces. The silicone oil (yellow) is dyed with the fluorophore. Condensed water, the surfaces' micro- and nanostructures, and the surrounding air do not fluoresce and appear dark. a) and b) Condensing droplets on bare micro structured surfaces. The droplets become initially visible as spheroids on the pillars' tops, outlined by the fluorescent lubricant with LSCM. a) top: Vertical cross section through micropillars. Several droplets form on each pillar's top face. Bottom: Illustration of the initial condensation recording for clarification. b) 3-D view of the surface, showing lubricant distribution and condensed water droplets on the pillars' top (dark spots). c) On bare micro structured surfaces, condensing droplets coalesce, until a single, lubricant covered droplet resides on each pillar top, covered with lubricant. The yellow spots on the lubricant coat are either caused by oil patches or dye aggregates. d) On hierarchically structured surfaces, multiple drops remain on the pillars top faces. Illustrations of respective surfaces and condensate droplets (cf. Fig B.47 for raw data for c) and d)) e) Averaged lubricant displacement $\langle h \rangle - \langle h \rangle_0$ over time for micro- e) and hierarchically structured f) surfaces, within the first 100 seconds of the experiment. $\langle h \rangle_0 = 10$ μm refers to the lubricant height at $t = 0$ s. The height of the lubricant in between the pillars $\langle h \rangle(t)$ is spatially averaged over the dashed line (inset). Substrates are cooled down to -12 °C (red), -14 °C (dark green), -17 °C (light green), -20 °C (blue) and -22 °C (purple).

focal plane several μm above the micropillar base allows to accurately trace the frost. The higher focal plane also ensures that the lubricant within the micro-pillar array does not contribute to the integrated fluorescence intensity signal. Sometime after the initial 100 seconds, circular frost patches of increased fluorescence signal can be observed on the surfaces, Fig B.40a. The patches propagate over the surface, Fig B.40b, with an average front speed of $u_{\text{ice}} = 1.4 \pm 0.5$ μm/s, Fig B.48. To understand the formation and propagation of frost, we reconsider the situation where we have one large water droplet on each micro-pillar-top, Fig B.49. Freezing is initiated by the formation of stable, heterogeneous nucleation sites (ice crystals) in the liquid droplets at the pillar-liquid interface [33]. In general, freezing is a random process due to the inherently stochastic nature of nucleation [34]. Hence, the droplets do not freeze simultaneously, but instead in a staggered manner. Vapour pressure over liquid water exceeds that over frozen droplets by a ratio of approximately 1.1 at -12 °C [35]. This generates a vapour flux along the vapor pressure gradient. Water vapor molecules attach at the interface of the frozen droplet towards air. Small spikes and edges on the interface (perturbations) causes compression of the vapour field locally above the solid-vapour interface, yielding higher supersaturation. This amplifies the growth of the small spikes and edges (Mullins-Sekerka type of instability), giving rise to the formation of frost dendrites [36]. Ice bridges grow out from the frozen droplet, past the spacing distance of micro-pillars, reaching adjacent liquid droplets. Upon contact with the ice bridges, adjacent droplets freeze immediately [21]. This process repeats, enabling a frost cluster to grow gradually [4].

Depletion Zones

Frost propagation is accompanied by capillary-induced suction of lubricant into the dendritic frost domains, as reflected by the high fluorescence intensity in the frost, Fig B.40a-b. Further, directly in front of the propagating frost (2-3 pillars), the reflection signal (cyan) is noticeably more pronounced. This results from the pillar's top faces that were initially coated by an approximately 1 μm thick layer of lubricant, Fig 2a. Plain SU-8 has a higher refractive index ($n_{\mathrm{SU-8}} \approx 1.6$) [37] compared to silicone oil ($n_{\mathrm{SiOil}} \approx 1.4$)32. Thus, a stronger reflection signal indicates lubricant depleted zones. Depletion zones, however, do range further than only 2-3 pillars in front of the propagating frost, as we visualize with magnified (10× objective lens) top view recordings of the frost front, Fig B.40c Movie S1 [38]. Here, the frost propagates from the left to the right side within the field of view. To the left of the dashed white line, the irregular yellow domains reveal the frost-covered areas. To the right, the pillars are still covered by a single droplet per pillar (cyan). Fig B.40d shows the average fluorescence intensity within the dashed box of panel Fig B.40c. Right in front of the frost front, the integrated fluorescence intensity signal passes a minimum, and then gradually rises again further ahead of the frost. This unravels the presence of depletion zones, ranging $100 - 200$mum, in the direction normal to the frost front. Frost propagation ends when the condensed water droplets are entirely transformed into frost. The surface is then mostly covered with frost, leaving only small uncovered islands. The final area covered by frost depends on the amount of vapour which is initially induced into the frosting chamber.

Frost Induced Lubricant Depletion on Microstructured LIS

To monitor the dynamics of lubricant depletion during frost propagation, we return to the microscopic field of observation, centered on 4 half-pillars (100× objective lens, 40 μm × 40 μm). On micro structured surfaces, the average lubricant height was then measured for 420 s at two characteristic

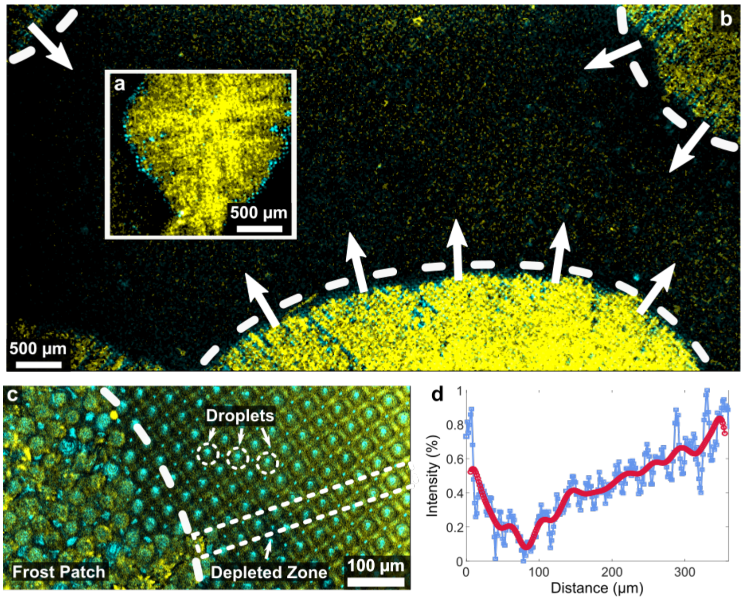

Figure B.40: Frost formation and propagation on lubricant infused surfaces. Frost patches form and propagate on the surface, while holding a large amount of fluorescence dyed lubricant (yellow). Simultaneously, the reflection light is monitored (cyan). a) Macroscopic top view of a freshly formed frost patch reveals a region with increased reflection signals in the vicinity of the patch's perimeter (cyan). Because unlubricated SU-8 ($n_{\mathrm{SU-8}} \approx 1.6$) reflects light better than lubricant ($n_{\mathrm{SiOil}} \approx 1.4$), increased reflection signal implies a lubricant depleted zone. Outside the frost patch, lubricant appears black. b) Frost patches propagating over the lubricant infused micro-pillar array (field of view: 6440 μm × 3220 μm). The frost grows ($u_{\mathrm{ice}} = 1.4 \pm 0.5$ μm/s) from the sides into the field of view. Images were taken at a rate of $0.96 s^{-1}$ c) Magnified frost front (cf. Movie S1). Region of depletion marked in the dashed box. d) Typical fluorescence intensity signal along the dashed box shown in Fig. 3c. The blue line is the raw signal, while the red line is noise (via low-pass) filtered. The periodicity in the blue curve agrees with the spacing of the micro-pillars. The optical signals are integrated over a depth of approximately 20 μm.

locations (visualized by the red and the blue curves), Fig B.41a. One location was eventually covered with frost (blue curve) while the other remained uncovered (red curve). As the profiles of the blue and the red curve nearly overlap in the condensation phase, for $t < 100$ s, we deduce that early depletion is unaffected by the location of the field of observation. However, while the decrease of lubricant height of the red curve changes only marginally after 100 s, $\langle h \rangle(t)$ may crosses over into a steep decrease (blue curve). Considering the global process of frost propagation in Fig B.40a, it becomes clear why frosting-induced depletion dynamics bifurcates into two distinctively different types, per red and blue curve. For the blue curve, the frost front approaches the field of observation, sucking the lubricant from the array into the frost dendrites. This becomes notable at the cross-over time $t_{\mathrm{co}} \approx 310$ s, at which the two linear slopes (Fig B.41a dashed lines), before and after cross-over intersect. At the last time-point shown ($t_{\mathrm{end}} = 420$ s), the frost front arrives at the field of observation and dendritic frost is clearly visible (cf. Fig B.41b-c). Lubricant cloaks the frozen water, revealing the morphology of the frost features. For the red curve, only far-range lubricant depletion from a distant frost patch influenced the lubricant height. This led to significantly slower depletion dynamics. Eventually, the surface is only partially covered with frost patches because all condensed water has been converted into frost. The height depletion of the red curve stabilizes, as the field of observation resides at an uncovered region. Thus, after the condensation period of $t > 100$ s, the evolution of the average height $\langle h \rangle(t)$ in Fig B.41a depends on the field of observation and the lubricant dynamics is governed by the proximity to frost patches.

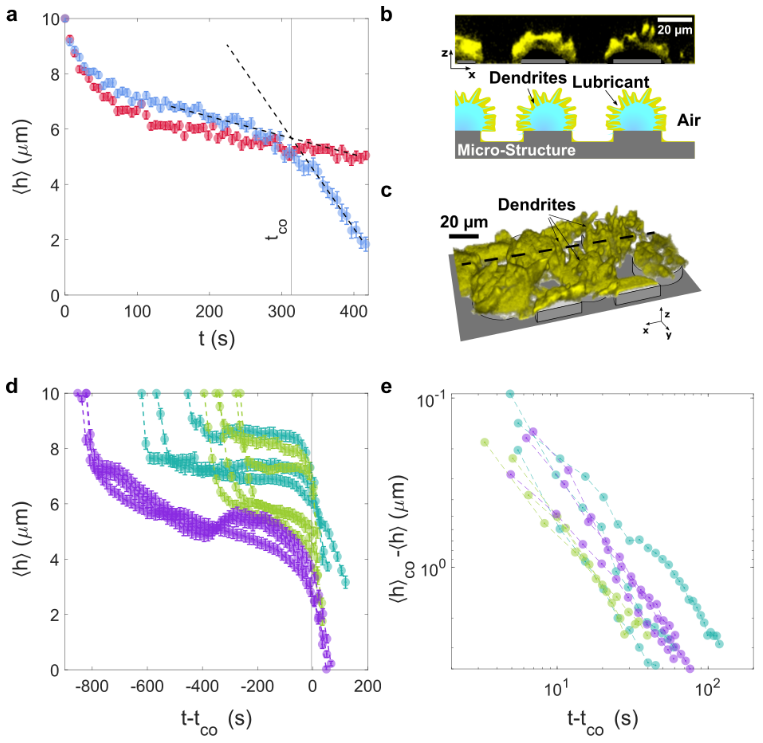

Figure B.41: Lubricant depletion during condensation-frosting. a) Averaged height of lubricant over time during condensation-frosting at −12 °C. $t = 0$ s corresponds to the beginning of observation on bare micro structured surfaces. Red and blue curves correspond to different locations of measurement on the substrate. Frost may (blue) or may not (red) propagate through the field of observation. Time, t_{co}, refers to the onset of frost depletion by finding the linear intersection between the condensation and frosting regime (dashed lines). b) LSCM images of vertical cross section and c) three-dimensional LSCM image showing frost covered by lubricant. d) Lubricant height evolution on micro- (−22 °C, purple) and hierarchically structured surfaces (−17 °C, turquoise and −22 °C, light green). Initial offsets are due to the condensation regime. Curves are time-shifted such that t_{co} (cross-over between condensation and frosting) coincides for all measurements. t_{co} depends on the location of observation, the supercooling of the surface and the humidity. e) Lubricant reorganization during frosting as logarithmic plot, focusing on the time domain after the cross-over time, t_{co} reveals identical dynamics.

Frost Induced Lubricant Depletion on Hierarchical LIS To understand whether the two-step depletion depends on degrees of surface roughness, we compared measurements on both micro- and hierarchically structured LIS. Fig B.41d-e shows the evolution of lubricant height on micro- (−22 °C, purple) and hierarchically structured surfaces (−17 °C, turquoise and −22 °C, light green).

Qualitatively, the lubricant evolution on the two surface types did not differ. However, the cross-over time t_{co} is not identical across various measurements due to stochastic nucleation delay. After shifting the curve such that t_{co} coincides for all measurement, the long-term depletion dynamics follows the same power law, $\langle h \rangle \sim t^{1.27}$, Fig B.41e. This hints that the long-term depletion dynamics does not depend on the roughness of the micropillars. As each set-point temperature experiment was conducted on the same surface, we note that the surfaces' original filling could be restored, after removing the ice via melting and evaporation.

Modelling Frosting Induced Lubricant Depletion on LIS

Next, we aim to understand the coupling between lubricant flow and frost formation/propagation. The frost dendrites (Fig. 4c) form a dynamically arranging porous network into which the lubricant can wick. The wicking of the lubricant is facilitated by a higher capillary suction pressure exerted on the lubricant by the dendritic structure than that exerted by micropillars. The pressure difference due to capillary suction can be estimated as

$$\Delta p = \gamma_{\mathrm{SiOil}} \left(\frac{1}{r_{\mathrm{MP}}} - \frac{1}{r_{\mathrm{ice}}} \right) \tag{B.49}$$

The pressure difference is governed by the differing capillary radii of the lubricant in the micro-pillar array, r_{MP} and in the dendritic network, r_{ice}, Eq (B.49). The capillary radius in the micro-pillar array is given by the geometry of micro-pillar spacing ($r_{\mathrm{MP}} \approx 10$ μm, cf. Methods). For an effective suction flux of lubricant into the dendritic structures, r_{ice} has to be smaller than r_{MP}. The surface tension of the lubricant (silicone oil) is denoted with γ_{SiOil}. The suction of lubricant into the dendritic structure generates its flow in the space between the micro-pillars. To model lubricant dynamics, we develop a theoretical framework of the flow during the frost propagation (cf. SI S5). To this end, we introduce a set of coordinates with the origin at the travelling front of the frost and $x = [0, \infty)$ being parallel to the horizontal plane. The micro-pillars are not directly considered but incorporated through an increased viscosity of the lubricant ($\eta_{\mathrm{SiOil}} = 2.9$ Pa s, cf. SI S4), which is, therefore, considered continuous, Fig B.42a. The initial lubricant height is taken to be the same as the height of the micropillars, $h_0 = 10$ μm. The capillary number ($\mathrm{Ca} = u_{\mathrm{ice}} \eta_{\mathrm{SiOil}} / \gamma_{\mathrm{SiOil}}$), which relates the viscous to the interfacial forces, is based on the propagation velocity of the frost front, u_{ice}; here η_{SiOil} is the dynamic viscosity of the lubricant. The small capillary number, $\mathrm{Ca} \approx 2 \times 10^{-4}$, enables a suitable long-wave approximation23 for the velocity profile of the lubricant, u, along the vertical height $y = [0, \langle h \rangle]$, namely

$$u(x, y) = \frac{\gamma_{\mathrm{SiOil}}}{\eta_{\mathrm{SiOil}}} \frac{\partial \kappa}{\partial x} \left(y - \frac{y^2}{2} \right) - u_{\mathrm{ice}}. \tag{B.50}$$

The pre-factor $\partial\kappa/\partial x$ is the average measure of the change of film curvature [39] when crossing the frost front. Considering mass conservation yields the evolution equation for the average lubricant height perpendicular to the frost domain (cf. Methods),

$$\frac{\partial}{\partial x}\left(\frac{\gamma_{\text{SiOil}}}{3\eta_{\text{SiOil}}}\frac{\partial\kappa}{\partial x}\langle h\rangle^3 - u_{\text{ice}}\right) = 0. \tag{B.51}$$

To determine the average height of the lubricant film, we solve Eq (B.51) numerically (cf. SI S6). Computations are carried out by a well-resolved finite difference method [40]. The number of grid points was chosen to ensure convergence. Eq (B.49) enters as a boundary condition at the frosting front. We set r_{ice} to 6 μm, which yields a good agreement between experimental observations and the numerical results. The chosen value for r_{ice} also aligns well with optical observations of the frost structure (Fig B.41b-c). Fig B.42b shows a vertical cross section of the film profile. Consistently with experimental observations (cf. Fig B.41d), we observe a lubricant depleted zone just ahead of the frost front.

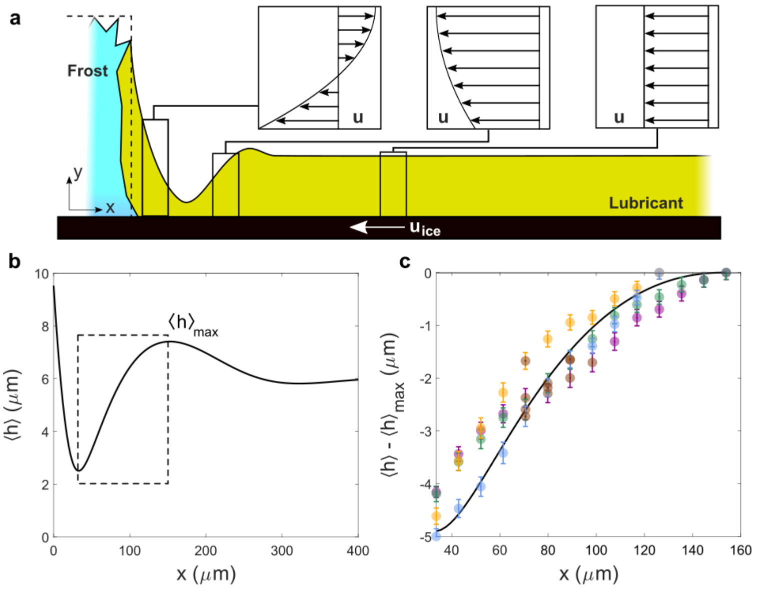

Figure B.42: Lubricant film profile in front of the propagating frost. a) Schematics of propagating frost front. The lubricant experiences a flow due to the suction induced by the dendritic frost domain. The insets sketch the velocity profiles at different positions. In the comoving frame, the velocity is $u = -u_{\text{ice}}$, at the base at $y = 0$ due to no-slip. b) The lubricant height profile is calculated using the long-wave approximation. In the vicinity of the frost front, the lubricating film thins sharply, generating a depleted zone. c) Calculated lubricant profile (solid line) in the dashed box of b). The coloured squares show repeated experimental measurements of the fast depletion process, corresponding to $t > t_{\text{co}}$ in Fig B.41. Absolute values are shown relative to $\langle h\rangle_{\max}$.

The resulting average lubricant height, together with the corresponding vertical velocity profiles at representative locations are sketched in Fig B.42a and its insets. In the model, the lubricant moves towards the frost in the comoving frame with $u = u_{\text{ice}}$, Fig B.42a, with uniform velocity far away from the frost front. The frost domain generates a suction pressure per Eq (B.49) due to the fine dendritic geometry. The suction into the frost domain generates a lubricant depleted zone that precedes the frost front. This results in a dimple in the overall height profile, Fig B.42a, b; this dimple leads to free surface curvature gradients that affect the flow. Towards the frost front, the curvature of the dimple induces a suction pressure, resulting in a higher lubricant flow. Passing the depletion zone, the curvature becomes positive, facilitating a backflow. Therefore, the width and the height of the depletion zone are governed by two independent effects: The growth speed of the frost, u_{ice}, and the frost suction pressure. We discuss their respective effects on the height profile, starting with u_{ice}. For larger values of u_{ice}, the depletion zone is supplied by more lubricant and becomes more narrow and thicker. Additionally, the lubricant flux into the frost domain is also enhanced due to the higher availability of lubricant in the direct vicinity of the frost front. A strong suction pressure results in a deep and narrow depletion zone. Note that the suction pressure counteracts the capillary pressure within the micropillar array domain, per Eq (B.49), so that the net lubricant flux can be tuned to effectively zero if the length-scales characterizing the capillary structure of the micro-pillar array and the frost approach each other, *i.e.* $r_{\text{MP}} \approx r_{\text{ice}}$. To test whether the simulations quantitatively reproduce the experimental data, we compare the lubricant profiles between simulations and experiments, Fig B.42c. First, we transition the experimental results to the comoving frame and define $x = x_{\text{min}} + u_{\text{ice}}\ (t_{\text{end}} - t)$, so that x measures the distance from the moving front. Here,x_{min} is chosen as the location in the comoving frame, where the depleted zone of the numerically calculated height (cf. Fig B.42b) is minimal. The time t_{end} is defined as the time at which the experimentally monitored lubricant film height is minimal (e.g. $t_{\text{end}} = 420$ s in the blue curve, Fig B.41a). Finally, we express the results relative to the maximum height $\langle h \rangle_{\text{max}}$ of the numerical solution shown in the dashed box in Fig B.42b. Fig B.42c plots the numerical results together with the experimental data obtained from the red curve in Fig B.41a and similar curves in repeat experiments. We find excellent agreement between experimental and theoretical results, indicating that the proposed model contains all important ingredients needed to capture the relevant physical effects.

Conclusion

Confocal microscopy is a powerful tool for obtaining quantitative information about condensation and frost formation on lubricated surfaces, since it enables clear discrimination between the water/frost, lubricant and the surrounding air. The formation of frost dendrites during condensation-frosting induces a strong suction pressure. This leads to direct lubricant drainage and depletion. Drainage was essentially the same for micro- and hierarchically structured surfaces. Although detrimental at the first sight, we note that frost induced lubricant depletion is reversible. Evaporation or sublimation of water restores the lubricant impregnated surface, accompanied by its characteristic features such as low friction. This is facilitated by the special properties of silicone oil, whose excellent spreading behaviour often results in complete surface coverage.17, 32 During frost formation, lubricant drainage is coupled to the speed of the dynamically forming frost front, which continuously soaks up the lubricant. These two driving mechanisms (frost propagation and capillary suction) induce lubricant depletion during frosting on liquid infused surfaces. Interestingly, for optimally robust anti-frosting surfaces, this implies a contradicting strategy: a) Reduce frost growth speed by increasing the spacing between micro-pillars [4, 21, 41]. b) Increase capillary forces within the micro-pillar array by reducing the spacing between micro-pillars. We expect that such improved understanding behind the mechanism of condensation-frosting on lubricated surfaces will foster the optimal design of next-generation frost-resistant lubricant-infused surfaces.

Methods

Fabrication of Lubricant Infused Surface

The rigid micro-pillar surface was manufactured by spincoating an epoxy based SU-8 photoresist (SU-8 5, MicroChem) on a glass slide (24 × 60 mm^2, 170 ± 5 μm thickness, Menzel-Gläser).The glass slides were cleaned by acetone and subsequently activated by oxygen plasma under 300 W for 5 min. SU-8 photoresist was then spin-coated (500 rpm for 5 s followed by 3000 rpm for 30 s, SÜSS MicroTec) on the glass slides. The coated slides were heated at 65 °C for 3 min, 95 °C for 10 min, and then at 65 °C for 30 min, respectively. Subsequently, the samples were slowly cooled down within 2 h and exposed to UV light (mercury lamp, 350 W) under a photolithography mask for 14 s (masker aligner SÜSS MicroTec MJB3 UV400). To cross-link the photoresist, the samples were heated at 65 °C for 1 min, 95 °C for 3 min and 65 °C for 30 min, and then cooled down slowly. Next, the samples were immersed in the SU-8 developer solution for 6 min, washed with isopropanol and deionized water, and then dried in air. The micro-pillar array on the glass slide was cut to a circular area of approximately 3 cm^2. Thereafter, it was plasma cleaned and infused with 0.56 μl/cm^2 of lubricant liquid per substrate area. The wettability of flat, plasma cleaned SU-8 was measured by wetting experiments and characterized by an advancing contact angle of 12±2°.

Fabrication of Nanopatterned Hierarchical LIS

To achieve nanopatterned hierarchical SLIPS, an additional scale of nanoroughness was conferred to microstructured SLIPS. To achieve this, surface functionalized nanoparticles were synthesized. The surface functionalization comprises of two components, an -epoxy terminated variant and an -amine terminated variant. The -epoxy terminated variant was synthesized by a methoxy-based sol-gel method, by stirring 1 g of fumed silica (Aldrich, 7 nm) in 50 ml of deionized water and 2.6 ml of (3-Glycidyloxypropyl)trimethoxysilane (Aldrich, 99.9 %) at 500 rpm, 20, 72 hours. The -amine terminated variant was synthesized by an ethoxy-based sol-gel method, by stirring 1 g of fumed silica (Aldrich, 7 nm) in 50 ml of toluene (200 ppm water) and 2.8 ml of aminopropyltriethoxysilane (Aldrich, 99.9 %) at 500 rpm in a round-bottom flask, under reflux at 80for 72 hours. Surfaces were prepared in excess reaction ratios, at 30 μmol/m^2. Resulting colloidal solutions were then centrifuged at 1000 rpm for 10 minutes and washed in their respective solvents (50 ml) for 3 cycles before being dried in a vacuum oven (50 mbm, 60) overnight. Thermogravimetric analysis reveal that nanoparticles are functionalized to ca. 10 w/w% in both instances (-amine and -epoxy variants). Both nanoparticle variants were dispersed (separately) in isopropanol (2 mg/ml) by magnetic stirring (500 rpm) for 24 h, followed by ultra-sonication for 1 h. The surfaces (170 μm thick glass slides decorated with micropillars) were first cleaned via oxygen plasma under 120 W for 2 min. The surfaces were then dipped into the amine-functionalized nanoparticle dispersion for 10 s. The surfaces were dried in the ambient for 2 h. Thereafter, they were dipped into the epoxy-functionalized nanoparticle dispersion, again for 10 s. The hierarchically coated surfaces were then dried overnight (24 h) before use. Prior to lubricant infiltration, the surface was plasma cleaned. The wettability of flat, plasma cleaned, nanoparticle coated SU-8 was measured by wetting experiments and characterized by an advancing contact angle of below 10°.

Lubricant and Dye

For the lubricant, we used a silicone oil (vinyl terminated polydimethylsiloxane, Gelest; surface tension: $\gamma_{\mathrm{SiOil}} \approx 20\,\mathrm{mN/m}15$). A fluorescence marker (Lumogen Red F300, BASF, excitation at 532 nm, emission at 610 nm) was added to the silicone oil. To enhance the solubility of the fluorescence dye in silicone oil, the fluorescence dye was initially dissolved in chloroform (Chloroform, 99.8+%, Fisher Chemical). The dye-chloroform concentration was diluted down to $c_{\mathrm{LumogenRed/CHCl_3}} = 0.1$ mg/ml and ultra-sonicated for 1 min. The dye-chloroform solution was mixed with the silicone oil such that a Lumogen Red-silicone oil concentration of $c_{\mathrm{LumogenRed/SiOil}} = 0.1$ mg/ml was received. The mixture was stirred for 5 min. Afterwards, the mixture was exposed to 40 °C and 50 mbar for 24 h under vacuum-assisted evaporation. We did not observe changes in the interfacial tension by the dye nor an accumulation of the dye at the interfaces.

Humidity and Temperature Control

To control the temperature of the lubricant infused surface, the sample was mounted on a cooling element within the frosting chamber (volume: 240 ml, Fig B.44, Linkam, THMS600). The cooling element is closed-loop controlled within a temperature range of -196 °C to 600 °C and a cooling rate up to 100 K/min. To control the chamber's humidity, two nitrogen gas lines were used: One water vapour enriched (humidified) line and another line with dry nitrogen gas. We utilized a water-bubbler system to enrich the first gas line with water. The sample was cooled down alongside continuous purging of the chamber using the dry steam at 10 l/min. The temperature was kept at the desired set-point for 5 min before commencement of the experiment. Thereafter, the flow rate of the dry nitrogen gas line was set to 4 l/min and the flow rate of the humidified gas line to 2 l/min. Both lines are connected such that the respective gas streams mix. The mixed stream was introduced into the frosting chamber for 30 s.

Laser Scanning Confocal Microscopy

The experiments were monitored with a custom-built, inverted Laser Scanning Confocal Microscope. The microscope is controlled with a LabVIEW program. The microscope has two illuminating lasers (Cobolt DLC$^{\mathrm{TM}}$ 25; wavelength: blue 473 nm; green 532 nm). The laser beam is sent through a magnifying objective lens to the lubricant infused surface. The objective lens (dry; Leica HC PL FLUOTAR 2.5x/0.07; OLYMPUS UPIanSApo 10x/0.40; OLYMPUS LMPIanFLN 100x/0.80) of the microscope is mounted on a piezo table to translate the sample within a domain of up to 200 μm in the vertical direction. The horizontal plane is sampled with a counter rotation scanner (Cambridge Technology, 215H Optical Scanner) which sweeps with a sampling rate of 7910 ± 15 Hz in one direction. The horizontal plane of view spans an area of 40 $\mu\mathrm{m} \times 40$ μm. The observed height was 20 μm. This spatial configuration allowed a recording frequency of 1/6.6 Hz. The combined reflection-fluorescence modes enable discrimination between the bulk liquid lubricant phase and the surface features on the lubricant infused surface.

Height Extraction

The captured point cloud of the substrate from the microscope was processed with the open source package ImageJ and a custom MATLAB script. This reconstructs the spatial distribution of lubricant film (Fig B.50). The lubricant height h is measured in the space centrically in between the micro-pillars. The field of observation allows a collection of 128 sampling points which corresponds to a length of 70 μm. This corresponds to the centre of one micro-pillar to another. The points are given with $x_i\{i|i \in N \text{ and } 1 \leq i \leq 128\}$. This height profile is arithmetically averaged, which yields a scalar value, namely $\langle h \rangle = 1/128 \sum_i h(x_i)$.

Water Vapour Diffusion to the Substrate

The condensation of the water droplets is driven by diffusion (cf. SI S3). Diffusion equation of water vapour is given with

$$\frac{\partial c}{\partial t} = D \frac{\partial^2 c}{\partial y^2}. \tag{B.52}$$

Here, c is the water concentration, t is the time, and the diffusivity is given by D. The diffusion within the horizontal and vertical planes are considered separately, because the respective length scales differ in orders of magnitude, $\mathcal{O}(l_{\text{vert}}) \approx 10^{-3}$ m and $\mathcal{O}(l_{\text{horz}}) \approx 10^{-6} - 10^{-9}$ m. Hence, only the vertical direction z is considered. A solution of Eq (B.52) is given by [42]

$$\frac{c - c_1}{c_0 - c_1} = \text{erf}\left(\frac{y}{\sqrt{Dt}}\right) \tag{B.53}$$

The constants c_0 and c_1 are determined using the initial concentration (c_0) in the whole domain while the saturation concentration (c_1) at the substrate depends on the set-point temperature. Eq (B.53) was fitted to the monitored relative humidity in the frosting chamber (Fig B.46b). The fit revealed a diffusivity of $D = 0.14$ cm^2/s. The condensing mass flux per area is obtained by

$$m'' = -D\frac{\partial c}{\partial y}|_{y=0} = (c_1 - c_0)\,\bar{m}_{\text{vapor}}\sqrt{\frac{D}{\pi t}}, \tag{B.54}$$

with $\bar{m}_{\text{vapor}}$ being the mole mass of water vapor.

Long-Wave Approximation

We consider incompressible lubricant flow during frost propagation and fluid mechanics conservation laws (cf. SI S4). The flow is characterized by the capillary number (Ca $\approx 2\times10^{-4}$) and the Reynolds number is based on the front propagation speed, u_{ice} (Re $= \rho_{\text{SiOil}} u_{\text{ice}} h_0 / \eta_{\text{SiOil}} \approx 2.8 \times 10^{-10}$). For such small values of Ca and Re, and considering the separation of length scales in the vertical and in-plane direction, it is appropriate to consider the problem within the long-wave approach (cf. [43] and references therein). This approach leads to the following equations for the depended variables (velocity $(u, v)^T$ and pressure p) that in steady state read as

$$-\frac{\partial p}{\partial x} + \eta_{\text{SiOil}}\frac{\partial^2 u}{2} = 0, \tag{B.55a}$$

$$\frac{\partial p}{\partial y} = 0, \tag{B.55b}$$

$$\frac{\partial u}{\partial x} + \frac{\partial v}{\partial y} = 0. \tag{B.55c}$$

We chose no-slip at $y = 0$ for the velocity and no-stress at $y = \langle h \rangle>$ for the shear tensor. The pressure at $y = \langle h \rangle$ is given by the Laplace pressure $p = \gamma_{\text{SiOil}}\kappa$. Since $p \neq f(y)$, Eq (B.55a) can be integrated twice leading to Eq (B.50), and Eq (B.55c) gives v. The evolution of the average film height $\langle h \rangle$ is then given by

$$\frac{d\langle h \rangle}{dt} = v = \frac{\partial \langle h \rangle}{\partial t} + u\frac{\partial \langle h \rangle}{\partial x} \tag{B.56}$$

Note that the velocities $(u, v)^T$ in Eq (B.55c) are evaluated at $y = \langle h \rangle$. By introducing $(u, v)^T$ into Eq (B.55c), and considering steady state solutions only ($\partial\langle h \rangle / \partial t = 0$), we obtain Eq (B.51).

Author Contributions

L.H. and W.S.Y.W. constructed the experimental setup. W.S.Y.W. and K.I.H. fabricated the surfaces. V.D. and L.H. carried out the experiments. L.H. conducted the data analysis. V.D. helped with data interpretation. L.H. and L.K. developed the long wave approximation and wrote the numerical solver. L.H., W.S.Y.W. and D.V. contributed to experimental planning, data analysis, and manuscript preparation. L.H., W.S.Y.W., L.K., and D.V. wrote the manuscript. All authors reviewed and approved the manuscript.

Acknowledgements

This work was supported by the European Union's Horizon 2020 research and innovation program LubISS No. 722497 (W.W, V.D, D.V.), the ERC Advanced Grant No. 340391 "SUPRO" (D.V.), the German Research Foundation (DFG) with the Priority Programme 2171 (L.H., D.V.), the Collaborative Research Center 1194 (L.H.), the Max Planck – Univ. Twente Center for Complex Fluid Dynamics (D.V.), the Max Planck Graduate Center (K.I.H.), US National Science Foundation grants NSF CBET-1604351 and DMS-1815613, and NJIT Faculty Seed Grant (LK). We thank R. Berger for AFM measurements and K. Maisenbach for supporting with Figure 1d. We thank M. D'Acunzi, P. Baumli, H.- J. Butt, A. Naga, M. Schremb, A. Sharifi, P. Stephan, C. Tropea and P. Vuristo for stimulating discussions and for technical support.

References

1. Pruppacher, H. R. & Klett, J. D. *Microphysics of Clouds and Precipitation: Reprinted 1980* Second. ISBN: 94-009-9905-4 (New York, Boston, Dordrecht, London, Moscow, 2012).
2. Sastry, S. Ins and Outs of Ice Nucleation. *Nature* **438,** 746–747. ISSN: 0028-0836, 1476-4687 (Dec. 2005).
3. Walker, C. *et al.* Desublimation Frosting on Nanoengineered Surfaces. *ACS Nano* **12,** 8288–8296. ISSN: 1936-0851 (Aug. 2018).
4. Guadarrama-Cetina, J., Mongruel, A., González-Viñas, W. & Beysens, D. Percolation-Induced Frost Formation. *EPL* **101,** 16009. ISSN: 0295-5075 (Jan. 2013).
5. Nath, S., Ahmadi, S. F. & Boreyko, J. B. A Review of Condensation Frosting. *Nanoscale Microscale Thermophys. Eng.* **21,** 81–101. ISSN: 1556-7265, 1556-7273 (Apr. 2017).
6. Laforte, J., Allaire, M. & Laflamme, J. State-of-the-Art on Power Line De-Icing. *Atmos. Res.* **46,** 143–158. ISSN: 01698095 (Apr. 1998).
7. Berry, W. B., Sachs, J. L. & Kleinman, R. I. *Radio Frequency (RF) Third Rail Deicing-a Comparison with Heated Rail* in *Proceedings of the IEEE/ASME Joint Railroad Conference* (eds Godley, D. P. & Hawthorne, K. L.) (Apr. 1993), 41–45. ISBN: 0-7803-0963-4.
8. InternationalTelecommunicationUnion. Propagation Data and Prediction Methods Required for the Design of Earth-Space Telecommunication Systems. *Recommendation ITU-R* **P Series,** 618–12 (2015).
9. Meuler, A. J. *et al.* Relationships between Water Wettability and Ice Adhesion. *ACS Appl. Mater. Interfaces* **2,** 3100–3110. ISSN: 1944-8244 (Nov. 2010).

10. Golovin, K. *et al.* Designing Durable Icephobic Surfaces. *Sci. Adv.* **2,** e1501496. ISSN: 2375-2548 (Mar. 2016).
11. Mitridis, E. *et al.* Metasurfaces Leveraging Solar Energy for Icephobicity. *ACS Nano* **12,** 7009–7017. ISSN: 1936-0851 (July 2018).
12. Kreder, M. J., Alvarenga, J., Kim, P. & Aizenberg, J. Design of Anti-Icing Surfaces: Smooth, Textured or Slippery? *Nat. Rev. Mater.* **1,** 15003. ISSN: 2058-8437 (Jan. 2016).
13. Lv, J., Song, Y., Jiang, L. & Wang, J. Bio-Inspired Strategies for Anti-Icing. *ACS Nano* **8,** 3152–3169. ISSN: 1936-0851, 1936-086X (Apr. 2014).
14. Niemelä-Anttonen, H. *et al.* Icephobicity of Slippery Liquid Infused Porous Surfaces under Multiple Freeze–Thaw and Ice Accretion–Detachment Cycles. *Adv. Mater. Interfaces* **5,** 1800828. ISSN: 2196-7350 (2018).
15. Kim, P. *et al.* Liquid-Infused Nanostructured Surfaces with Extreme Anti-Ice and Anti-Frost Performance. *ACS Nano* **6,** 6569–6577. ISSN: 1936-0851 (Aug. 2012).
16. Lafuma, A. & Quéré, D. Slippery Pre-Suffused Surfaces. *EPL* **96,** 56001. ISSN: 0295-5075, 1286-4854 (Dec. 2011).
17. Wong, T.-S. *et al.* Bioinspired Self-Repairing Slippery Surfaces with Pressure-Stable Omniphobicity. *Nature* **477,** 443–447. ISSN: 0028-0836, 1476-4687 (Sept. 2011).
18. Ishino, C., Reyssat, M., Reyssat, E., Okumura, K. & Quéré, D. Wicking Within Forests of Micropillars. *EPL* **79,** 56005. ISSN: 0295-5075, 1286-4854 (Sept. 2007).
19. Rykaczewski, K., Anand, S., Subramanyam, S. B. & Varanasi, K. K. Mechanism of Frost Formation on Lubricant-Impregnated Surfaces. *Langmuir* **29,** 5230–5238. ISSN: 0743-7463 (Apr. 2013).
20. Witt, K. E., Ahmadi, S. F. & Boreyko, J. B. Ice Wicking. *Phys. Rev. Fluids* **4,** 024002 (Feb. 2019).
21. Nath, S. & Boreyko, J. B. On Localized Vapor Pressure Gradients Governing Condensation and Frost Phenomena. *Langmuir* **32,** 8350–8365. ISSN: 0743-7463 (Aug. 2016).
22. Acheson, D. J. *Elementary Fluid Dynamics* 1st. ISBN: 978-0-19-859679-0 (1990).
23. Barrie, J. A. & Machin, D. The Sorption and Diffusion of Water in Silicone Rubbers: Part I. Unfilled Rubbers. *J. Macromol. Sci. Phys.* **3,** 645–672. ISSN: 0022-2348, 1525-609X (Dec. 1969).
24. Kajiya, T., Schellenberger, F., Papadopoulos, P., Vollmer, D. & Butt, H. J. 3D Imaging of Water-Drop Condensation on Hydrophobic and Hydrophilic Lubricant-Impregnated Surfaces. *Sci. Rep.* **6,** 23687. ISSN: 2045-2322 (Electronic) 2045-2322 (Linking) (Apr. 2016).
25. Xiao, R., Miljkovic, N., Enright, R. & Wang, E. N. Immersion Condensation on Oil-Infused Heterogeneous Surfaces for Enhanced Heat Transfer. *Sci. Rep.* **3,** 1988. ISSN: 2045-2322 (Electronic) 2045-2322 (Linking) (2013).
26. Anand, S., Rykaczewski, K., Subramanyam, S. B., Beysens, D. & Varanasi, K. K. How Droplets Nucleate and Grow on Liquids and Liquid Impregnated Surfaces. *Soft Matter* **11,** 69–80. ISSN: 1744-6848 (Dec. 2014).
27. Princen, H. M. The Equilibrium Shape of Interfaces, Drops, and Bubbles. Rigid and Deformable Particles at Interfaces. *Colloids Surf.* **2,** 1–84 (1969).
28. Smith, J. D. *et al.* Droplet Mobility on Lubricant-Impregnated Surfaces. *Soft Matter* **9,** 1772–1780. ISSN: 1744-683X, 1744-6848 (2013).
29. De Gennes, P.-G., Brochard-Wyart, F. & Quéré, D. *Capillarity and Wetting Phenomena: Drops, Bubbles, Pearls, Waves* 1st. ISBN: 0-387-21656-1 (New York, USA, 2010).
30. Daniel, D., Timonen, J. V. I., Li, R., Velling, S. J. & Aizenberg, J. Oleoplaning Droplets on Lubricated Surfaces. *Nat. Phys.* **13,** 1020–1025. ISSN: 1745-2481 (Oct. 2017).

31. Schellenberger, F. *et al.* Direct Observation of Drops on Slippery Lubricant-Infused Surfaces. *Soft Matter* **11,** 7617–7626. ISSN: 1744-683X, 1744-6848 (2015).
32. Sokuler, M. *et al.* The Softer the Better: Fast Condensation on Soft Surfaces. *Langmuir* **26,** 1544–1547. ISSN: 0743-7463 (Feb. 2010).
33. Na, B. & Webb, R. L. A Fundamental Understanding of Factors Affecting Frost Nucleation. *Int. J. Heat Mass Transf.* **46,** 3797–3808. ISSN: 0017-9310 (2003/09/01/).
34. Kashchiev, D. *Nucleation* 1st. ISBN: 978-0-08-053783-2 (Oxford, UK, Feb. 2000).
35. Murphy, D. M. & Koop, T. Review of the Vapour Pressures of Ice and Supercooled Water for Atmospheric Applications. *Q. J. R. Meteorol. Soc.* **131,** 1539–1565. ISSN: 0035-9009 (2005).
36. Saito, Y. *Statistical Physics of Crystal Growth* 1st. ISBN: 981-238-628-9 (Singapore, 1996).
37. Piruska, A. *et al. Characterization of SU-8 Optical Multimode Waveguides for Integrated Optics and Sensing on Microchip Devices* in *Microfluidics, BioMEMS, and Medical Microsystems IV* (eds Papautsky, I. & Wang, W.) **Proc. SPIE 6112** (Jan. 2006), 611207.
38. Hauer, L. *et al.* How Frost Forms and Grows on Lubricated Micro- and Nanostructured Surfaces. *ACS Nano* **15,** 4658–4668. ISSN: 1936-0851, 1936-086X (Mar. 2021).
39. Snoeijer, J. H. Free-Surface Flows with Large Slopes: Beyond Lubrication Theory. *Phys. Fluids* **18,** 021701. ISSN: 1070-6631 (Feb. 2006).
40. Diez, J. A., Kondic, L. & Bertozzi, A. Global Models for Moving Contact Lines. *Phys. Rev. E* **63,** 011208 (2000).
41. Petit, J. & Bonaccurso, E. General Frost Growth Mechanism on Solid Substrates with Different Stiffness. *Langmuir* **30,** 1160–1168. ISSN: 0743-7463, 1520-5827 (Feb. 2014).
42. Crank, J. *The Mathematics of Diffusion* ISBN: 0-19-853411-6 (1979).
43. Kondic, L. Instabilities in Gravity Driven Flow of Thin Fluid Films. *SIAM Rev.* **45,** 95–115. ISSN: 0036-1445 (2003).
44. Oh, S. H., Lee, K.-C., Chun, J., Kim, M. & Lee, S. S. Micro Heat Flux Sensor Using Copper Electroplating in SU-8 Microstructures. *J. Micromech. Microeng.* **11,** 221 (2001).
45. Nagai, H. *et al.* Thermal Conductivity Measurement of Liquid Materials by a Hot-Disk Method in Short-Duration Microgravity Environments. *Mater. Sci. Eng. A* **276,** 117–123. ISSN: 0921-5093 (Jan. 2000).
46. Rayleigh, L. LIX. On Convection Currents in a Horizontal Layer of Fluid, When the Higher Temperature Is on the under Side. *The London, Edinburgh, and Dublin Philosophical Magazine and Journal of Science* **32,** 529–546 (1916).
47. Kleiber, M. & Joh, R. in *VDI-Wärmeatlas* Tenth, 249–294 (Berlin, Heidelberg, 2006). ISBN: 978-3-540-32218-4.
48. Wen, B. & Hesse, M. A. *Rayleigh Fractionation in High-Rayleigh-Number Solutal Convection in Porous Media* Web Page. 2018.
49. Rudolph, N. & Osswald, T. A. *Polymer Rheology: Fundamentals and Applications* 1st, 61–64 (Munich, Germany, 2014).
50. *CLEARCO Viscousity Temperature Chart* Web Page.
51. Bruus, H. *Theoretical Microfluidics* 1st, 48–51 (New York, USA, 2008).
52. Slattery, J. C. *Advanced Transport Phenomena* 1st (New York, USA, 1999).
53. Butt, H.-J., Graf, K. & Kappl, M. *Physics and Chemistry of Interfaces* 3rd, 11 (Weinheim, Germany, 2013).
54. Casey, J. *Exploring Curvature* 1st, 218 (Braunscheig, Germany, 1996).
55. Hirsch, C. *Numerical Computation of Internal and External Flows: The Fundamentals of Computational Fluid Dynamics* Second, 141–197 (Burlington, USA, 2007).

56. Shampine, L. F. & Reichelt, M. W. The Matlab ODE Suite. *SIAM J. Sci. Comput.* **18,** 1–22 (1997).

Supplementary Information

Supplementary Figures

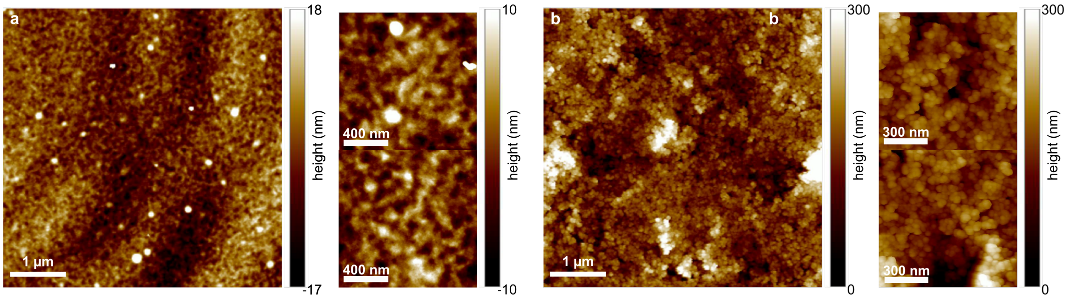

Figure B.43: Roughness of Bare and Nanoparticle Coated Micropillar Tops. The topography was measured with Atomic Force Microscopy (AFM, Dimension icon with ScanAsyst) in tapping mode in air. a) Bare micropillar top (field of measurement: 5 μm^2) with an average arithmetic roughness of 3.8 nm. The highest and the lowest points in this measurement are separated by 71 nm. b) AFM measurements on two additional, bare micropillar tops. The average arithmetic roughness for the top image is 2.4 nm and for the bottom 2.7 nm (field of measurement: 1 μm^2, respectively). This yields an average arithmetic roughness value of 3.4 ± 0.3 nm. c) Nanoparticle coated micropillar top (field of measurement: 5 μm^2) with an average arithmetic roughness of 36.9 nm. The highest and the lowest points in this measurement are separated by 613 nm. d) AFM measurements on two additional, nanoparticle coated micropillar tops. The average arithmetic roughness for the top image is 33.7 nm and for the bottom 27.7 nm (field of measurement: 1 μm^2, respectively). This yields an average arithmetic roughness value of 35.1 ± 1.7 nm.

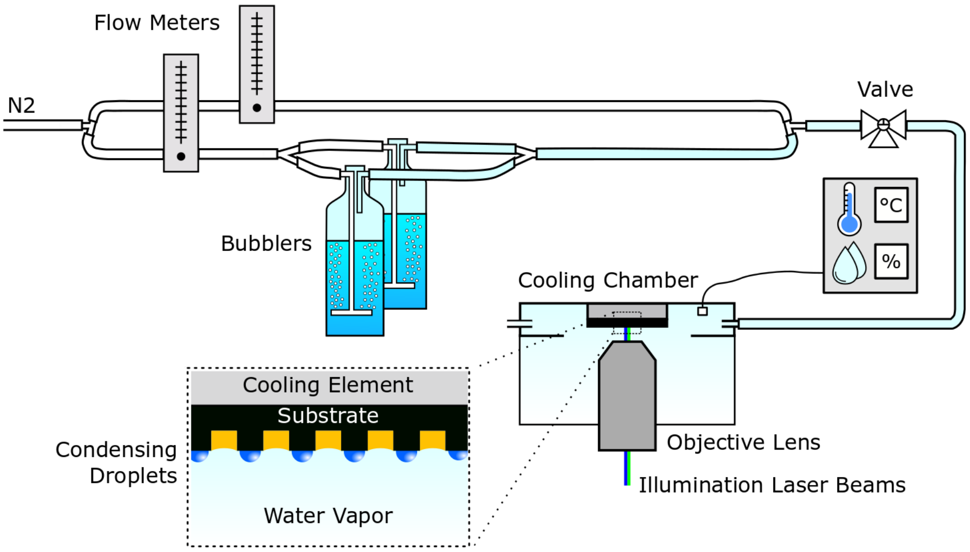

Figure B.44: Experimental Set-up for Condensation Frosting. Schematics of the experimental setup. The substrate is inversely mounted on the cooling element (Linkam, THMS-600) over the objective lens of the confocal microscope. We use a blue (wavelength: 473 nm) and a green (wavelength: 532 nm) laser beam for illumination. The cooling element is controlled thermoelectrically and additionally cooled with liquid nitrogen. Dry nitrogen gas is mixed with the humidified gas stream to set the humidity in the cooling chamber. The humid atmosphere in the chamber initiates condensation of liquid water droplets on the cooled substrate.

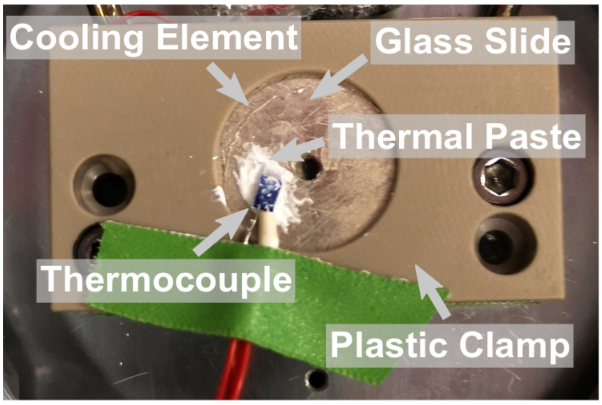

Figure B.45: Calibration of the Substrate Temperature. To calibrate the temperature on the substrate ($T_{\text{set-point}}$), we used a glass slide. A circular glass slide was clamped to the cooling element (Linkam, THMS-600). The cooling element was cooled down from ambient temperature to -15 °C with 2 K/min. Thereafter we let the system equilibrate for 10 minutes. The temperature of the cooling element is measured internally with a thermocouple which is not visible (inside the cooling element). We stuck a second thermocouple to the top side of the glass slide with thermal paste to increase the heat conduction between the thermocouple and the glass slide. The measurement showed an offset of $T_{\text{set-point}} = -12$ °C and $T_{\text{cooling element}} = -15$ °C. This yields an offset temperature of $\Delta T = 3$ K.

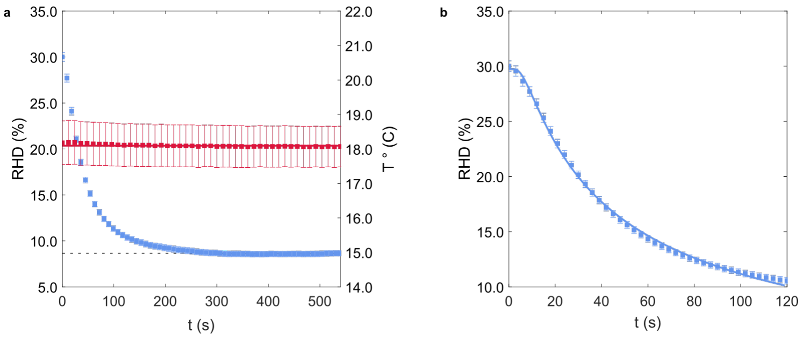

Figure B.46: Relative Humidity. Relative humidity (% RHD; blue) and temperature (T; red) measurement during the experiment in the humidity chamber. The values were averaged from 14 experiment repetitions on different days.Error bars represent the relative error. The distance between the sensor and the substrate is approximately 2 cm a) Relative humidity and temperature sampling of a whole experiment. The relative humidity (blue) decays to approximately 4.0 ± 0.3 % RHD and stays constant at this value. The temperature (red) stays constant at 18.1 ± 0.6 °C (solid red line). b) Relative humidity within the first 120 s of the experiment. The measured values align well with a diffusion transport of the water vapor to the substrate (solid blue line).

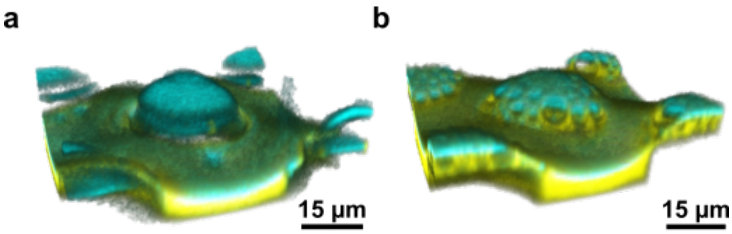

Figure B.47: Laser Scanning Confocal Raw Data. Raw data of Fig B.39c and Fig B.39d. The reflection signal appears in cyan while the fluorescence signal appears in yellow. a) Plain micropillar after humidified nitrogen carrier gas is introduced. b) Nanoparticle coated micropillar after humidified nitrogen carrier gas is introduced.

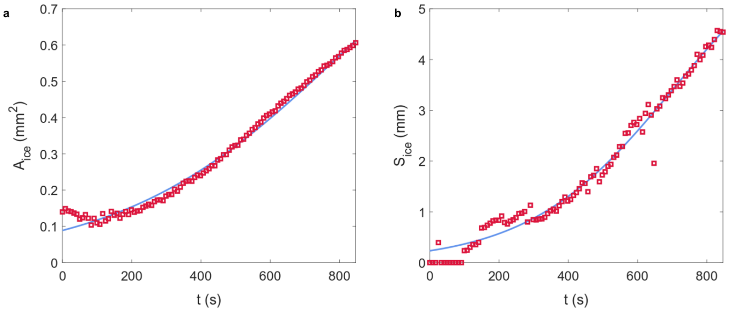

Figure B.48: Area of Frost Patches. We monitor the frost patch evolution and extract the area and the perimeter *via* image processing. The red squares in the plot represent the measurement and the solid blue line a fitted logistic growth function. The evolution of the frost patch area A_{ice} is given by the time derivative $\dot{A}_{\text{ice}} = \oint_{S_{\text{ice}}} u\mathrm{d}S$ where u is the front propagation velocity and $\mathrm{d}S$ the line element of the perimeter S_{ice}. We define the growth speed of the frost front as the averaged velocity of the patch's propagation speed, namely $u_{\text{ice}} = \oint_{S_{ice}} u\mathrm{d}S / \oint_{S_{ice}} \mathrm{d}S$. Hence, the averaged frost front speed is $u_{\text{ice}} = \dot{A}_{\text{ice}}/S_{\text{ice}}$. By averaging u_{ice} over time and three experimental repetitions, we find $u_{\text{ice}} = 1.4 \pm 0.5$ μm/s.

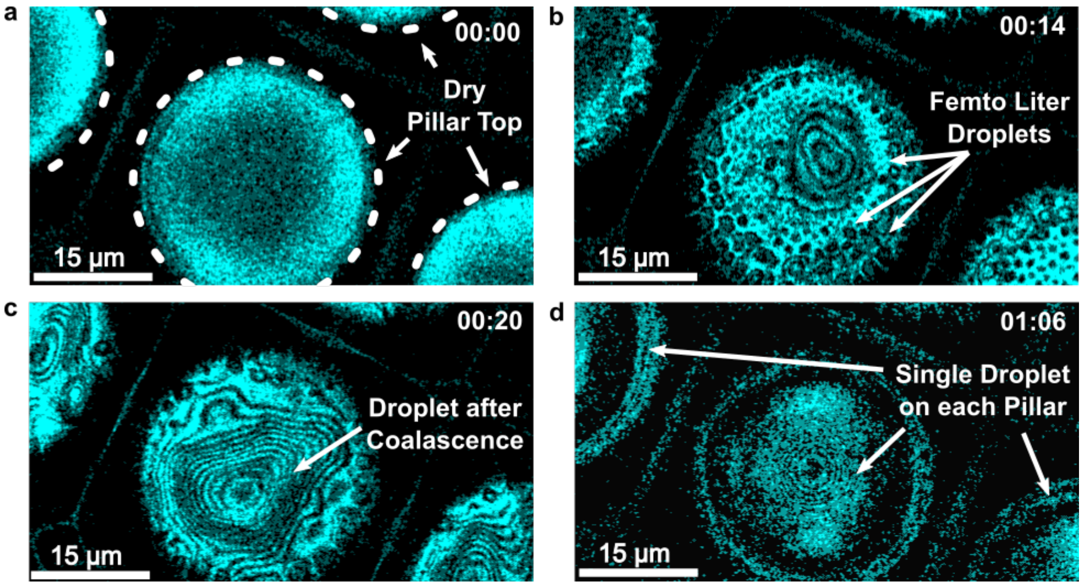

Figure B.49: Reflection images of condensation of droplets on micro-pillars at −12 °C surface temperature (see also Video S1). In the upper right corner of each image, the time is given in mm:ss. We start counting the time when humidified nitrogen is introduced into the frosting chamber. a) Dry pillars. b) Shortly after the humidified nitrogen stream is introduced into the frosting chamber, femto liter droplets (diameter ≈ 1 μm) become visible on the micro-pillar tops. We are measuring in reflection mode because we cannot add a dye to condensed water. Condensed droplets appear as dark spots. c) Droplets coalesce and larger drops form. The interference pattern indicates that the droplets grew in size. d) Condensation ends with a single droplet on each micro-pillar top.

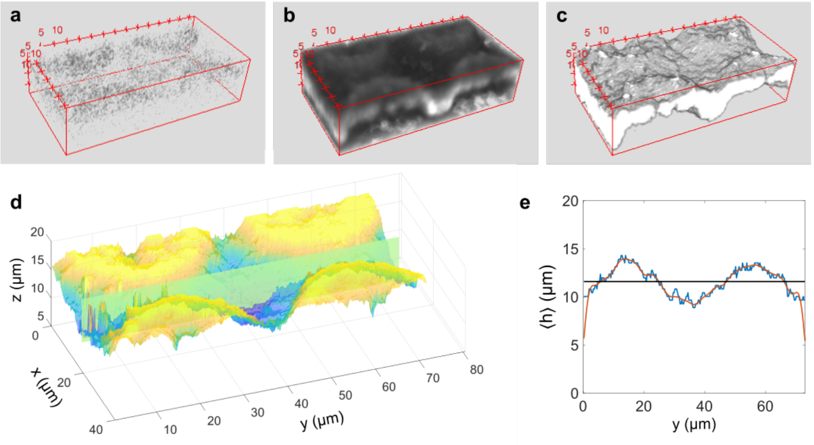

Figure B.50: Image processing and height extraction of the lubricant profile. a) - c) are typical images which were preprocessed with ImageJ. a) Raw point cloud (128 × 128 × 51 pixels) of fluorescence signal. b) 3-dimensional Gauss filter with pixel radius of 6. c) Thresholding filter. d) Surface reconstruction conducted using a custom MATLAB script. The lubrication height is extracted from within the green vertical xz-plane. e) Height extraction: The blue line represents the extracted data while the orange line is the low-pass filter.

Discussion on Laser Beam Illumination

To investigate whether the laser beam induced heating affects the results we designed the following two experiments: In a first set of experiments, we conduct a typical condensation frosting experiment, Fig SB.51a. The surface was cooled down to -25 °C while the atmosphere was maintained dry (¡5% RH, 18 °C). We introduce humidified nitrogen carrier gas for 60 seconds into the frosting cell, such that the relative humidity rises to 32%. The frost formation was recorded in a field of view of 6440 μm × 3220 μm with a 2.5x magnification lens (*cf.* manuscript). The field of view was sampled with the laser beam at a rate of 0.96s^{-1}, which corresponds to continuous illumination and is representative of the experiments. We repeated this experiment a second time were the field of observation was sampled only once every 2 minutes, leaving the surface unilluminated for the majority of time. It appears that within our experimental accuracy the formation and growth of the frost patch was identical under both conditions. The minor differences in the two experiments reflect the stochastic nature of frost formation, Fig 4 d. In a second set of experiments, we investigated the effect of laser beam illumination on melting/evaporation of the frost, Fig SB.51b. Therefore, we introduced a constant gas stream of dry nitrogen (room temperature) into the chamber after the frost on the surface becomes stationary. Image acquisition was conducted continuously (at a rate of 0.96s^{-1}) or only every 2 minutes while the laser was turned off between successive images. For both sampling rates the frost entirely disappeared after approximately 14 minutes. We deduce from these experiments that laser illumination does not influence the formation and growth of frost, beyond the inherent stochastics of frost. Further, the time scales for melting/evaporation of frost are unaffected.

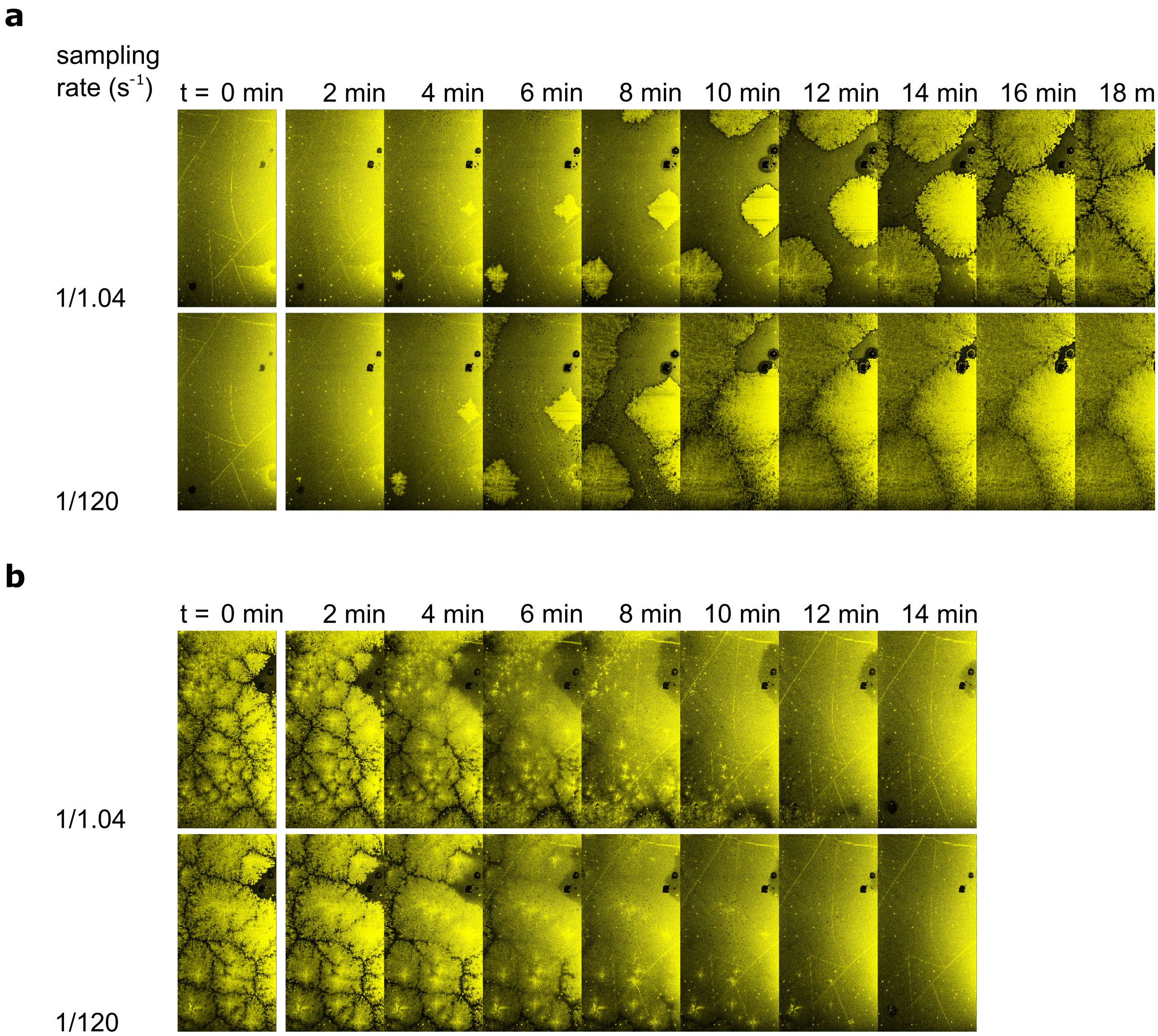

Figure B.51: **Influence of laser beam illumination on frosting and melting.** Fluorescence microscopy of the process. The lubricant appears in yellow. Each frame is 6440 µm long and 3220 µm wide. a) Frost formation with continuous illumination (top row) and minor illumination (once every 2 minutes, bottom row). b) Melting and evaporation of frost with continuous illumination (top row) and minor illumination (once every 2 minutes, bottom row).

Discussion on Energy Sink for Nucleation

This is provided by two contributing factors. Firstly, the thermal conductivity of the rigid epoxy based SU-8 material ($\lambda_{SU-8} \approx 0.2$ W/m K) [44] is higher than the thermal conductivity of the lubricant silicone oil ($\lambda_{SiOil} \approx 0.1 - 0.2$ W/m K)[45]. Hence, the surface of the micro-pillars is colder than the surface of the liquid, in between. Consequently, a higher supersaturation prevails at these locations, making nucleation more likely. Secondly, the surface energies favour condensing droplets on the pillars instead of on the lubricant for two reasons: a) The micro-pillar tops were hydrophilized prior to infiltration, lowering the surface energy, γ_{sl}, between the water nucleus and the solid SU-8 surface; and b) the thin lubricant layer on the micro-pillar tops facilitates a lower interfacial energy, γ_{lv}, between the nucleus and the surrounding lubricant (silicone oil). Hence, the required critical free energy for stable nucleus formation at the pillar's top face is significantly reduced

Discussion of Governing Mechanisms Responsible for Vapor Transport to the Substrate

Water vapor diffuses from the supersaturated atmosphere to the substrate. Additionally, the vertical temperature gradient between the substrate and the atmosphere may induce natural advection currents of the water vapor [46]. To investigate whether diffusion or advection processes govern the vapor transport, we calculate the Rayleigh number, Ra, which represents a special form of the Péclet number. The Péclet number compares advection fluxes to diffusive fluxes, while the Rayleigh number does the same but assumes the special case of advection flux, namely gravity driven buoyancy. The Rayleigh number is defined as

$$Ra = \frac{\Delta \rho g l^3}{\eta D}. \tag{B.57}$$

The density difference between the far-field atmosphere ($T_\infty = 18$ °C) and the substrate ($T_{\text{set-point}} = -12$ °C) was calculated using the ideal gas law and a relative humidity of 30 %. This yields a density difference of $\Delta\rho = 0.139$ kg/m^3. The acceleration due to gravity is $g = 9.81$ m/s^2. $\eta = 1.75 \times 10^{-5}$ Pa s and $D = 0.247$ cm^2/s [47] are the dynamic viscosity of humid air and the diffusivity of water in nitrogen, respectively. The characteristic length scale is set as the distance between the substrate and the objective lens $l \approx 2$ mm. This leads to a Rayleigh number of Ra ≈ 25. Therefore, temperature gradient induced advection can be ignored [48].

Discussion on Viscosity

The viscosity in a silicone oil bulk flow at $T = 25$ °C is given with the reference viscosity $\eta_{\text{SiOil,ref}} = 194$ mPa s (200 cSt, vinyl terminated polydimethylsiloxane, Gelest). We investigate the lubricant flow in a micro-pillar array at $T = -12$ °C. Due to the temperature dependency of the viscosity

[49], we expect a value different from $\eta_{\mathrm{SiOil,ref}}$ for our considered case. Furthermore, the presence of the micro-pillars imposes additional shear friction compared to a free bulk flow (without micro-pillars). Instead of considering complex flow in micro-pillar geometry, we instead consider simpler version of a channel flow, as described in what follows. As a final result, we obtain the the effective viscosity, which includes the modifications due to a) the low temperature, with the temperature factor $\alpha\,(T = -12\ ^{\circ}\mathrm{C})$ and b) the imposed friction by the micro-pillars with the geometrical factor β_{geo}. Both factors together yield the effective viscosity

$$\eta_{\mathrm{SiOil}} = \alpha\,(T)\,\beta_{\mathrm{geo}}\eta_{\mathrm{SiOil,ref}}. \tag{B.58}$$

The temperature factor is given [50] by $\alpha\,(T = -12\ ^{\circ}\mathrm{C}) = 2.9$.

In order to find the geometrical factor β_{geo}, we consider the viscous pressure drops, $\Delta p^{I}_{\mathrm{vis}}$ and $\Delta p^{II}_{\mathrm{vis}}$, in in a free bulk flow, and in the flow with micro-pillars, respectively. We start by discussing the free bulk flow. Assume a Poisson flow of silicone oil restricted by two side walls, a base and a free interface at the top, Fig SB.52 a,b. The side walls have a height of H and a pitch distance from one wall to the other of D. The silicone oil has a volume flux Q which flows in the y-direction. The viscous pressure drop can be calculated as [51]

$$\Delta p^{I}_{\mathrm{vis}} = L\frac{Q}{DH}\frac{3\eta_{\mathrm{SiOil,ref}}}{H^2}\left[1 - \sum_{m=1,odd}^{\infty}\frac{1}{m^5}\frac{384}{\pi^5}\frac{H}{D}\tanh\left(m\pi\frac{D}{4H}\right)\right]^{-1}. \tag{B.59}$$

The length over which the pressure drops is denoted by L, and m is the m-th Fourier mode of the lubricant velocity. Note that for $H/D \ll 1$, the side walls have negligible effect on friction within the flow. In this case, the free bulk flow on a plane is recovered, and the pressure drop reads

$$\Delta p^{I}_{\mathrm{vis}} = L\frac{Q}{DH}\frac{3\eta_{\mathrm{SiOil,ref}}}{H^2}. \tag{B.60}$$

Now, we introduce obstacles into the flow domain and compare the viscous pressure drop in this new situation. In the experimental system, the obstacles are represented by the micro-pillar array. Here, we idealize the experimental system and approximate the micro-pillars by n channels, separated by walls, Fig B.52 c. The height of the introduced walls is the same as of the side walls. We chose $H = 10\ \mu\mathrm{m}$, motivated by the micro-pillar height. The pitch distance between the walls is set to $D/n = d = 10\ \mu\mathrm{m}$, which coincides with the distance between the micro-pillars. The volume flux in a channel i is Q_i and the pressure drop is

$$\Delta p^{II}_{\mathrm{vis}} = L\frac{Q_i}{dH}\frac{3\eta_{\mathrm{SiOil,ref}}}{H^2}\left[1 - \sum_{m=1,odd}^{\infty}\frac{1}{m^5}\frac{384}{\pi^5}\frac{H}{d}\tanh\left(m\pi\frac{d}{4H}\right)\right]^{-1}. \tag{B.61}$$

Finally we compare the total pressure drop, $\Delta p^{II}_{\mathrm{vis}}$, of the system with obstacles to the pressure drop of the system without obstacles (with $H/D \ll 1$) to find the geometrical factor. We constrain the volume flux by specifying $nQ_i = Q$. The geometrical factor reads

$$\beta_{\mathrm{geo}} = \frac{\Delta p^{II}_{\mathrm{vis}}}{\Delta p^{I}_{\mathrm{vis}}} = 5.8 \tag{B.62}$$

Note that β_{geo} is independent of the channel length, L, and only depends on the ratio d/H. Introducing $\alpha\,(T = -12\ °\mathrm{C})$ and β_{geo} into Eq. (B.58), we find a dynamic viscosity $\eta_{\mathrm{SiOil}} = 3.2$ Pa s. We point out that this value for the effective viscosity still overestimates the real viscosity because we approximate the micro-pillar array by a line of channels. This remark is supported by the fact that we obtained optimal match between experimental data and simulation with an effective viscosity of $\eta_{\mathrm{SiOil}} = 2.9$ Pa s.

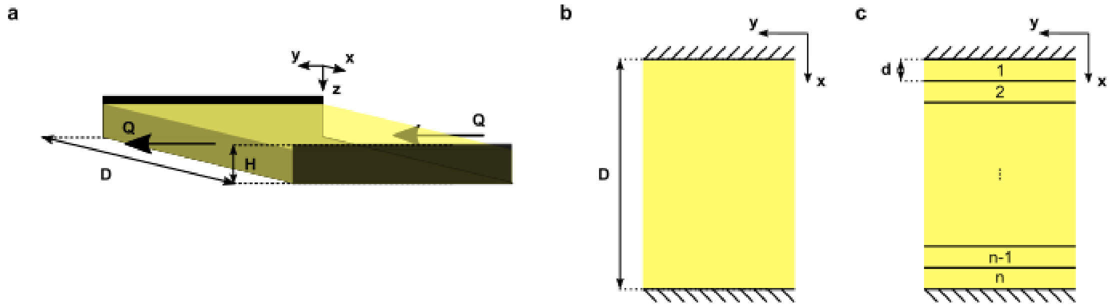

Figure B.52: **Schematic of silicone oil flow.** a) Silicone oil flows with a volume flux Q in the y-direction. The flow is restricted by side walls of height $H = 10\ \mu$m. b) Top view of the flow domain. The two side walls are separated by a distance D. c) The experimental system that includes a micro-pillar array is idealized by channels of the same width as the pitch distance between the micro-pillars, $d = 10\ \mu$m

Lubricant Reorganization during Condensation Frosting: Long-Wave Approximation

In the following, we report the theoretical framework that we use to model the lubricant flow. We start by discussing a general form of the conservation equation of mass and momentum [52], followed by the discussion of the appropriate boundary conditions. By nondimensionalizing the governing equations, we identify the dominant terms, and then formulate an asymptotic description of the flow problem. We introduce a standard finite difference discretization scheme for the derived governing equation in order to find the lubricant film height. Note that the notation slightly deviates from the one utilized in the main text of the manuscript. For clarity, we start by defining the nomenclature used in this section.

Nomenclature

Properties with physical dimension are marked with a tilde.

Position:	$[\tilde{x}, \tilde{y}]^T$
Velocity:	$[\tilde{u}, \tilde{v}]^T$
Lubricant height:	$\tilde{h}$
Density:	ρ
Dynamic viscosity:	η
Kinematic viscosity:	ν
Perturbation wave length:	λ
Initial lubricant height:	h_0
Frost propagation speed:	$\tilde{u}_{\text{ice}}$
Differential operators (Φ is a general property)	
Derivative ($\tilde{x}$ is chosen as an example):	$\frac{\partial \Phi}{\partial \tilde{x}}$ or $\partial_{\tilde{x}}\Phi$ or $\Phi_{\tilde{x}}$
Nabla operator:	$\nabla = [\frac{\partial}{\partial \tilde{x}}, \frac{\partial}{\partial \tilde{y}}]^T$
Total time derivative:	$\frac{d\Phi}{d\tilde{t}} = \frac{\partial \Phi}{\partial \tilde{t}} + \tilde{u}\frac{\partial \Phi}{\partial \tilde{x}} + \tilde{v}\frac{\partial \Phi}{\partial \tilde{y}}$

Domain

We introduce a set of coordinates and fix the origin in the vertical direction at the base and in the horizontal direction at the frost front, as illustrated in Fig B.53.

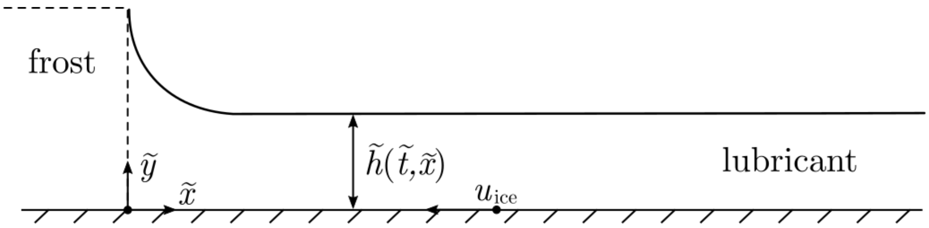

Figure B.53: Schematics of the flow domain. Coordinate system is fixed at the frost front.

Governing equations; general form

Mass conservation:

$$\frac{\partial \rho}{\partial \tilde{t}} + \frac{\partial (\rho \tilde{u})}{\partial \tilde{x}} + \frac{(\partial \rho \tilde{v})}{\partial \tilde{y}} = 0 \,. \tag{B.63}$$

For an incompressible fluid, such as the lubricant, the density ρ is constant, and (B.63) becomes

$$\frac{\partial \tilde{u}}{\partial \tilde{x}} + \frac{\partial \tilde{v}}{\partial \tilde{y}} = 0 \,. \tag{B.64}$$

Momentum conservation in the x-direction gives

$$\rho \left(\frac{\partial \tilde{u}}{\partial \tilde{t}} + \tilde{u}\frac{\partial \tilde{u}}{\partial \tilde{x}} + \tilde{v}\frac{\partial \tilde{u}}{\partial \tilde{y}} \right) = -\frac{\partial \tilde{p}}{\partial \tilde{x}} + \eta \left(\frac{\partial^2 \tilde{u}}{\partial \tilde{x}^2} + \frac{\partial^2 \tilde{u}}{\partial \tilde{y}^2} \right) \,. \tag{B.65}$$

Momentum conservation in the y-direction gives

$$\rho\left(\frac{\partial\tilde{v}}{\partial\tilde{t}}+\tilde{u}\frac{\partial\tilde{v}}{\partial\tilde{x}}+\tilde{v}\frac{\partial\tilde{v}}{\partial\tilde{y}}\right)=-\frac{\partial\tilde{p}}{\partial\tilde{y}}+\eta\left(\frac{\partial^2\tilde{v}}{\partial\tilde{x}^2}+\frac{\partial^2\tilde{v}}{\partial\tilde{y}^2}\right)\ . \tag{B.66}$$

The location of the lubricant height $\tilde{h}(\tilde{x},t)$ is given by the condition

$$\tilde{h}(\tilde{t},\tilde{x})=\tilde{y}\ . \tag{B.67}$$

The evolution of lubricant height is obtained by applying the total time derivative $d/d\tilde{t}$ to Eq. (B.67) (at $\tilde{y}=\tilde{h}$):

$$\frac{\partial\tilde{h}}{\partial\tilde{t}}+\tilde{u}\frac{\partial\tilde{h}}{\partial\tilde{x}}=\tilde{v}\ . \tag{B.68}$$

Boundary conditions

At $\tilde{x}=0$, the stresses in the lubricant and in the frost are continuous:

$$-\tilde{p}+\eta\frac{\partial\tilde{u}}{\partial\tilde{x}}=-\tilde{p}_{\text{ice}}\ . \tag{B.69}$$

For $\tilde{x}\to\infty$, the stress in the lubricant vanishes:

$$-\tilde{p}+\eta\frac{\partial\tilde{u}}{\partial\tilde{x}}=0\ . \tag{B.70}$$

At $\tilde{y}=0$, the lubricant satisfies the no-slip and no-penetration boundary condition:

$$\tilde{u}=-\tilde{u}_{\text{ice}},\ \ \tilde{v}=0\ . \tag{B.71}$$

At $\tilde{y}=\tilde{h}$ the shear stress of the lubricant becomes zero and the pressure is determined by the Laplace-Young boundary condition specifying pressure jump at the interface [53]

$$\eta\frac{\partial\tilde{u}}{\partial\tilde{y}}=0,\ \ \tilde{p}=-\gamma\tilde{\kappa} \tag{B.72}$$

Interfacial curvature

The curvature at the interface $\tilde{y}=\tilde{h}$ is determined [54] by $\tilde{\kappa}=\nabla\cdot\mathbf{n}_\Sigma$, with $\mathbf{n}_\Sigma$ being the normal vector at the interface. The curvature becomes

$$\tilde{\kappa}=\frac{\partial_{\tilde{x}\tilde{x}}\tilde{h}}{\left(1+\left(\partial_{\tilde{x}}\tilde{h}\right)^2\right)^{3/2}} \tag{B.73}$$

Capillary pressure in the ice domain

$$\tilde{p}_{\text{ice}}=-\frac{\gamma}{R_{\text{ice}}} \tag{B.74}$$

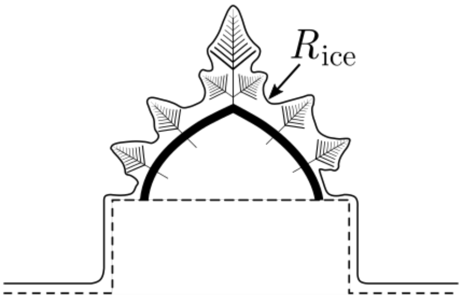

Figure B.54: Lubricant film covering frozen drop and dendrites. Frozen drop sits on top of a micropillar.

Dimensionless variables

We nondimensionalize the variables as follows:

$$x \equiv \tilde{x}/\lambda,\ y \equiv \tilde{y}/h_0,\ t \equiv \tilde{t}\tilde{u}_{\text{ice}}/\lambda,\ h \equiv \tilde{h}/h_0,$$

$$\epsilon \equiv h_0/\lambda,\ u \equiv \tilde{u}/\tilde{u}_{\text{ice}},\ v \equiv \epsilon\tilde{v}/\tilde{u}_{\text{ice}},\ p \equiv \tilde{p}\epsilon^{-1}\lambda/\gamma$$

$$\text{Ca} = \frac{\tilde{u}_{\text{ice}}\eta}{\gamma}, \qquad \text{Re} = \frac{\tilde{u}_{ice}h_0}{\nu} \ .$$

Here, Ca and Re are the capillary number and the Reynolds number, respectively. We define a horizontal scale λ, utilizing the capillary number, as

$$\lambda = h_0\left(3\text{Ca}\right)^{-1/3} . \tag{B.75}$$

Eq. (B.75) relates $\epsilon = h_0/\lambda$ with the capillary number Ca; note that $\text{Ca} \sim \mathcal{O}\left(\epsilon^3\right)$.

Non-dimensional governing equations

Mass conservation:

$$\frac{\partial u}{\partial x} + \frac{\partial v}{\partial y} = 0 \ . \tag{B.76}$$

Momentum conservation, x-direction:

$$\epsilon\text{Re}\left(\frac{\partial u}{\partial t} + u\frac{\partial u}{\partial x} + v\frac{\partial u}{\partial y}\right) = -3\frac{\partial p}{\partial x} + \epsilon^2\frac{\partial^2 u}{\partial x^2} + \frac{\partial^2 u}{\partial y^2} \ . \tag{B.77}$$

Momentum conservation, y-direction:

$$\epsilon^3\text{Re}\left(\frac{\partial v}{\partial t} + u\frac{\partial v}{\partial x} + v\frac{\partial v}{\partial y}\right) = -3\frac{\partial p}{\partial y} + \epsilon^2\left(\epsilon^2\frac{\partial^2 u}{\partial x^2} + \frac{\partial^2 u}{\partial y^2}\right) \ . \tag{B.78}$$

Evolution of lubricant height ($y = h$):

$$\frac{\partial h}{\partial t} + u\frac{\partial h}{\partial x} - v = 0 \; . \tag{B.79}$$

Interfacial curvature:

$$\kappa = \frac{\partial_{xx} h}{\left(1 + \epsilon^2 \left(\partial_x h\right)^2\right)^{3/2}} \; . \tag{B.80}$$

Long-wave approximation for $\epsilon^2, \epsilon\mathrm{Re} \ll 1$

Momentum conservation, x-direction:

$$\frac{\partial^2 u}{\partial y^2} = 3\frac{\partial p}{\partial x} \; . \tag{B.81}$$

Momentum conservation, y-direction:

$$0 = \frac{\partial p}{\partial y} \; . \tag{B.82}$$

Interfacial curvature:

$$\kappa = \frac{\partial^2 h}{\partial x^2} \; . \tag{B.83}$$

The mass conservation, Eq. (B.76) and the evolution equation for the film height, Eq. (B.79) preserve their respective form. Figure SB.55 shows the resulting domain in terms of non-dimensional variables.

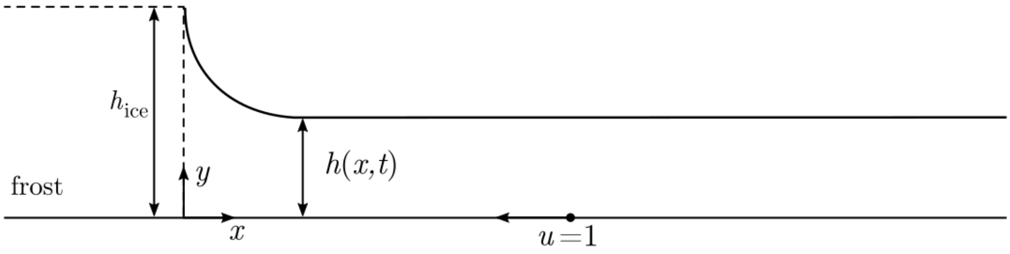

Figure B.55: Considered domain in terms of nondimensional variables.

Thin film equation

The velocities u and v at $y = h$ can be found by integrating equations (B.76), (B.81) and (B.82). Together with the no-slip and no-penetration condition at the base, the no-shear condition, and the Laplace-Young condition at $y = h$, we find

$$u(y = h) = \frac{3}{2}\frac{\partial \kappa}{\partial x}h^2 - 1 \; , \tag{B.84}$$

$$v(y=h) = -\left[\frac{\partial^2 \kappa}{\partial x^2} h^3 + \frac{1}{2}\frac{\partial \kappa}{\partial x}\frac{\partial h}{\partial x} h^2\right] \ . \tag{B.85}$$

Inserting equations (B.84)- (B.85) into Eq. (B.79), we obtain the evolution equation for the film height, h,

$$\boxed{\frac{\partial h}{\partial t} + \frac{\partial}{\partial x}\left[\frac{\partial \kappa}{\partial x} h^3 - h\right] = 0 \ .} \tag{B.86}$$

Boundary conditions

Utilizing the boundary conditions (B.69) and (B.70), yields

at $x = 0$:

$$\frac{\partial^2 h}{\partial x^2} + \left(\frac{\mathrm{Ca}^2}{3}\right)^{1/3} \frac{\partial u}{\partial x} = \frac{h_0}{R_{\mathrm{ice}}} (3\mathrm{Ca})^{-2/3} \ , \tag{B.87}$$

and for $x \to \infty$:

$$\frac{\partial^2 h}{\partial x^2} + \left(\frac{\mathrm{Ca}^2}{3}\right)^{1/3} \frac{\partial u}{\partial x} = 0 \tag{B.88}$$

Since $\mathrm{Ca}^2 \ll 1$, the second term on the left hand side of Eq. (B.87) (due to the normal compression) can be neglected. For closure, two further boundary conditions are required. Since the lubricant wets the ice, it is reasonable to assume a film height which matches the height of the ice front h_{ice} at $x = 0$. Since there is no inflow for $x \to \infty$, we specify zero flux there. To summarize, the four boundary conditions read as follows:

at $x = 0$:

$$h = h_{\mathrm{ice}} \ , \tag{B.89}$$

$$\frac{\partial^2 h}{\partial x^2} = \frac{h_0}{R_{\mathrm{ice}}} (3\mathrm{Ca})^{-2/3} \ , \tag{B.90}$$

and at $x \to \infty$:

$$\frac{\partial^3 h}{\partial x^3} = 0 \ , \tag{B.91}$$

$$\frac{\partial^2 h}{\partial x^2} = 0 \ . \tag{B.92}$$

Initial condition

Eventually we are only interested in the steady state solution of Eq. (B.86. However, in order to solve this equation, we need an initial condition. Hence, we choose an arbitrary function for $h(t=0)$ which satisfies the boundary conditions. We use

$$h(x) = h_{\text{ice}} \left(\alpha + (\alpha - 1) e^{-x\beta} \right) \ , \tag{B.93}$$

where $\alpha \in (0, 1]$ and

$$\beta = \sqrt{\frac{\lambda}{\epsilon R_{\text{ice}} \alpha h_{\text{ice}}}} \ .$$

Discretization of Long-Wave Equation

Space domain

The flux term in Eq. (B.86) is discretized using a standard finite difference scheme [55]. The grid points are equally spaced, with a spacing of $L/N = \Delta x$, and the physical domain is specified by $x \in [0, L]$. The grid points lie within the computation domain and are defined starting at $\Delta x/2$:

$$x_i = i \cdot \Delta x - 0.5 \Delta x \qquad i \in [1, N+1]. \tag{B.94}$$

The film height and the derivatives needed are specified as follows [43]:

$$h(x_i - 0.5\Delta x) \approx h_{1,i} = \frac{h(x_i) + h(x_{1+i})}{2} \ , \tag{B.95}$$

$$h_{xx}(x_i) \approx h_{xx,i} = \frac{h(x_{i+1}) - 2h(x_i) + h(x_{i-1})}{\Delta x^2} \ , \tag{B.96}$$

$$h_{xxx}(x_i - 0.5\Delta x) \approx h_{xxx,i} = \frac{h_{xx,i+1} - h_{xx,i}}{\Delta x} \ . \tag{B.97}$$

The approximated flux term, j_i, becomes

$$j_i = h_{xxx,i} \left(h_{1,i} \right)^3 - h_{1,i}. \tag{B.98}$$

Finally, the derivative of the flux is calculated as

$$dj_i = \frac{j_{i+1} - j_i}{\Delta x}. \tag{B.99}$$

Discrete boundary conditions

In order to describe the fluxes we need additional points, outside of the computational domain. We do this by introducing two (ghost) points on both sides: $\{i \in \mathbb{W}_{\setminus 0} | i = [1, N] \cup [-2; -1; N+2; N+3]\}$. On these points we need to find values of h_1, which is possible by utlizing the boundary conditions, equations (B.89) - (B.92). We obtain a set of equations, describing h_1 in the ghost field

$$h(x=0) = h_{\text{ice}} \approx h_{1,1} \ , \tag{B.100}$$

and

$$h_{xx}(x=0) = \frac{h_0}{R_{\text{ice}}} (3\text{Ca})^{-2/3} \approx \frac{h_{xx,-1} + h_{xx,1}}{2} \ . \tag{B.101}$$

Note that $h_{xx,-1}$ and $h_{xx,1}$ are calculated using Eq. (B.96), and that calculation of $h_{xx,-1}$ involves the $i = -2$ ghost point. The points at the right boundary are linked to the boundary condition by

$$h_{xxx}(L) = 0 \approx h_{xxx,N+1} \tag{B.102}$$

and

$$h_{xx}(L) = 0 \approx \frac{h_{xx,N} + h_{xx,N+1}}{2}. \tag{B.103}$$

$h_{xxx,N+1}$ is calculated using Eq. (B.97). Note that its calculation requires the use of the $N+3$ ghost point.

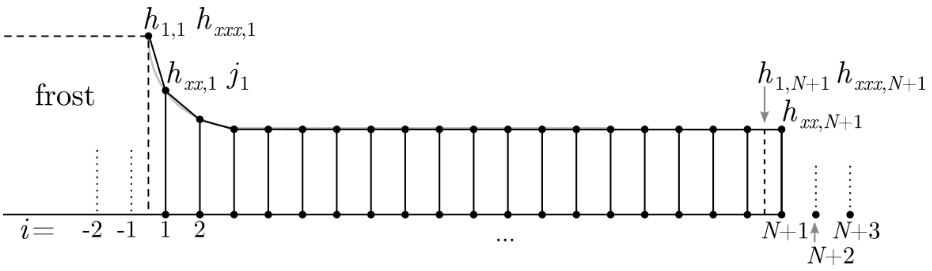

Figure B.56: Spatial discretization with N points and 4 ghost points.The vertical dashed line to the left corresponds to $x = 0$ and the one to the rigth to $x = L$.

Time domain

The continuous time, discrete space form of Eq. (B.86) reads

$$\frac{dh}{dt} \approx dj_i. \tag{B.104}$$

for $t \in [t_0, t_f]$. The time derivative is discretized using numerical differentiation formulae (NDF) [56]. This method provides good convergence for stiff ODE systems.

Steady state

To consider the steady state solution of the discretized Eq. (B.86), we evaluate the change between two subsequent discrete time steps $k-1$ and k,

$$\epsilon_k = \left\| dj_k \right\|_2 - \left\| dj_{k-1} \right\|_2 . \tag{B.105}$$

with $\left\| dj_k \right\|_2$ being the L2-norm of the k-th time step. We define the steady state for $\left\| \epsilon_k \right\|_2 \leq 10^{-5}$.

B.5 Frost Spreading and Pattern Formation on Microstructured Surfaces

Lukas Hauer, William SY Wong, Azadeh Sharifi-Aghili, Lou Kondic, and Doris Vollmer Physical Review E 104, no. 4 (2021): 044901.

Abstract

Frost is found in nature as a symphony of nucleation and heat/mass transport, cascading from angstroms to several meters. Here, we use laser-induced fluorescence microscopy to investigate the pattern formation of frost growth in experiments which tune the mesoscopic length scale by using microstructured pillar arrays as a frost condenser surface. By controlling the degree of surface supercooling and the amount of condensate, different modes of frost patterning are uncovered, ranging from complete surface coverage to fractal-looking and limited-coverage structures of spiky appearance.

Introduction

Condensation-frosting is the process of frost formation on partially wettable surfaces. Due to the high availability of water vapor in the atmosphere, condensation-frosting is abundant in nature and technology. Understanding this process is not only fascinating for its complexity but also highly important since frosting becomes detrimental in many technical applications. Condensation frosting starts with i) condensation [1–3] of supercooled droplets, followed by ii) the solidification of isolated droplets [4–6], and iii) subsequent frost spreading, starting from a solidified droplet [7, 8]. In step iii), frost spreads by draining water from surrounding liquid droplets. Spreading evolves in one of two possible modes, where the ratio of droplet diameter to inter-droplet spacing is pivotal: if droplets are sufficiently large and distributed densely, frost propagates fast *via* connecting frost bridges. This spreading mode is characterized as diffusion (through air) followed by freezing of the connected droplets. The second mode is facilitated when individual droplets condense too sparsely. Droplets evaporate entirely before inter-droplet frost bridges can connect them (*i.e.* dry zones form) [9]. In this second case, frost grows solely *via* diffusion, similarly to snowflakes in clouds [10]. Which of these two spreading modes applies is determined by isolated droplet-to-droplet interactions which are fully characterized in one dimension [11–13]. When droplets condense on surfaces, we show that this, however, is an insufficient description of frosting: intermediate spreading modes emerge due to collective effects that account for interactions between multiple droplets in two dimensions. In this

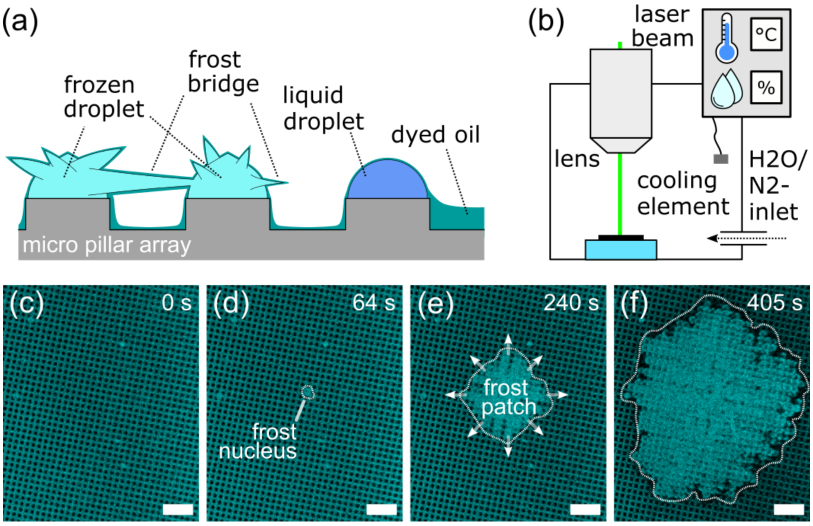

Figure B.57: (a) Cross-sectional schematic of frost spreading on micropillar array. Droplets sit on top of pillars. Frost bridges grow from frozen droplets toward liquid ones. Silicone oil is distributed in between the pillars and cloaks the droplets. (b) Experimental setup. (c-f) Frost formation and spreading: (c) Surface at $t = 0$ s. Silicone oil in between the micro-structure is cyan while the micropillar tops are black. (d) After some time ($t = 64$ s), one droplet starts freezing (*i.e.* frost patch nucleates). (e-f) Frost patch grows outwards by successively connecting neighboring droplets with frost bridges. Here, $RH = 34\%$, $T_{set} = -35$ °C; scale bar is 200 μm. Temperatures on the surface were measured to be 3 K higher than T_{set}.

case, regions of interconnected droplets and dry zones can occur simultaneously. Here, we explore the patterns of frost, grown under the full spectrum of spreading modes, selected by modifying the amount of available condensed water and varying the set-point temperature (-20 to -45 °C), which affects frost patch nucleus formation. To control the droplet distribution, we use microstructured surfaces as a frost-condenser. An infused fluorophore dyed silicone oil helps to increase the contrast between surface and frost patterns which were observed *via* laser-induced fluorescence (LIF) microscopy. This imagining technique provides a large field of view (2.5x magnification) and appropriate time resolution for transient frost pattern formation. Silicone oil cloaks water regardless of its aggregate state, which increases the visibility of frost but also affects frost spreading by slowing down the inter droplet vapor transport. We estimate the magnitude of vapor transport retardation by developing a resistance model and discuss it in the context of frost spreading. Furthermore, we find that patterns formed in intermediate spreading modes show fractal structure [14–16], therefore slowing down the coverage speed of the frost [11]. Different topographies are formed, depending on the amount of available atmospheric water. The number and size of frost patches can be tuned by surface temperature.

Surface Preparation and Experimental Set-up

Frost condenser surfaces were fabricated as follows: 170 μm thick glass slides were coated with a rigid microstructure (SU-8) by photolithography. The microstructure is characterized by circular pillars (diameter: 30 μm, height: 10 and 20 μm) in a square lattice configuration (30 μm edge-to-edge distance). Fluorophore powder (Lumogen Red F300, BASF) was dissolved in silicone oil (polydimethylsiloxane 200 cSt, Gelest). The dyed oil was infiltrated into the microstructure. Silicone oil cloaks condensed water with an approximately $\delta \approx 10^{-8}$ m thick layer [17, 18] and creeps into the spreading frost patch [19]. The diffusive mobility of water in silicone oil ($D = 2 \times 10^{-9}$ m^2/s [20]) allows water molecules to easily pass through the oil [21]. Hence, the silicone oil does not insulate water vapor transport but rather constitutes a resistance towards the diffusing water molecules. However, it helps to visualize the frost patches by increasing the contrast on the surface. The impregnated microstructure is placed on a Peltier element which cools the surface down to controllable subzero temperatures T_{set}. To form frost, the cooled surface is sealed in an environmental chamber. Nitrogen gas with preset water vapor content (*i.e.* relative humidity RH) is introduced into the chamber for 30 s. Thereafter, the system relaxes to a steady-state. All processes (*i.e.* frost formation and spreading) on the surface were monitored *via* laser-induced fluorescence (LIF) microscopy operated with a 2.5x objective lens (dry; Leica HC PL FLUOTAR 2.5x/0.07), Fig.B.57(b).

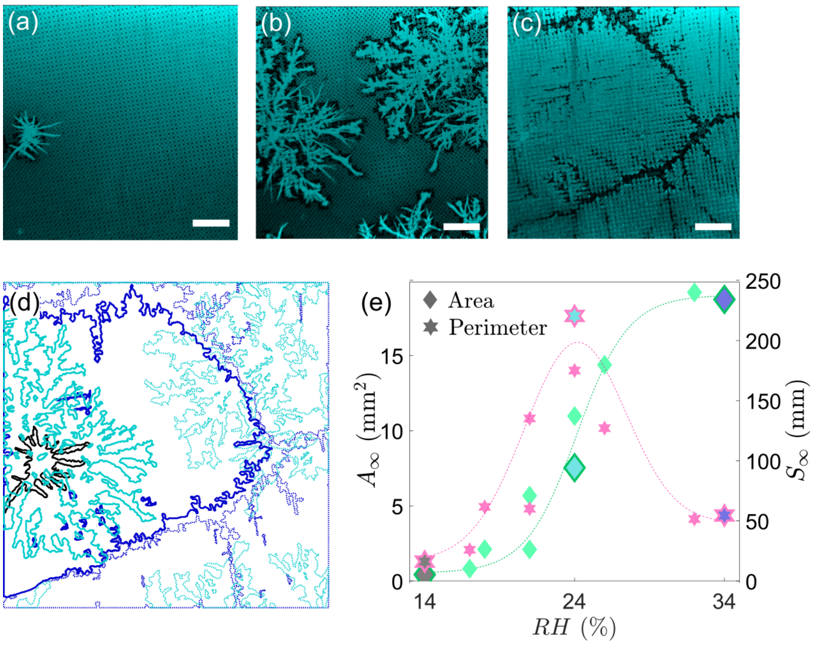

Figure B.58: Frost patterns for different relative humidity, RH, and $T_{set} = -30$ °C at the steady state. (a) $RH = 14\%$. A single frost patch with arbitrarily directed frost spikes. (b) $RH = 24\%$. Multiple frost patches form. (c) $RH = 34\%$. The surface is nearly entirely covered by frost. Scale bars are 500 μm. (d) Boundary contour of frost patches, $RH = 14\%$ (black), $RH = 24\%$ (turquoise) and $RH = 34\%$ (blue) overlaid. For all three RH-configurations, frost patches (solid thick lines) were triggered from the same defect. Other neighboring frost patches are outlined with faint lines. (e) Area, A_∞, (green diamonds), and perimeter, S_∞, (pink stars) versus RH. Filled symbols at 14%, 24% and 34% RH correspond to patterns in (d). The area of frost coverage increases monotonously with peak relative humidity, while the perimeter passes a maximum around $RH = 24\%$. The dotted line serves as a guide to the eye.

Frost Formation and Spreading

Right after humidified nitrogen gas is introduced into the sealed chamber, supercooled droplets condense on the micropillar tops, Fig. B.57(c). Condensation of droplets is accompanied by falling relative humidity in the chamber, from supersaturation to saturation, with respect to the cooled surface [21]. Supercooled droplets remain liquid for some time before they randomly start to freeze. Freezing of a droplet becomes visible *via* LIF due to accumulation of lubricant leading to change in contrast, Fig. B.57(d). We identify a single frozen droplet as the nucleus of a frost patch. The frost patch grows as a continuous domain from the nucleus outwards, Fig. B.57(e). The growth of the domain is facilitated by the vapor flux, coming from liquid droplets. In Sec. B.5, we introduce a framework of this flux. While the frost patch grows, the region right in front of the frost patch becomes darker, making the perimeter more pronounced. This is caused by local oil depletion, *i.e.* oil is sucked into the dendritic frost patch [19], Fig. B.57(f). The frosting process ends when all liquid water on the cooled surface becomes either solid as part of the frost patches or vapor as it re-evaporates back into the atmosphere. As set-point temperature and relative humidity RH are the expected governing system parameters, we varied those and discuss their respective impact, starting with RH.

Frost Spreading at Differing Humidity

RH is determined by the water content in the nitrogen flux at an ambient temperature of 20 ± 2 °C. We discuss three characteristic configurations at which the relative humidity peaked at 14%, 24%, and 34%. Each configuration is observed in a steady state ($t \to t_\infty$) and the field of observation ($3220\ \mu\text{m} \times 3220\ \mu\text{m}$) is kept on the same surface spot, Fig. B.58(a)-(c). For $RH = 14\%$, only a single frost patch formed, Fig. B.58(a) and Supplemental Video[8]. While this patch starts forming frost bridges, neighboring droplets completely evaporate before the bridges reach them. The cascading process is interrupted. Still, water vapor from evaporating droplets slowly attaches on the single frost patch, forming randomly directed spiky tips. Increasing the water content to an intermediate amount ($RH = 24\%$) leads to the formation of three visible frost patches within the field of observation, Fig. B.58(b) and Supplemental Video[9]. Each frost patch grows larger, compared to the patch in drier atmosphere. During growth, frost bridges reach out for their neighboring liquid droplets to connect them. However, this does not always occur, as reflected by the dark regions between branches, which are not covered by frost. Instead, they evaporate entirely before frost bridges can reach them, leaving empty micropillar tops behind. The pattern shows branching arms, angled at approximately 45° to the main arm. This roots from the anisotropy under which the frost patch grows, imposed by the micro-arry lattice. For a very humid atmosphere, the nucleated frost patches connect nearly all liquid droplets on the surface, Fig. B.58(c) and Supplemental Video[10]. Growing frost patches halt when they approach each other, separated by a ‘ditch’. Overlaying the boundary contours of the frost patch patterns, grown by the three RH-configurations, unravels descriptively how different amounts of water content in the atmosphere lead to different patterns and how they are related, Fig. B.58(d). Frost at $RH = 14\%$ nucleated from a surface defect. The same surface defect triggered frost for the other two RH-configurations. The size of the regions uncovered by frost gradually decreases with increasing atmospheric humidity. While frost covered area, A_∞, increases monotonously (green diamonds) with relative humidity, the cumulative perimeter, S_∞ (pink stars), passes a maximum, Fig. B.58(e). This indicates that increased atmospheric humidity not only leads to more surface coverage (increased A_∞) but also to smoother frost patch perimeters (decreased S_∞). The minimum of S_∞ and A_∞ at $RH = 14\%$ stems from the solely diffusive driven growth mode which is fundamentally different from the other two cases. Droplets do not connect, leading to a small frost patch with small S_∞ and A_∞.

---

[8] See Supplemental Movie S1 at [22] for frost formation and spreading at $RH = 14\%$ and $T_{set} = -35$ °C.

[9] See Supplemental Movie S2 at [22] for frost formation and spreading at $RH = 24\%$ and $T_{set} = -35$ °C.

[10] See Supplemental Movie S3 at [22] for frost formation and spreading at $RH = 34\%$ and $T_{set} = -35$ °C.

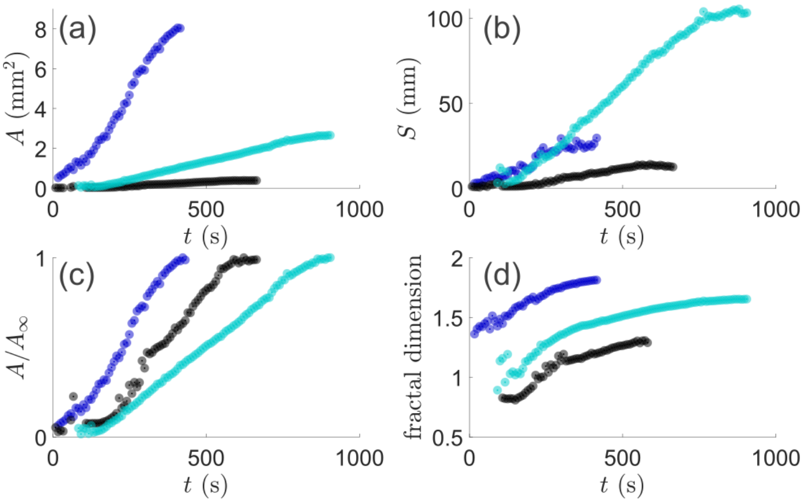

Figure B.59: Evolution of frost patch over time for $RH = 14\%$ (black), $RH = 24\%$ (turquoise) and $RH = 34\%$ (blue). (a) Covered area, $A(t)$; (b) Perimeter $S(t)$; (c) Normalized area, $A(t)/A_\infty$; and (d) fractal dimension, d_f.

Table B.4: Steady state area A_∞ and perimeter S_∞ for dry, intermediate and humid RH-configurations. t_∞ is the total time taken for steady state to be reached. Data corresponds to steady state patterns with high precision extraction. Plane of 6440 μm × 3220 μm.

RH(%)	A_∞ (mm^2)	S_∞ (mm)	t_∞ (s)	$d_{f,\infty}$ [11]
14	0.5	16	720	1.3
24	7.5	220	940	1.7
34	18.7	55	540	1.9

Dynamic Tracking of Spreading Frost Patches

To understand how different patterns emerge, we track the evolution of covered area, $A(t)$, and perimeter, $S(t)$, of the frost patches during their formation and growth for all three RH-configurations, Fig. B.59(a)-(b). The field of observation was increased to 5031 μm × 1962 μm to obtain better sampling statistics. The dynamically acquired data-set was processed *via* outlier filtering, Appx. B.5. Data points with poor signal to noise ratio in the early stage of the experiments ($t < 60$ s) were excluded. To validate the dynamic measurements, we conducted measurements on surfaces with enhanced frost detection and a larger field of view, after reaching a steady state ($t \to t_\infty$), Tab. B.4. Note that the trends of A_∞ and S_∞ are consistent between dynamic (Fig. B.59(a)-(b)) and static measurements (Tab. B.4).

Normalizing the recorded data by A_∞ shows that $A(t)$ evolves for all three cases as a stretched S-shaped curve, Fig. B.59(c). The normalized plot reveals that area growth is fastest when the humidity is at its highest (blue curve), followed by the lowest RH-configurations (black curve). This is reflected in the average frost front speed, which is 1.4 ± 0.7 μm/s for the highest and 0.2 ± 0.1 μm/s for the lowest humidity, Appx. B.5. Even though growth times for $RH = 14\%$ ($t_\infty = 720$ s) and $RH = 34\%$ ($t_\infty = 540$ s) are comparable, the former grows much slower, which stems from a fundamentally different growth mode. For $RH = 14\%$, the frost patch grows mainly by forming spiky tips. These tips are only able to grow as long as the gaseous ambient is supersaturated with respect to the surface (or the nucleus). This condition holds as long as condensing droplets evaporate back into the atmosphere. The evaporation of the droplets constitutes the time-limiting factor. For $RH = 34\%$, t_∞ is governed by successively connected droplets *via* ice bridges, which is a diffusion-type process. As freezing of connected droplets is fast compared to the growth of frost bridges, the diffusion process is sped up as the droplet size increases [7]. Interestingly, the intermediate RH-configuration appears to exhibit the longest growth time (turquoise curve) with an average frost front speed of 0.08 ± 0.04 μm/s. Droplets do connect *via* frost bridges, however, this process is occasionally interrupted by the premature droplet evaporation before frost bridges could reach them. These 'dead-ends' throttle the growth. The existing literature considers the frost spreading by bifurcating in two possible modes: i) successful inter-droplet bridge connection (as for $RH = 34\%$) or ii) disjoint, diffusive growth (as for $RH = 14\%$) [7, 13]. Notably, here we show that frost may spread not only obeying these two strictly binary modes, but instead its spreading can be tuned. In between the two extreme scenarios fractal-like branching arms develop, generating frost patterns of variable surface coverage.

Fig. B.59(d) shows the fractal dimension d_f (computed using box-counting method [23]) of the growing patches. For all three configurations, d_f grows monotonously and converges to differing steady state values for the respective humidity configurations. We measured the fractal dimension for steady states, $d_{f,\infty}$, again with enhanced frost detection, Tab. B.4. For $R = 34\%$, $d_{f,\infty} \approx 1.9$, which is characteristic for correlated aggregation process, where the fractal dimension is slightly lower than the ordinary Euclidean dimension (*i.e.* 2) [24]. This result can be understood considering that all condensed droplet connect and contribute to the frost patch. For $RH = 24\%$, $d_{f,\infty} \approx 1.7$. This value characterizes diffusion limited aggregates [14]. This is in line with the observation that not all droplets are successively connected but some spots are left dry. Finally, for the driest scenario ($RH = 14\%$) $d_{f,\infty} \approx 1.3$. This value does not correspond to either correlated or diffusive limited aggregation. This supports the interpretation for $RH = 14\%$ being a different mode of growth.

Frost Spreading at Differing Temperature

To understand the influence of temperature, we varied the T_{set} within -20 °C and -45 °C, while the humidity peaked at $RH = 28 \pm 1\%$. The steady state frost patterns formed at $T_{set} = -25$ °C is characterized by few large frost patches, Fig. B.60(a). Each patch developed branching arms separated by unconnected areas (fine, dark boundaries) within each patch. Decreasing the temperature to $T_{set} = -35$ °C results in comparatively more, but smaller frost patches, Fig. B.60(b). For $T_{set} = -45$ °C this trend almost reaches the theoretical limit, of one drop per pillar, Fig. B.60(c). At this limiting condition, condensing droplets do not freeze in a staggered manner, but simultaneously

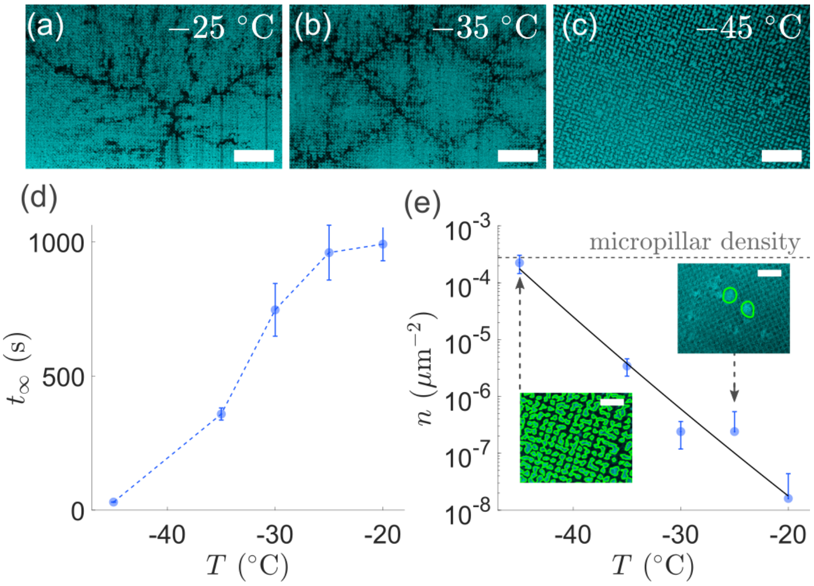

Figure B.60: Steady state frost pattern for $RH = 28 \pm 1\%$. Set point temperature T_{set} is (a) -25 °C, (b) -35 °C, and (c) -45 °C. Scale bars are 500 μm. The dependence of the relaxation time, t_∞ (d) and of the number of nuclei per area, n (e) on imposed temperature T_{set}. The insets show that fewer nuclei formed at $T_{set} = -25$ °C and many nuclei formed at $T_{set} = -45$ °C set point temperature. Nuclei boundaries are emphasized in green. Dashed line depicts micro-pillar density (upper nucleus limit), solid line shows an exponential fit shown in Eq. B.106. Scale bar in insets is 200 μm.

right after condensation. This creates almost as many frost patches as the number of micropillars on the surface. We observe that steady states are reached faster (*i.e.* smaller t_∞) for decreasing T_{set}, Fig. B.60(d). The reason for smaller t_∞ lies in the increased number of frost patch nuclei per area, n, which we count as soon as they emerge, Fig. B.60(e). The highest possible number of frost patch nuclei is limited by the micropillar density of the surface, which is demarcated by the dashed line. Plotting the counted n against the T_{set} indicates an Arrhenius behaviour of the frost patch nucleation,

$$n \sim \exp(-g(T_{set})/k_B T), \tag{B.106}$$

as depicted by the black solid line in the plot. Here, k_B is the Boltzmann constant and T the droplets' temperature. Frost nucleus formation is linked to overcoming the energetic barrier $g(T_{set}) \approx 10 k_B T$ (*i.e.* freezing). The value for $g(T_{set})$ is obtained by fitting Eq. (B.106) to the counted n. The black line in Fig. B.60(e) corresponds to the fit. Note, that the trend of n indicates a vanishing nucleation barrier for lower T_{set}.

Water Vapor Transport in Cloaked Droplet Array

Spreading of the frost domain is facilitated by the growth of frost bridges, emerging from the nucleus. Here we briefly discuss a framework for the governing vapor transport, which provides a basic rational that is useful for understanding the experimental results. The saturation concentration of water around each droplet is different, depending on its aggregate state [25]. This roots from differing chemical potentials of liquid and frozen water at equal temperature. If a frozen droplet neighbours a liquid droplet, the water concentration increases from the frozen to the liquid drop. Therefore, diffusive water transport is facilitated from the liquid to the solid droplet, Fig. B.61(a). Water molecules attach on the frozen surface, S, at a rate of

$$J = D \nabla c \cdot \boldsymbol{n}, \tag{B.107}$$

where ∇c is the gradient of the water concentration on the nucleus' surface S and $\boldsymbol{n} = \nabla S / \|\nabla S\|$ is the surface normal vector. Although droplets are three-dimensional objects, the mass flow on their surface per Eq. (B.107) acts dominantly from droplet to droplet, in the plane of the substrate. We assume that the vapor transport is in quasi-equilibrium, yielding a divergence free flux field *i.e.* $\nabla \cdot J = 0$. Droplets are cloaked by a thin layer of silicone oil, independently of their aggregate state (liquid or frozen) [17, 18]. Water is soluble in silicone oil [20], which leads to migration of water molecules from the droplets into the silicone oil layer. Directly at the shared interface between water and silicone oil, the water molecules are in local equilibrium. This implies that here, silicone oil is saturated with water. In steady-state, the mass flux from from liquid to frozen droplet scales as

$$J = \left(c_{sat,s} - c_{sat,l}\right) / R, \tag{B.108}$$

where $c_{sat,l}$ and $c_{sat,f}$ are the saturation concentration of water around a liquid and a frozen droplet, respectively. While water molecules migrate through silicone oil and through air, they experience in each phase a different diffusive resistance, *i.e.* R_{SiOil} and R_{air}, respectively. Those resistances appear in series, Fig. B.61(b). Hence, they add up to a total resistance as

$$R = R_{SiOil} + R_{air} + R_{SiOil} = \frac{\delta_{air}}{D_{air}} + 2\frac{\delta}{D}. \tag{B.109}$$

Here, the diffusivity of water vapor in air is $D_{air} = 3 \times 10^{-5}$ m^2/s [26]. The distance, separating droplets in air is here denoted with δ_{air}. Considering that $i = 1, 2, ..., m$ droplets are distributed on the surface, we can evaluate the flux j_{ij} at position $\boldsymbol{x}_i$, coming from a droplet at position $\boldsymbol{x}_j$ per

$$j_{ij} = \frac{c_i - c_j}{\frac{\delta_{ij}}{D_{\mathrm{air}}} + 2\frac{\delta}{D}}. \tag{B.110}$$

This expression for the flux does not only account for the fluxes between a liquid and a frozen droplet but between any two arbitrary droplets $i,\ j$. The resistance will then depend on the separation distance between these $i,\ j$ droplets, which computes as $\delta_{ij} = \|\boldsymbol{x}_i - \boldsymbol{x}_j\|$. The concentrations $c_i,\ c_j$ are determined by the aggregate state of the $i,\ j$-th droplets, respectively, and are assumed to correspond to the saturation vapor concentration of either liquid or solid water, namely

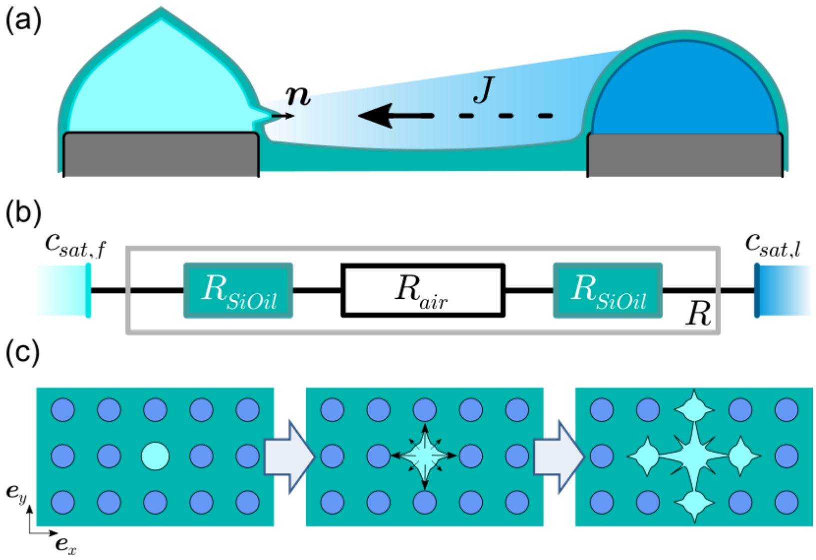

Figure B.61: Diffusive flux from liquid to frozen droplet. (a) Schematics of water vapor gradient from liquid to solid droplet. Water attaches on the solid droplet, forming an emerging frost bridge. Both, the liquid and the solid droplet are cloaked by a thin silicone oil layer. (b) Serial flux resistance. Water molecules are saturated on the solid ($c_{sat,s}$) and on the liquid ($c_{sat,l}$) droplet interface towards silicone oil. Water travels from the liquid droplet trough the first silicone oil layer (R_{SiOil}), then through air (R_{air}) and then, again, through a silicone oil layer (R_{SiOil}) before it finally attaches on the solid droplet.

$$c_i = \begin{cases} c_{sat,s} & \text{if droplet is frozen} \\ c_{sat,l} & \text{if droplet is liquid.} \end{cases} \tag{B.111}$$

In order to determine the total flux to a droplet at $\boldsymbol{x}_i$, Eq. (B.110) has to be summed up over all other droplets j, as

$$J_i = \sum_{j, j \neq i}^{m} j_{ij}. \tag{B.112}$$

Frost bridges gradually accumulate mass per Eq. (B.107) and grow towards the neighboring liquid droplets. When the frost bridge connects with a neighboring liquid droplet, the droplet freezes immediately. At the freshly frozen droplet, new frost bridges grow toward their neighboring liquid droplets, Fig. B.61(c). This cascading process leads to growth of a continuous frost domain.

The flux on a frozen droplet from gradually further separated liquid ones is plotted in Fig. B.62(a). Here, we consider a frozen droplet at fixed $i = i^*$. In the plot, the flux j_{i^*j} is non-dimensionalized with the flux-magnitude within the silicone oil, *i.e.* $\delta / (\Delta c\ D)$ where $\Delta c = c_{sat,s} - c_{sat,l}$. To non-dimensionalized the separation distance δ_{i^*j}, we choose the scale $D / (\delta\ D_{air})$. In the immediate vicinity of the frozen droplet, the fluxes are strong, and become gradually weaker, as further away the liquid droplets are located. At a certain distance, the flux becomes drastically weaker with increasing separation distance. In our system, this crossover occurs at approximately 600 μm from the frozen droplet. This cross-over can be explained by revisiting Eq. (B.110): we note that at $\delta_{i*j} \approx 600$ μm both terms in the denominator become comparable. This implies, that fluxes in the direct vicinity of a frozen droplet are limited by the resistance that water molecules experience in silicone oil. We hypothesize that the interplay between fluxes per Eq. (B.112) and the amount of condensed water will determine the outcome of frost spreading. This estimate of governing flux resistance is only valid for fluxes from liquid droplets to a single frozen one. On larger scales, however, this criterion is not necessarily fulfilled anymore. We expect that the picture becomes more complicated, once frost patches are formed and spread on the surface.

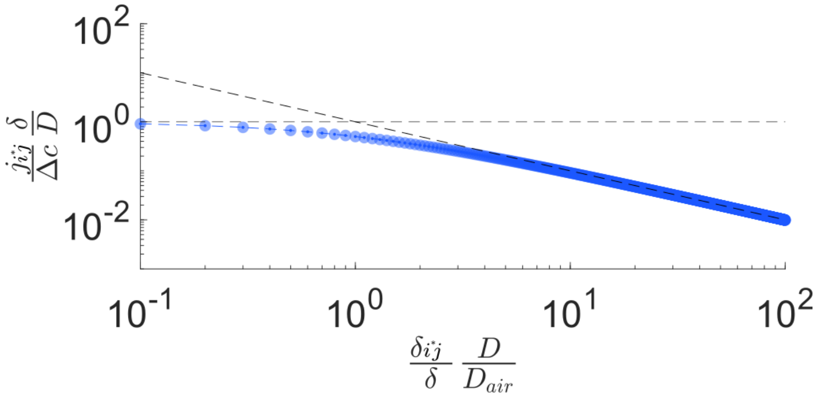

Figure B.62: Non-dimensional vapor flux as a function of non-dimensional separation distance (here, the distance between pillars is 0.1; each circular symbol corresponds to a pillar site). Individual flux components j_{i^*j}. Regime of oil limited transport (horizontal dashed line) crosses over into air limited transport (inclined dashed line). The respective dashed lines are plotted by using the discussed flux expression j_{i^*j} with only one of the two resistance components.

Conclusion

To summarize, tuning the relative humidity produces different modes of spreading; in between the two cases of droplets fully interconnected by frost bridges (leading to almost complete surface coverage), and pure diffusion driven growth (leading to spiky-looking objects covering a small part of the domain), we find a mixture of both modes, which exhibits fractal-like properties. Further, the set-point temperature is a direct proxy for the frost patch nucleus formation which is limited by the energy barrier. We note that the formation of branching arms appears to be inherently encoded in the condensation-frosting process. The weaker manifestation of the branching arms for lower set-point temperatures is, hence, rather a consequence of a faster approach to steady state caused by increased number of nucleating sites. We hope that our results will inspire further experimental and theoretical work that will lead to a comprehensive understanding of pattern formation occurring during frosting.

Acknowledgments

This work was supported by the German Research Foundation (DFG) with the Priority Programme 2171 (L.H., D.V.), the European Union's Horizon 2020 research and innovation program LubISS No. 722497 (W.W, D.V.), the Max Planck – Univ. Twente Center for Complex Fluid Dynamics (D.V.), US National Science Foundation grants NSF CBET-1604351 and DMS-1815613, and NJIT Faculty Seed Grant (L.K.). We thank Hans-Jürgen Butt, Abhinav Naga and Peter Stephan for stimulating discussions.

Apendix A: Running Median Outlier Filter

The running median outlier filter is excluding data points which exceed three scaled median absolute deviations (sMAD) within their direct environment. We used the the MATLAB function isoutlier() for this purpose. The running median φ_i^m in a set $[\phi_i]$ defines the median of m points, at a centric position i. The running median in an environment of *eg.* $m = 10$ points reads

$$\varphi_i^{10} = (\phi_j), \tag{B.113}$$

with $j = [i-5, i+5]$. sMAD is defined as

$$\text{sMAD}_i = c\ (|\phi_j - \varphi_i^{10}|), \tag{B.114}$$

with $c = -1/(\sqrt{2}(3/2))$. Hence, we find

$$\phi_i = \begin{cases} \phi_i & \text{for } \phi_i \leq 3\text{sMAD} \\ \varnothing & \text{for } \phi_i > 3\text{sMAD}. \end{cases} \tag{B.115}$$

Apendix B: Average Frost Front Propagation Speed

In order to compute the average frost front propagation speed, we consider how the area $A(t)$ grows, by means of an expanding perimeter $S(t)$, with a velocity $\boldsymbol{v}_{ice}$ at the perimeter:

$$\frac{dA}{dt} = \dot{A} = \oint (\boldsymbol{n} \cdot \boldsymbol{v}_{ice})\, dS \tag{B.116}$$

Here, $\boldsymbol{n} = \nabla S / \|\nabla S\|$ is the perimeter's normal vector. We spatially average the velocity, normal to the perimeter, over the perimeter, yielding

$$\bar{v}_{ice} = \frac{\oint (\boldsymbol{n} \cdot \boldsymbol{v}_{ice})\, dS}{\oint\, dS}. \tag{B.117}$$

With $\oint\, dS = S(t)$, Eq. (B.116), and Eq. (B.117), we find

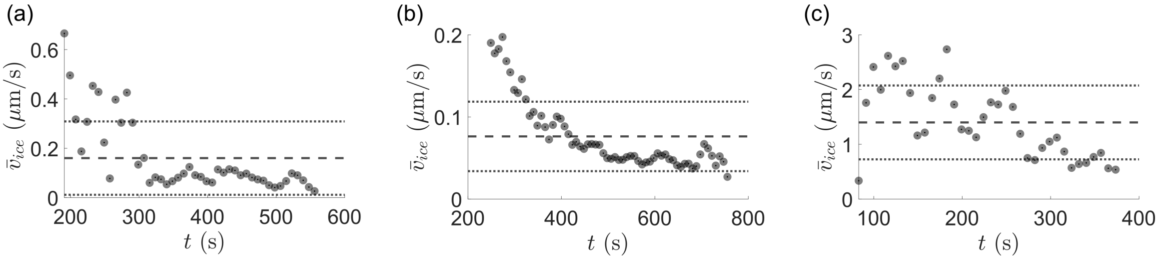

Figure B.63: Average frost front propagation speed for a) $RH = 14\%$, b) $RH = 24\%$ and c) $RH = 34\%$. The dashed line corresponds to the time-averaged speed which is a) 0.2 ± 0.1 μm/s, b) 0.08 ± 0.04 μm/s and c) 1.4 ± 0.7 μm/s. The dotted lines demarcate the 1-sigma (standard deviation) band.

$$\bar{v}_{ice} = \frac{\dot{A}}{S}. \tag{B.118}$$

We compute $\dot{A}$ from the measurements, *cf.* Fig. B.59(a). In order to make the derivative estimate of each data point more robust, we utilize 4 neighbouring points (2 preceding, 2 succeeding) and compute the linear regression. The derivative is taken as the linear regression's slope. Fig. B.63 shows $\bar{v}_{ice}$ for the data in Fig. B.59(a)-(b). Finally, we compute the time mean and its standard derivation of $\bar{v}_{ice}$ during the main phase (100-800 seconds) of the frost growth.

References

1. Zhao, H. & Beysens, D. From Droplet Growth to Film Growth on a Heterogeneous Surface: Condensation Associated with a Wettability Gradient. *Langmuir* **11,** 627–634. ISSN: 15205827 (1995).
2. Beysens, D. Dew Nucleation and Growth. *C. R. Phys.* **7,** 1082–1100. ISSN: 16310705 (2006).
3. Anand, S., Rykaczewski, K., Subramanyam, S. B., Beysens, D. & Varanasi, K. K. How Droplets Nucleate and Grow on Liquids and Liquid Impregnated Surfaces. *Soft Matter* **11,** 69–80. ISSN: 1744-6848 (Dec. 2014).
4. Na, B. & Webb, R. L. A Fundamental Understanding of Factors Affecting Frost Nucleation. *Int. J. Heat Mass Transf.* **46,** 3797–3808. ISSN: 0017-9310 (2003/09/01/).
5. Marín, A. G., Enríquez, O. R., Brunet, P., Colinet, P. & Snoeijer, J. H. Universality of Tip Singularity Formation in Freezing Water Drops. *Phys. Rev. Lett.* **113,** 1–5. ISSN: 10797114 (2014).
6. Libbrecht, K. G. Physical Dynamics of Ice Crystal Growth. *Annu. Rev. Mater. Res.* **47,** 271–295. ISSN: 1531-7331 (2017).
7. Guadarrama-Cetina, J., Mongruel, A., González-Viñas, W. & Beysens, D. Percolation-Induced Frost Formation. *EPL* **101,** 16009. ISSN: 0295-5075 (Jan. 2013).
8. Nath, S., Ahmadi, S. F. & Boreyko, J. B. A Review of Condensation Frosting. *Nanoscale Microscale Thermophys. Eng.* **21,** 81–101. ISSN: 1556-7265, 1556-7273 (Apr. 2017).
9. Boreyko, J. B. & Collier, C. P. Delayed Frost Growth on Jumping-Drop Superhydrophobic Surfaces. *ACS Nano* **7,** 1618–1627. ISSN: 1936-0851, 1936-086X (Feb. 2013).
10. Pruppacher, H. R. & Klett, J. D. in *Microphysics of Clouds and Precipitation* Second, 191–209 (New York, Boston, Dordrecht, London, Moscow, 2004).

11. Petit, J. & Bonaccurso, E. General Frost Growth Mechanism on Solid Substrates with Different Stiffness. *Langmuir* **30,** 1160–1168. ISSN: 0743-7463, 1520-5827 (Feb. 2014).
12. Nath, S. & Boreyko, J. B. On Localized Vapor Pressure Gradients Governing Condensation and Frost Phenomena. *Langmuir* **32,** 8350–8365. ISSN: 0743-7463 (Aug. 2016).
13. Nath, S., Ahmadi, S. F. & Boreyko, J. B. How Ice Bridges the Gap. *Soft Matter* **16,** 1156–1161. ISSN: 1744-683X, 1744-6848 (2020).
14. Witten, T. A. & Sander, L. M. Diffusion-Limited Aggregation, a Kinetic Critical Phenomenon. *Phys. Rev. Lett.* **47,** 1400–1403. ISSN: 00319007 (1981).
15. Mandelbrot, B. How Long Is the Coast of Britain? Statistical Self-Similarity and Fractional Dimension. *Science* **156,** 636–638. ISSN: 00368075 (1967).
16. Ben-Jacob, E. From Snowflake Formation to Growth of Bacterial Colonies. *Contemp. Phys.* **34,** 247–273. ISSN: 0010-7514 (1993).
17. Bergeron, V. & Langevin, D. Monolayer Spreading of Polydimethylsiloxane Oil on Surfactant Solutions. *Phys. Rev. Lett.* **76,** 3152–3155. ISSN: 0031-9007, 1079-7114 (Apr. 1996).
18. Daniel, D., Timonen, J. V. I., Li, R., Velling, S. J. & Aizenberg, J. Oleoplaning Droplets on Lubricated Surfaces. *Nat. Phys.* **13,** 1020–1025. ISSN: 1745-2481 (Oct. 2017).
19. Wong, W. S. Y. *et al.* Capillary Balancing: Designing Frost-Resistant Lubricant-Infused Surfaces. *Nano Lett.* **20,** 8508–8515. ISSN: 1530-6984 (Dec. 2020).
20. Tamai, Y., Tanaka, H. & Nakanishi, K. Molecular Simulation of Permeation of Small Penetrants through Membranes. 1. Diffusion Coefficients. *Macromolecules* **27,** 4498–4508. ISSN: 0024-9297, 1520-5835 (Aug. 1994).
21. Hauer, L. *et al.* How Frost Forms and Grows on Lubricated Micro- and Nanostructured Surfaces. *ACS Nano* **15,** 4658–4668. ISSN: 1936-0851, 1936-086X (Mar. 2021).
22. Hauer, L., Wong, W. S. Y., Sharifi-Aghili, A., Kondic, L. & Vollmer, D. Frost Spreading and Pattern Formation on Microstructured Surfaces. *Phys. Rev. E* **104,** 044901 (Oct. 2021).
23. Liebovitch, L. S. & Toth, T. A Fast Algorithm to Determine Fractal Dimensions by Box Counting. *Phys Lett. A* **141,** 386–390. ISSN: 03759601 (1989).
24. Vold, M. J. Computer Simulation of Floc Formation in a Colloidal Suspension. *J. Colloid Sci.* **18,** 684–695. ISSN: 00958522 (1963).
25. Murphy, D. M. & Koop, T. Review of the Vapour Pressures of Ice and Supercooled Water for Atmospheric Applications. *Q. J. R. Meteorol. Soc.* **131,** 1539–1565. ISSN: 0035-9009 (2005).
26. Cussler, E. L. *Diffusion: Mass Transfer in Fluid Systems* 3rd ed (Cambridge, UK, 2009).